

Charge Density Analysis of Low-Valent Tetrels

Dissertation

zur Erlangung des mathematisch-naturwissenschaftlichen Doktorgrades

„Doctor rerum naturalium“

der Georg-August-Universität Göttingen

im Promotionsprogramm Chemie

der Georg-August University School of Science (GAUSS)

vorgelegt von

Benedikt Niepötter

aus Hannover

Göttingen, 2015

Betreuungsausschuss

Prof. Dr. Dietmar Stalke, Institut für Anorganische Chemie, Georg-August Universität

Prof. Dr. Sven Schneider, Institut für Anorganische Chemie, Georg-August Universität

Mitglieder der Prüfungskommission

Referent: Prof. Dr. Dietmar Stalke, Institut für Anorganische Chemie,
Georg-August Universität

Korreferent: Prof. Dr. Sven Schneider, Institut für Anorganische Chemie,
Georg-August Universität

weitere Mitglieder der Prüfungskommission

Prof. Dr. Thomas Waitz, Institut für Anorganische Chemie, Georg-August Universität

Prof. Dr. Ricardo Mata, Institut für Physikalische Chemie, Georg-August Universität

Dr. Francesca Fabbiani, Abteilung für Kristallographie, Georg-August Universität

Dr. Heidrun Sowa, Abteilung für Kristallographie, Georg-August Universität

Tag der mündlichen Prüfung: 15.01.2016

'Aut inveniam viam aut factiam.'
– I shall either find a way or make one.
Hannibal

Table of Contents

Abbreviations	v
1 Introduction	1
2 Single Crystal X-ray Diffraction.....	4
2.1 The Diffraction Condition.....	4
2.2 The Structure Factor.....	6
2.3 The Atomic Form Factor	8
2.4 The Independent Atom Model.....	9
2.5 Expansion of the IAM	9
2.6 Quality Indicators	10
2.6.1 Data Quality Indicators	11
2.6.2 Model Quality Indicators.....	13
3 Quantum Theory of Atoms in Molecules.....	17
3.1 Atomic Basin	18
3.2 Bonding between Atoms.....	18
3.3 Open and Closed Shell Interactions.....	20
3.4 Ellipticity	21
3.5 Non-covalent Interactions.....	21
4 Thermal Diffuse Scattering.....	23
4.1 Experimental Details	25
4.1.1 Data Collection.....	25
4.1.2 Data Reduction.....	26
4.1.3 Model Refinement.....	30
4.2 Errors in the data.....	33
4.2.1 Differences in the Multipole Model.....	33
4.2.2 Model quality.....	34
4.3 Resolution Dependent Scaling.....	37
4.3.1 Influence on the Model Quality.....	37
4.3.2 Influence on the MM.....	40
4.3.3 Course of the Scale Factor.....	41
4.4 Influence of the Box Size	41
4.4.1 Identification of the 'Best' Box	43
4.4.2 Influence on the Model.....	50
4.4.3 Influence on the Data	50
4.5 Empirical correction.....	54
4.5.1 Influence on the Model Quality.....	56
4.5.2 Influence on the Model.....	57
4.6 Conclusion.....	61

5	Chemistry of Low Valent Silicon	63
5.1	Multiple Bonds.....	63
5.2	Silylenes.....	65
5.3	Silaallenes and Silylones.....	66
	5.3.1 Cyclic Alkyl Amino Carbenes as Ligands	68
	5.3.2 Silylone (cAAC) ₂ Si.....	69
5.4	Experimental Charge Density Study of (cAAC ^{cy}) ₂ Si.....	71
	5.4.1 Data Collection	71
	5.4.2 Data Reduction.....	71
	5.4.3 Model Refinement.....	73
	5.4.4 Resolution-dependent Errors in (cAAC ^{cy}) ₂ Si.....	77
5.5	Topological Analysis of the EDD.....	82
	5.5.1 Topology of the Si–C bonds.....	83
	5.5.2 Topology around the Nitrogen Atoms.....	91
	5.5.3 Intramolecular Interactions.....	97
5.6	Conclusion	99
6	Unveiling Disorder in [Ge₈{N(SiMe₃)₂]₆]	101
7	Cross-validation.....	105
7.1	Cross-validation in Macromolecular Crystallography.....	105
7.2	Cross-validation in Charge Density Investigations.....	106
	7.2.1 Cross-validation using <i>XD2006</i>	107
	7.2.2 Example I: Mg(0) or Mg(+II).....	109
	7.2.3 Example II: Validation of Refinement Strategies	110
7.3	Conclusion	116
8	Summary and Outlook.....	117
9	Crystal Structure Determination in Collaboration.....	121
9.1	Crystal Selection and Manipulation	121
9.2	Data Acquisition.....	121
9.3	Data Processing and Model Refinement.....	121
9.4	Determined Structures.....	123
	9.4.1 Structures determined for Dr. Kartik C. Mondal	123
	9.4.2 Structures determined for Dr. Sudipta Roy.....	132
	9.4.3 Structure determined for Mykyta Tretiakov	136
	9.4.4 Structure determined for Dr. Chandrajeet Mohapatra.....	137
	9.4.5 Structures determined for Svenja Warratz	138
	9.4.6 Structure determined for Dr. Jie Li	140
	9.4.7 Structure determined for Dr. Dhandapani Ganapathy	141

10	Appendix	142
10.1	Additional Information on the Refinement of 1	143
10.2	Additional Information on the Refinement of 2	145
10.3	Tested Boxes for Compound 1.....	147
10.4	Tested Boxes for Compound 2.....	150
10.5	Additional Information on the Refinement of 3	152
10.6	Tested Boxes for Compound 3.....	156
10.7	Additional Information on the Properties of 3	157
10.8	Properties of the EDD of 3 without Corrections	164
10.9	Refinement Strategy for Cross-Validation of 3	170
10.10	Properties of the EDD of 3 with Chemcons	171
11	Danksagung.....	177
12	References	179
13	Curriculum vitae.....	187

Abbreviations

BCP	Bond Critical Point
cAAC	cyclic Alkyl Amino Carbene
CCD	Charge Coupled Device
CCP	Cage Critical Point
CGMT	<i>Carter, Golddar, Malrieu and Trinquier</i>
CR	<i>Clementi and Roetti</i>
Dipp	2,6-Diisopropylphenyl
ED	Electron Density
EDD	Electron Density Distribution
HF	<i>Hartree-Fock</i>
IAM	Independent Atom Model
MM	<i>Hansen & Coppens</i> multipole model
NBO	Natural Bond Orbital
NCI	Non-Covalent Interactions
NHC	N-Heterocyclic Carbene
QTAIM	Quantum Theory of Atoms in Molecules
RCP	Ring Critical Point
RDG	Reduced Density Gradient
SCM	<i>Su, Coppens and Macchi</i>
TDS	Thermal Diffuse Scattering
VSCC	Valence Shell Charge Concentration
VSEPR	Valence Shell Electron Pair Repulsion

1 Introduction

Silicon such as its lighter congener carbon exhibits four valence electrons and thus usually has four bonding partners. Compounds with a silicon atom connected to less than four bonding partners are called low valent. These silicon compounds usually show a very high reactivity. However, using the concept of kinetic stabilisation several compounds containing low valent silicon have been reported to date.^[1-8] The two most prominent classes of compounds containing low valent silicon are probably the disilenes and the silylenes, in which silicon has the oxidation state +II (Figure 1). Especially the silylenes have gained attention in the recent past because of their strong donor ability, which renders them as potential ligands in various catalytic reactions.^[9-12]

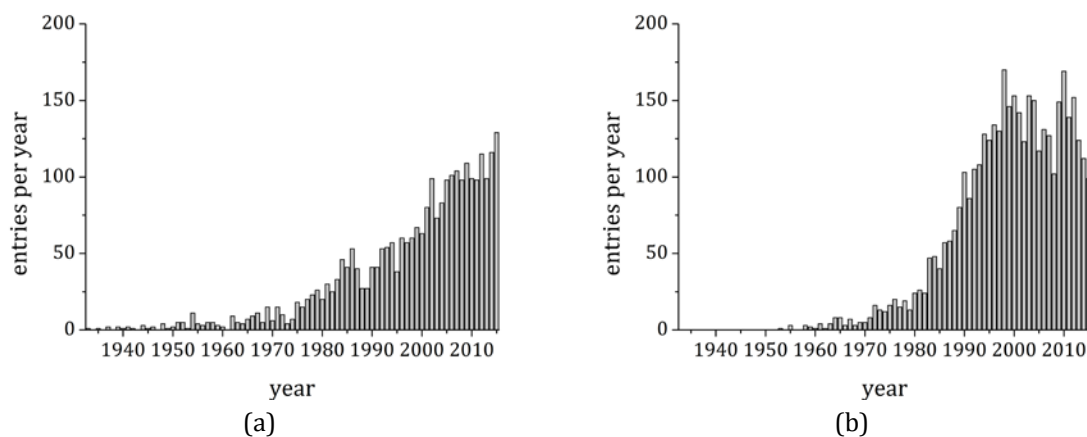


Figure 1: Annual number hits for scifinder® search with keyword: silene (a) and silyene (b).

In contrast to low valent silicon of oxidation state +II, reports on silicon of oxidation state zero are extremely rare. In 2003 *Kira et al.*^[13] synthesised a trisilaallene containing a silicon in formal oxidation state zero. In 2008 *Robison et al.*^[14] reported on a disilicon stabilised by two N-heterocyclic carbenes (NHCs). Another adduct of two cyclic alkyl amino carbenes (cAACs) with disilicon was reported recently.^[15] This work will focus on the structural analysis on an even more interesting class of silicon(0) compounds, the silylones. This class of divalent silicon compounds showing two non-bonding lone pairs was first synthesised by *Roesky et al.*^[16] in 2013. To date only one further example has been published (Figure 2).^[17]

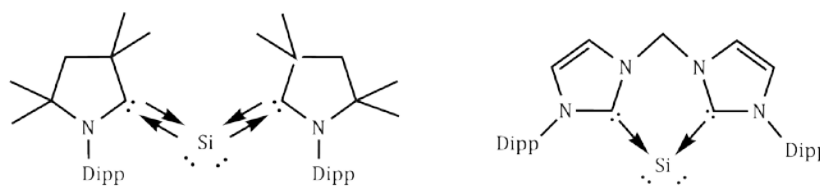


Figure 2: Lewis diagrams of the silylones by Roesky et al.^[16] and Driess et al.^[17]

The bonding situation in silylones usually is described by two donor-acceptor bonds between ligand molecules and a central silicon atom. In the following an arrow will be used in order to indicate this donor-acceptor interaction. However, in contrast to a normal dash in the Lewis diagram this arrow does not include two electrons, which therefore will be drawn separately. However, the applicability of this bonding model, originating from the field of 'coordination chemistry', at low valent main group elements is debated vigorously.^[18-21]

Therefore, it is essential to investigate the structure of these low valent silicon compounds experimentally. Consequently, this work will investigate the electron density distribution (EDD) of a silylone via experimental charge density study based on high-resolution X-ray data. Doubtlessly the EDD is one of the most information rich observables in natural science, allowing deep insights into a compound's structure, which is the key for a deeper understanding of the fundamental rules of chemistry.^[22-23] As X-rays are mainly scattered by electrons, single crystal X-ray diffraction is a powerful tool to investigate a compound's structure experimentally. The field of X-ray crystallography has developed tremendously since the first publication about the interference of X-rays with a crystal in 1912 by *Friedrich, Knipping and von Laue*^[24] and the first structures obtained from X-ray crystallography by father and son *Bragg*^[25-26]. The development in the field of detection devices, more brilliant X-ray tubes as well as synchrotrons, the easy and cheap access to computational time and improvements of the software enabled X-ray structure determination nowadays to be completed within hours. By this X-ray structure determination has become a standard analytical method, because it is the easiest way to obtain a three dimensional structure.

However, the information about the bonding drawn from these standard X-ray structure determinations is limited. Moreover, since a direct correlation between bond length and bond strength is not given^[27] more precise studies, such as experimental charge density studies, are needed to extract information from the EDD. Yet, these studies are far from being routine and especially an investigation of low valent silicon compounds pushes experimental charge density investigations to their limit.^[28] In these investigations the model becomes very complex, because the extremely reactive compounds need bulky substituents in order to be stabilised kinetically. The complexity of the model raises questions about the reliability and validity of the derived model. In routine crystal structure analysis, a rule of thumb is that the data to parameter ratio should be larger than ten to give a reasonable model. However, for charge density studies a simple limit for the data to parameter ratio cannot be given and new methods have to be developed in order to avoid overfitting.^[29-31] Another challenge when investigating such complex compounds, such as silylones, is the precision of the results. Since charge density studies are carried out in order

to extract the subtle bonding features systematic errors, which distort the outcome of the study, should be minimized or at least corrected for. Certainly one of most important neglected systematic errors in experimental charge density studies is thermal diffuse scattering (TDS). This resolution- and temperature-dependent inelastic scattering adds intensity to the *Bragg* maxima. Thus the modelled EDD is distorted as well, which may lead to false interpretations.

Therefore, the following points are essential in order to perform a reasonable analysis of a silylone's bonding situation; reduction of or correction for systematic errors,^[32] development of refinement procedures as well as tools for the analysis of the model quality.^[29] Consequently this work will not only concentrate on the topological analysis of the EDD, but also will focus on the correction of TDS induced errors (Section 4) and on the use of cross-validation in charge density refinements (Section 7). In this way a charge density investigation can give a much deeper insight into the silylone's structure and answer questions about the bonding type from an experimental study.^[33-45] The results of this investigation will be given in Section 5. However, first a short introduction into the most important principals of the structure investigation using X-ray diffraction data (Section 2) and of the topological analysis of EDDs will be given (Section 3).

2 Single Crystal X-ray Diffraction

The following chapter will give a short overview of the main principles of single crystal X-ray diffraction. It will start with a short introduction into the theoretical principles of diffraction. Following this, the standard independent atom model (IAM) and the more precise *Hansen & Coppens* multipole model (MM)^[46-47] will be discussed. The last part of this section will deal with common indicators for data and model quality.

2.1 The Diffraction Condition

By the definition of the *International Union of Crystallography* a crystal is a material that has essentially a sharp diffraction pattern.^[48] All these crystals, with only a few exceptions, show periodic repetition in all three dimensions. The smallest building block of such a crystal is referred to as the unit cell. Each point r in the unit cell can be described by their fractal coordinates x, y, z in a, not necessarily orthogonal, coordination system given by the three vectors $\vec{a}, \vec{b}, \vec{c}$ that span the unit cell (Eq. 2-1.)

$$r = x \cdot \vec{a} + y \cdot \vec{b} + z \cdot \vec{c} \quad \text{Eq. 2-1}$$

Repeating this building block in all three dimensions leads to a description of the whole crystal. The crystal thus can be understood as a lattice. According to the rules of optics, interference can appear if a lattice is exposed to waves of a wavelength in the range of the lattice distances. Thus interference appears by exposing crystals to X-rays, since the distances in a crystal lattice are normally in the range of a few Ångström.

On a microscopic level, the incident wave forces the electrons in the atoms to a temporarily excited state. The corresponding energy difference is released from the atom by the emission of a photon of the same wavelength as the incident beam. This process is called elastic scattering. Herby the atom becomes the starting point of a new radial wave. However, arising from energy transfer also inelastic scattering can appear, leading to small changes in the wavelength of the diffracted beam. Even though the intensities from inelastic scattering are much smaller than from elastic, they have to be taken into account in some cases (see Section 4).^[49] However in the following, only elastic scattering will be taken into account.

To understand the condition under which a scattered wave can be observed let P_1 and P_2 be two scattering centres with a difference vector \vec{R} . The phase of the wave scattered at P_1 has a path difference Δ to the wave scattered at P_2 (Figure 3a). A maximum in the diffraction

pattern can be observed, whenever it comes to constructive interference. Therefore, the path difference Δ has to be an integer multiple of the wavelength λ .

$$\Delta = \vec{R} \cdot (\vec{k}_0 - \vec{k}) = n \cdot \lambda \quad n \in \mathbb{Z} \quad \text{Eq. 2-2}$$

Herein \vec{k}_0 denotes the wave vector of the incident wave and \vec{k} the one of the scattered wave, respectively. In term of the three dimensions of a crystal lattice this can be rewritten to the following equations.

$$\begin{aligned} \vec{a} \cdot \overline{\Delta k} &= |\vec{a}| \cdot |\overline{\Delta k}| \cdot \cos(\overline{\Delta k}, \vec{a}) = h \cdot \lambda \\ \vec{b} \cdot \overline{\Delta k} &= |\vec{b}| \cdot |\overline{\Delta k}| \cdot \cos(\overline{\Delta k}, \vec{b}) = k \cdot \lambda \quad h, k, l \in \mathbb{Z} \\ \vec{c} \cdot \overline{\Delta k} &= |\vec{c}| \cdot |\overline{\Delta k}| \cdot \cos(\overline{\Delta k}, \vec{c}) = l \cdot \lambda \end{aligned} \quad \text{Eq. 2-3}$$

Herein $\overline{\Delta k}$ is the difference of the wave vectors. The integers h , k and l are called *Miller indices* and are used to characterise a reflection. In one dimension all scattered waves for a given incident wave vector \vec{k}_0 lie on the surface of a cone. Thus the necessary condition, the *Laue condition*^[24], for constructive interference in three dimensions is, that the difference wave vector $\overline{\Delta k}$ is a vector to a point in a reciprocal lattice, which can be expressed in terms of the basis vectors \vec{a}^* , \vec{b}^* , \vec{c}^* .

$$\begin{aligned} \overline{\Delta k} &= h \cdot \vec{a}^* + k \cdot \vec{b}^* + l \cdot \vec{c}^* = h_{hkl} \\ \text{with } &= \frac{\vec{b} \times \vec{c}}{V}, \quad \vec{b}^* = \frac{\vec{a} \times \vec{c}}{V}, \quad \vec{c}^* = \frac{\vec{b} \times \vec{a}}{V} \end{aligned} \quad \text{Eq. 2-4}$$

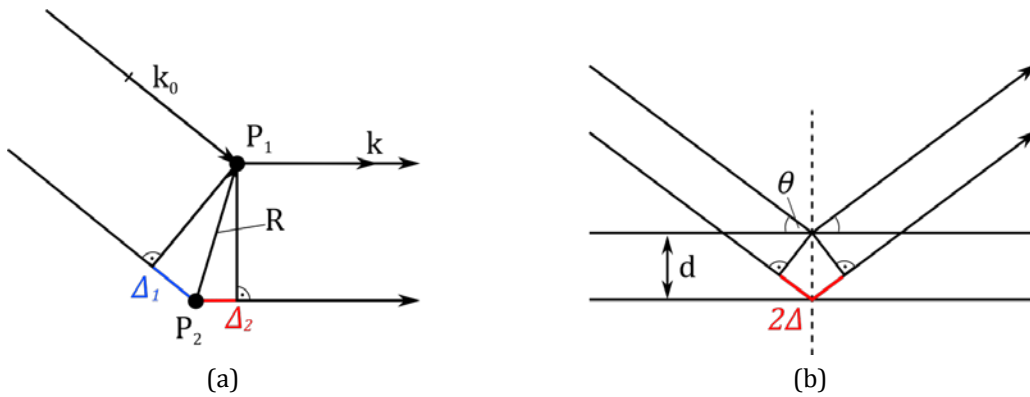


Figure 3: Scattering of X-rays according to Laue (a) and Bragg (b).

An alternative way of description of the diffraction condition is the following. Three points of the crystal lattice can be used to define a plane. These planes can be used to describe the scattering of X-rays in terms of a reflection as it was done by *W. L. Bragg* and *W. H. Bragg*

(Figure 3b).^[50] The lattice planes intersect the axis of the unit cell in $1/h$, $1/k$ and $1/l$. Therefore, the planes are characterised by (hkl) . Again, constructive interference only appears if the path difference between the reflected waves is an integer multiple of the wavelength λ . The condition for constructive interference can thus be written as

$$2\Delta = 2d_{hkl} \cdot \sin(\theta) = n \cdot \lambda \quad n \in \mathbb{Z} \quad \text{Eq. 2-5}$$

with $d_{hkl} = 1/h_{hkl}$ the distance between two lattice planes and θ the incident angle of the X-ray beam with respect to these planes. This condition is known as *Bragg's law*.

2.2 The Structure Factor

The intensity of a reflection hkl is determined by the arrangement of the atoms in the crystal. The electrons of each atom in the unit cell are the starting points for a scattered wave. The spatial arrangement of the electrons in the unit cell is described by the electron density $\rho(r)$ (ED). Thus the wave vector that results from the superposition of these waves, the structure factor F_{hkl} , is dependent on the ED.

$$\vec{F}_{hkl} = \int_V \rho(r) \cdot e^{2 \cdot \pi \cdot i \cdot h_{hkl} \cdot r} dr \quad \text{Eq. 2-6}$$

Consequently, the EDD is obtained from the structure factors by *Fourier* transformation.^[51]

$$\rho(r) = \frac{1}{V} \sum_{h_{hkl}} \vec{F}_{hkl} \cdot e^{-2 \cdot \pi \cdot i \cdot h_{hkl} \cdot r} \quad \text{Eq. 2-7}$$

If all structure factors \vec{F}_{hkl} are known, the ED at each point r can be calculated. The structure factor can be expressed by the intensity $|F_{obs}|$ and the phase ϕ of the measured wave at a point hkl of the reciprocal space. The intensity I_{hkl} of a reflection hkl is given by

$$I_{hkl} = \frac{e^4 \cdot \lambda^3 \cdot \Omega}{m^2 \cdot c^4 \cdot V^2} \cdot I_0 \cdot L \cdot P \cdot T \cdot E \cdot |F_{hkl}|^2. \quad \text{Eq. 2-8}$$

Thus the intensities are proportional to square of the absolute value of the structure factor F_{hkl} .^[52] Herein e and m are the charge and the mass of an electron; c is the velocity of light. Ω and V describe the volume of the crystal and the unit cell, respectively. I_0 is the intensity of the incident X-ray beam and λ its wavelength. For a given experiment all these factors remain constant. The contributions of the Lorentz factor L , polarization factor P , transmission factor T and the extinction factor E can be eliminated during the data processing.

Consequently, the absolute value of the structure factor F_{hkl} is available from the intensity of the reflection I_{hkl} . However, the phase ϕ of the structure factor is not measurable directly from the X-ray diffraction experiment. Therefore, during the structure solution the phases are reconstructed approximately from the data itself.^[53-55] In the next step, the structure refinement, the EDD obtained after structure solution is used to derive a model that represents the atomic structure. This model is refined by least square methods, in which the difference between the calculated and the observed structures factors of the model, F_c and F_o , are minimised. During the refinement progress the phase information is ameliorated by reconstruction from the model.

Furthermore, the model refinement cures for additional shortcomings. For an unbiased calculation of the EDD an infinite number of error-free observed structure factors would be needed. However, e.g. truncation errors are inevitable because the experimental resolution is limited to $\lambda/2$. During the model refinement these truncation errors as well as experimental errors in the intensities are reduced.

2.3 The Atomic Form Factor

The number of waves scattered from an atom is dependent on the number of electrons. However, the electrons are not located point-like at the atom centre but distributed around the core. This distribution is described by the atomic ED $\rho_a(r)$. The *Fourier* transformed of this atomic ED is called the atomic form factor f .

$$f_{hkl} = \int_V \rho_a(r) \cdot e^{2\cdot\pi\cdot i\cdot h_{hkl}\cdot r} dr \quad \text{Eq. 2-9}$$

The structure factor \vec{F}_{hkl} for a given reflection h_{hkl} can be calculated by summation over all waves scattered at the individual atom a at position r_a with an atomic form factor f_a .

$$\vec{F}_{hkl} = \sum_a f_a(hkl) \cdot e^{-2\cdot\pi\cdot i\cdot h_{hkl}\cdot r_a}. \quad \text{Eq. 2-10}$$

The expansion of the ED of an atom results in a small shift introduced to the points of crystal lattice, since an atom can no longer be assumed to be point like. As a result, the scattering power of an atom and consequently of the whole crystal is reduced with the scattering angle θ .

The atomic form factor can be further divided into a contribution of the core and the valence density. The distribution of the core electrons is much more point-like than the one of the valence density. Therefore, the core electrons scatter up to much higher θ values while the valence electrons only diffract up to a much smaller angle (Figure 4).^[52]

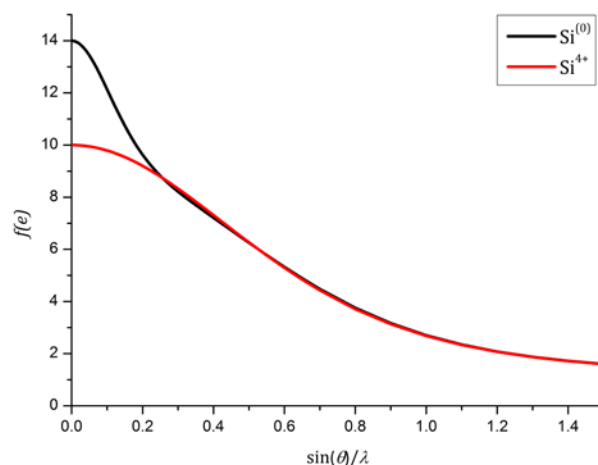


Figure 4: Atomic scattering factors of the neutral silicon atom and silicon core based on tabulated values computed from the SCM scattering bank.^[56-57] The difference in the scattering factor appears only at low θ values.

2.4 The Independent Atom Model

In the independent atom model (IAM) approximation the atoms are assumed to be spherical, non-interacting and neutral. The ED $\rho_a(r)$ of each atom a is calculated from quantum mechanical calculations. The *Fourier* transformation of these atomic electron densities are used to calculate the structure factors for a model according to Eq. 2-10.

During the refinement the differences between the observed structure factors F_o and the ones calculated for the model F_c are minimized by allowing the atoms to change their fractional coordinates x , y and z . Additionally the thermal movement of each atom is modelled by up to six atomic displacement parameters U_{ij} , because the time scale of a diffraction experiment is larger than the one of the thermal movement in the crystal. As a result, the scattering power at higher resolution is lowered, as only a thermally smeared picture of the EDD can be measured. This thermal movement is treated by an addition of a normal probability distribution function $p_a(r)$ onto the atomic density distribution $\rho_a(r)$. The Fourier transform of this probability distribution $q_a(r)$ is described by six additional atomic displacement parameters U_{ij} modelling an anisotropic ellipsoid

$$q_a(h_{hkl}) = e^{-2\cdot\pi^2\cdot h_{hkl}^T [U]_a \cdot h_{hkl}} \quad \text{Eq. 2-11}$$

with $[U]_i$ the symmetric matrix containing the values U_{ij} . In some cases, only one parameter U_{11} is refined leading to an isotropic description. Taking the thermal smearing of the ED into account the structure factor of a reflection hkl can be calculated from the IAM by ^[49,52]

$$\vec{F}_{hkl} = \sum_a f_a(hkl) \cdot e^{-2\cdot\pi\cdot i \cdot h_{hkl} \cdot r_a} \cdot e^{-2\cdot\pi^2\cdot h_{hkl}^T [U]_a \cdot h_{hkl}}, \quad \text{Eq. 2-12}$$

2.5 Expansion of the IAM

Several models have been developed in order to take the ED into account that is located at the area between atoms or in the non-bonding regions.^[46-47,58-64] The most prominent is the *Hansen & Coppens* multipole model (MM).^[46-47] In the MM the EDD of each atom $\rho_a(r)$ is no longer spherical and neutral. The density of an atom is described by the combination of a spherical core density, a spherical valence density and an aspherical valence density.

$$\rho_a(r) = P_c \rho_c(r) + P_v \kappa^3 \rho_v(\kappa r) + \sum_{l=0}^{l \max} \kappa'^3 R_l(\kappa' r) \sum_{m=-l}^l P_{lm} d_{lm}(\vartheta, \varphi) \quad \text{Eq. 2-13}$$

The core $\rho_c(r)$ and the spherical part of the valence density $\rho_v(\kappa r)$ are taken from *Hartree-Fock* (HF) or relativistic HF atomic wave functions.^[56-57,65] The aspherical part of the density is again separated into a spherical and an aspherical part. For the spherical part $R_l(\kappa' r)$ usually Slater type functions from energy optimization of free atoms are used. The aspherical part is modelled by spherical harmonics d_{ml} . The parameters κ and κ' allow the valence density to contract or expand.

The population of the core and valence density can be adjusted by the parameters P_c and P_v , respectively. The population of the spherical valence density is called monopole population. The population parameters P_{lm} are called multipole populations. Their expansion is usually truncated at $l = 4$, the hexadecapole level. The population parameter P_{00} gives together with P_v the number of valence electrons. All other terms with $l \neq 0$ integrate to zero and thus just lead to a distortion of the valence density. The *Fourier* transform of the density modelled by the multipoles gives the atomic form factor for the aspherical atom. The resulting equation can be found in the literature but is, for the sake of clarity, not shown here.^[46,51]

Besides the expansion of spherical atom by the MM it is also possible to treat the atomic displacement in a more sophisticated way. A commonly used method is the three dimensional *Gram-Charlier* expansion, first introduced in 1974 by *Johnson & Levy*.^[66] In this expansion the *Fourier* transformed of the probability distribution p is now given by

$$q(h) = \left[1 - \frac{4}{3}\pi^3 i c^{jkl} h_j h_k h_l + \frac{2}{3}\pi^4 c^{jklm} h_j h_k h_l h_m + \dots \right] \cdot q_0(h) \quad \text{Eq. 2-14}$$

where c^{jkl} , c^{jklm} , ... are the third-, fourth-, ... order tensorial *Gram-Charlier* coefficients and q_0 is the harmonic atomic displacement (see Eq. 2-11).^[51,67-68]

2.6 Quality Indicators

The refinement of a MM up to hexadecapole level including the expansion and contraction parameters and without any symmetry restrictions adds 27 parameters to the nine parameters of the IAM resulting in up to 36 parameters per atom. The use of *Gram-Charlier* expansion up to third order raises this number by 10 the use of third and fourth order by 25. In order to guarantee the convergence of the model and to avoid overfitting of the data, special requirements on the data quality and the refinement procedure have to be imposed. Because of the high number of parameters, it is unavoidable to measure diffraction data up to very high resolution (1 \AA^{-1} or 0.5 \AA) in order to make sure that the data to parameter ratio is sufficient. Moreover, the more point-like core electrons scatter to high angles while the diffuse bonding electrons scatter at relatively low angles. As a result, the high-resolution

data allows a better deconvolution of thermal motion, bonding features and core electrons. Furthermore it is crucial to collect the low-order data with extraordinary care since the important information about the bonding electrons only goes into the low resolution data. E.g. for silicon nearly all information about the valence electrons is stored in the reflection with $\sin(\theta)/\lambda < 0.3$ (Figure 4).

The refinement of a MM has to be done with special care likewise. In order to handle any problems that may arise in the convergence or from correlation between the model parameters their number is increased step by step. The model itself should be investigated carefully after each step. In the following a couple of quality indicators are presented that allow an estimation of the quality of both data and model, respectively. However, the criteria should not be seen as a gold standard but more as guidelines. Details about the data reduction and the refinement procedure can be found in the experimental section of the refinements.

2.6.1 Data Quality Indicators

The data quality can be judged at different points of the data collection and processing. The first and of course crucial step of selecting the crystal should be done with special care.^[69] Once the 'perfect' crystal is chosen and the data collection was successful, the decision whether a dataset is good enough to run a MM refinement can be made on the basis of the statistics after data processing. Programs such as *SADABS*^[70-71] and *XPREP*^[72] can be used to analyse the data. The most prominent of these criteria are probably the residual values (R values) for the internal agreement between symmetry related structure factors, R_{int} , and the residual for the errors of the structure factor, R_{sigma} . However, since the R_{int} is not independent of the multiplicity, which should be very high for charge density datasets (>4 for all data and >10 for the inner data), it is strongly recommended to use the multiplicity independent residual values $R_{r.i.m}$ and $R_{p.i.m}$.^[73-74]

$$R_{int} = \frac{\sum_h \sum_i |F_{o,i}^2(h) - \langle F_o^2(h) \rangle|}{\sum_h F_o^2(h)} \quad R_{sigma} = \frac{\sum_h \sigma(F_o^2(h))}{\sum_h F_o^2(h)}$$

Eq. 2-15

$$R_{r.i.m.} = \frac{\sum_h \left(\frac{N}{N-1}\right)^{1/2} \sum_i |F_{o,i}^2(h) - \langle F_o^2(h) \rangle|}{\sum_h F_o^2(h)} \quad R_{p.i.m.} = \frac{\sum_h \left(\frac{1}{N-1}\right)^{1/2} \sum_i |F_{o,i}^2(h) - \langle F_o^2(h) \rangle|}{\sum_h F_o^2(h)}$$

All these residuals can be calculated in resolution shells using the program *XPREP*^[72]. Boundaries for charge density datasets are hard to define. However, one could state that the R values for the low resolution data (<1 Å) should not be larger than a few per cent. For the higher resolution data, the internal agreement factor usually increases. At best $R_{r.i.m}$ and $R_{p.i.m}$

should be smaller than 10 % or 0.1, respectively, for the whole resolution range but this is definitely a too harsh condition for a general disqualifier. Values of up to 20 % might in some cases also be acceptable. Anyhow, the course of the residuals with the resolution should be smooth (see Figure 5). Furthermore, *XPREP*^[72] gives information on the completeness, the multiplicity and the significance (I/σ) of the data. Of course, the goal should always be to measure all possible reflections so the completeness is 100 %. Furthermore, the multiplicity should be at least four for all data and for the low-order data at least ten.

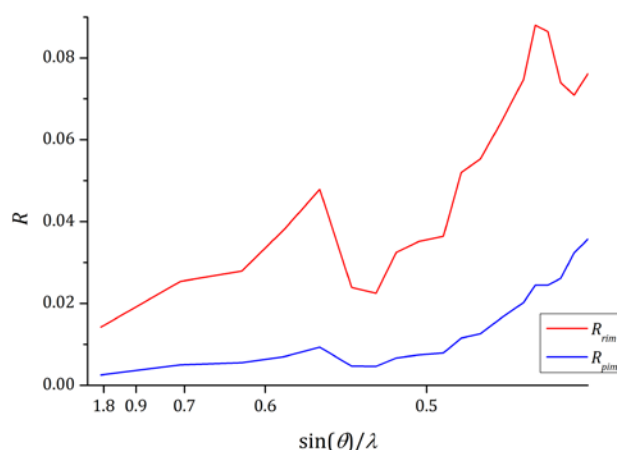


Figure 5: Exemplary course of $R_{r.i.m}$ (black) and $R_{p.i.m}$ (red).

Another powerful tool to judge on the data quality is the upper limit of the significance of the data. In 2010 *Diederichs*^[75] published the indicator $(I/\sigma)_{asymptotic}$ to estimate the systematic instrument errors.

$$(I/\sigma)_{asymptotic} = \frac{1}{g} \quad \text{Eq. 2-16}$$

The parameter g is determined during the error model creation in *SADABS*, where the σ_{raw} were adjusted to fit to a χ^2 statistic.

$$\sigma_{cor}^2 = (K \cdot \sigma_{raw})^2 + (g \cdot \langle I \rangle)^2 \quad \text{Eq. 2-17}$$

Using plots of I/σ versus I the data quality can easily be investigated. Although these plots were initially designed for macromolecular X-ray crystallography these plots are also useful for small molecule crystallography.^[76] The plots are automatically generated by the program *SADABS*. For a good dataset $(I/\sigma)_{asymptotic}$ should reach at least 60. However, within this work it will be shown that it is strongly dependent on the integration routine (see Section 4.4) and should therefore be used with care.

2.6.2 Model Quality Indicators

The quality of the results of a MM refinement can be monitored by various quality criteria. Similar to refinements of the IAM it is common to use R values, which measure the agreement of the calculated and observed structure factors. However, unlike in most IAM refinements the standard value is not the R_1 based on F but the R_1 based on F^2 .^[77] It has to be noted that this is not the weighted wR_2 usually used as an alternative to the R_1 .

$$R_1(F) = \frac{\sum_h ||F_o(h)| - |F_c(h)||}{\sum_h |F_o(h)|} \quad R_1(F^2) = \frac{\sum_h |F_o^2(h) - F_c^2(h)|}{\sum_h F_o^2(h)}$$

Eq. 2-18

$$wR_2 = \sqrt{\frac{\sum_h w(F_o^2(h) - F_c^2(h))^2}{\sum_h wF_o^2(h)^2}}$$

In the case of an IAM the standard criterion for the $R_1(F)$ is usually 5 % and for wR_2 10 %, respectively. The residuals after a satisfactory MM certainly are much lower and lie frequently in the range of a few per cent for the $R_1(F^2)$. However, it has to be said clearly that these values only mirror the fit between the calculated and observed structure factors. Consequently, the R values improve for example if systematic errors are fitted into the model. Therefore, it is essential to use other ways to determine the data quality as well. The criteria to judge on a refinement besides R values should at least include: the deviation of the $\sum F_o^2 / \sum F_c^2$ quotient with the resolution, the appearance of the normal probability plot^[78], a residual density analysis^[79] and of course the chemical and physical reasonableness of the model itself.

2.6.2.1 DRK-Plot

A closer inspection of observed and calculated structure factors is possible using the $\sum F_o^2 / \sum F_c^2$ quotient with resolution first described by *Zavadnik et al.*^[80] (Figure 6). The quotient can be analysed by using the program *DRKplot*^[78] available within the *WinGX*^[81] suite. The optimum would be a quotient of unity over the whole resolution range. However, even an excellent dataset will show deviations within $\pm 2\%$ and variation up to $\pm 5\%$ are often seen. Of course, these deviations should be checked carefully, but in some cases these errors might be acceptable. A strong variation in the high-resolution range might indicate problems with the deconvolution of the thermal movement. Errors in the low-order data usually indicate problems with the very strong low-order data. These should be checked with special care because of their importance for the valence density. However, it should always be kept in mind that much less data points contribute to the quotient in this resolution range. Therefore, it might be distorted by single bad data points.

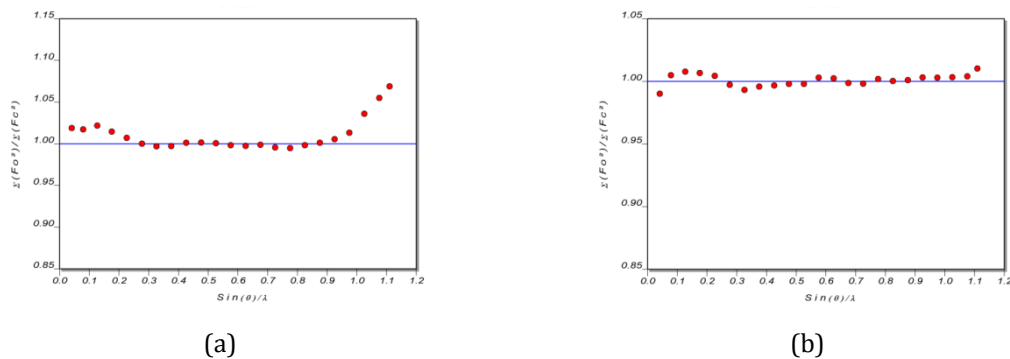


Figure 6: Plot of $\sum F_o^2 / \sum F_c^2$ vs. $\sin(\theta) / \lambda$ (DRK-plot) indicating an overestimation of the high-order data (a) and showing no serious errors (b).

Another helpful quality indicator for the refined model, as well as the data, is the normal probability plot, which also can be produced using *DRKplot*^[78] (Figure 7). As shown by *Abrahams and Keve*^[77,82] the distribution of

$$\Delta R(h) = \frac{F_o^2(h) - F_c^2(h)}{\sigma^2(h)} \tag{Eq. 2-19}$$

should be *Gaussian*, if no systematic errors are present. For the normal probability plot an ordered statistic of ΔR is plotted against the quantiles of the expected distribution. The absence of any systematic error can easily be seen by a slope of one and a zero intercept of zero. A slope larger than unity would indicate that the estimated standard deviations are too small. This is normally the case for datasets measured with Charge Coupled Device (CCD) detectors. However, by applying small changes to the weighting scheme (Eq. 2-20) a distribution closer to a normal distribution can be achieved.

$$w(h) = \left[\sigma^2(h) + \left(a \left(\frac{1}{3} F_o^2(h) + \frac{2}{3} F_c^2(h) \right) \right)^2 + b \left(\frac{1}{3} F_o^2(h) + \frac{2}{3} F_c^2(h) \right) \right]^{-1} \tag{Eq. 2-20}$$

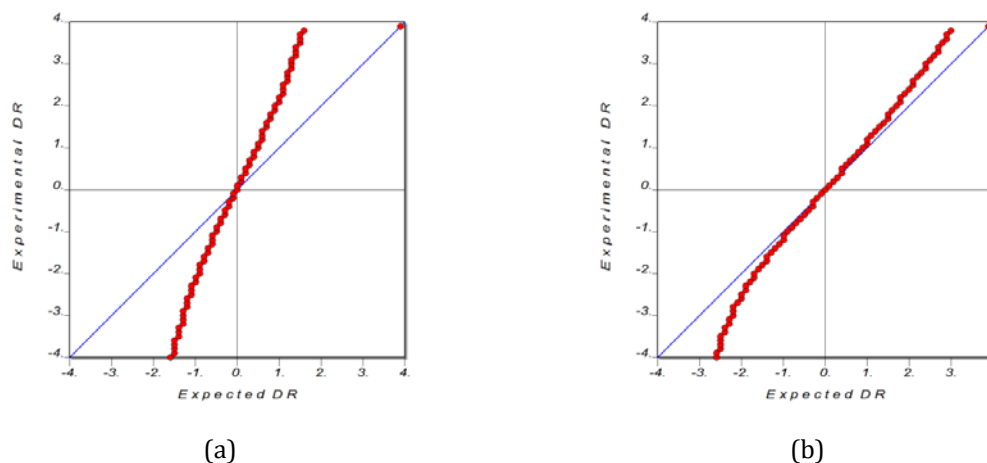


Figure 7: Normal probability plot indicating an underestimation of the standard deviation (a) and showing no serious errors in the standard deviation (b).

2.6.2.2 Residual Density Analysis

The residual density distribution $\Delta\rho(r)$ is a measure for all errors and shortcoming of the dataset and the model. It can be calculated directly from the observed and calculated structure factor.^[79]

$$\Delta\rho(r) = \frac{1}{V} \sum_h (|F_o| - |F_c|) \cdot e^{i\phi_c} \cdot e^{-2\pi i h r} \quad \text{Eq. 2-21}$$

After a MM refinement the residual density distribution should be ‘flat’ and ‘featureless’. The flatness of the residual density distribution is normally quantified by its highest peak and deepest hole, the maximum and the minimum value of the residual density. Features in the residual density are harder to quantify. However, it is a parameter worth looking at, as the least-squares refinement minimizes the flatness, but not the featurelessness of the residual density distribution.^[79] One way to investigate the features is to plot the residual density distribution together with the model (Figure 8).

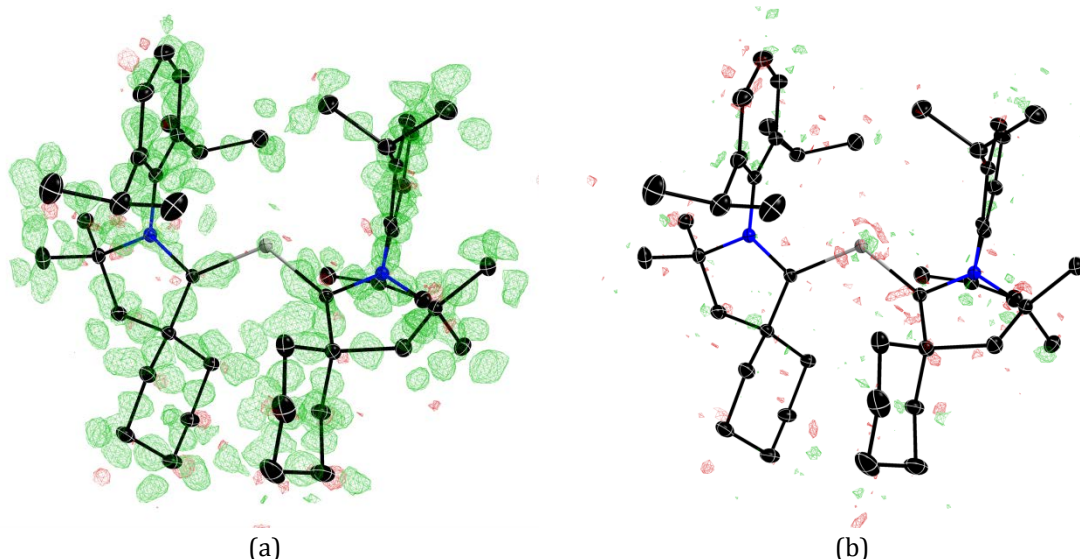


Figure 8: Residual density map after IAM (a) and after MM refinement (b). Atomic displacement parameters are depicted at 50 % probability level. Hydrogen atoms are omitted for clarity. Positive residual density is shown in green negative in red. Isolevels are depicted at $\pm 0.16 e \cdot \text{\AA}^{-3}$ (a) and $\pm 0.09 e \cdot \text{\AA}^{-3}$ (b).

In order to quantify the features in the residual density one can analyse the distribution regarding its fractal dimension d_f . This concept was introduced to charge density refinements by Meindl & Henn in 2008.^[79] Using the program *JNK2RDA*^[79] the fractal dimension can be plotted against the residual density (Figure 9). For a perfect model without any errors and without any noise the $d_f(0)$ should peak close to 3 and the shape of the graph would mimic a parabola. However, even for theoretical data without noise this maximum is never reached. A value close to or above $d_f(0)=2.7$ turned out to be indicative for a very good

model. Values of $d^f(0) \sim 2.6$ as well as shoulders or broad tails only on one side of the plot are indicators for problems in the model or data.^[79]

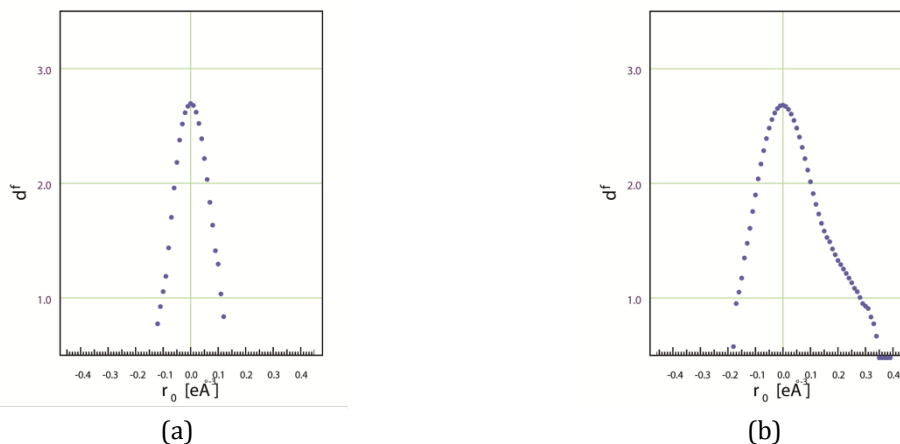


Figure 9: Fractal dimension plot indicating nearly featureless residual density (a) and showing structured positive residual density (b).

Another useful indicator introduced by *Meindl & Henn* is the number of gross residual electrons.^[79]

$$e_{gross} = \frac{1}{2} \int |\Delta\rho(r)| dV \quad \text{Eq. 2-22}$$

e_{gross} can be understood as the number of wrongly assigned electrons in the unit cell and therefore describes the errors introduced by the model, the data and random noise. Therefore e_{gross} in particular is suitable for the comparison of different datasets or refinement strategies.

3 Quantum Theory of Atoms in Molecules

The EDD on its own is only of little help for analysing the bonding features because it is dominated by the concentrated core electrons (Figure 10a). In order to investigate the bonding in a molecule the information about the bond has to be extracted from the ED. The simplest tool to do so is to subtract a reference density, such as the density of the IAM, from the density obtained after MM refinement. The result is the so-called deformation density that is no longer dominated by the core electrons because these are also included in the IAM refinement. The electrons of the bonding region become visible (Figure 10b). However, for a classification of the bonding this method is not sensitive enough in most cases.

Therefore, the quantum theory of atoms in molecules (QTAIM) by *Bader*^[83] is used to investigate the bonding situation in most experimental charge density studies. According to *Bader* the EDD can be partitioned uniquely into subsystems, the atoms in molecules. The properties of a molecule, therefore, can be described by the sum of the properties of the atoms it is composed of.^[84-86] The bonding situation between these atoms are analysed using the second derivative of the ED, the *Laplacian*, which indicates charge concentration or depletion and is much more sensitive than the ED itself (Figure 10c).^[87] The following chapter will give an overview about the most important properties used to identify and characterise bonding in molecules.

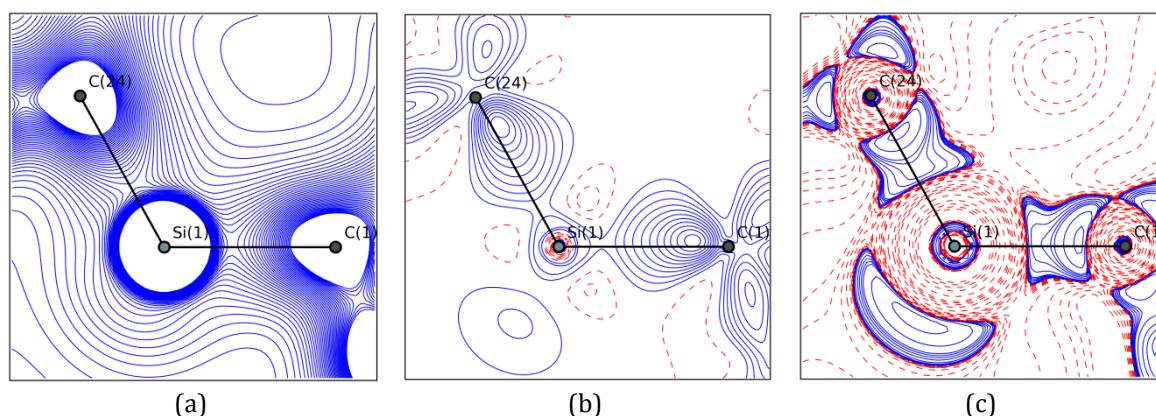


Figure 10: Electron density (a), deformation density (b) and Laplacian (c) in the same plane.

3.1 Atomic Basin

An atom in a molecule can be defined as a disjoint spatial sub-region of the real space with the help of the gradient, $\nabla\rho(r) = \left(\frac{\partial\rho}{\partial x}, \frac{\partial\rho}{\partial y}, \frac{\partial\rho}{\partial z}\right)^T$, of the scalar field $\rho(r)$. The gradient is a vector directed along the largest increase in the ED and links a minimum or saddle point in the ED with a maximum or saddle point. All paths ending in one maximum, which is at the core of each atom, belong to one sub-region (Ω). These basins are boarded by a surface where the gradient vanishes. This surface is called zero-flux surface (S).^[85-86]

$$\nabla\rho(r) \cdot n(r) = 0, \quad \forall r \in S, n(r) \perp S \quad \text{Eq. 3-1}$$

Integration of the ED in this basin gives the *Bader* charge. The definition of the atomic basin includes another important element of QTAIM, the bond paths and the bond critical point (BCP) (Figure 11).

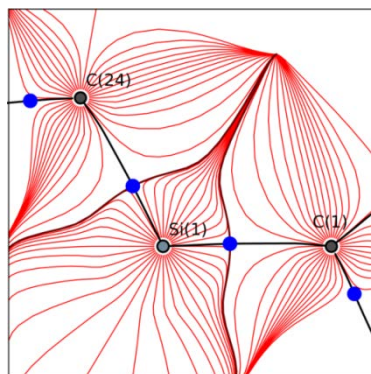


Figure 11: Gradient paths (red) of the ED. Intersection of the zero-flux surface shown in maroon. Bond path depicted as black line the critical points are shown as blue dots.

3.2 Bonding between Atoms

An extraordinary gradient path is the path that connects a saddle point with exactly two maxima of the ED. This path, following local maxima in two directions of space, acts as privileged exchange channels in the ED and is called bond path.^[88-90] Two atoms linked by a bond path can be regarded as bonded. However, it has to be stressed out that this bonding neither has to be a two centre two electron bond ^[89], nor that the interaction has to be attractive.^[87,91] As already mentioned above, gradient paths originate and end in extrema of the ED, in which the gradient vanishes. These points are called critical points.

Table 1: Classification of critical points.

(m,n)	Topology in $\rho(r)$	Type
(3,-3)	local maximum	nuclear position
(3,-1)	maximum in two directions minimum in one direction	bond critical point (BCP)
(3,+1)	maximum in one directions minimum in two directions	ring critical point (RCP)
(3,+3)	local minimum	cage critical point (CCP)

Critical points are characterised by the rank m of *Hessian* matrix $H(r)$ (Eq. 3-2) of the ED and the sum of the signs n of the three eigenvalues $\lambda_1 < \lambda_2 < \lambda_3$. By this the critical points are divided into bond-, ring- and cage critical points as well as nuclear positions (Table 1).^[87]

$$H(r) = \begin{pmatrix} \frac{\partial^2 \rho}{\partial x^2} & \frac{\partial^2 \rho}{\partial x \partial y} & \frac{\partial^2 \rho}{\partial x \partial z} \\ \frac{\partial^2 \rho}{\partial y \partial x} & \frac{\partial^2 \rho}{\partial y^2} & \frac{\partial^2 \rho}{\partial y \partial z} \\ \frac{\partial^2 \rho}{\partial z \partial x} & \frac{\partial^2 \rho}{\partial z \partial y} & \frac{\partial^2 \rho}{\partial z^2} \end{pmatrix} \quad \text{Eq. 3-2}$$

The trace of the Hessian, also called *Laplacian* $\nabla^2 \rho(r)$, displays whether the ED is locally concentrated ($\nabla^2 \rho(r) < 0$) or depleted ($\nabla^2 \rho(r) > 0$) (Figure 10c). The *Laplacian* can be used to investigate the EDD along the bond as well as in the non-bonding area.

$$\nabla^2 \rho(r) = \frac{\partial^2 \rho}{\partial x^2} + \frac{\partial^2 \rho}{\partial y^2} + \frac{\partial^2 \rho}{\partial z^2} = \lambda_1 + \lambda_2 + \lambda_3 \quad \text{Eq. 3-3}$$

Maxima in the *Laplacian* which are not located in close proximity to the core of an atom are referred to as valence shell charge concentrations (VSCCs). It has been shown that the VSCCs match the number and location of lone pairs of the VSEPR model.^[84,92-94] However, it has to be pointed out that the VSCCs cannot generally be equated with lone pairs.^[95]

3.3 Open and Closed Shell Interactions

Within the QTAIM framework it is possible to distinguish between different bonding types. Usually two classes of interaction are distinguished. Closed shell interactions, such as ionic or van der Waal's bonds, are dominated by the kinetic energy $G(r)$. In open shell interactions on the other hand the main contribution is the potential energy $V(r)$. This bonding type is found in covalent or polar interactions.^[87,90] Using the relation

$$\frac{1}{m} \left(\frac{h}{4\pi} \right)^2 \nabla^2 \rho(r) = V(r) + 2 \cdot G(r) \quad \text{Eq. 3-4}$$

the value of the *Laplacian* at the BCP can be used for the classification of a bond. A negative value of the *Laplacian* indicates an open shell interaction. The positive curvature along the interaction (λ_3) is larger than the sum of the negative curvatures perpendicular to the interaction ($\lambda_1 + \lambda_2$). In total the charge is concentrated at the BCP and the ED is found to be relatively high. In contrast, for closed shell interaction the ED is usually low. The *Laplacian* is positive, indicating small curvature in the direction of the bonding ($\lambda_3 < (\lambda_1 + \lambda_2)$).^[87,96] Additionally the ratio $|\lambda_1|/\lambda_3$ is found to be smaller than unity for closed shell and larger than unity for open shell interactions, respectively.^[87] Even though this classification was found to be very helpful for several interactions, problems can appear especially for polar bonds.^[37] Arising from the domination of the atomic basin of the more electronegative, the exact location of the BCP is sometimes difficult.^[97] Therefore the *Laplacian* distribution along the whole bond path should be taken into account, because small changes in the location of the BCP can have a large influence on the value of the *Laplacian*.^[44]

Cremer & Kraka^[96] introduced the classification of bonding interactions based on the total electronic energy density $H(r)$.

$$H(r) = G(r) + V(r) \quad \text{Eq. 3-5}$$

These energy distributions are available from the experimental EDD according to the approximation by *Abramov*.^[98] This enables a classification of the bonding interaction without restrictions to the atomic number.^[99] Open shell interactions are characterised by a negative total electronic energy density, $H(r) \leq 0$, and a relative kinetic energy that is less than unity, $G(r)/\rho(r) \leq 1$. Closed shell interaction reveal a total energy density greater than zero and a relative kinetic energy greater than one, $H(r) \geq 0$ and $G(r)/\rho(r) \geq 1$.^[91]

3.4 Ellipticity

Another parameter used to classify a bonding interaction is the ellipticity ϵ . The two negative eigenvalues of the *Hessian* matrix, λ_1 and λ_2 , which are perpendicular to the direction of the bond path, can be used to determine the deviation of the ED from a cylindrical shape (Figure 12).^[100-101]

$$\epsilon = \frac{\lambda_1}{\lambda_2} - 1 \quad \text{Eq. 3-6}$$

Accumulation of ED in one direction can be considered as an indication for π -contribution to the bond. The major axis of the elliptical contours is defined by the negative eigenvalues of smallest magnitude, λ_2 . However, it is strongly recommended to consider the ellipticity along the whole bond path as, especially for polar bonds, the BCP is not necessarily indicative for the polarisation plane of the valence density.^[102]

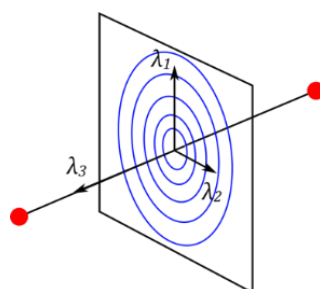


Figure 12: Spatial orientation of the eigenvalues of the Hessian matrix.

3.5 Non-covalent Interactions

Although the QTAIM approach is very successful in extracting chemical insights from the ED^[33-40,42-45,103] it is sometimes said to have a too localised understanding of bonding.^[104] Therefore, further tools are needed to investigate for example non-covalent interactions (NCI) such as hydrogen bonds, London dispersion or non-attractive interactions such as steric repulsion. *Johnson et al.*^[105] and *Contreras-García et al.*^[106] reported on such a tool based on the reduced density gradient (RDG), $s(r)$, which is a fundamental dimensionless quantity from the density functional theory.

$$s(r) = \frac{|\nabla\rho(r)|}{2 \cdot (3\pi)^{1/3} \cdot \rho(r)^{4/3}} \quad \text{Eq. 3-7}$$

The value of the RDG can be understood as the deviation of the ED from a homogeneous electron gas.^[107] The RDG assumes large values at points with low ED e.g. far away from

atoms. Its lower bound is zero at the positions where the gradient vanishes. A NCI is indicated by a low RDG and a low ED. This can easily be visualized in a diagram of s vs. ρ . The graph of $s(\rho)$ normally takes on the shape of $a \cdot x^{-1/3}$, so the RDG becomes very large for low densities. NCIs are depicted by troughs in the graph of the RDG versus the ED (Figure 13a). To distinguish between attractive and repulsive interaction a diagram of s vs. $\text{sign}(\lambda_2) \cdot \rho$ is analysed. For attractive interactions the second eigenvalue of the *Hessian* matrix, so the largest one perpendicular to the interaction direction, is negative. For non-bonding interactions the opposite is true (Figure 13b).^[104-106]

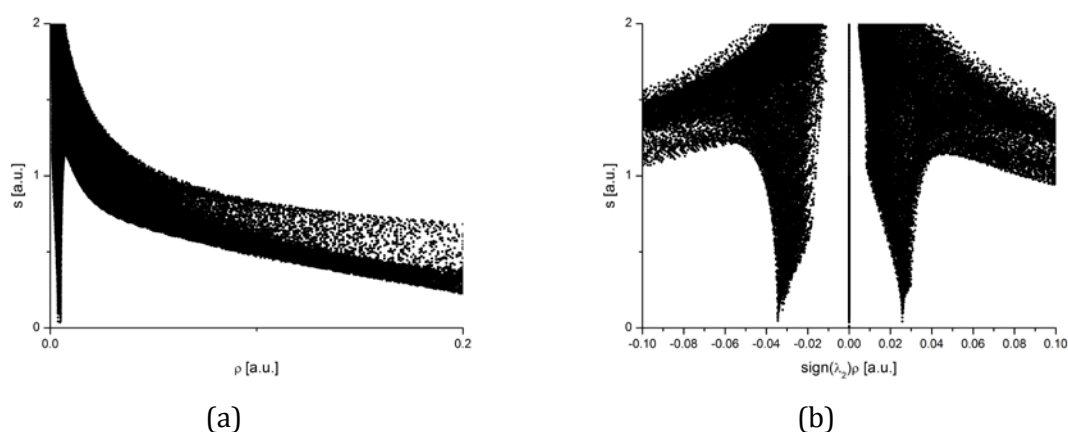


Figure 13: Plots of the RDG versus the ED (a) and the ED multiplied by the sign of the second *Hessian* eigenvalue (b).

It is possible to visualise these regions of NCI as well as their type by plotting the sign of the second *Hessian* eigenvalue onto an isosurface of the RDG at a reasonable level (Figure 14). The best value for the level of this isosurface can be determined with the plot of the RDG versus the ED. An isosurface can be found whenever a BCP for the interaction is found. However, the opposite is not true. By this the NCI descriptor represents a good extension to the existing concept of QTAIM, leading to a better description of non-localised or repulsive interactions.^[104]

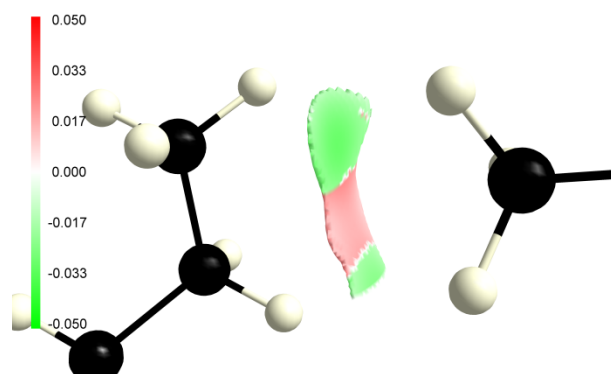


Figure 14: Isosurface of the RDG $s=0.5$. The surface is coloured according to $\text{sign}(\lambda_2) \cdot \rho$ in a.u.; green attractive interactions, red repulsive.

4 Thermal Diffuse Scattering

The assumption that the measured intensity, I_{meas} , is proportional to square of the absolute value of the structure factor (Eq. 2-8) holds only true if inelastic scattering is not taken into account. More precisely the measured intensity is the sum of the *Bragg* intensity, a contribution caused by thermal diffuse scattering (TDS) and the background.^[108]

$$\begin{aligned} I_{meas}(h) &= I_{Bragg}(h) + I_{TDS}(h) + \text{background} \\ &= I_{Bragg}(h) \cdot (1 + \alpha) + \text{background} \end{aligned} \quad \text{Eq. 4-1}$$

The contribution of TDS (α) to the measured intensity is not always negligible and can cause errors, especially in charge density investigations.

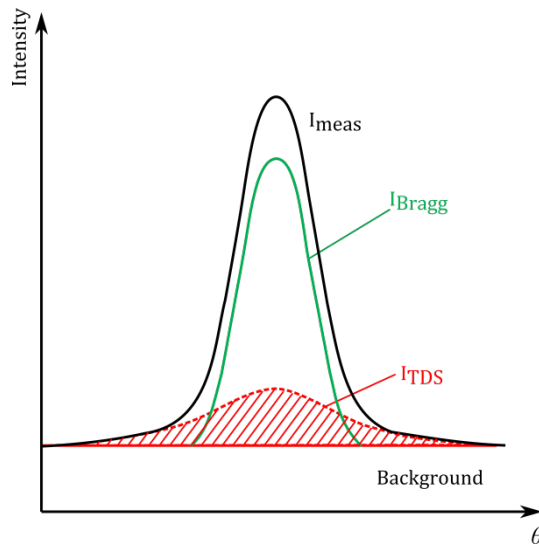


Figure 15: Schematic plot of the intensities around the Bragg reflection. Profile of the measured intensity drawn as black solid, of the Bragg intensity as green solid and of the TDS intensity as dashed red line.

TDS is the contribution of the inelastic part of the scattering that arises from the exchange of at least one vibrational quantum (phonon) with the crystal. Consequently, the wavelength of the diffracted beam is changed. TDS is separated into high-frequency optic and low-frequency acoustic modes. The one-phonon acoustic modes peak at the position of the *Bragg* maximum (Figure 15). However, the TDS peak is broader than the *Bragg* peak. Its fraction of the measured intensity is not constant but increases with the scattering angle θ . Ignoring TDS thus has a direct influence on the atomic displacement parameters. The remaining TDS modes mainly contribute to the flat background and are erased by the background subtraction.^[108-113]

TDS is not merely an error in the measured intensities. It can give useful information about the lattice dynamics. However, it is very hard to measure, because the energy difference of the scattered wave is just in the range of ~ 0.1 eV. In contrast, the normal X-ray line width is 1-5 eV. This makes the TDS contribution hard to detect during X-ray diffraction experiments.^[110,113] Nonetheless a detection can be achieved using ultra high energy resolution X-ray experiments^[114] or Mössbauer γ -radiation^[115]. Moreover, novel approaches to model TDS using synchrotron radiation and Monte Carlo computer simulations have been described by *Welberry et al.*^[116]

For X-ray crystal structure determination in general and for charge density studies in particular the main interest concerning TDS is to minimize it or correct the measured intensities. In general TDS is dependent on the softness of the material and the temperature at the data collection. Thus the easiest way to prevent TDS would be to measure the data at the lowest possible temperature e.g. by using liquid helium cooling. However, using liquid helium for the crystal cooling is much more expensive than using liquid nitrogen. Therefore first trials of calculating the TDS contribution α were done based on detailed knowledge of the lattice dynamics or the elastic constants of the crystal, which are not available in most cases.^[110-111] Moreover it was shown that the TDS contribution is not only dependent on the elastic constants of a compound but also on the crystal's size, the scattering vector value, the divergence and monochromaticity of the beam, the initial scan interval, the detector aperture and many more parameters.^[113,117] In addition investigations by *Stevenson & Harada*^[110-111,118] showed that in comparison the experimental conditions are more important for the TDS correction than the softness of the crystal.

Therefore, several techniques were developed to obtain the TDS contribution from the analysis of the diffraction pattern. As mentioned above the shape of the TDS peak is broader than the one of the *Bragg* peak. This was used by *Jennings*^[119] in 1970 to determine the TDS contribution without knowing the elastic constants or measuring the inelastic scattering directly. It was further developed by *Blessing*, who fitted a triangle to this peak broadening.^[120-121] Founded on this idea *Stash & Zavodnik*^[80,122] developed a method to determine the TDS correction factor during the integration routine. Based on the assumption that the TDS contribution for low-order reflection is negligible, they measured the TDS broadening from the difference between the low and the high-order reflection profile. By fitting a TDS peak profile to this broadening they were able to gain the TDS correction factor for reflections of a certain θ -interval. The resolution dependence of the correction factor α was finally deduced by fitting these points to a polynomial (Eq. 4-2).

$$\alpha = a \cdot \left(\frac{\sin(\theta)}{\lambda}\right)^2 + b \cdot \left(\frac{\sin(\theta)}{\lambda}\right)^3 \quad \text{Eq. 4-2}$$

Within this approximation the first term of Eq. 4-2 describes an isotropic approximation of TDS with a constant scan volume, while the second term takes account of the change in the scan volume with increasing resolution.^[80,122] However, all these experimental corrections were developed for datasets that were collected with point detectors. Therefore, they are inapplicable in the current era of area detectors. Consequently, in most single crystal structure determinations today, the errors that are introduced by TDS, are more or less ignored. However, the effects of not correcting for TDS are entirely underestimated, especially in the view of the fact that the contribution of TDS for high-order reflection is often larger than 35%.^[118] The main effect of TDS is that the size of the atomic displacement parameters and their principal axis are determined wrongly.^[118,123] For routine structures this might be acceptable, because the errors ‘only’ affect the displacement parameters, which already ‘mop up’ a lot of other effects. However, for any study interested in the charge distribution another effect of TDS plays an important role: The heights of the maxima in the electron density are changed without displacing them.^[124]

Therefore, it is unavoidable to correct at least for the errors that are introduced by TDS. In the following two examples are presented, which show signs of errors introduced by TDS. Firstly, these signs are discussed and secondly an empirical correction of the errors caused by TDS is introduced.^[125]

4.1 Experimental Details

4.1.1 Data Collection

For this study six different datasets from two compounds were used, which are partly already published. However, the data processing and the refinements carried out and presented in this study are completely new. Thereby, it is guaranteed that all programs used for the data reduction were up to date and that the models, which are refined for the different datasets are comparable.

The first example, di-(tris(3,5-dimethylpyrazolyl)methane)-magnesium(II) ($[\text{Mg}\{(\text{pz}^*)_3\text{C}\}_2]$ ($\text{pz}^* = 3,5\text{-dimethylpyrazolyl}$)) (**1**), crystallizes in the trigonal space group $R\bar{3}$ (Figure 16a).^[126-127] The asymmetric unit contains one sixth of the whole molecule. The magnesium atom is located at the $\bar{3}$ -axis, the bridging carbon atom C(6) is located at the 3-fold axis. The remaining atoms are located at general positions.

The second example is 9-diphenylthiophosphinylantracene (SPANH) (**2**). The compound crystallizes in the triclinic space group $P\bar{1}$ with two complete molecules in the asymmetric unit. All atoms are located at general positions (Figure 16b).^[68,128-130]

For each compound three datasets at two different machines were collected. Datasets **1-TXS-100K**, **1-TXS-15K**, **2-TXS-100K**, **2-TXS-15K** were measured on a Bruker D8 three circle goniometer equipped with a Bruker TXS-Mo rotating anode with INCOATEC Helios mirror optics and an APEX II detector. The temperature for the datasets, measured at 100 K, was controlled using a Bruker Kryoflex II device. For the datasets measured at 15 K the machine was equipped with an Oxford Helijet open stream liquid helium cooling device. The datasets **1-I μ S-100K** and **2-I μ S-100K** were measured on a Bruker D8 three circle goniometer equipped with an INCOATEC Mo I μ S with QUAZAR mirror optics and an APEX II detector. The crystal cooling at 100 K was done with a Bruker Kryoflex II device.

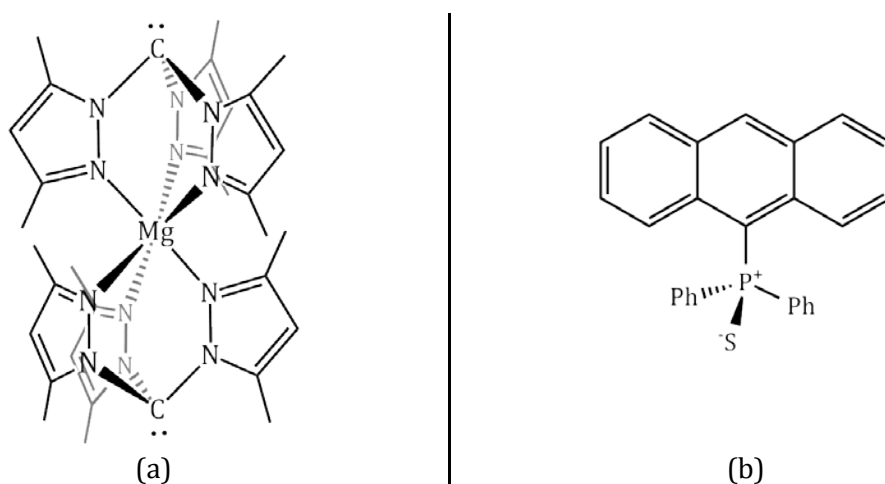


Figure 16: Lewis formulae of **1** (a) and **2** (b).

4.1.2 Data Reduction

All datasets were integrated with *SAINT 8.30C*^[131]. The first integration was done with box size refinement enabled starting from $x, y, z = 0.8^\circ$. The threshold for the spot-shape update was set to $10 I/\sigma$. All other values were kept fixed at their default values. Afterwards scaling, absorption correction and error model determination were applied with *SADABS 2014/2*^[71]. The weighting scheme for the error model was refined using individual K for each run and an overall g (see Eq. 2-17).

The quality indicators for all datasets, except for **1-I μ S-100K**, reveal a suitable data quality for charge density refinements. The deviation between the symmetry equivalent reflections is at an acceptable range for all dataset (Figure 17 and Figure 18). The **1-I μ S-100K** dataset even shows the lowest residual for the low-order data. However, the completeness and multiplicity for the high-order data for this dataset is too low for a meaningful MM refine-

ment.^[76] The refinement against this dataset was added for comparison only. For the other two datasets of this compound, **1-TXS-100K** and **1-TXS-15K**, the completeness and multiplicity is excellent (Table 2). Completeness and multiplicity for the datasets of **2** are entirely somewhat inferior (Table 3). However, this is expected because of the low symmetry space group. Taken this into account these values are acceptable for the MM refinement.

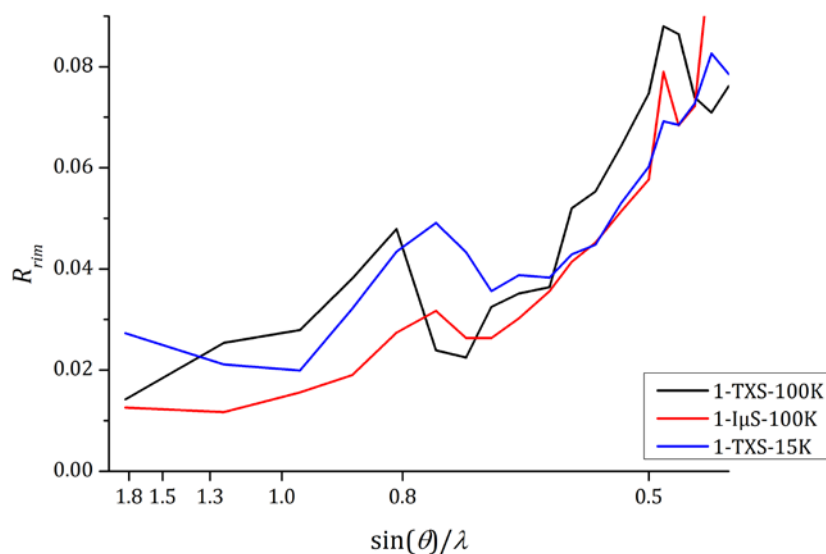


Figure 17: Course of R_{rim} with resolution for compound 1.

Table 2: Completeness and multiplicity for the datasets of compound 1.

$\sin(\theta)/\lambda$	#hkl (theo.)	1-TXS-100K		1-lμS-100K		1-TXS-15K	
		comp.	mult.	comp.	mult.	comp.	mult.
Inf-1.83	94	100.00	34.22	100.00	11.30	98.94	21.91
1.83-1.22	222	100.00	25.05	100.00	14.31	100.00	26.10
1.22-0.97	312	100.00	26.42	100.00	13.15	100.00	22.05
0.97-0.85	309	100.00	29.20	99.35	13.81	100.00	22.19
0.85-0.77	316	100.00	26.51	99.68	12.57	100.00	24.45
0.77-0.71	344	100.00	25.57	100.00	11.47	100.00	22.59
0.71-0.67	306	100.00	24.53	99.35	8.19	100.00	17.87
0.67-0.64	279	100.00	23.36	96.77	4.98	100.00	13.39
0.64-0.61	333	100.00	22.30	95.80	4.71	100.00	12.71
0.61-0.58	420	100.00	21.23	94.52	4.51	100.00	9.45
0.58-0.56	332	100.00	20.26	91.57	4.21	100.00	6.08
0.56-0.54	360	100.00	19.13	91.67	2.94	100.00	5.84
0.54-0.52	440	100.00	15.13	89.77	2.19	100.00	5.59
0.52-0.50	524	100.00	13.53	88.17	2.10	100.00	5.37
0.50-0.49	264	100.00	12.73	84.85	1.97	100.00	5.19
0.49-0.48	328	100.00	12.39	82.93	1.84	100.00	4.89
0.48-0.47	330	100.00	6.92	82.42	1.79	100.00	4.82
0.47-0.46	380	100.00	4.74	24.10	1.39	100.00	4.58
0.46-0.45	365	96.71	4.19	-	-	100.00	4.37

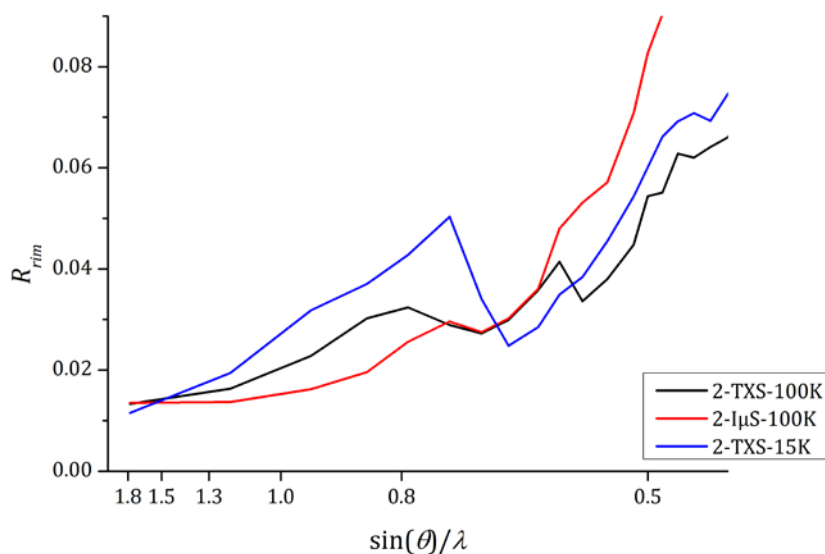


Figure 18: Course of R_{rim} with resolution for compound 2.

Table 3: Completeness and multiplicity for the datasets of compound 2.

$\sin(\theta)/\lambda$	#hkl (theo.)	2-TXS-100K		2-IµS-100K		2-TXS-15K	
		comp.	mult.	comp.	mult.	comp.	mult.
Inf-1.78	731	99.86	10.79	99.73	7.96	99.86	4.81
1.78-1.19	1741	100	13.76	99.60	10.20	99.83	4.51
1.19-0.94	2513	100	11.71	99.88	12.90	100.00	3.67
0.94-0.82	2515	100	10.89	99.96	12.43	100.00	4.53
0.82-0.75	2298	99.96	13.16	100.00	11.24	99.74	4.92
0.75-0.69	2801	99.68	9.79	100.00	9.28	98.61	4.44
0.69-0.65	2464	99.07	8.08	99.80	6.25	96.14	2.36
0.65-0.62	2295	98.69	7.67	99.74	5.89	95.64	1.96
0.62-0.59	2788	98.39	7.24	99.61	5.62	94.30	1.88
0.59-0.57	2190	98.08	6.70	99.32	5.28	93.33	1.80
0.57-0.55	2535	97.71	3.96	99.05	5.06	92.62	1.76
0.55-0.53	2900	97.45	3.63	98.83	3.55	91.55	1.69
0.53-0.51	3377	97.01	3.49	98.40	3.34	90.79	1.62
0.51-0.50	1942	96.76	3.36	97.79	3.20	89.75	1.55
0.50-0.49	2064	96.17	3.26	97.77	3.07	89.15	1.52
0.49-0.48	2255	96.05	3.16	97.12	2.97	88.96	1.48
0.48-0.47	2428	95.51	3.06	96.99	2.86	87.60	1.42
0.47-0.46	2652	95.32	2.93	96.64	2.73	86.50	1.36
0.46-0.45	2918	94.86	2.8	95.24	2.50	85.02	1.29
0.45-0.44	4825	87.63	2.23	20.06	1.24	16.15	0.71

4.1.3 Model Refinement

The structures were solved by direct methods (*SHELXT*)^[53] and refined by full-matrix least squares methods against F^2 .^[132-133] The position and the atomic displacement parameters of the non-hydrogen atoms were refined against high-order data ($d < 0.6 \text{ \AA}$). The hydrogen atoms were identified by a difference *Fourier* analysis using the low-order data ($d > 1 \text{ \AA}$). The hydrogen atoms were placed on their corresponding peaks in the difference *Fourier* map and the distances were set to their distances from neutron diffraction experiments.^[134] The U_{iso} values of the hydrogen atoms were constrained to 1.5 times U_{eq} of their pivot atoms for terminal sp^3 carbon atoms and 1.2 times for all other carbon atoms. For compound **1** one of the two methyl groups in the asymmetric unit was found to be disordered (H5A-F). The two positions were refined using a riding model with variable cone angle and free rotation in two parts (two 'AFIX 137' commands). The occupation factor refined to $\sim 50\%$ for all datasets. Therefore, it was set to exact 50% for the starting model of the MM refinement. The IAMs served as the starting model for the multipole refinements of compound **1**. The starting models for the refinements of compound **2** were obtained by the *INVARIOM* tool^[135].

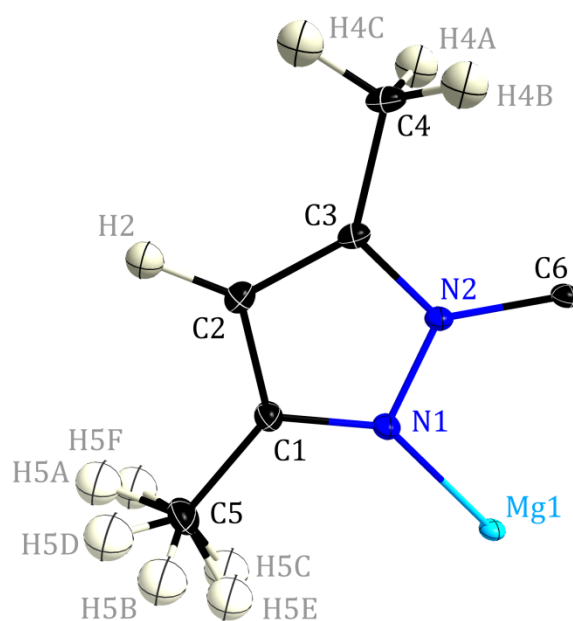


Figure 19: The molecular structure of compound **1**. Only the asymmetric unit is shown. Anisotropic displacement parameters are depicted at the 50% probability level.

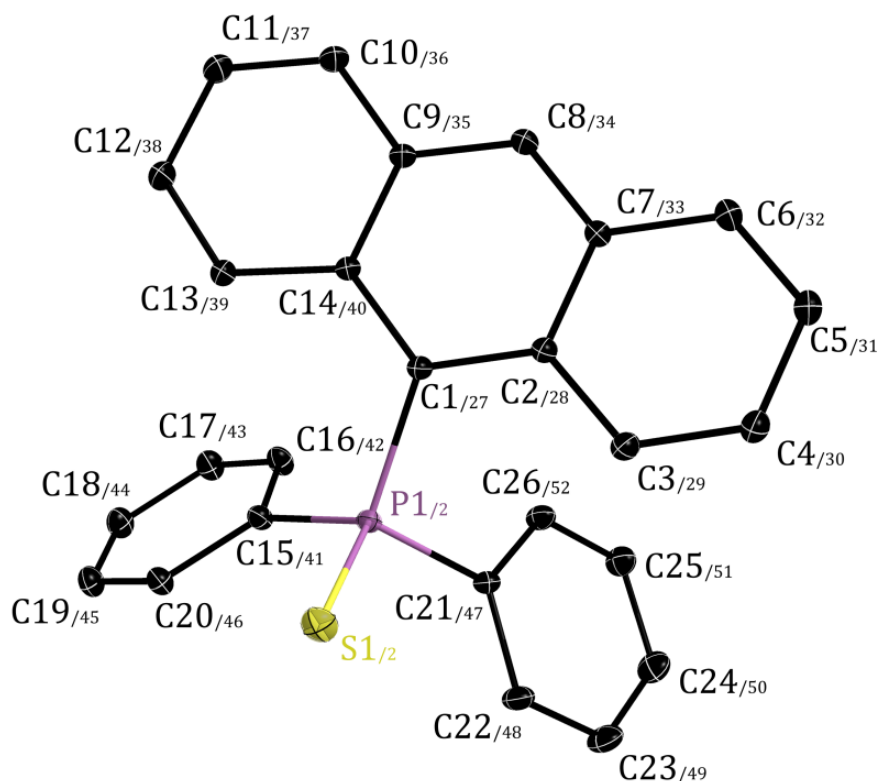


Figure 20: The molecular structure of compound **2**. Only one molecule of the asymmetric unit is shown. Hydrogen atoms are omitted for clarity. Anisotropic displacement parameters are depicted at the 50% probability level.

The MM refinement was performed against F^2 using the program *XDLSM* implemented in the *XD2006* program package^[136]. The core and the spherical valence densities were composed of STO-HF atomic wave functions reported by *Su, Coppens and Macchi*^[56-57] (SCM bank file for compound **1**) and *Clementi and Roetti*^[65,137] (CR bank file for compound **2**). The parameters κ and κ' were used to adjust the radial fit of these functions. For compound **1** the refinement of κ' did not fully converge and κ of magnesium refined to physically unreasonable values. Therefore, κ of Mg1 and κ' of all atoms were not refined. All remaining contraction/expansion coefficients for non-hydrogen atoms were refined. Hereby the multipoles of one atom type were forced to have the same κ' . For the hydrogen atoms the values were kept fixed during the refinement at $\kappa = 1.1$ and $\kappa' = 1.18$.^[138] The spherical harmonics expansions were truncated at the hexadecapolar level for all non-hydrogen atoms except Mg1. Hydrogen atoms were treated by bond directed dipoles. For the magnesium atom only the monopole population was refined (see Section 7.2.2.).

Herbst-Irmer et al.^[68] reported on the anharmonic motion in **2**. Therefore, S(2), P(2) as well as C(47)-C(52) were refined using *Gram-Charlier* coefficients up to third order for the 100 K datasets; for the 15 K dataset only S(2) was refined anharmonically. For all remaining non-hydrogen atoms of **2** and all non-hydrogen atoms of **1** the anisotropic harmonic approximation was used. The atomic displacement parameters of the hydrogen were treated

equally to the IAM. The hydrogen atom positions were refined against the low-order data ($\sin(\theta)/\lambda < 0.5$); the distances were reset to the distances from neutron diffraction experiments after each step.

The monopole and dipole populations of the hydrogen atoms at the disordered methyl group (H5A-F) were constrained to sum up to the populations of the non-disordered methyl group (H4A-C), because it is not possible to refine the side occupation factor in *XD2006*. By this the two positions of the disordered group were allowed to change their occupancy via their mono- and dipole population. However, this does not ensure that the side occupation factor for the monopole and the dipole is the same. Therefore, the population of mono- and dipoles were set to the same occupation in the last step and were constrained to have a fix ratio. The ratio was found to be nearly 0.45 to 0.55 after the MM refinement for all datasets and thus was set to exactly this value for all datasets.

In order to stabilize the refinement, the multipole parameters for several atoms were constraint to be the same (chemical constraints) and local non-crystallographic symmetry restrictions for the multipolar expansion were applied (see appendix). To avoid overfitting both were not released. The parameters were introduced in the refinement routines in a stepwise manner. In the final step all parameters (except κ') were refined together until convergence was reached. (The refinement strategy is given in detail in the appendix). However, for some refinements with resolution-dependent scaling (see Section 4.3) and with fixed box sizes (see Section 4.4) the convergence criteria of 10^{-6} max (shift/su) was not reached. The highest observed max (shift/su) was 10^{-3} .

4.2 Errors in the data

The examination of the models obtained from the different datasets emphasizes two serious problems for both compounds. On the one hand the models do not fully fulfil the quality criteria for a sensible MM refinement. On the other hand, comparing the model parameters and the properties of the EDD, significant differences especially between the 15 and 100 K datasets, appear (Figure 21).

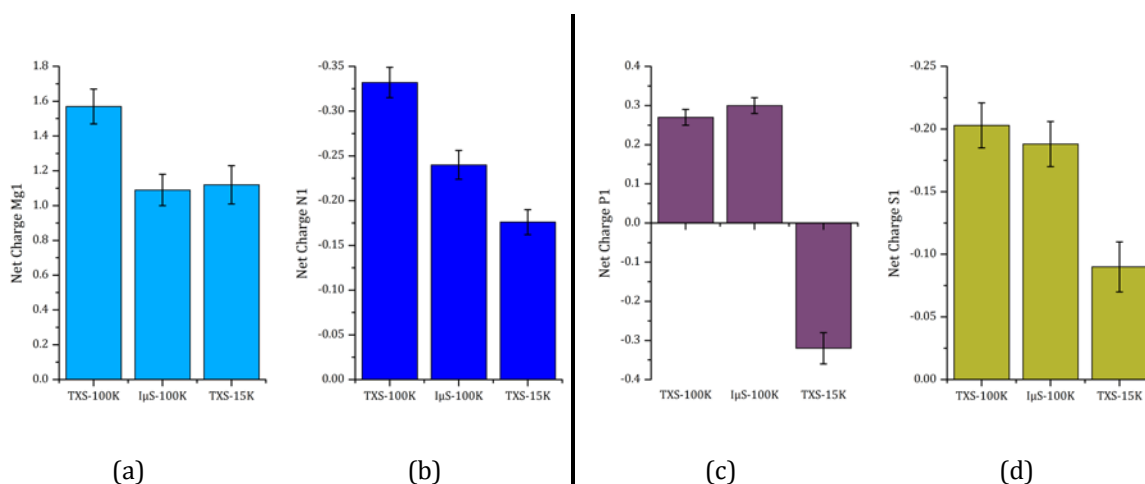


Figure 21: Net charges for Mg1 (a) and N1 (b) in **1** as well as charges for P1 (c) and S1 (d) in **2**.

4.2.1 Differences in the Multipole Model

For compound **1** the Mg1 net charge of the model obtained from the **1-TXS-100K** (1.57(10)) dataset is larger than for **1-TXS-15K** (1.12(11)). The net charge of the **1-IµS-100K** model is closer to the one of **1-TXS-15K** (1.09(9)). However, it should be kept in mind that this dataset does not fully fulfil the restrictions for a charge density dataset. The same tendencies are also recognisable for the net charges of N(1) and N(2). Yet, here the charges for the **1-IµS-100K** (-0.24(16) and -0.107(18)) dataset lie in between the charge for the **1-TXS-100K** (-0.332(17) and -0.236(18)) and the **1-TXS-15K** dataset (-0.176(14) and -0.071(15)). For compound **2** the net charges of P1 are similar for **2-TXS-100K** (0.27(2)) and **2-IµS-100K** (0.30(2)). Again the charge of the **2-TXS-15K** dataset is much smaller (-0.32(4)). This charge is comparable to the net charge that can be deduced from the INVARIOM model (-0.1742), that was calculated for **2** (Table 7). Differences in the charges of S1 are smaller but still present. Again the 100K dataset results in similar charges (-0.203(18) and -0.188(18)) while the charge for the 15K dataset is smaller (-0.09(2)). These differences in the model parameters also manifest themselves in the properties of the EDD, especially in the *Bader* charges. The largest difference in the *Bader* charge (0.39 e) can be found for the P1 between **2-TXS-100K** and **2-TXS-15K** (Table 7).

4.2.2 Model quality

The residual density after the MM refinement is still considerably high. The highest peaks in the residual density maps are located very near or even at the core positions (Table 4). The dataset **2-TXS-15K** and **1-TXS-15K** are exceptions. In the first no such peak is visible and in the latter the peak in proximity to the core position is less prone, too. The residual density near Mg1 might be explained by its location on a $\bar{3}$ position where residual density could be expected. However, the residual density close to other atoms cannot be explained.

The fractal dimension plots display a pronounced deformation from parabolic shape at the positive side, especially for datasets **1-TXS-100K** and **2-I μ S-100K** (Figure 22). Additionally, a small deformation on the negative side of the fractal dimension plot for the model of compound **2** is also visible, which might be ascribed to unresolved anharmonic motion.

Table 4: Highest peak of the residual density map. Peaks in close proximity to core positions are marked in red.

	peak	distance from next atom	height [e \cdot \AA^{-3}]		peak	distance from next atom	height [e \cdot \AA^{-3}]
1-TXS-100K	PK1	0.00 \AA from Mg1	0.28	2-TXS-100K	PK1	0.06 \AA from S1	0.28
	PK2	0.06 \AA from C6	0.18		PK2	-	0.23
	PK3	0.09 \AA from C5	0.17		PK3	0.03 \AA from S2	0.22
1-IμS-100K	PK1	0.00 \AA from Mg1	0.26	2-IμS-100K	PK1	0.01 \AA from P2	0.38
	PK2	0.04 \AA from C6	0.22		PK2	0.03 \AA from S2	0.38
	PK3	0.04 \AA from C4	0.20		PK3	0.05 \AA from S1	0.36
1-TXS-15	PK1	0.59 \AA from C5	0.24	2-TXS-15K	PK1	-	0.26
	PK2	0.35 \AA from Mg1	0.22		PK2	0.53 \AA from S2	0.22
	PK3	0.03 \AA from C4	0.18		PK3	0.57 \AA from S1	0.20

Problems are also exposed in an examination of the $\sum F_o^2 / \sum F_c^2$ quotient with resolution. The plots generated by the program *DRKplot*^[78] reveal a continuous overestimation of the observed structure factors at higher angles and problems in the low-order region. The latter is to be expected, because the reflections in this region carry the information about the valence electrons. Problems with single reflections in this region tend to dominate the outcome of the plot leading to a high deviation from unity, because only a few reflections contribute to one point in the low-order region.^[76,139] For example, the first data point in Figure 23a arises from only one poorly determined reflection *-1 1 1*. However, for the points at higher resolution this domination of single data points is no problem as several hundred reflections contribute to each point in this region. Thus the deviation in this region indicates a systematic overestimation of the observed structure factor for all datasets except for **2-TXS-15K**.

For dataset **1-TXS-100K** this overestimation vanishes after refining κ for Mg1. Yet, for the other two datasets this effect was not visible. The κ of Mg1 refines to the unreasonable value of 3.19(6) for the **1-TXS-100K** dataset, in contrast to 1.14(4) for the **1- μ S-100K** dataset. For the 15 K dataset it is determined as 0.84(3). Therefore, the refinement of the κ for Mg1 was disabled for all datasets in order to ensure comparable refinement strategies and to minimize effects from unreasonable values.

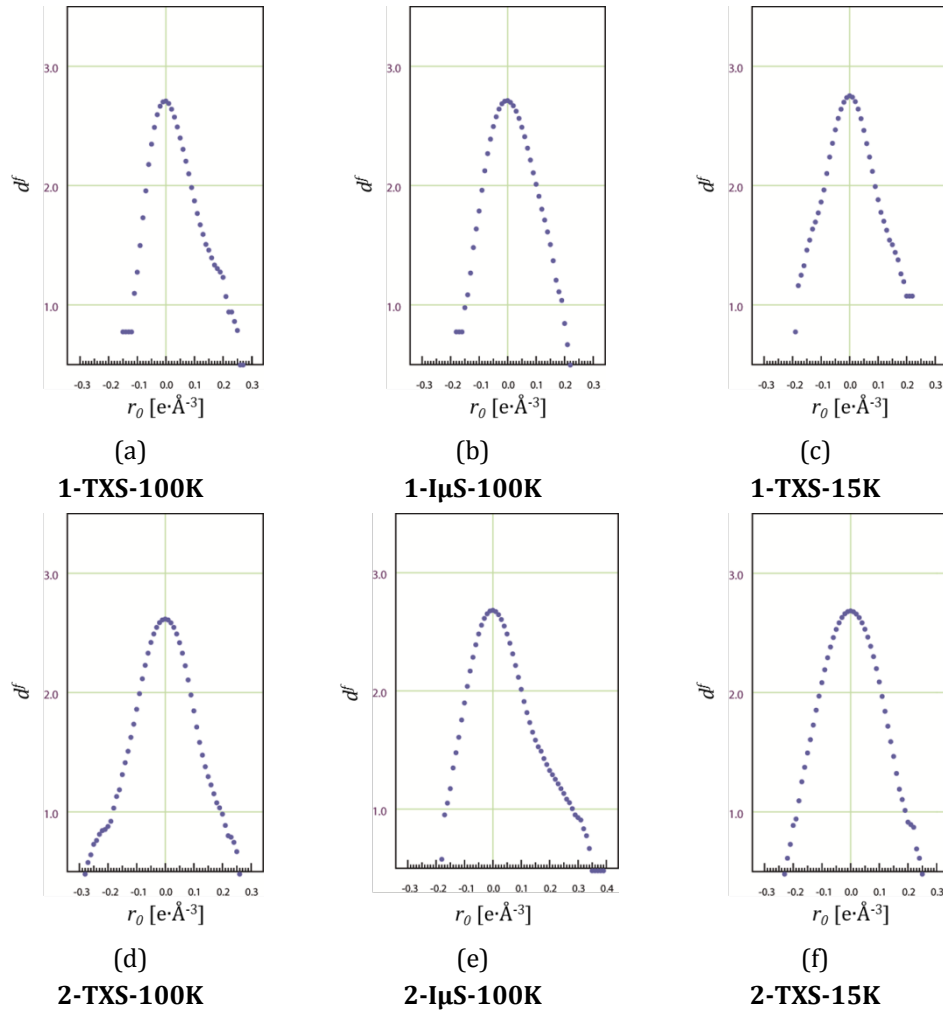


Figure 22: Fractal dimension plots for the dataset of **1** and **2**.

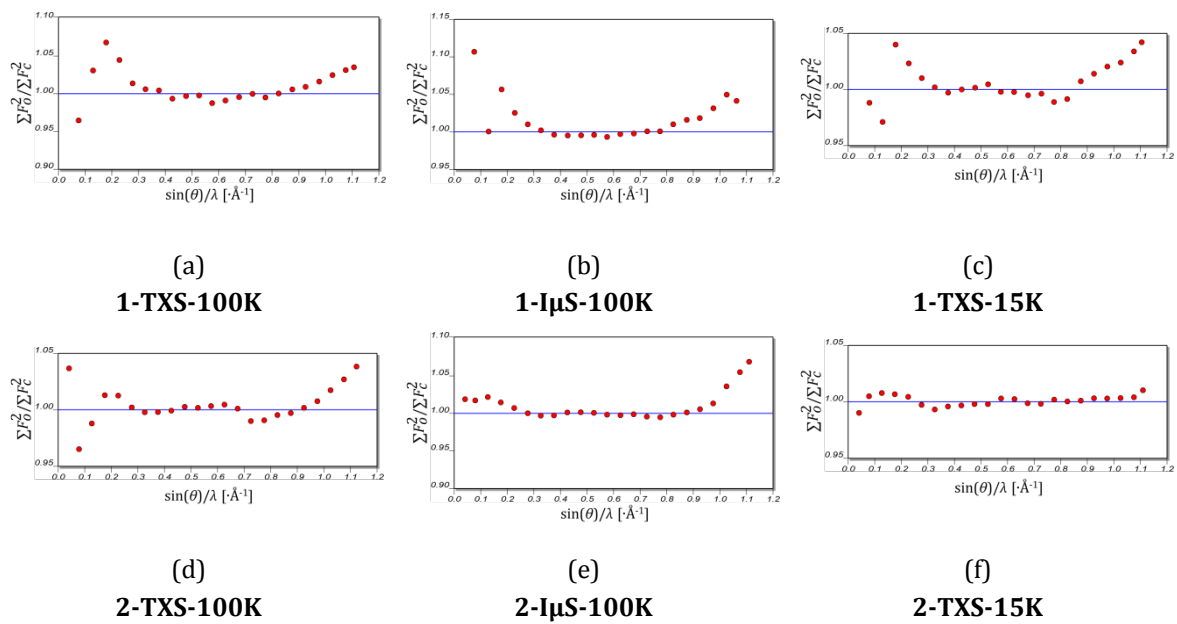


Figure 23: Plot of $\Sigma F_o^2 / \Sigma F_c^2$ vs. $\sin(\theta) / \lambda$ (DRK-plot) for **1** and **2**.

4.3 Resolution Dependent Scaling

The DRK-plots unveil a continuous increase of the $\Sigma F_o^2/\Sigma F_c^2$ quotient above $\sim 0.6 \text{ \AA}^{-1}$. Therefore, resolution dependent scale factors were used during the refinement of the MM.^[140] The dataset was divided into 10 resolution batches. The first batch covers the reflection up to 0.2 \AA^{-1} . The width of the remaining nine batches is 0.1 \AA^{-1} each.

4.3.1 Influence on the Model Quality

By applying resolution-dependent scaling during the refinement the quality indicator exhibits large improvements of the models. Of course, the R values improve a lot (see appendix). However, as additional scaling factors were applied to the refinement this does not necessarily truly improve the model quality. Though an improvement of the model can already be observed by a visual inspection of the residual density map, it becomes obvious that the resolution-dependent scaling reduces the features (Figure 24) but not simply deletes all problems. The potential anharmonic motion at C4 in **1** for example is still visible. An investigation of the highest peaks reveals that resolution-dependent scaling reduces the residual density in close proximity to the core positions while other peaks stay unchanged (Table 5).

Table 5: Highest peak of the residual density map. Peaks in close proximity to core positions are marked in red.

	peak	distance from next atom	height [$\text{e}\cdot\text{\AA}^{-3}$]		peak	distance from next atom	height [$\text{e}\cdot\text{\AA}^{-3}$]
1-TXS-100K	PK1	-	0.15	2-TXS-100K	PK1	-	0.28
	PK2	-	0.15		PK2	0.46 \AA from C5	0.23
	PK3	0.35 \AA from H4B	0.13		PK3	0.46 \AA from C37	0.22
1-IμS-100K	PK1	-	0.16	2-IμS-100K	PK1	-	0.31
	PK2	-	0.15		PK2	0.01 \AA from P2	0.24
	PK3	0.39 \AA from H4B	0.14		PK3	0.04 \AA from S2	0.24
1-TXS-15	PK1	0.59 \AA from C5	0.22	2-TXS-15K	PK1	-	0.26
	PK2	-	0.17		PK2	0.53 \AA from S2	0.22
	PK3	0.68 \AA from C4	0.13		PK3	0.57 \AA from S1	0.21

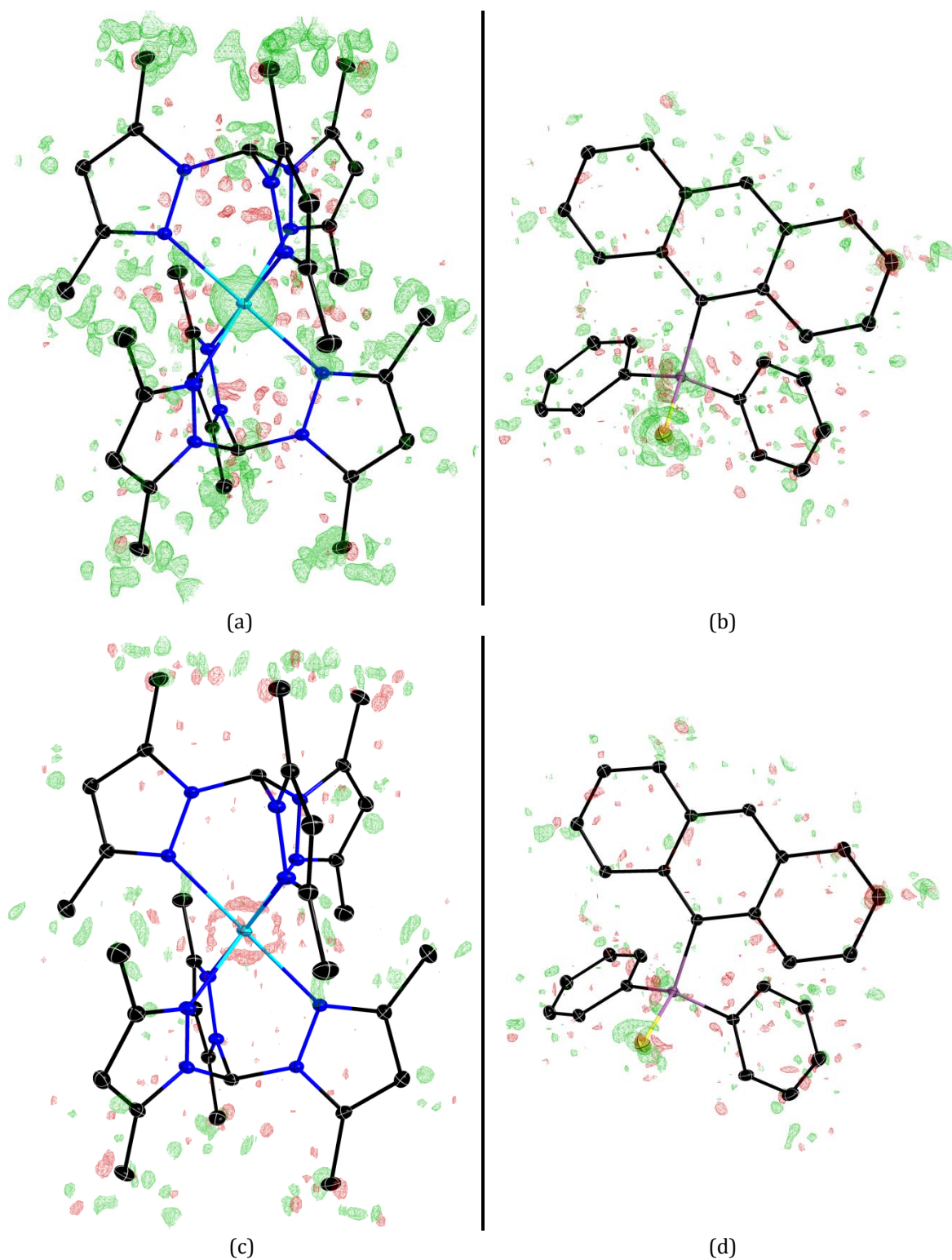


Figure 24: Residual density after MM refinement against 100 K data (**1-TXS-100K** and **2-l μ S-100K**) with 1 scale factor (a, b) and 10 scale factors (c, d). Atomic displacement parameters are depicted at 50 % probability level. Hydrogen atoms are omitted for clarity. Positive residual density is shown in green, negative in red. Isolevels are depicted at $\pm 0.08 e \text{ \AA}^{-3}$ (a, c) and $\pm 0.1 e \text{ \AA}^{-3}$ (b, d).

In order to quantify the improvement of the model it seems appropriate to use the residual density analysis by *Meindl & Henn*. The fractal dimension plots exhibit a reduction of the shoulder on the positive side (Figure 25). For **1-TXS-100K** and **1-I μ S-100K** the resulting plot is nearly perfect, but also for the other datasets the deviation from the parabolic shape is drastically reduced. As a consequence, e_{gross} is decreased as well (Table 6). However, the maximum fractal dimension, $d^f(0)$, does not change. This can be explained by the fact that the resolution-dependent scaling only reduces the structured high residual density, while the very low density stays untouched. Therefore, e_{gross} is more useful to quantify the improvement.

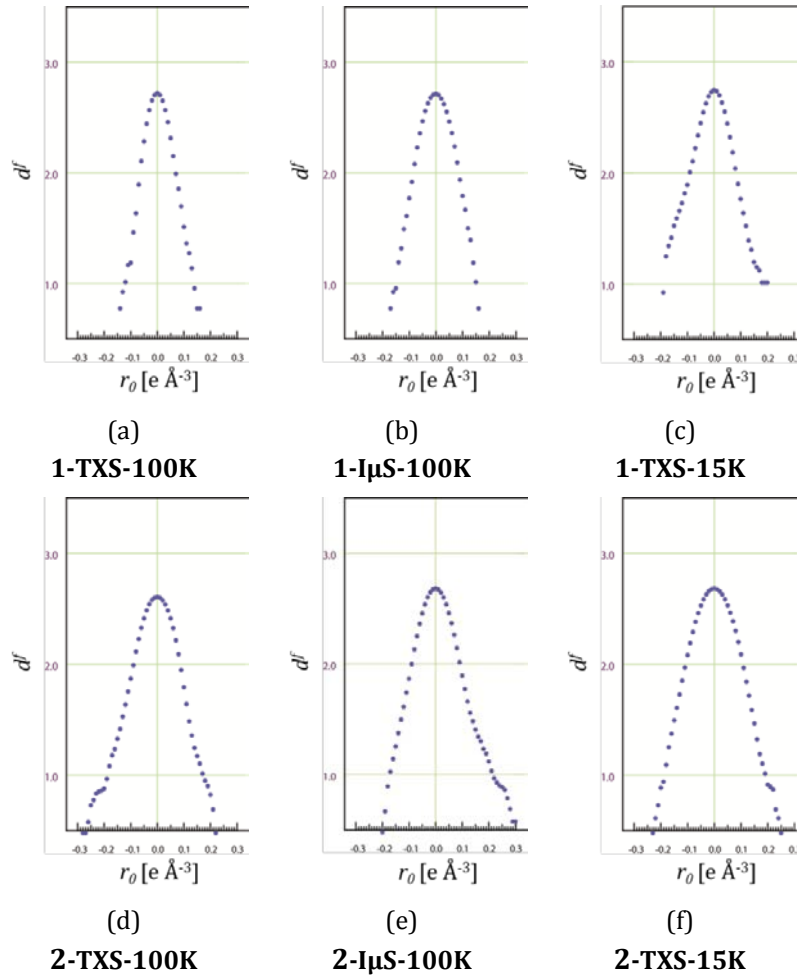


Figure 25: Fractal dimension plots for the dataset of **1** and **2** after refinement of resolution-dependent scaling.

Table 6: $d^f(0)$ and e_{gross} for **1** and **2** after refinement with and without resolution-dependent scaling.

		1-TXS-100K	1-IμS-100K	1-TXS-15K	2-TXS-100K	1-IμS-100K	1-TXS-15K
1 scale factor	$d^f(0)$	2.71	2.71	2.75	2.62	2.68	2.68
10scale factors		2.72	2.71	2.75	2.61	2.68	2.68
1 scale factor	e_{gross}	28.6	35.3	31.4	27.4	28.1	31.8
10scale factors		25.2	32.8	30.6	27.5	26.6	31.6

4.3.2 Influence on the MM

The resolution-dependent scaling does not only improve the model quality; the derived models also show smaller deviations (Table 7). For the refinements with resolution-dependent scaling all datasets of compound **1** reveal net charges for Mg1 between 0.61 and 0.69. The net charges are decreased for all datasets in relation to their single scale factor model. The changes for net charge of Mg1 for the **1-TXS-15K** dataset are smaller than for the **1-TXS-100K** dataset. This echoes the observed residual density for the single scale factor models, because they indicate more electrons around the Mg1 especially for the 100 K datasets. For N1 and N2 small and barely significant differences between the datasets are still detectable. Yet, the biggest difference is no longer between the **1-TXS-100K** and **1-TXS-15K** dataset, but between these two dataset and the **1-I μ S-100K** dataset, whose data quality is, as already mentioned, much worse.

Similar tendencies can be detected for the datasets of compound **2**. As implied by the residual density distribution the net charges are reduced. The net charges of P1 for the 100 K datasets (-0.11(3) and -0.15(3)) are now negative, too. The difference to the net charge of the **2-TXS-15K** dataset (-0.22(4)) is smaller than three standard deviations. While the models derived from the 100 K datasets change significantly by introducing resolution-dependent scaling, changes for the models from the 15 K datasets are much smaller. For the net charge of S1 no change in the net charge can be observed for any dataset. However, the difference between the datasets is relatively small anyhow.

Table 7: Selected net and Bader charges for **1** and **2**.

Atom	1 scale factor			10 scale factors			INVARIOM
	TXS-100K	I μ S-100K	TXS-15K	TXS-100K	I μ S-100K	TXS-15K	
1 Mg1 (Net/ Bader)	1.57(10)	1.09(9)	1.12(11)	0.66(9)	0.67(9)	0.61(11)	-
	1.81	1.71	1.72	1.62	1.63	1.61	-
	-0.332(17)	-0.240(16)	-0.176(14)	-0.119(16)	-0.162(15)	-0.113(14)	-
	-0.72	-0.72	-0.62	-0.65	-0.69	-0.64	-
	-0.236(18)	-0.107(18)	-0.071(15)	-0.048(16)	-0.061(17)	-0.017(15)	-
	-0.90	-0.82	-0.78	-0.77	-0.78	-0.77	-
2 P1 (Net/ Bader)	0.27(2)	0.30(2)	-0.32(4)	-0.11(3)	-0.15(3)	-0.22(4)	-0.1742
	1.41	1.46	1.80	1.94	2.00	1.89	-
	-0.203(18)	-0.188(18)	-0.09(2)	-0.205(18)	-0.186(19)	-0.07(3)	-0.1646
	-0.55	-0.53	-0.58	-0.64	-0.61	-0.54	-
S1 (Net/ Bader)							

4.3.3 Course of the Scale Factor

The resolution dependencies of the scale factors show a typical course that mimics a u-shape (Figure 26). All datasets, except **2-TXS-15K**, reveal a minimum between 0.6 and 0.8 Å⁻¹. The curves for the 15 K datasets seem to have a much flatter shape than the 100 K datasets. A rise in the scale factor for the 15 K dataset is only observable for **1-TXS-15K**. Moreover, the difference between the 15 and 100 K datasets is even larger than already indicated by the DRK-plots and the **1-TXS-15K** dataset now exhibits a different behaviour. The increase of the **1-TXS-15K** dataset starts at a higher resolution than for the 100 K datasets and is also smaller. The **2-TXS-15K** dataset does not show any increase of the scale factor at higher angles. This indicates a smaller error for the 15 K datasets.

The course of the scale factor demonstrates that this correction seems to be a way of curing resolution- and temperature-dependent errors. An increasing scale factor k means that the measured intensities for these reflections are too high compared to the other data, because k scales the calculated and observed structure factors ($F_o^2 = F_c^2 \cdot k^2$). This is consistent with the hypothesis that these errors are at least partly introduced by TDS.

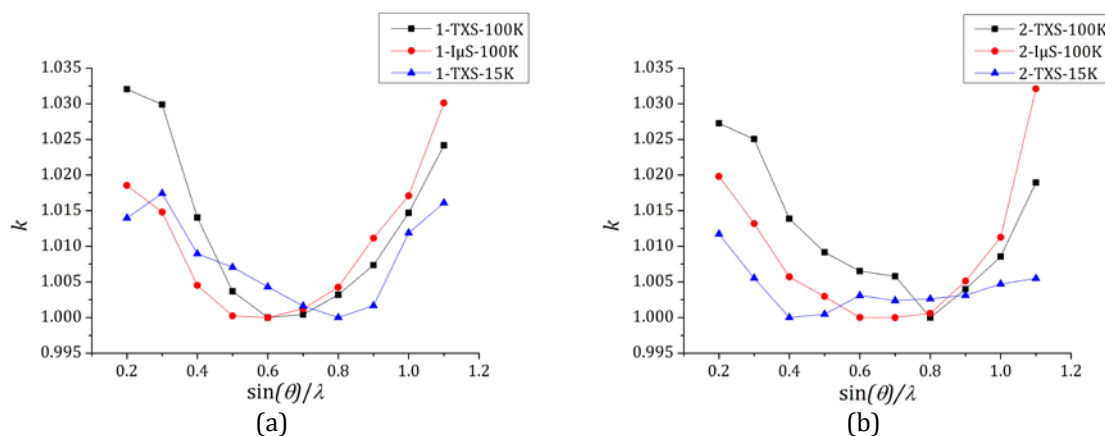


Figure 26: Resolution dependence of the scale factors for datasets **1** (a) and **2** (b). All scale factors were normalized at their minimum.

4.4 Influence of the Box Size

The integration with *SAINTE*^[131] is based on the method developed by *Kapsch*^[141]. The program determines the background and an active mask, marking which pixels are to be analysed. It refines the cell and the orientation matrix based on a given threshold of I/σ and determines the size and the shape of the spots. Finally, it integrates the intensity within a so-called integration box.

This box is defined by an angular range X, Y and Z, defined by the parameters 'SPOTSIZE', 'YSPOTSIZE' and 'SPREAD' in the *saint.ini* file. During the integration routine in *SAINTE*, the size

of the integration box is refined, which can be disabled by setting the parameter 'FIXSPOTSIZE' = 1. For routine datasets the only requirement for the box size is that it should be large enough to accommodate every profile and small enough to get good information about the spot profile.^[142] However, analysing the spot sizes reveals unexpectedly large boxes, especially in the x and y direction. The boxes in z seem to be smaller. Moreover, the box sizes show a large deviation (Table 8).

Table 8: Minimum and maximum integration box sizes after integration with box size refinement.

Box size		1-TXS-100K	1- μ S-100K	1-TXS-15K	2-TXS-100K	2- μ S-100K	2-TXS-15K
x	min	0.828	1.043	0.795	0.967	1.024	0.946
	max	0.876	1.202	1.240	1.243	1.228	1.213
y	min	0.817	0.861	0.642	0.679	0.823	0.723
	max	1.160	0.940	1.138	0.900	0.900	0.883
z	min	0.474	0.662	0.391	0.359	0.636	0.411
	max	0.712	0.741	1.117	0.577	0.949	0.571

TDS is known to cause a broadening of the *Bragg* profile. Thus it could lead to integration boxes that are determined too large, especially for reflections at high resolution (see red box in Figure 27). By reducing the box size, it should be possible to reduce the errors that are introduced by TDS in principle (see blue box in Figure 27). In a first trial the refined box size was shrunk by a constant factor. However, the influence on the models derived from the integrations was small, which can be explained by the large deviation between the box sizes. Therefore, further tests were performed using fixed boxes.

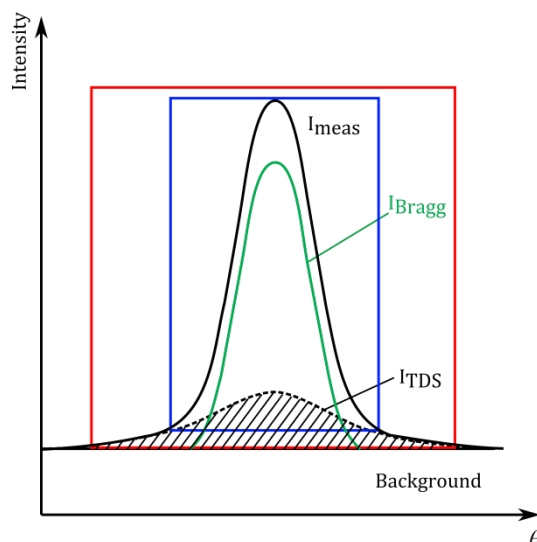


Figure 27: Schematic plot of the intensities around the Bragg reflection. Profile of the measured intensity is drawn as black solid, of the Bragg intensity as green solid and of the TDS intensity as dashed line. The red rectangle schematically depicts the integration box including TDS, the blue rectangle is the one that tries to minimize the TDS contribution.

4.4.1 Identification of the ‘Best’ Box

In order to investigate the influence of the box size five different box sizes were tested, varying from $x, y, z = 0.6^\circ$ to $x, y, z = 0.2^\circ$. The integration of the data with these much smaller fixed boxes leads to a significant improvement of the model after the MM refinement (Figure 28). This improvement is apparent in various quality indicators such as R values and the e_{gross} . Moreover, the heights of the peaks located near the core position are reduced, while other peaks remain unchanged in their heights. Additionally, to the improvement in the model obtained from the refinements with just one scale factor the difference between these models and the resolution-dependent refinements gets smaller. The identification of the ‘best’ box size is possible by using the R value, the e_{gross} and the peaks and holes of the residual density map. These indicators decrease with decreasing box size. If the integration box gets too small, the quality of the model gets significantly worse. This indicates that the *Bragg* intensities are unjustifiably pruned (box 5 in Figure 28).

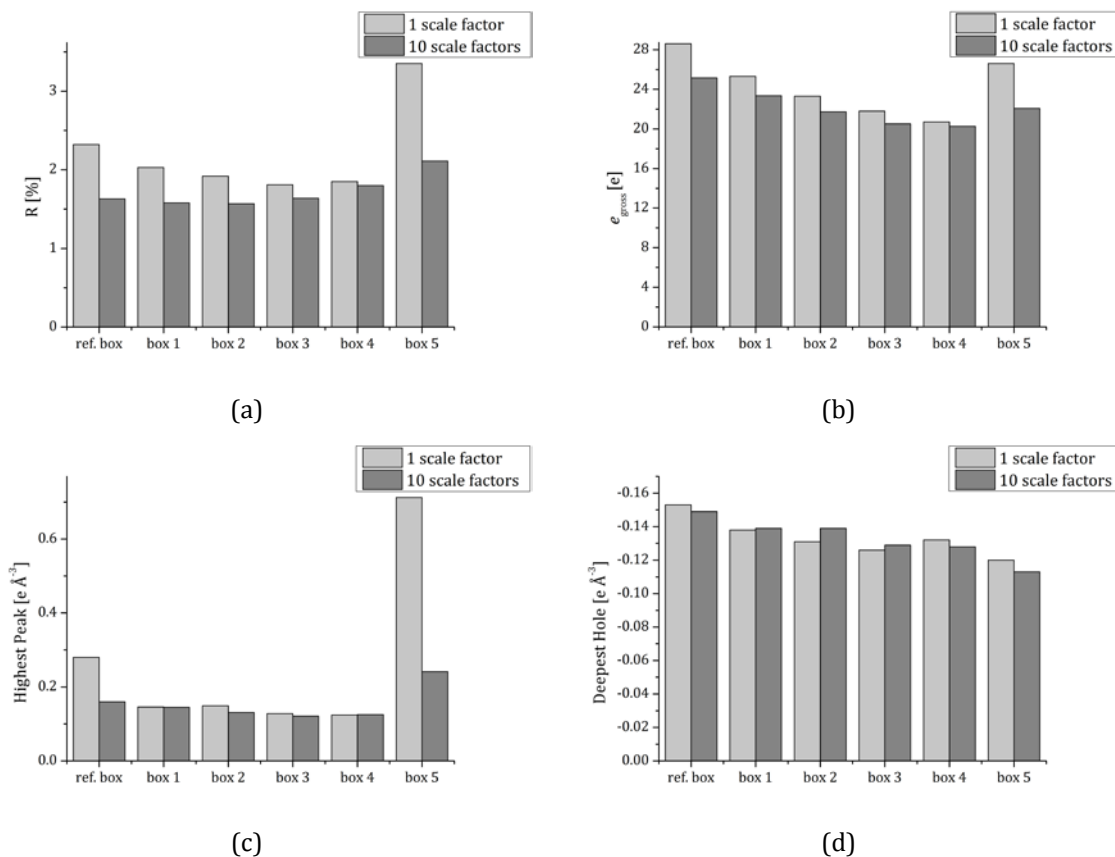


Figure 28: Residual value (a), e_{gross} (b), highest peak (c) and deepest hole (d) for **1-TXS-100K** after multipole refinement. Values for the refinement with resolution-dependent scaling are depicted in dark, those without in pale grey. (box 1: $x=0.6^\circ y=0.6^\circ z=0.6^\circ$; box 2: $x=0.5^\circ y=0.5^\circ z=0.5^\circ$; box 3: $x=0.4^\circ y=0.4^\circ z=0.4^\circ$; box 4: $x=0.3^\circ y=0.3^\circ z=0.3^\circ$; box 5: $x=0.2^\circ y=0.2^\circ z=0.2^\circ$).

For the dataset **1-TXS-100K** the best results were found for $x, y, z = 0.3^\circ$ (box 4 in Figure 28). Compared with the refined box size, the $R(F^2)$ for the one scale factor model decreases

from 2.32 % to 1.85 %, e_{gross} from 28.6 e to 20.7 e and the highest peak in the residual map from 0.280 e \AA^{-3} to 0.124 e \AA^{-3} . However, the deepest hole shows only small changes (from $-0.152 \text{ e \AA}^{-3}$ to $-0.126 \text{ e \AA}^{-3}$). Further investigations were carried out to test the influence of a more precisely determined box size (see appendix). A box size of $x = 0.3^\circ$, $y = 0.45^\circ$, $z = 0.4^\circ$ ('best' box) appears to give the best model. However, the differences to a box with $x, y, z = 0.3$ are small.

For the **2- μ S-100K** dataset the same procedure also leads to an improvement of the model quality. As 'best' box size $x, y, z = 0.5^\circ$ (box 2 in Figure 29) was determined. Further tests with additional box sizes did not result in better models (see appendix). With this integration box the $R(F^2)$ decreases by 0.02 percentage points to a value of 1.74 %. e_{gross} is 26.1 e, which is 2 e smaller than for the model with refined box sizes. The highest peak in the residual map is now 0.324 e \AA^{-3} (0.400 e \AA^{-3} in ref. box). Moreover, it is no longer located near the position of a nucleus but 0.52 \AA from P1. However, in contrast to the dataset **1-TXS-100K** the deepest hole becomes larger as well. Again an undersized box reveals worsening of the model quality (box 3 and 4 in Figure 29).

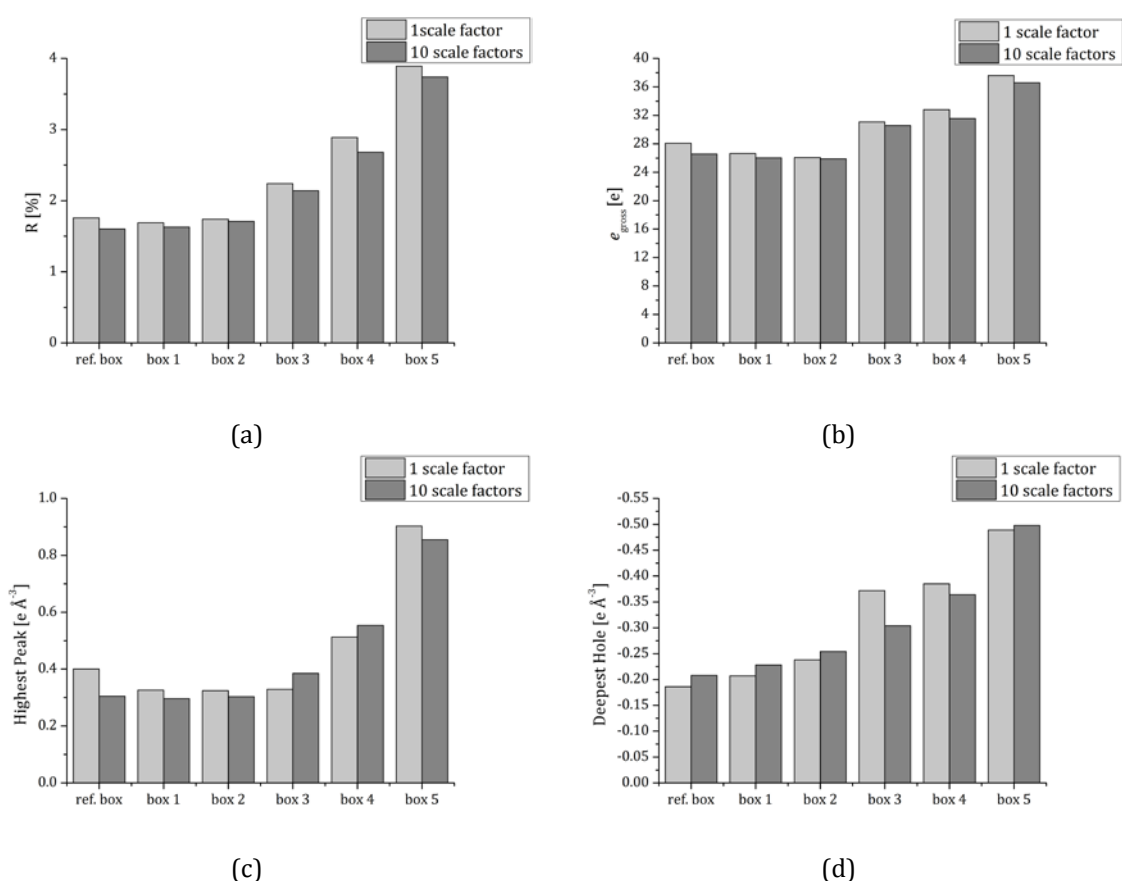


Figure 29: Residual value (a), e_{gross} (b), highest peak (c) and deepest hole (d) for **2- μ S-100K** after multipole refinement. Values for the refinement with resolution-dependent scaling are depicted in dark, those without in pale grey. (box 1: $x=0.6^\circ y=0.6^\circ z=0.6^\circ$; box 2: $x=0.5^\circ y=0.5^\circ z=0.5^\circ$; box 3: $x=0.4^\circ y=0.4^\circ z=0.4^\circ$; box 4: $x=0.3^\circ y=0.3^\circ z=0.3^\circ$).

In the same way optimal integration boxes were determined for all datasets (see appendix). It becomes apparent that the improvement of the models is smaller for the 15 K datasets in relation to the 100 K models. For **1-TXS-15K** the e_{gross} of the 'best' box size is only 1.2 e better than the one obtained for the refined box. For **2-TXS-15K** the reduction of the box size does not improve the model at all.

The improvement of the model quality can also be observed in the changes of the resolution-dependence of the scale factors when the box sizes are reduced. The 'best' box size minimizes the difference between the one scale factor model and the model obtained with resolution dependent scaling. Thus the deviation of the scale factor with the resolution could be used as a quality indicator for the box size. A box size chosen too small, thus leading to a worsening of the overall model quality, can also easily be identified by a significant change in the course of the scale factor (Figure 30).

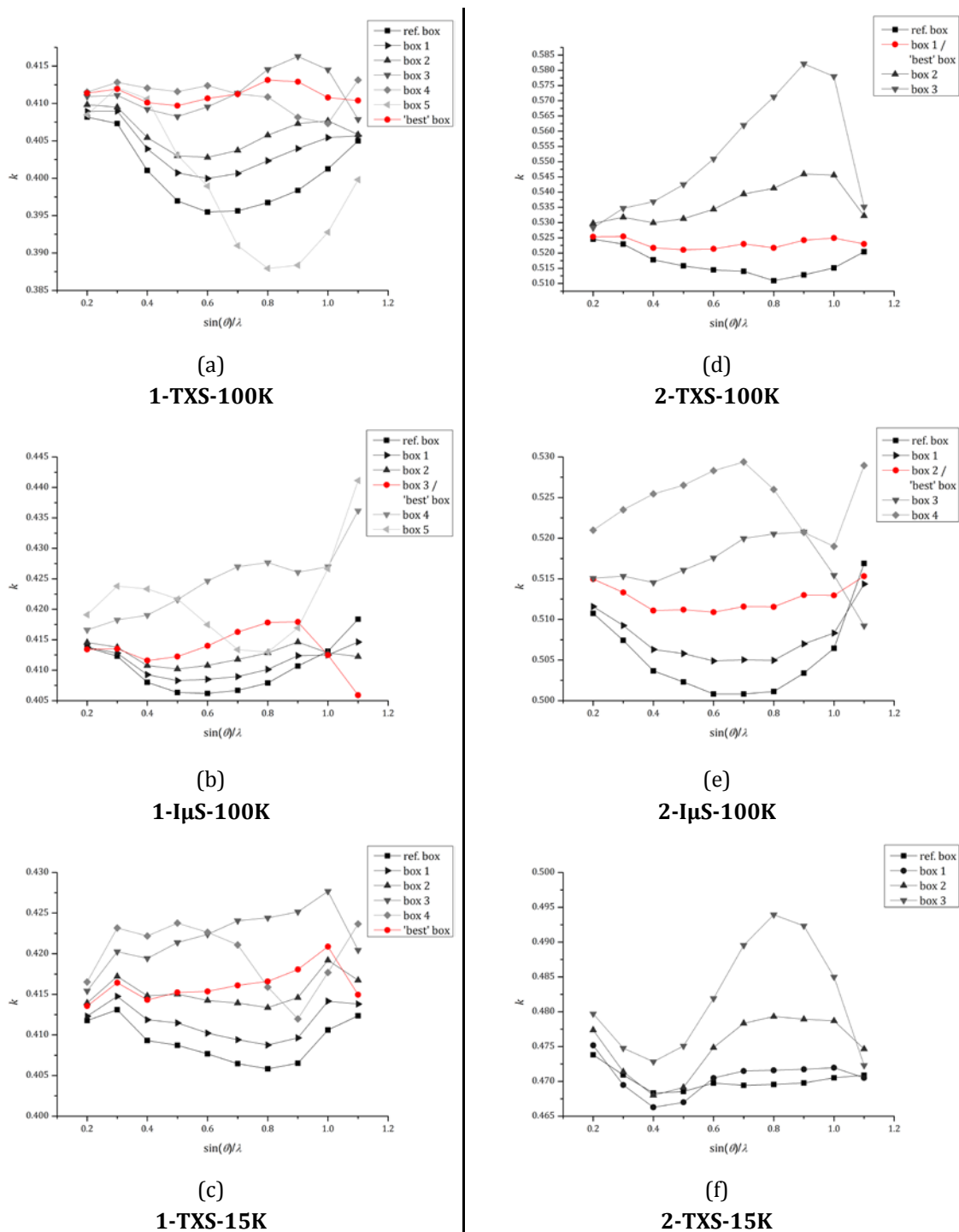


Figure 30: Resolution dependence of the scale factors for dataset **1-TXS-100K** (a), **1-μS-100K** (b), **1-TXS-15K** (c), **2-TXS-100K** (d), **2-μS-100K** (e) and **2-TXS-15K** (f) with different integration box sizes. 'Best' box is highlighted in red. (box 1: $x=0.6^\circ$ $y=0.6^\circ$ $z=0.6^\circ$; box 2: $x=0.5^\circ$ $y=0.5^\circ$ $z=0.5^\circ$; box 3: $x=0.4^\circ$ $y=0.4^\circ$ $z=0.4^\circ$; box 4: $x=0.3^\circ$ $y=0.3^\circ$ $z=0.3^\circ$; box 5: $x=0.2^\circ$ $y=0.2^\circ$ $z=0.2^\circ$; 'best' box: **1-TXS-100K** $x=0.3^\circ$, $y=0.45^\circ$, $z=0.4^\circ$, **1-μS-100K** $x=0.4^\circ$, $y=0.4^\circ$, $z=0.4^\circ$, **1-TXS-15K** $x=0.5^\circ$, $y=0.6^\circ$, $z=0.4^\circ$; **2-TXS-100K** $x=0.6^\circ$, $y=0.6^\circ$, $z=0.6^\circ$, **2-μS-100K** $x=0.5^\circ$, $y=0.5^\circ$, $z=0.5^\circ$)

Nonetheless, in some cases the course of the scale factor with the resolution still mimics a u-shape (Figure 30e) or shows deviation from a constant line for high-order data (Figure 30b). For the dataset **2- μ S-100K** it is possible to further reduce the deviation in scale factors by small changes of the box size ($x = 0.5^\circ$, $y = 0.4^\circ$ and $z = 0.4^\circ$). However, this integration box does not give a better model than the one obtained from the refined box sizes (see appendix). This shows the vulnerability of applying such a simple correction method, as to reduce the box size for the integration. Even though a further reduction of the box size would improve the high-order reflections, this would introduce errors to low-order reflections and thus the benefit of the correction would be negated.

However, in all cases, except for **2-TXS-15K**, a reduced box size was found to flatten the course of the scale factor and at the same time this step improved the overall model quality. For the dataset **2-TXS-15K** none of the tested boxes gives a better result than the refinement with refined integration box and the course of the scale factor cannot be improved, either. This fits nicely with the fact that the refinement with resolution-dependent scaling likewise does not improve the model and supports the hypothesis of TDS.

A marked improvement can be observed in the normal probability plot (Figure 31). The error of the model, derived from the integration with 'best' boxes, displays a distribution that is much closer to a normal distribution than for the model obtained from refined boxes. This indicates that the correction removes systematic errors. Simultaneously the $(I/\sigma)_{asymptotic}$, that is intended to estimate the systematic errors in the data, decreases for the integration boxes, which result in the 'best' models (Figure 32). However, the $(I/\sigma)_{asymptotic}$ seems to be unreasonably high for the refined integration boxes. For example for **1-TXS-100K** the $(I/\sigma)_{asymptotic}$ is 116.0, which is nearly twice the value reported for very carefully collected low temperature data of [2,2]-paracyclophane.^[76,139] Thus this value might be estimated too high, thus indicating an underestimation of the systematic errors. A much lower value seems to be more appropriate. On the other hand, the value of 21.5 for the 'best' fixed box might be suffering from the introduction of additional errors. The same trend is also observed for the other datasets although the decrease in $(I/\sigma)_{asymptotic}$ is smaller. All in all, it becomes obvious that the value for $(I/\sigma)_{asymptotic}$ is strongly dependent on the integration routine. Moreover, it seems that integration with refined box sizes can lead to unjustifiably high values. Therefore $(I/\sigma)_{asymptotic}$ should be used with special care.

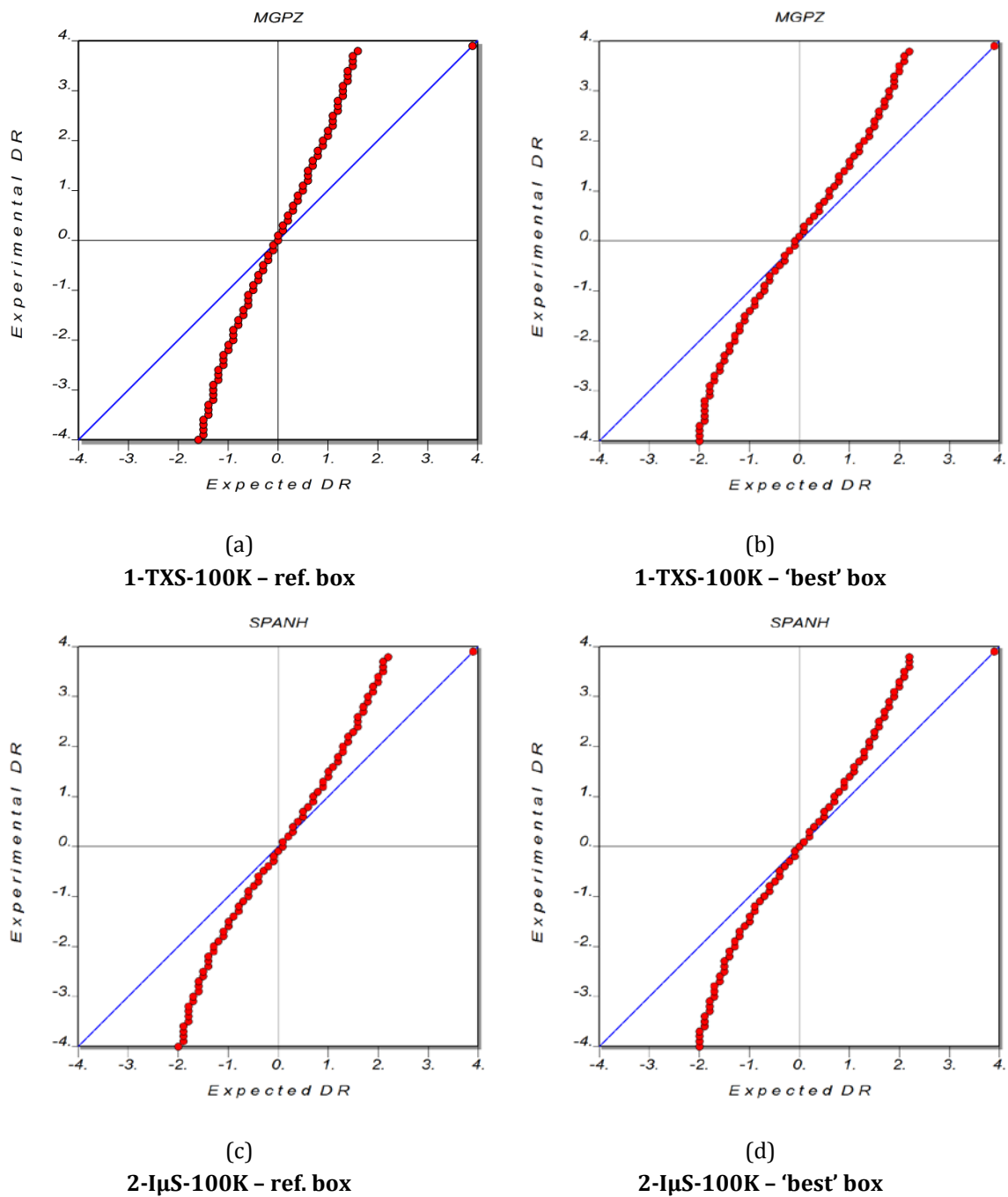


Figure 31: Normal probability plot after MM refinement for integration with refined box size (a, c) and with 'best' fixed box (b, d).

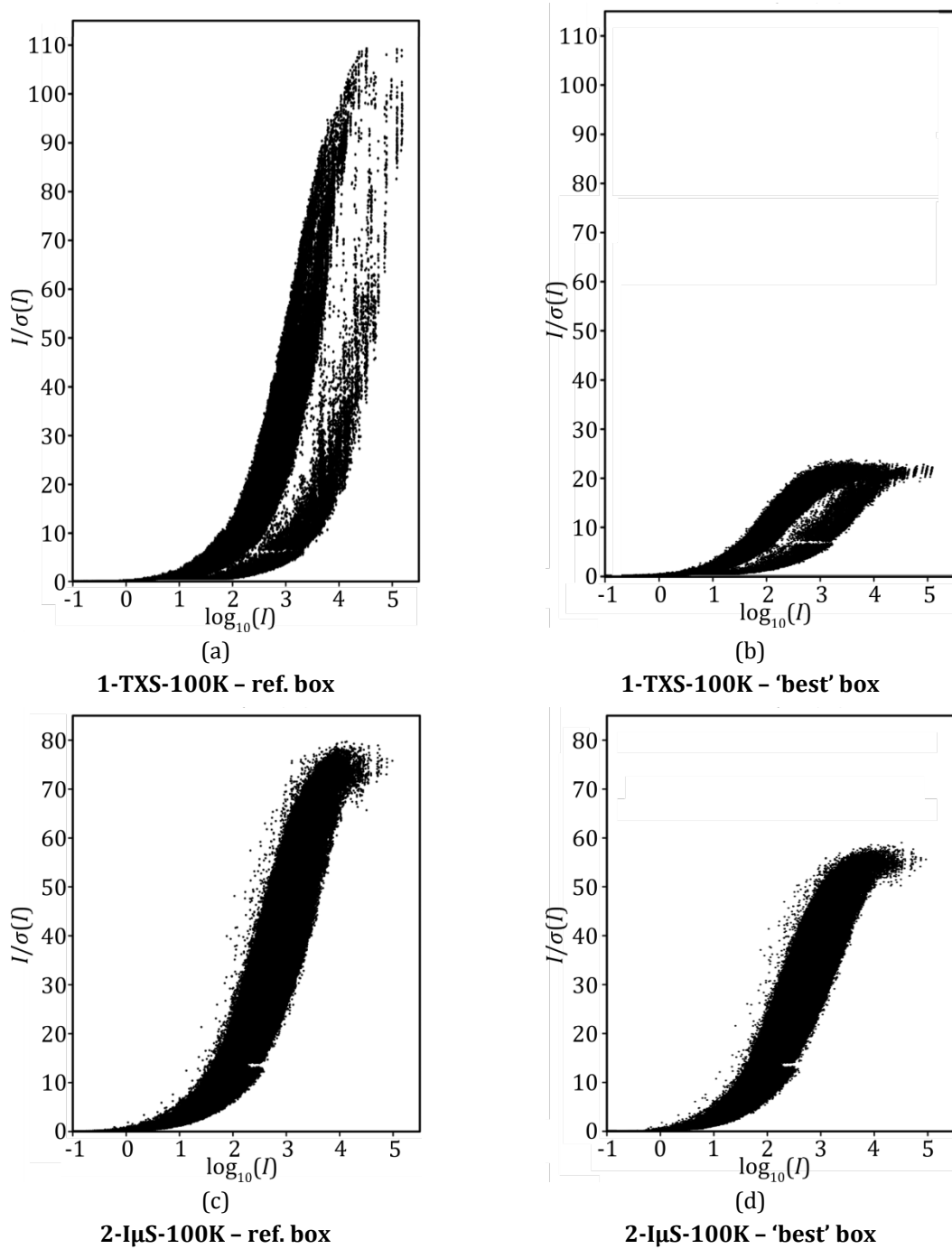


Figure 32: Diederichs plots generated by SADABS for integration with refined box size (a, c) and with 'best' fixed box (b, d)

4.4.2 Influence on the Model

After the integration with the 'best' fixed box size the one scale factor models, obtained for the different datasets of **1** and **2**, reveal no significant differences in their model parameters, similar to the refinement with resolution dependent scaling (Table 12 and Table 13). The net charges of Mg1 for the model obtained with the best box (0.59(11)), 0.52(12) and 0.58(11)) exhibit an only marginal smaller value than with refined box and resolution-dependent scaling (0.66(9), 0.67(9) and 0.61(11)). The net charges for N1 and N2 are also comparable to the values derived from the refinement using resolution-dependent scaling. For compound **2** the same trend is true. The net charge of P1 for the 100K datasets obtained after the refinement against 'best' box data (-0.10(2) and -0.08(3)) is comparable to charges after the refinement with resolution-dependent scaling (-0.11(3) and -0.15(3)). The value of the 15K dataset (-0.09(2)) is also in accordance with these values.

In marked contrast to the refinements using resolution-dependent scaling against refined boxes sizes, the atomic displacement parameters are increased by reducing the box size. By applying resolution-dependent scaling the displacement parameters do not change at all (Table 12 and Table 13). This might be caused by the high correlation between the U values and these scale factors.

An enormous change can also be observed in the scale factor itself. The scale factors of the models from refined box sizes are more than 2 % larger than for the models from the 'best' boxes (Table 12 and Table 13). As suggested by the course of the scale factors the intensities of the high-order reflections are overestimated. Therefore, the scale factors in the refinement without resolution-dependent scaling are underestimated. As described by *Stevens & Coppens*^[143], there is a direct correlation between the correct determination of the scale factor and the residual density, especially at nuclear positions, where the uncorrected models show positive residual density. As a result, the monopole populations and thus the net charges are determined wrongly. This bias seems to be reduced by a smaller box size.

4.4.3 Influence on the Data

In order to investigate the influence of reducing the box size on the data, the TDS correction factor was calculated for each reflection hkl . Assuming that the intensity derived by integration with the 'best' box is the 'true' *Bragg* intensity and that the intensity derived with the larger, refined box size is the *Bragg* intensity plus the TDS contribution, Eq. 4-1 can be rewritten:

$$I_{\text{ref.Box}} = I_{\text{fix}} + I_{\text{TDS}} = I_{\text{fix}} \cdot (1 + \alpha). \quad \text{Eq. 4-3}$$

Thus the correction factor α for each reflection can be calculated by:

$$\alpha = \frac{I_{\text{ref.Box}} - I_{\text{fix}}}{I_{\text{fix}}} \quad \text{Eq. 4-4}$$

For the calculation the two datasets were scaled using the reflection with $\sin(\theta)/\lambda < 0.2 \text{ \AA}^{-1}$, because these reflections should not be affected by TDS. The correction factor α was calculated for each reflection that is present in both datasets. From these α values the robust weighted mean^[144] was calculated in batches sized 0.02 \AA^{-1} and a polynomial, defined by Eq. 4-2, was fitted to these mean values.^[80,122] The calculated α values and the polynomial fit are shown in Figure 33.

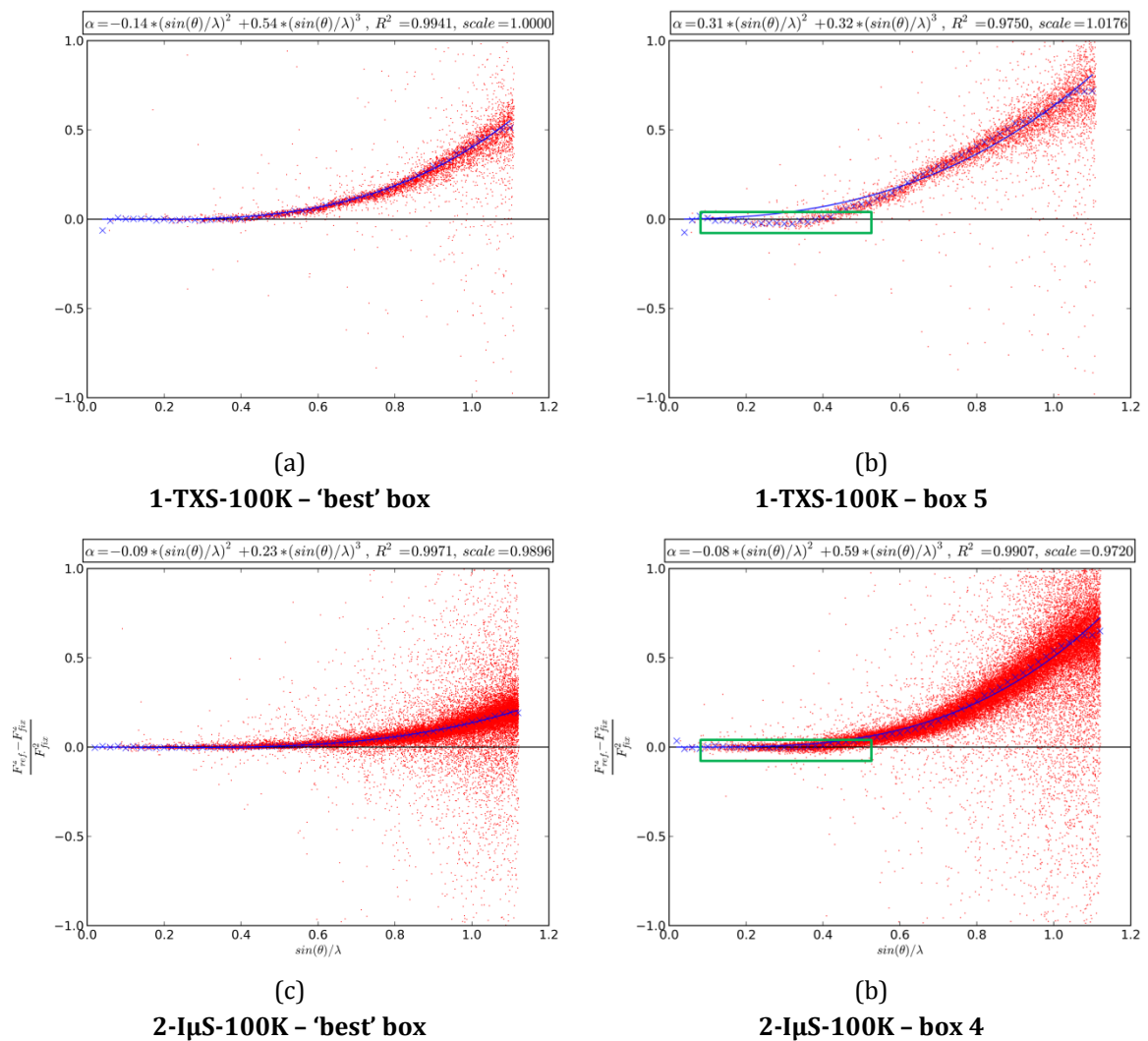


Figure 33: α vs. $\sin(\theta)/\lambda$ plots for the 'best' and a too small integration box for **1-TXS-100K** and **2-I μ S-100K**. The correction factor for each reflection is depicted as a red dot, the mean value in 0.02 \AA^{-1} intervals as a blue cross. The fitted curve is shown as a blue line. The area with accumulated negative α values is highlighted in green.

The distribution of the α values clearly reveals that a reduction of the box size only leads to changes in the intensities of the high-order data, while the intensities of the low-order reflections do not change. The agreement of the fitted curve with the mean values is good for the 'best' boxes. However, for the unjustifiably small boxes deviation between 0.2 and 0.4 \AA^{-1} as well as at high resolution can be observed. Moreover, if the integration box is chosen too small a fall of the α values to below zero can be observed for reflections between 0.2 and 0.4 \AA^{-1} (green box in Figure 33). Since the data points from 0 to 0.2 \AA were used to scale the data, the fall to below zero for the reflections between 0.2 and 0.4 \AA^{-1} indicates that not only the intensities of high-order reflections are changed, but the reflections below 0.2 \AA^{-1} are reduced as well.

It is quite remarkable that the parameter a in Eq. 4-2 is zero or slightly negative for all 'best' box sizes. Therefore, in order to test the influence of the correction factor on the model, several artificial, TDS-contaminated datasets were produced from the model obtained after MM refinement against the **1-TXS-100K** 'best' box dataset.

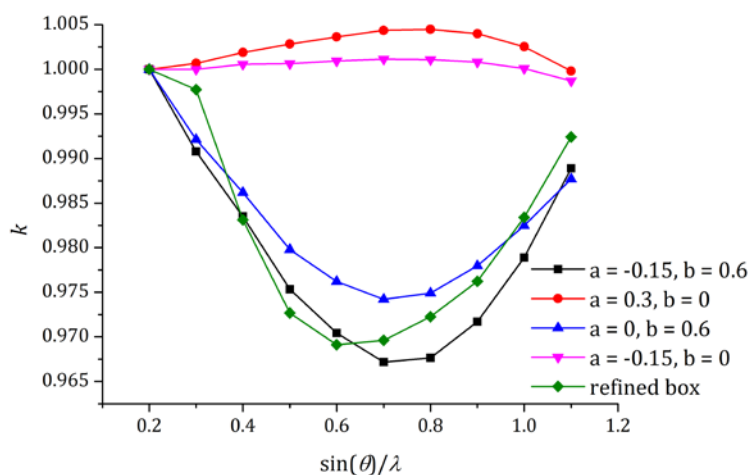


Figure 34: Resolution dependence of the scale factors for artificial, TDS-contaminated datasets. All scale factors were normalized at the first value.

It becomes obvious from the course of the scale factor for the different TDS contributions that the whole course of the scale factor for the refined box size (green) can be modelled with a correction factor similar to that obtained by the fit against the 'best' box data (black). It might be expected that only the increase for the high-order reflections is attributable to TDS, because in this resolution range it adds most to the *Bragg* intensity. However, this is not the case.

The most important part of the correction seems to be the cubic term (blue). The influence of the, squared term seems to be small (red and magenta). This becomes even more apparent after inspecting the influences on the model. A TDS contribution with $a = 0$ and

$b = 0.6$ changes the atomic displacement parameter and the monopole population. However, a contribution of $a = 0.3$ and $b = 0$ is nearly completely absorbed by the atomic displacement parameters. The changes in other parameters are barely significant (Table 9 and Table 10).

Table 9: Influence on the model parameter with $a = 0.0$, $b = 0.6$ ordered by the significance of the change (Diff/su). For the sake of clarity only the first three atomic displacement parameters are shown.

Parameter	Value without contamination	Value with contamination	Diff / su
H(4A) U11	0.02862(2)	0.02427	181.2
H(2) U11	0.02073(2)	0.01724	174.5
Mg(1) U11	0.01522(18)	0.012281	163.3
⋮	⋮	⋮	⋮
C(1) KS	1.0014(11)	1.0149	12.6
N(1) M1	5.155(9)	5.268	12.4
N(2) M1	5.04(10)	5.14	9.8

Table 10: Influence on the model parameter with $a = 0.3$, $b = 0.0$ ordered by the significance of the change (Diff/su). For the sake of clarity only the first three atomic displacement parameters are shown.

Parameter	Value without contamination	Value with contamination	Diff / su
H(4A) U11	0.02862(2)	0.02621	100.3
H(2) U11	0.02073(2)	0.01880	96.1
Mg(1) U11	0.01522(18)	0.013625	88.6
⋮	⋮	⋮	⋮
C(4) KS	0.9575(15)	0.9516	3.8
C(1) KS	1.0014(11)	0.9974	3.7
C(4) M1	4.218(16)	4.258	2.4

4.5 Empirical correction

The errors that are introduced by TDS can in good approximation be corrected manually by adjusting the integration box size. But in addition to the problems described above, which hamper the identification of the 'best' box, this procedure has another big disadvantage. Dozens of integrations with different box sizes have to be performed and, arising from the sometimes very time consuming MM refinement, it can take weeks or months to find the setting that gives the best model. Therefore, a less time consuming procedure is needed that can be computerized.

Therefore, a simple routine was developed that is able to deduce the 'best' TDS correction factor α directly from a refinement against data integrated with refined box sizes. In a 'nested intervals' approach, different correction factors are tested in a refinement with resolution-dependent scaling. The procedure starts with $a = 0$ and $b = 0.1$, as the tests with theoretical TDS contamination revealed that b is the most important factor. In order to keep the computational time to a minimum only a two-step refinement is performed. The refinement starts from the model obtained by refinement against the uncorrected data using resolution-dependent scaling. In the first step, only the resolution-dependent scale factors are refined, followed by a refinement of all parameters (except κ) in the second step. Compared to the complete refinement protocol no differences in the resulting models are detectable. After the refinement the standard deviation of the scale factors from their mean value is calculated. This is used as a quality indicator for the correction. Next the factor b is raised and another refinement is done, if the quality indicator reveals an improvement of the model. If the quality indicator shows no improvement, a is treated in the same manner. In the very last step a full refinement with only one scale factor is performed against the corrected data.

This procedure was found to work quite well, leading to correction factors, which are in good accordance to those obtained from the 'best boxes'. The change in course of the scale factor with the resolution for the different datasets is summarized in Figure 35. The 100 K datasets of **1** both reveal correction factors that are very similar (**1-TXS-100K**: $a = -0.15$, $b = 0.7$; **1-I μ S-100K**: $a = 0.0$, $b = 0.7$). However, the **1-TXS-15K** dataset exhibits a much smaller correction factor ($a = 0.0$, $b = 0.3$). This is in good accordance with the findings from resolution-dependent scaling and from integration with fixed box sizes, which indicate similar errors for the 100 K datasets but much smaller errors for the 15 K data. The correction factors determined for the datasets of compound **2** show similar results. The 100 K datasets show almost equal correction factors (**2-TXS-100K**: $a = -0.05$, $b = 0.45$; **2-**

$1\mu\text{S-100K}$: $a = -0.15, b = 0.5$), while for the 2-TXS-15K dataset a correction factor of $a = 0.0$ and $b = 0.1$ was determined to be the best.

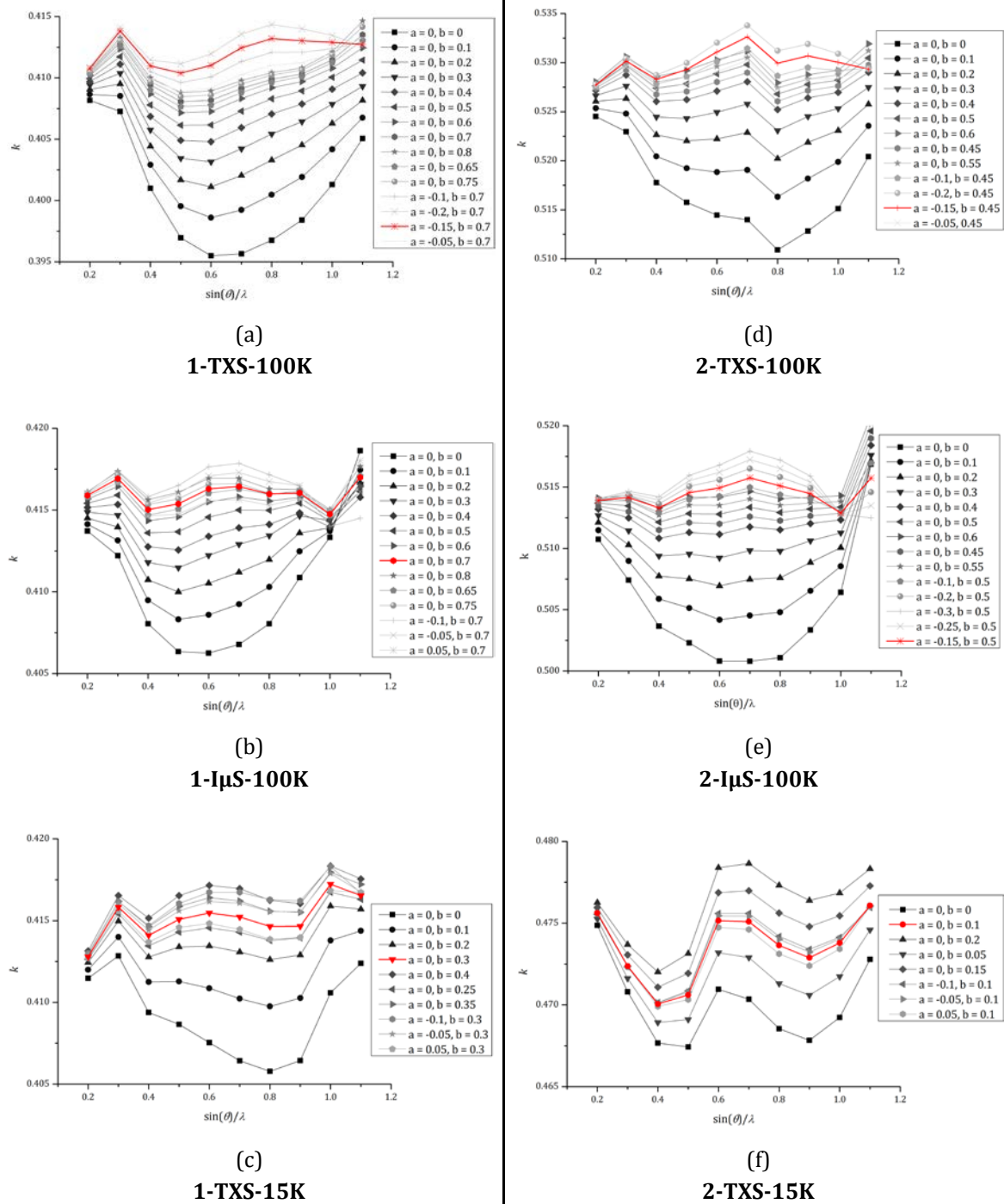


Figure 35: Resolution dependence of the scale factors for datasets 1-TXS-100K (a), $1\text{-I}\mu\text{S-100K}$ (b), 1-TXS-15K (c), 2-TXS-100K (d), $2\text{-I}\mu\text{S-100K}$ (e) and 2-TXS-15K (f) with different correction factors. 'Best' factor is highlighted in red.

4.5.1 Influence on the Model Quality

The quality of the models obtained after the refinement against empirically corrected data is similar to that obtained with the ‘best’ box size (see appendix). The residual $R(F^2)$ drops for all models in relation to the uncorrected model, except for the **2-TXS-15K** dataset (Table 11). The highest peaks are also significantly smaller. For the **1-TXS-100K** dataset the height is more than halved. The **2-TXS-15K** dataset again forms an exception. The highest peak of the supposed corrected model is slightly higher than for the uncorrected (Table 11). This behaviour is also mirrored in the fractal dimension plots (Figure 36). They indicate a large improvement for all datasets but the **2-TXS-15K**. Thus it seems as though a correction is not needed for this dataset. For the other datasets, however, the correction certainly is a large improvement, leading to a reduction of e_{gross} up to 5.7 e (Table 11).

Table 11: Model quality indicators for the MM before and after application of the empirical correction.

		1-TXS-100K	1-μS-100K	1-TXS-15K	2-TXS-100K	2-μS-100K	2-TXS-15K
ref. box	<i>dev. scale</i>	4.53E-03	3.86E-03	2.46E-03	4.23E-03	4.93E-03	2.29E-03
α cor.	<i>factor</i>	1.15E-03	7.07E-04	1.18E-03	9.90E-04	9.03E-04	1.96E-03
ref. box	R [%]	2.32	2.38	2.13	1.78	1.77	1.95
α cor.		1.66	2.12	2.03	1.57	1.52	2.08
ref. box	e_{gross} [e]	28.6	35.3	31.4	27.4	28.1	31.8
α cor.		22.9	29.8	29.0	26.2	23.4	31.0
ref. box	<i>highest peak</i>	0.28	0.164	0.231	0.267	0.4	0.252
α cor.	[e·Å ⁻³]	0.130	0.139	0.186	0.206	0.278	0.264
ref. box	<i>deepest hole</i>	-0.153	-0.186	-0.187	-0.287	-0.186	-0.236
α cor.	[e·Å ⁻³]	-0.121	-0.152	-0.184	-0.248	-0.204	-0.289

In comparison to the results after reducing the box size the tested procedure has one big advantage, besides the fact that it is much faster. The errors that are introduced by the integration of all reflections with the same box size are not present when using the correction factor. This problem showed up for the 100 K datasets of compound **2** especially. The box sizes leading to the flattest curve of the scale factor did not improve the model. Using the empirically determined correction factor circumvents this problem by using the refined boxes for the integration.

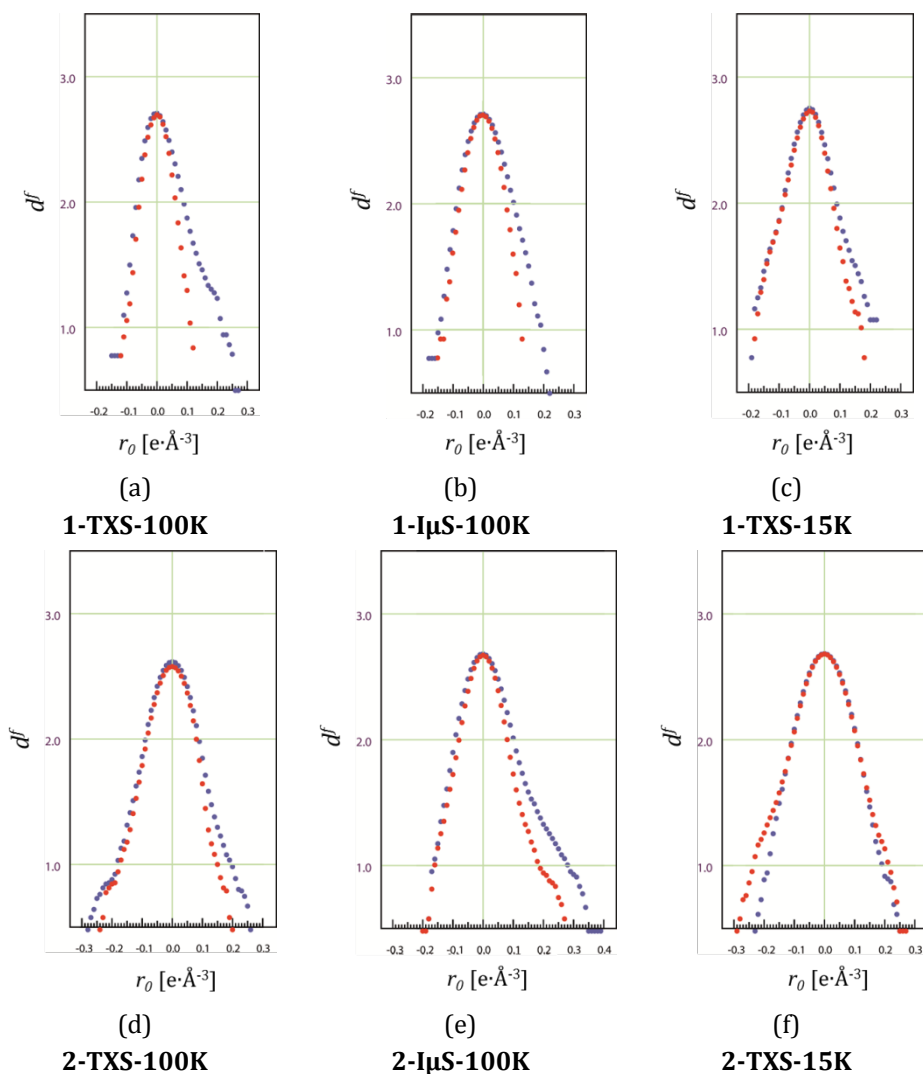


Figure 36: Fractal dimension plots for the datasets **1-TXS-100K** (a), **1- μ S-100K** (b), **1-TXS-15K** (c), **2-TXS-100K** (d), **2- μ S-100K** (e) and **2-TXS-15K** (f) before (blue) and after (red) application of the empirical correction.

4.5.2 Influence on the Model

Since the correction factors obtained by the empirical correction differ only slightly from those obtained by the 'best' box sizes, it is not very surprising that the models do not show large differences, either. The values of some representative model parameters are summarized in Table 12 and Table 13. The net charges for Mg1 tend to be slightly larger than for the models obtained from the 'best' box. The net charges for N1 and N2 are slightly larger for **1-TXS-100K** and **1-TXS-15K**, as well. For **1- μ S-100K** the charges are slightly smaller compared to those from 'best' box. However, none of these differences are significant.

The agreement between the different models for the datasets of compound **2** after the empirical correction is even better than for the 'best' boxes. The net charges of P1 between

the datasets finally show no significant differences anymore. The net charges of S1 are not changed by the correction leaving small differences between the 100 K and the 15 K data similar to what is found with the 'best' boxes.

Thus the empirical correction is not only much faster but also gives better results than the optimization of the box size. However, a direct physical meaning of the correction factor is unfortunately not given. As shown by the investigation of the theoretical TDS contaminated data especially the squared term a of the correction factor is hard to determine, since it mainly effects the atomic displacement parameters and only has a small influence on the course of the scale factor. Arising from the fact that the correct absolute displacement parameters are unknown there is no chance to validate the derived a values. As a and b are derived by a refinement with resolution-dependent scale factor, which does not change the displacement parameters, the correction factor cannot be expected to have any direct physical meaning.

Table 12: Selected model parameters for **1-TXS-100K**, **1- μ S-100K** and **1-TXS-15K**. For each datasets three ways of data treatments are shown: Refinement against the refined box size (Ref. Box), against the manual chosen fixed integration box (Best Box**) and against a corrected *.hkl file. The correction factors were obtained by the above described procedure. In the first line of each dataset values for one scale factor refinement in the second values with resolution-dependent scaling were shown.

parameter	1-TXS-100K			1- μ S-100K			1-TXS-15K		
	Ref. Box	Best Box	α cor.	Ref. Box	Best Box	α cor.	Ref. Box	Best Box	α cor.
1 scale scale factor	0.39573(16)	0.41138(17)	0.41082(15)	0.40721(21)	0.41358(23)	0.41604(20)	0.40764(16)	0.41518(16)	0.41491(16)
1 scale Net charge Mg(1)	1.57(10)	0.59(11)	0.78(8)	1.09(9)	0.52(12)	0.64(8)	1.12(11)	0.58(11)	0.59(10)
10scale	0.66(9)	0.56(12)	0.64(8)	0.67(9)	0.61(12)	0.63(8)	0.61(11)	0.55(12)	0.61(10)
1 scale Net charge N(1)	-0.332(17)	-0.154(15)	-0.120(14)	-0.240(16)	-0.134(17)	-0.152(16)	-0.176(14)	-0.112(14)	-0.107(13)
10scale	-0.119(16)	-0.154(16)	-0.098(15)	-0.162(15)	-0.147(17)	-0.152(16)	-0.113(14)	-0.110(14)	-0.108(13)
1 scale Net charge N(2)	-0.236(18)	-0.043(16)	-0.046(15)	-0.107(18)	-0.050(19)	-0.055(18)	-0.071(15)	-0.017(15)	-0.015(15)
10scale	-0.048(16)	-0.049(16)	-0.035(15)	-0.061(17)	-0.068(19)	-0.059(18)	-0.017(15)	-0.017(15)	-0.016(15)
1 scale U_{eq} , Mg(1)	0.0103	0.0129	0.0135	0.0107	0.0124	0.0141	0.0063	0.0073	0.0082
10scale	0.0105	0.0129	0.0136	0.0108	0.0124	0.0141	0.0064	0.0074	0.0082
1 scale U_{eq} , N(1)	0.0120	0.0145	0.0151	0.0123	0.0140	0.0158	0.0074	0.0083	0.0092
10scale	0.0121	0.0145	0.0152	0.0124	0.0141	0.0158	0.0074	0.0084	0.0092
1 scale U_{eq} , N(1)	0.0109	0.0134	0.0140	0.0112	0.0128	0.0146	0.0067	0.0076	0.0085
10scale	0.0110	0.0134	0.0141	0.0113	0.0129	0.0146	0.0067	0.0077	0.0085

* This parameter was not refined in the final refinement protocol.

** Best box **1-TXS-100K** $x = 0.3$, $y = 0.45$, $z = 0.4$, **1- μ S-100K** $x = 0.4$, $y = 0.4$, $z = 0.4$ and **1-TXS-15K** $x = 0.5$, $y = 0.6$, $z = 0.4$. Correction factor α **1-TXS-100K** $a = -0.15$, $b = 0.7$, **1- μ S-100K** $a = 0.0$, $b = 0.7$ and **1-TXS-15K** $a = 0.0$, $b = 0.3$.

Table 13: Selected model parameters for **2-TXS-100K**, **2-I μ S-100K** and **2-TXS-15K**. For each datasets three ways of data treatments are shown: Refinement against the refined box size (Ref. Box), against the manual chosen fixed integration box (Best Box**) and against a corrected *.hkl file. The correction factors were obtained by the above described procedure. In the first line of each dataset values for one scale factor refinement in the second values with resolution-dependent scaling were shown.

parameter	2-TXS-100K			2-I μ S-100K			2-TXS-15K		
	Ref. Box	Best Box	α cor.	Ref. Box	Best Box	α cor.	Ref. Box	Best Box	α cor.
1 scale scale factor	0.51547(8)	0.52153(7)	0.52848(7)	0.50081(9)	0.51059(10)	0.51428(9)	0.46950(9)	-	0.47324(10)
1 scale Net charge S1	-0.203(18)	-0.238(17)	-0.209(17)	-0.188(18)	-0.21(2)	-0.195(18)	-0.09(2)	-	-0.09(3)
10scale	-0.205(18)	-0.216(17)	-0.217(17)	-0.186(19)	-0.21(2)	-0.185(18)	-0.07(3)	-	-0.08(3)
1 scale Net charge P1	+0.27(2)	-0.10(2)	-0.33(3)	+0.30(2)	-0.08(3)	-0.38(3)	-0.32(4)	-	-0.69(4)
10scale	-0.11(3)	-0.13(3)	-0.17(3)	-0.15(3)	-0.20(3)	-0.26(3)	-0.22(4)	-	-0.26(5)
1 scale κ S	1.0290(10)	1.0000(10)	0.9798(9)	1.0236(12)	0.9949(13)	0.9753(11)	1.0022(16)	-	0.9795(16)
10scale	0.9916(13)	0.9887(12)	0.9835(17)	0.9892(14)	0.9851(16)	0.9811(14)	0.995(2)	-	0.993(2)
1 scale κ P	1.0467(17)	0.9914(15)	0.9512(14)	1.0384(19)	0.980(2)	0.9419(16)	0.973(2)	-	0.932(2)
10scale	0.976(2)	0.972(2)	0.963(2)	0.969(2)	0.962(3)	0.953(2)	0.968(3)	-	0.963(3)
1 scale $U_{eq,S}(1)$	0.0148	0.0152	0.0172	0.0150	0.0158	0.0170	0.0092	-	0.0100
10scale	0.0148	0.0153	0.0172	0.0151	0.0159	0.0171	0.0091	-	0.0100
1 scale $U_{eq,P}(1)$	0.0094	0.0098	0.0118	0.0094	0.0103	0.0116	0.0058	-	0.0066
10scale	0.0093	0.0098	0.0117	0.0096	0.0104	0.0116	0.0058	-	0.0067

** Best box **2-TXS-100K** $x = 0.6, y = 0.6, z = 0.6$, **2-I μ S-100K** $x = 0.5, y = 0.5, z = 0.5$, **2-TXS-100K** $a = -0.15, b = 0.5, 2$ -**I μ S-100K** $a = 0.05, b = 0.45$ and **2-TXS-15K** $a = 0.0, b = 0.1$.

4.6 Conclusion

Errors arising from TDS not only manifest themselves in the size and the principal axis of the atomic displacement parameters, but they can also lead to a distortion of the modelled EDD itself. Errors introduced by TDS could thus be one of the most important unsolved problems in modern charge density investigations. Of course the best prevention of TDS effects is to measure at the lowest possible temperature. However, apart from the much higher cost of using liquid helium for the cooling instead of nitrogen, errors can even occur with datasets measured at 15 K. The errors that occur certainly differ significantly with the investigated compound and thus not every measurement necessarily needs correction. However, the possibility of errors by unresolved TDS contribution to the *Bragg* intensities should always be taken into account.

Within this work it was shown that the refinement of resolution-dependent scaling can be used as a validation tool in order to decide whether a correction is needed. Evidence was found that a smooth u-shape of the course of the scale factor with resolution arises from peak broadening caused by the TDS contribution to the *Bragg* peak. However, the course should be checked carefully since resolution dependent scaling can mask other problems, as well. Residual density peaks near or even at the position of the nucleus are also a sign for potential TDS. By reducing the size of the integration box it is possible to obtain a nearly constant scale factor course. However, in some cases this crude method does not work perfectly, as it can introduce new errors to the intensities.

A solution for the problems arising from this crude correction method would be to introduce a TDS correction as advocated by *Zavodnik et al.*, which could describe the TDS contribution in a physically more meaningful way.^[80,122] By analysing the peak profile of the low-order reflections, it might be possible to derive a learned profile that could be used to evaluate the peak broadening of the high-order reflections. From this a correction could be calculated. Especially for data collected with the relatively new hybrid pixel detectors^[145-147], this should be a feasible method. However, such a correction necessarily has to be incorporated in the integration programs.

Therefore, the empirical correction method presented here is the best way to reduce the errors introduced to the MM by TDS at present. By using the deviation of the resolution-dependent scale factors from a constant value as a quality criterion a correction factor, modelled by $\alpha = a \cdot (\sin(\theta)/\lambda)^2 + b \cdot (\sin(\theta)/\lambda)^3$, can be determined. The improvement of the model quality by applying this correction is surprising (Figure 37). Moreover, the correction leads to a consistent model for datasets measured at different temperatures. It is

very important to emphasize, that this empirical correction does not simply remove all residual density, but rather clears only the residual peak located at the atomic positions, while all peaks elsewhere are still visible.

In contrast to a proper correction that could be embedded in the integration process, no physical meaning can be attributed to the derived correction factors a and b . It is quite remarkable that a is near zero or negative for all tested datasets, which might be due to the strong correlation between the scale factors and the displacement parameters. Thus the correction of other resolution dependent errors cannot be completely excluded and the results should be checked very carefully. However, the significantly reduced correction factors for the 15 K dataset indicate that the errors in the datasets are at least partly due to TDS. Even though the derived correction will definitely not fully mirror the real TDS contribution, it can definitely improve the model's quality.

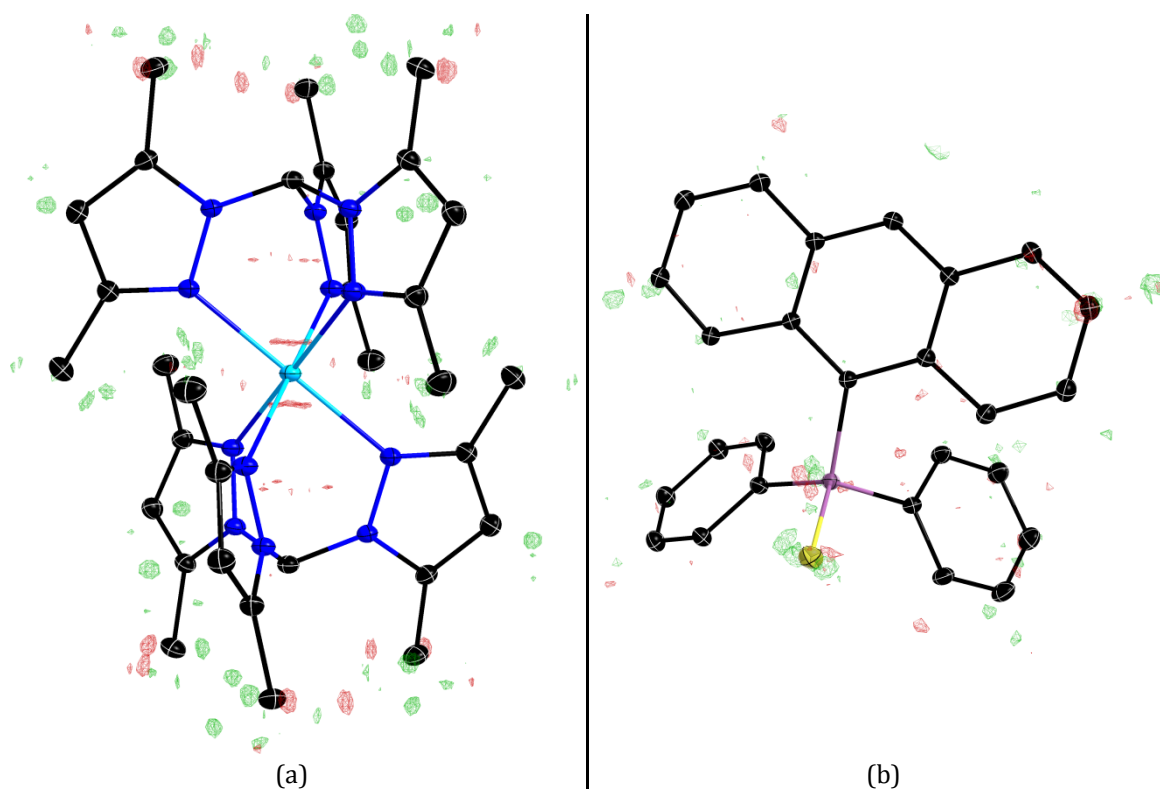


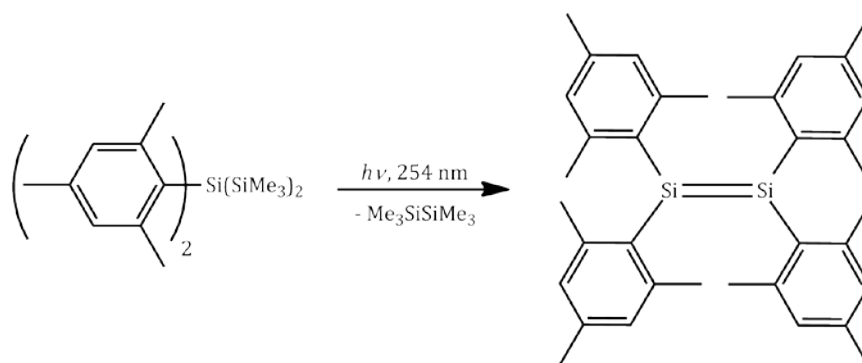
Figure 37: Residual density after MM refinement against empirical TDS corrected 100 K data (**1-TXS-100K** (a) and **2-IµS-100K** (b)) refined with 1 scale factor. Atomic displacement parameters are depicted at 50 % probability level. Hydrogen atoms are omitted for clarity. Positive residual density is shown in green, negative in red. Isolevels are depicted at $\pm 0.08 e \text{ \AA}^{-3}$ (a) and $\pm 0.1 e \text{ \AA}^{-3}$ (b).

5 Chemistry of Low Valent Silicon

This chapter will mainly focus on the bonding in silylones and the question whether these compounds are best described in terms of donor-acceptor bonds between ligand molecules and a central silicon atom or by covalent bonding in analogy to the allenes. Therefore, the EDD of a carbene stabilised silylone obtained from an MM refinement against high-resolution X-ray data will be analysed according to *Baders* QTAIM approach. Special attention will be paid at the correction of systematic errors such as TDS in order to guarantee reliable results. However, first some general aspects in accord to the bonding in low valent silicon compounds and the findings about silylones from previous theoretical studies will be presented.

5.1 Multiple Bonds

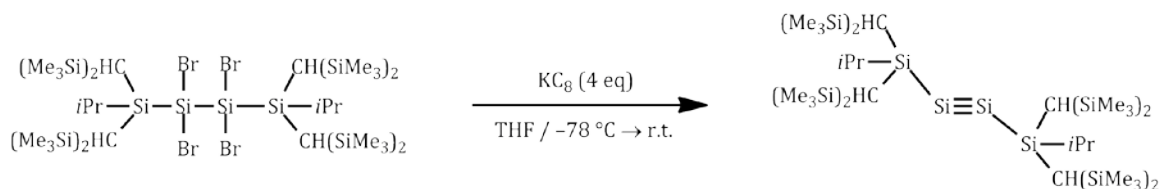
The first experimental proof of the formation of a Si=C double bond was already published by *Gusel'nikov & Flowers* in 1967. However, the major breakthrough for the investigation of stable low valent silicon compounds came in 1981 with the synthesis of the first stable compound containing a Si=C double bond by *Brook et al.*^[148] In the same year *West* and co-workers^[149] reported on the synthesis of a disilene via photolysis of 2,2-bis(mesityl)hexamethyltrisilane (Scheme 1).



Scheme 1: Synthesis of disilene according to *West et al.*^[149]

An crystallographic investigation of *West's* disilene^[150] revealed a geometry that is completely different from the one in allenes. Although the Si=Si bond (2.160(1) Å) is significantly shorter than a typical Si–Si single bond (2.34 Å)^[151], the bonding geometry of the disilene is not planar but shows a trans-bending angle of 18°. Several further disilenes have been reported to date. They all exhibit a more or less pronounced trans-bent geometry.^[1-2]

The synthesis of the first silylene was independently reported by *Sekiguchi et al.*^[152] and *Wiberg et al.*^[153]. The structure of *Sekiguchi's* silyne, which was obtained by reduction of the tetrabrominated precursor (Scheme 2), again shows the difference between low valent silicon compounds and their lighter congeners. In contrast to the structure of alkynes, *Sekiguchi's* silylene reveals a strong deviation from linear arrangement ($R-Si\equiv Si = 137.44(3)^\circ$).^[152] The $Si\equiv Si$ bond is $2.0622(9) \text{ \AA}$ and thus much shorter than a typical $Si-Si$ single (2.34 \AA)^[151] or a $Si=Si$ double bond (2.16 \AA)^[151]. However, the shortening is much smaller than for the carbon counterparts ($C-C$: 1.54 \AA , $C=C$: 1.34 \AA , $C\equiv C$: 1.202 \AA)^[151], which has led to a discussion about the bond order in silynes. An investigation of the bond order by *Pignedoli et al.*^[154-155] described the bonding in silynes as a double bond while *Sekiguchi et al.*^[152] as well as *Frenking et al.*^[156] concluded a triple bond.



Scheme 2: Synthesis of disilyne according to *Sekiguchi et al.*^[152]

The bonding in the trans-bent $Si=Si$ and $Si\equiv Si$ compounds can either be described in the view of natural localized molecular orbitals (left in Figure 38a and b) or delocalized canonical molecular orbitals (right in Figure 38a and b). In the first explanation the double bond is formed by two donor-acceptor bonds, the triplet bond by two donor-acceptor bonds and an additional π -bond. The close proximity of the lone pairs results in a repulsion of the two fragments. Consequently, the structure is bent. An alternative explanation of the trans-bent structures can be given by a second-order *Jahn-Teller* mixing of the σ^* - and π -orbitals. The mixing results in lower energies of the former π -orbital which is transformed into a nonbonding lone pair orbital.^[1-3]

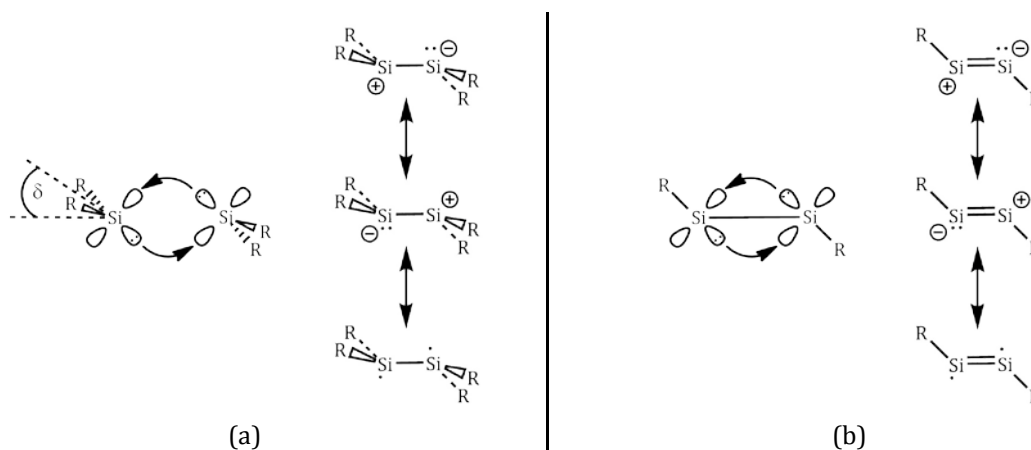
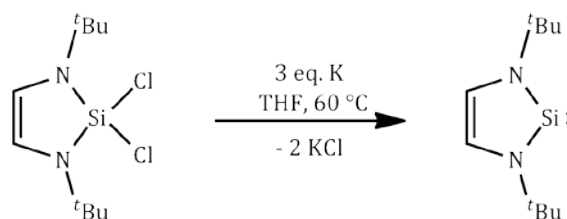


Figure 38: Simple bonding models for trans-bent silicon double and triple bonds. δ = trans-bent angle.

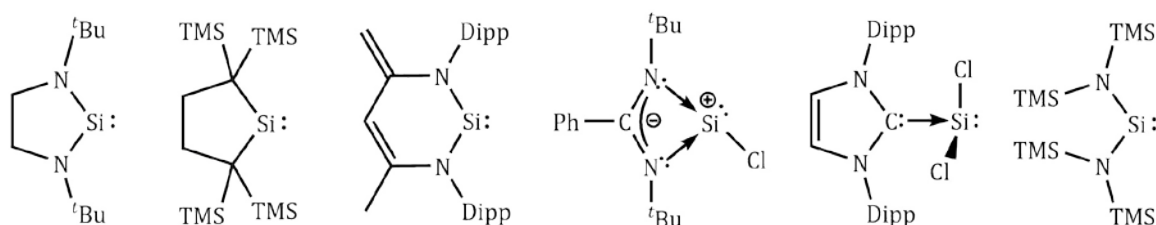
5.2 Silylenes

Another important class of low valent silicon compounds is formed by the divalent silicon(II) structures with a non-bonding lone pair, which are called silylenes. For a long time silylenes were only known as intermediates in organosilicon chemistry, in which their role maybe estimated as even more important than the one of carbenes in organic chemistry.^[4-7] Arising from their high reactivity silylenes usually decompose or polymerise at temperatures above 77 K and could therefore only be investigated in matrixes.



Scheme 3: Synthesis of *N*-heterocyclic silylene (NHSi) according to Denk et al.^[157]

The first isolable silylene that is stable at room temperature was synthesised in 1994 by Denk et al.^[157] via the reduction of the dihalogenated precursor with potassium in boiling THF (Scheme 3). The resulting silylene is the exact silicon congener the *Arduengo* carbene.^[158] In the following several cyclic and acyclic silylenes were synthesised (Scheme 4).^[159-164]



Scheme 4: Examples for isolable silylenes.^[159-165]

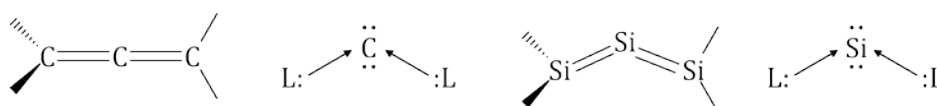
The electronic structure of silylenes is in strict contrast to the one of carbenes. While carbenes tend to favour a triplet ground state ($\Delta E_{S-T}(\text{H}_2\text{C})$ -14 kcal/mol), silylenes usually prefer a singlet ground state ($\Delta E_{S-T}(\text{H}_2\text{Si})$ 16.7 kcal/mol).^[166] The different electronic ground states can be used to explain the trans-bent structure in disilenes, which are formally built up from two silylenes. According to CGMT (*Carter, Golddar, Malrieu and Trinquier*)^[167-170] a planar structure is formed if the sum of the σ - and π -bond energies, $E_{\sigma-\pi}$, is larger than $2 \cdot \Delta E_{S-T}$. However, if $2 \Delta E_{S-T} < E_{\sigma-\pi}$ a trans-bent structure is formed. Thus the electronic ground state of the silylenes is of fundamental importance.

The multiplicity of the ground state can be influenced by adapting the steric and electronic characteristics of the substituents. It has been shown that electronegative substituents increase the gap between the singlet and the triplet state. The opposite effect is observed for

electropositive substituents. Additionally, singlet states are stabilized by π -donating groups, whereas π -accepting groups favour triplets.^[171-172] For carbenes the change of the multiplicity of the ground state is well-documented.^[173-174] However, even though a few triplet silylenes have been reported to date^[175-177] the chemistry of silylenes is still dominated by species with singlet ground state.

5.3 Silaallenes and Silylones

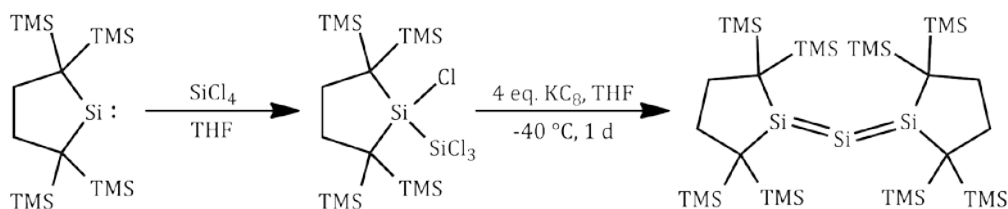
A new type of low valent tetrrels was introduced by *Frenking et al.*^[178-179] They suggested that several divalent carbon compounds such as the carbodiphosphorane $C(PPh_3)_2$ - known, since 1961^[180] - or the carbodicarbene $C(NHC)_2$, should be described as a central carbon(0) atom stabilized by two donor-acceptor bonds of the phosphorane ligands. In this new type of a low valent carbon compound all four valence electrons remain at the central atom, which thus exhibits two lone pairs. Quantum chemical calculations were able to show, that these compounds do not only have a very large first but also a large second proton affinity. Moreover, the frontier orbitals were found to be π - and σ - shaped lone pair orbitals. The term carbones was suggested in analogy to the carbenes.^[178-179] In contrast to the linear allenes, carbones show a bent structure of the L-C-L unit. Additionally, the two ligand planes are not perpendicular (Scheme 5). Experimental evidence for the existence of such donor-acceptor bonds between carbene molecules and a central carbon atom was given by the extremely bent structure of some allenes and their special reactivity.^[18,181-182]



Scheme 5: Schematic representation of an allene, a carbone, a silaallene and a silylone.

The bonding scheme, of a central tetrrel atom of formal oxidation state zero stabilized by two donors, is not limited to carbon as central atom, but can be extended to silicon, as well (Scheme 5). These compounds are called silylones.^[183]

In 2003 *Kira et al.*^[13] reported on the isolation and characterisation of the first trisilaallen, which was synthesised in a two-step reaction from a dialkylsilylene (Scheme 6). Another silaallene was reported by *Tanaka et al.*^[184]



Scheme 6: Synthesis of Trisilaallene according to Kira *et al.*^[13]

The Si=Si bond lengths in Kira's trisilaallene^[13] (2.177(1) and 2.188(1) Å) are in good agreement with known disilenes and the two C–Si–C planes are almost perpendicular (92.5°). However, the central Si–Si–Si unit exhibits a strongly bent geometry (Si–Si–Si: 136.49°). Kira *et al.* explained the bent geometry with a second order *Jahn-Teller* distortion associated with an effective mixing of the π - and σ^* -orbitals and suggested the term bent perpendicular allene.^[13,185-186] Further theoretical investigations of the trisilaallene model compound $\text{H}_2\text{Si}=\text{Si}=\text{SiH}_2$ revealed that the classical allenic structure with D_{2d} symmetry is not a minimum on the potential energy surface.^[187-189] The minimum structure of $\text{H}_2\text{Si}=\text{Si}=\text{SiH}_2$ was found to have a C_s symmetry with a rather acute bending angle of 69.4°. Cyclic and acyclic silylene structures as well as allene type bonding situations were discussed, revealing a strong dependency of the electronic structure on the bending angle. Calculation with bulkier substituents suggested that the bending angle in Kira's silaallene arises from steric repulsion stabilising the allenic character.^[189]

A description of the Kira's trisilaallene as a silylone was introduced by Frenking *et al.*^[190]. They performed quantum chemical calculations on a series of potential silylones, including Kira's trisilaallene. The calculated bond length (Si=Si: 2.239 Å) and angles (Si=Si=Si: 135.7°) are in good accordance with the experimental values. The proton affinities (257.9 kcal·mol⁻¹ and 187.29 kcal·mol⁻¹) were calculated to be in the same range as found for carbones (289.2 kcal·mol⁻¹ and 148.4 kcal·mol⁻¹) indicating a strong nucleophilic character of the central silicon atom. Additionally, the HOMO and HOMO-1 were identified as σ - and π -type lone pairs suggesting that Kira's trisilaallene should be described as a silylone.

In the following donating properties of several ligands have been investigated.^[183,190-194] These studies could show that the key factor for the bonding situation in silaallenes or silylones is given by the relative energies of the interacting fragments L: and the central atom Si. For a linear silaallene the central atom has to be in the triplet ^3P state and the ligands have to be in a triplet state, as well. However, for a silylone both fragments, the central silicon atom and the ligands, need a singlet state. Since silylenes usually have a singlet ground state, a silaallene can only be formed, if the bonding interaction between the triplet fragments exceeds the one between the singlet states and is able to compensate the excitation energies (Figure 39).^[183] Thus the singlet triplet gap of the donating ligand plays an important role.

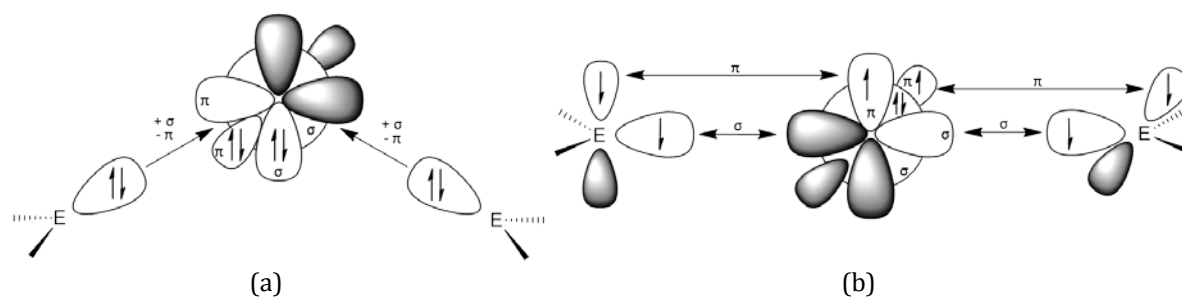
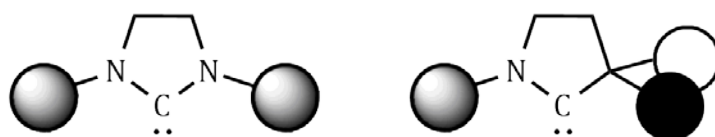


Figure 39: Schematic representation of the orbital interactions in (a) silylones and (b) silaallenes. Reproduced according to reference [183].

5.3.1 Cyclic Alkyl Amino Carbenes as Ligands

The central silicon atom in silylones cannot be only stabilised by silylenes but also by other σ -donating groups such as carbenes. *Frenking et al.*[190,192] investigated the electronic structure of several $(\text{NHC})_2\text{Si}$ structures showing that they should be regarded as silylones (siladicalcarbenes). This can be explained by the large excitation energy between singlet and triple state ($88.9 \text{ kcal}\cdot\text{mol}^{-1}$)[195].

In 2005 *Bertrand et al.*[196-197] introduced the cyclic alkyl amino carbenes (cAACs), which exhibit a much smaller excitation energy ($42.5 \text{ kcal}\cdot\text{mol}^{-1}$)[195] than regular NHCs. By replacing one of the π -donating nitrogen atoms at the α -position with an σ -donor alkyl group the cAACs become better σ -donors and π -acceptors than NHCs. Moreover, the presence of the quaternary carbon at the α -position enables a tailor-made adjustment of the steric environment.

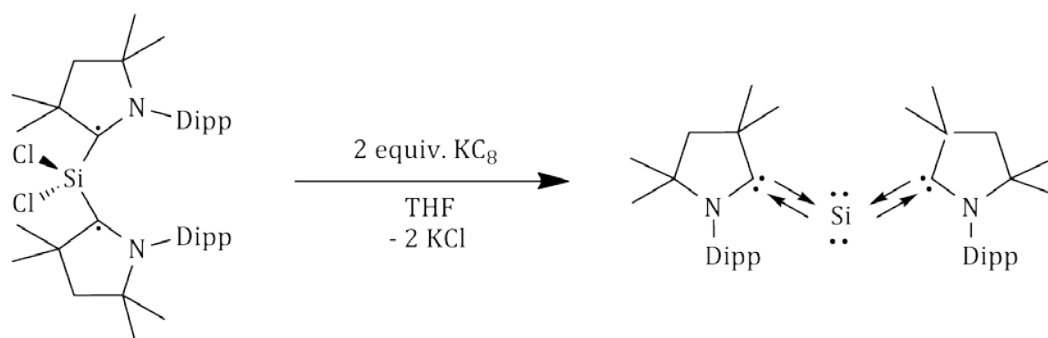


Scheme 7: Schematic representation of NHC (left) and cAAC (right) showing the different steric environment.

These properties have led to a series of unusual main group complexes[198], such as the borylene $(\text{cAAC})\text{BH}$ [199], the silcondichloride biradical $(\text{cAAC})_2\text{SiCl}_2$ [195], the germylone $(\text{cAAC})_2\text{Ge}$ [200] and a series of transition metal complexes $(\text{cAAC})_2\text{M}$ ($\text{M} = \text{Cr}, \text{Mn}, \text{Fe}, \text{Co}, \text{Ni}, \text{Cu}, \text{Zn}, \text{Pd}, \text{Au}, \text{Pt}$)[201-208], in which the metal centre is often in a formal oxidation state zero. Moreover, cAACs were used to activate small molecules such as CO [209] and H_2 [210] and were shown to be remarkable ligands in transition metal catalysis.[173,198] cAACs were found to be much better ligands for the palladium-catalysed α -arylation of carbonyl compounds than NHCs and the $[\text{Au}(\text{cAAC})]^+$ complexes were shown to catalyse the addition of ammonia to non-activated alkynes and allenes.[211] These remarkable properties and the outstanding reactivity render cAACs to be an interesting ligand system for further studies.

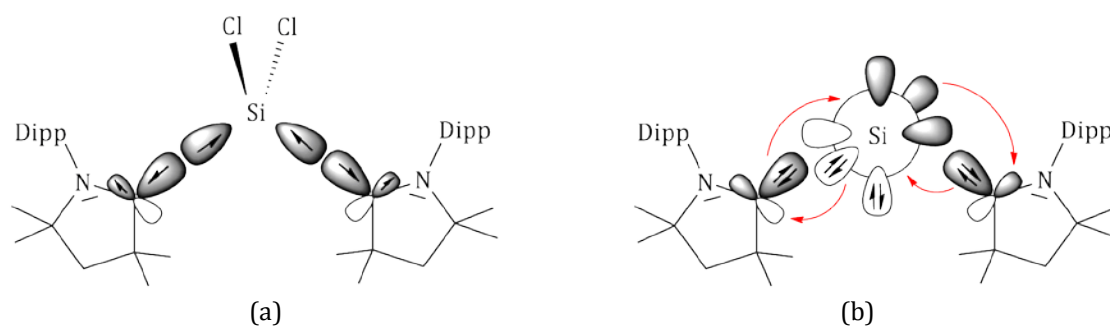
5.3.2 Silylone (cAAC)₂Si

In a joint effort with the *Roesky* group we reported on the structure of a divalent silicon atom stabilised by two cAACs.^[16] By reduction of the respective silondichlorid precursor (cAAC)₂SiCl₂^[195] two silylones with different alkyl residues next to the carbene carbon atom could be isolated and structurally characterised (Scheme 8).^[212] To date only one additional silylone stabilised by a bidentate NHC has been reported.^[17]



Scheme 8: Synthesis of cAAC stabilised silylone according to Roesky et al.^[16]

The structures of both silylones with cAAC ligands reveal a strongly bent C–Si–C unit. In the silylone with dimethyl substituted carbenes (cAAC^{Me})₂Si the C–Si–C angles of the two crystallographic independent molecules are found to be 117.70(8)° and 117.18(8)°.^[16] The silylone with cyclohexyl substituted carbene (cAAC^{cy})₂Si reveals a similar bent character with an C–Si–C angle of 118.16(6)°.^[212] The Si–C bond lengths in both silylones ((cAAC^{Me})₂Si: 1.8411(18) Å, 1.8417(17) Å, 1.8471(17) Å and 1.8482(17) Å; (cAAC^{cy})₂Si: 1.8407(13) Å and 1.8531(14) Å) were found to be comparable to the ones in the precursors (cAAC^{Me})₂SiCl₂ (1.8455(16) Å and 1.8482(17) Å) and (cAAC^{cy})₂SiCl₂ (1.843(2) Å and 1.854(2) Å), in which the bonding situations were proven to be an electron sharing bonds between carbenes and the SiCl₂ units both in triplet state (Scheme 9). However, the ground state of (cAAC)₂Si is the singlet state, substantiated quantum chemical calculations and by X-band EPR experiments.^[16] Small differences in the bond length between the two Si–C bonds can be found for the silylone with cyclohexyl groups at the α carbon atom of the carbene. The silylones with dimethyl groups do not show this effect. The Si–C bonds in both, (cAAC^{Me})₂Si and (cAAC^{cy})₂Si, are significantly longer than typical Si=C double bonds (1.702–1.775 Å)^[213] and slightly shorter than a standard Si–C single bond (1.87 Å)^[151]. The Si–C bonds are also much shorter than in NHCSiCl₂ (1.985(4) Å)^[165], which can be explained by the significant π-backdonation of the central silicon atom in the silylones (Scheme 9). The reported bond lengths are even slightly shorter than calculated for the (NHC)₂Si (1.869 Å)^[190,192], which is in good accordance with the findings that cAACs are better π-acceptors than NHCs.^[196–197]



Scheme 9: Schematic representation of the electron-sharing bond between triplet states in $(cAAC)_2SiCl_2$ ^[195] (a) and donor-acceptor bond between singlet states in $(cAAC)_2Si$ ^[16] (b).

A natural bond orbital (NBO) analysis of the silylone $(cAAC^{Me})_2Si$ revealed a localised σ lone pair orbital at the central silicon atom and a three-centre C–Si–C π -orbital (Figure 40), in which the second lone pair of the silicon is partially delocalised. The distribution was found to give 40% probability at the silicon and 30% at each carbon atom. Thus the best representation of the bonding situation was suggested to be as shown in Scheme 10. The term silylone for the bonding situation in $(cAAC^{Me})_2Si$ and $(cAAC^{cy})_2Si$ was preferred over silylene, because the largest probability of the π lone pair was found at the central silicon. Moreover, the high first and second PA ($PA(1) = 272.2 \text{ kcal}\cdot\text{mol}^{-1}$ and $PA(1) = 186.7 \text{ kcal}\cdot\text{mol}^{-1}$), which both take place at the central silicon atom, support the interpretation as a silylone.^[16]

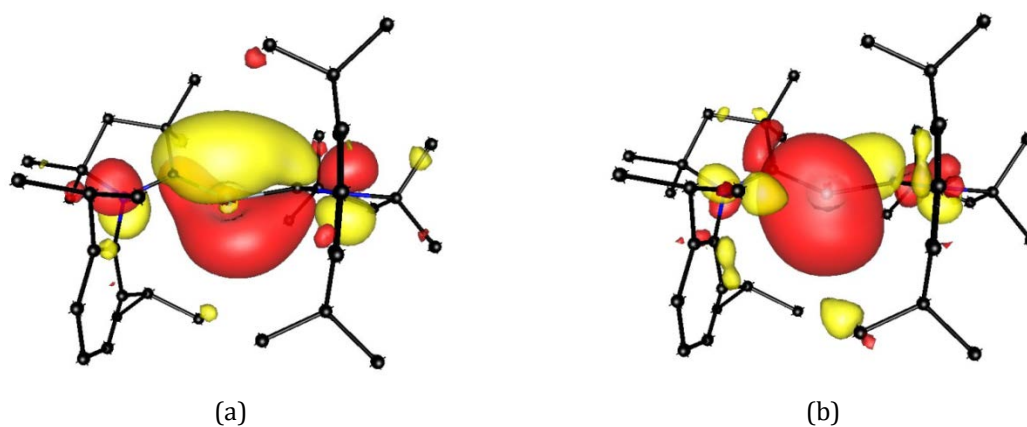
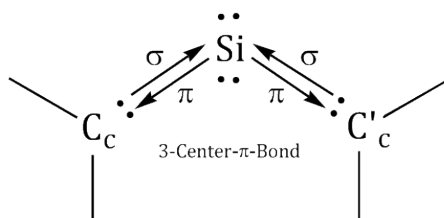


Figure 40: Plots of the HOMO (a) and HOMO-1 (b) of $(cAAC)_2Si$. Reprinted with permission from Roesky et al.^[16]



Scheme 10: Bonding in $(cAAC)_2Si$ from one σ lone pair orbital and a three-centre C–Si–C π orbital of which 40% is located at Si and 30% at each C atom.

5.4 Experimental Charge Density Study of (cAAC^{cy})₂Si

5.4.1 Data Collection

The crystals of (cAAC^{cy})₂Si · 0.5 *n*-hexane (**3**) used in this study were provided by *Dr. Kartik C. Mondal* from the group of *Prof. Herbert W. Roesky*. The compound crystallises in the triclinic space group $P\bar{1}$ with one molecule of (cAAC^{cy})₂Si and half a molecule of *n*-hexane in the asymmetric unit. The co-crystallized solvent molecule did not show any signs of disorder in a previous collected routine dataset. Therefore, the (cAAC^{cy})₂Si was chosen over the (cAAC^{Me})₂Si, since the latter crystallises with two molecules in the asymmetric unit, which would make the refinement much more complex.

A single crystal suitable for the measurement of a high-resolution dataset was chosen under a polarisation microscope and mounted from inert oil at low temperature using the X-Temp2 device.^[214-215] A high-resolution dataset ($d_{max} = 0.45\text{\AA}$) of **3** was collected on a Bruker D8 three circle goniometer equipped with a Smart APEX II CCD, a TXS Mo rotating anode, Incoatec Helios mirror optics and a Bruker Kryoflex II device. The data collection strategy was calculated using the program *COSMO* in the *APEX II* software suite^[216] and manually extended. The data were collected with omega-scans ($\Delta\omega = 0.4^\circ$) at fixed ϕ -angles and phi-scans ($\Delta\phi = 0.4^\circ$) at fixed ω -angles with a detector distance of 5 cm at exposure times between 1 (low-order) and 200 s (high-order data).

5.4.2 Data Reduction

The dataset was integrated with *SAINTE 8.30C*^[131]. The integration was performed with box size refinement enabled starting from $x = 0.8^\circ$, $y = 1.0^\circ$, $z = 0.6^\circ$. The threshold for the spot-shape update was set to $10 I/\sigma$. All other values were kept fixed at their default values. Afterwards scaling, absorption correction and error model determination were applied with *SADABS 2014/2*^[71]. The weighting scheme for the error model was refined using individual K for each run and an overall g (see Eq. 2-17).

The quality indicators reveal a suitable data quality for charge density refinements. The deviation between the symmetry equivalent reflections is in an acceptable range (Figure 41 and Table 14).^[76] Completeness and multiplicity of the low-order data are extraordinary, especially when the low symmetry of the space group is taken into account. At higher angle the dataset does not show this high completeness and multiplicity. Yet, the dataset is nearly complete up to a resolution of 0.45\AA .

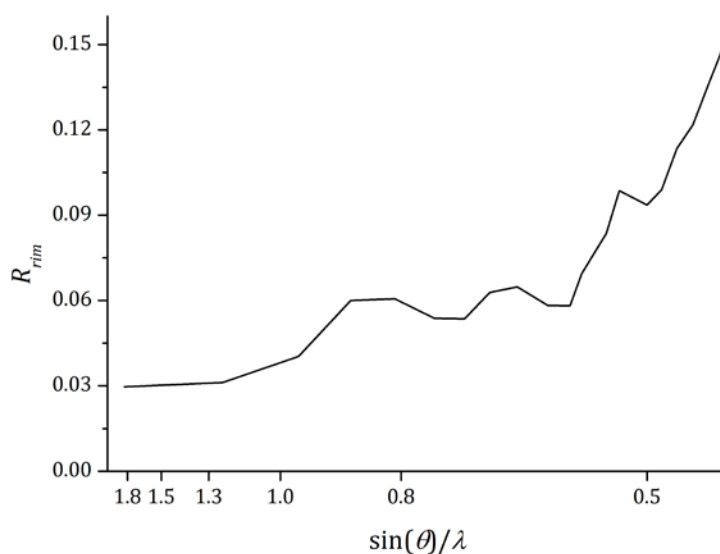


Figure 41: Course of R_{rim} with resolution for compound 3.

Table 14: Completeness, multiplicity and R_{rim} for the datasets of compound 3.

$\sin(\theta)/\lambda$	#hkl (theo.)	comp.	mult.	R_{rim}
Inf-1.83	741	100.0	39.64	0.0297
1.83-1.22	1762	99.9	36.10	0.0312
1.22-0.97	2494	100.0	31.95	0.0403
0.97-0.85	2402	100.0	25.49	0.0600
0.85-0.77	2558	100.0	19.95	0.0606
0.77-0.71	2729	100.0	16.99	0.0537
0.71-0.67	2421	100.0	16.27	0.0535
0.67-0.64	2257	99.8	15.65	0.0628
0.64-0.61	2707	99.5	14.17	0.0648
0.61-0.58	3249	99.3	12.03	0.0582
0.58-0.56	2612	98.9	10.96	0.0581
0.56-0.55	1386	98.8	10.64	0.0695
0.55-0.53	3255	98.6	10.26	0.0836
0.53-0.52	1760	98.4	9.50	0.0986
0.52-0.50	4095	98.0	6.60	0.0936
0.50-0.49	2256	97.3	6.29	0.0990
0.49-0.48	2479	97.5	6.17	0.1134
0.48-0.47	2678	96.4	5.87	0.1218
0.47-0.46	2902	95.9	5.16	0.1370
0.46-0.45	3322	92.8	4.61	0.1524

5.4.3 Model Refinement

The structure was solved by direct methods (*SHELXT*)^[53] and refined by full-matrix least squares methods against F^2 .^[132-133] The positions and the atomic displacement parameters of the non-hydrogen atoms were refined against high-order data ($d < 0.6 \text{ \AA}$). The hydrogen atoms were identified by a difference *Fourier* analysis using the low-order data ($d > 1 \text{ \AA}$). The hydrogen atoms were placed on their corresponding peaks in the difference *Fourier* map and the C–H bond lengths were set to their distances from neutron diffraction experiments.^[134] The U_{iso} values of the hydrogen atoms were constrained to 1.5 times U_{eq} of their pivot atoms for terminal sp^3 carbon atoms and 1.2 times for all other carbon atoms. The IAM served as the starting model for the multipole refinement of compound **3**.

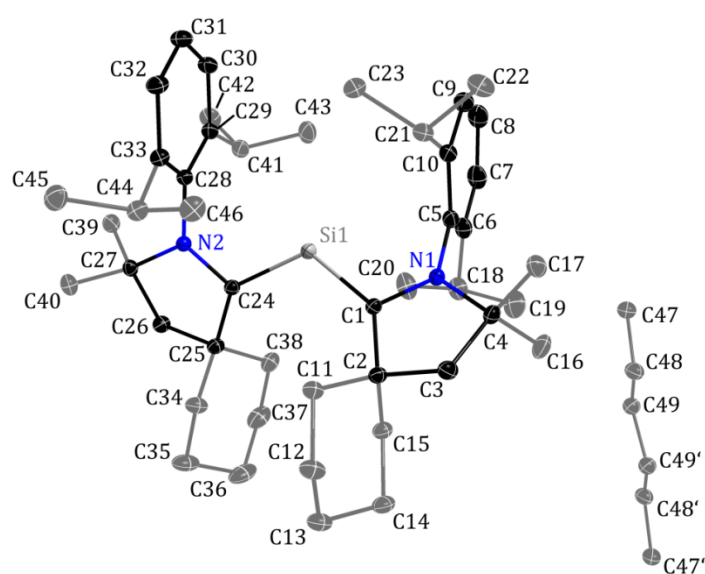


Figure 42: The molecular structure of compound **3**. Hydrogen atoms are omitted for clarity. Anisotropic displacement parameters are depicted at the 50% probability level.

The MM refinement was performed against F^2 using the program *XDLSM* implemented in the *XD2006* program package^[136]. The core and the spherical valence densities were composed of STO-HF atomic wave functions reported by Su, Coppens and Macchi^[56-57] (SCM bank file). The parameters κ and κ' were used to adjust the radial fit of these functions for non-hydrogen atoms. Hereby the multipoles of one atom type were forced to have the same κ' . For the hydrogen atoms the values were kept fixed during the refinement at $\kappa = 1.1$ and $\kappa' = 1.18$.^[138] For the silicon atom several different radial-function parameters were tried. However, the refinement using the standard values gave the best results. The expansion of the spherical harmonics was truncated at the hexadecapolar level for all non-hydrogen atoms. Hydrogen atoms were treated by bond directed dipoles. The hydrogen atom positions were refined against the low-order data ($d > 1 \text{ \AA}$); the distances were reset to

those from neutron diffraction experiments after each step. In the end anisotropic displacement parameters for the hydrogen atoms were calculated using the *SHADE server*.^[217]

In order to stabilize the refinement, the multipole parameters for several atoms were constraint to be the same (chemical constraints) and local non-crystallographic symmetry restrictions for the multipolar expansion were applied (see appendix). The parameters were introduced in the refinement routines in a stepwise manner and the local-symmetry and the chemical constraints were dismissed during the refinement. In the final refinement step all parameters (except κ) were refined together until convergence was reached. (The final refinement strategy is given in the appendix).

5.4.3.1 Anharmonic motion in (cAAC^{cy})₂Si

The residual density map of the model obtained after the above mentioned refinement protocol, is by no means flat and featureless. Structured shashlik-like residual density of alternating maxima and minima can be observed in close proximity to the two cyclo-hexyl groups (C11-C15; C34-C38) and the isopropyl group (C18-C20) (Figure 43a). Additionally, strange residual density features reveal around Si1. This structured residual density is also apparent in the fractal dimension plot, which shows broad shoulders at both sides (Figure 43b). As shown by *Herbst-Irmer et al.*^[68] this can be taken as a hint on potential anharmonic motion. However, a distinction between anharmonic motion and disorder of two positions in very close proximity is nearly impossible, especially when no multi-temperature data is available. Yet, as shown by *Herbst-Irmer et al.*^[68] the refinement of anharmonic motion in MM should be favoured over disorder in these cases. Other origins of the residual density such as problems with the local coordinate system or inconsistent chemical constrains can be excluded since both were dismissed during the refinement protocol. Consequently, anharmonic motion was introduced in a stepwise manner by the refinement of *Gram-Charlier* coefficients up to third order for Si1, C11-C15, C18-C20 and C34-C38, since neglecting anharmonic motion can lead to bias in the derived properties.^[68]

After the refinement of the anharmonic motion the residual density map no longer shows the typical alternating residual density (Figure 44) and the model quality (Table 15) is improved, as well. Although this can be taken as first evidence that the refinement of the *Gram-Charlier* coefficients is reasonable, the obtained model should be checked carefully.

Table 15: Model quality indicators for the MM refinement using harmonic and anharmonic thermal motion.

	R [%]	e_{gross} [e]	$d^l(0)$	highest peak [e·Å ⁻³]	deepest hole [e·Å ⁻³]
harmonic	2.96%	35.2	2.68	0.47	-0.37
anharmonic	2.47%	33.2	2.68	0.31	-0.24

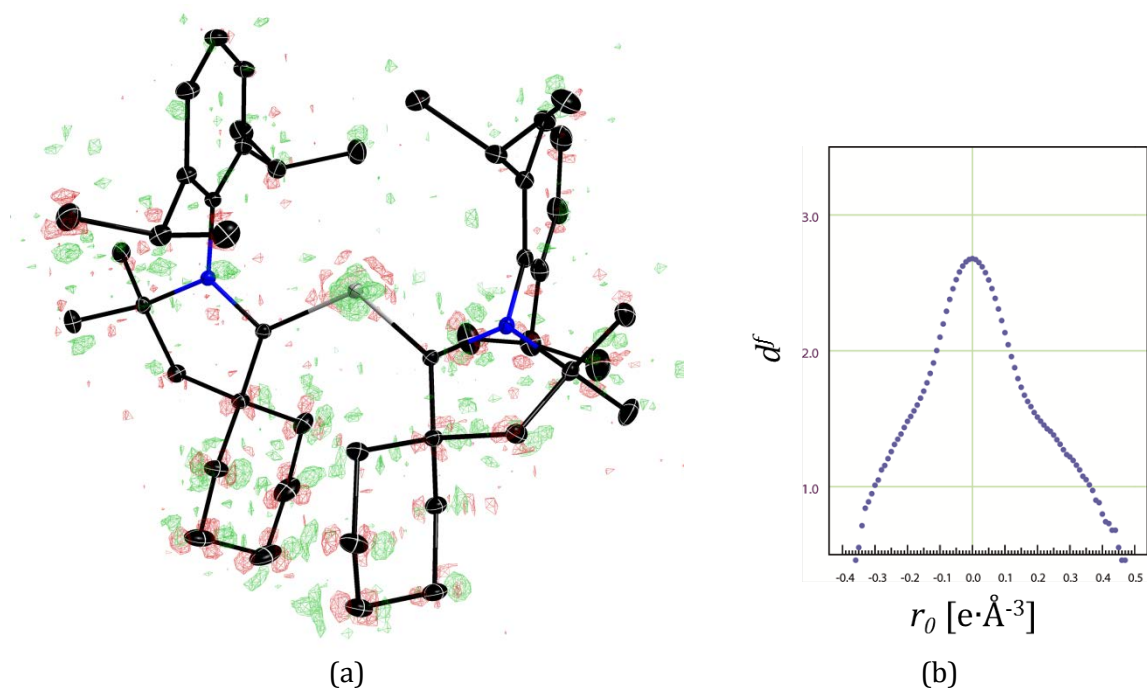


Figure 43: Residual density map (a) and fractal dimension plot (b) after MM refinement of **3**. Atomic displacement parameters are depicted at 50 % probability level. Hydrogen atoms are omitted for clarity. Positive residual density is shown in green, negative in red. Isolevel is depicted at $\pm 0.12 e \text{\AA}^{-3}$.

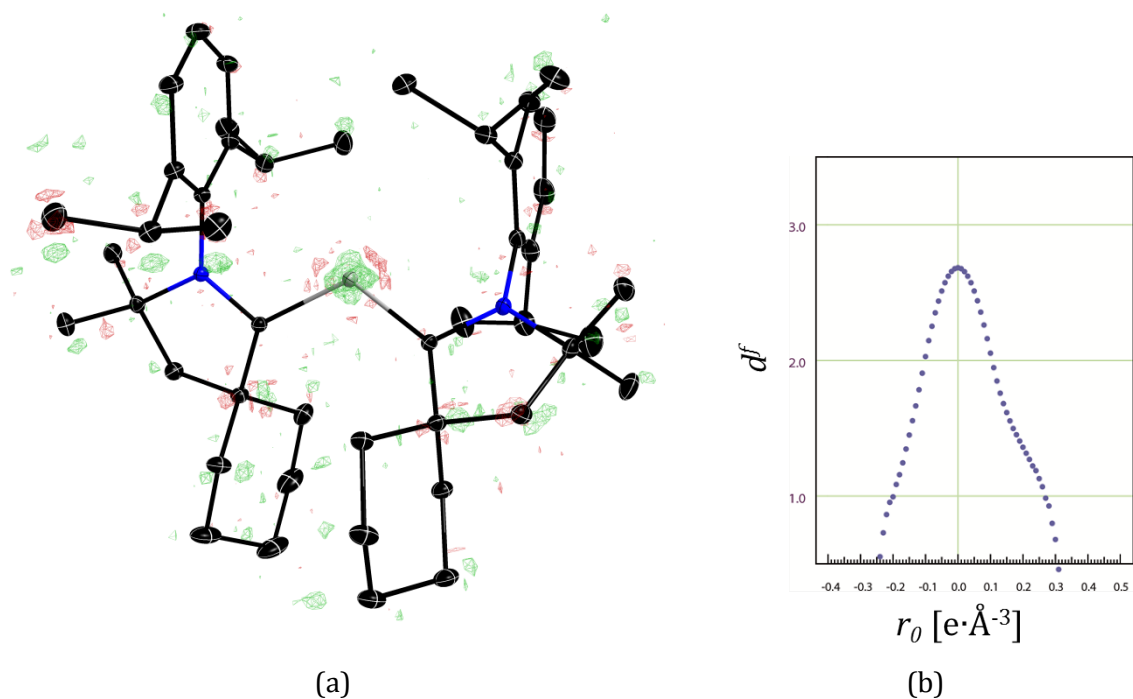


Figure 44: Residual density map (a) and fractal dimension plot (b) after MM refinement of **3** with Gram-Charlier coefficients. Atomic displacement parameters are depicted at 50 % probability level. Hydrogen atoms are omitted for clarity. Positive residual density is shown in green, negative in red. Isolevel is depicted at $\pm 0.12 e \text{\AA}^{-3}$.

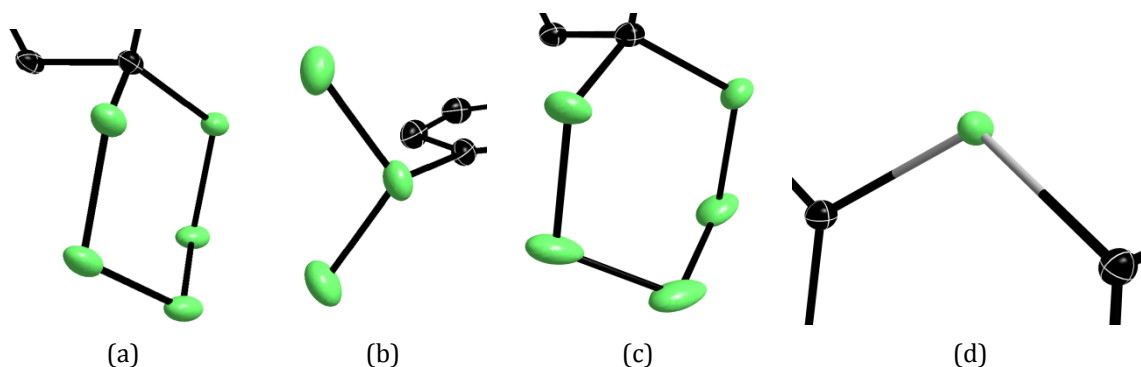


Figure 45: Probability density function is depicted at a level of 50 % after the refinement Gram-Charlier coefficients up to 3rd order for C11-C15 (a), C18-C20 (b), C34-C38 (c) and Si1 (d). PDFs calculated with MoleCoolQt^[218].

Herbst-Irmer *et al.*^[68] suggested a validation of the results by analysis of the probability density function (PDF) and the correlation of the model parameters. Figure 45 shows the PDFs for the anharmonic refined atoms. The deviation from the harmonic ellipsoids is only small and seems reasonable. The amount of negative density is very small. For Si1 the total integrated negative probability is 0.000 %. The highest total negative probability can be found for C13 (-0.072 %). However, this value is very low too and much lower than the values found to be critical by Scheringer.^[219] Thus the PDF seems to be reasonable, although small physically incorrect negative probability can be found for some atoms.

Another important quality criterion for the anharmonic refinement that has to be checked is the correlation of the Gram-Charlier coefficients with other model parameters. Especially the correlation with the multipole population should be checked carefully in order to ensure that the true minimum is reached.^[220] Correlation of more than 0.6 can be found between the individual Gram-Charlier coefficients and between the Gram-Charlier coefficients and the positional parameters. However, both correlations are rather typical. They barely exceed 0.8 and are thus acceptable. A correlation between Gram-Charlier coefficients and the multipole parameters could not be found. Thus, a distortion of the MM by the refinement is very unlikely and the refinement of Gram-Charlier coefficients up to third order was included in the final refinement strategy.

5.4.4 Resolution-dependent Errors in (cAAC^{cy})₂Si

Even after the refinement of anharmonic motion the residual density map still exhibits considerably high features, which are especially located around the silicon atom (Figure 49a). Moreover, the fractal dimension plot exhibits a shoulder on the positive side (Figure 49b). The analysis of the $\Sigma F_o^2 / \Sigma F_c^2$ quotient with the resolution reveals a continuous increase above 0.6 \AA^{-1} (Figure 46). As shown in Section 4 these findings indicate errors caused by TDS. Consequently, the different correction types presented in Section 4 were applied to the dataset in order to minimise the introduced error.

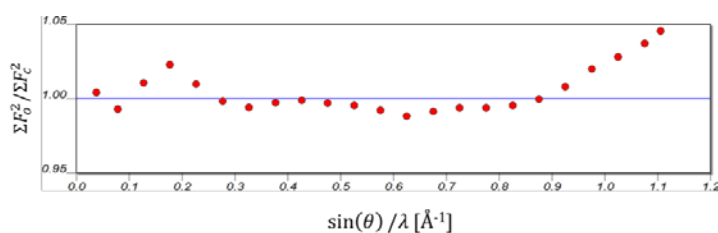


Figure 46: Plot of $\Sigma F_o^2 / \Sigma F_c^2$ vs. $\sin(\theta) / \lambda$ (DRK-plot) for **3**.

First a refinement with resolution-dependent scaling was performed. The dataset was divided into 10 resolution batches. The first batch covers the reflection up to 0.2 \AA^{-1} . The width of the remaining nine batches is 0.1 \AA^{-1} each. The refinement with resolution-dependent scale factors leads to an improvement of the model quality (Table 16). A closer inspection of the residual density reveals a reduction of the features especially around the silicon atom (Figure 49c and d). The $R(F^2)$ drops by 0.21 percentage point, the e_{gross} by 0.8 e. The highest peak slightly decreases by $0.03 \text{ e} \cdot \text{\AA}^{-3}$ while the deepest hole is not changed. The course of the scale factor with resolution mimics a u-shape (Figure 50).

All these findings are in very good accordance with those found for compound **1** and **2** in Section 4. However, the analysis of the DRK-plots exhibits a worsening of the agreement of the low-order reflection ($\sin(\theta) / \lambda < 0.1$) (Figure 47).

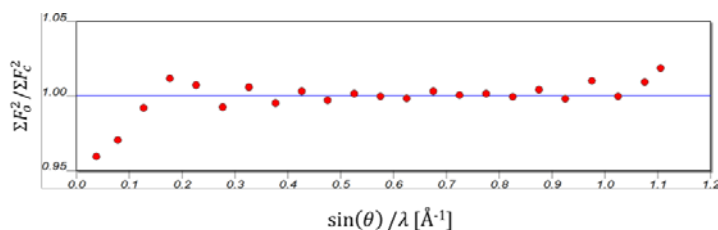


Figure 47: Plot of $\Sigma F_o^2 / \Sigma F_c^2$ vs. $\sin(\theta) / \lambda$ (DRK-plot) for **3** after refinement with resolution-dependent scaling.

The bad fit of calculated and observed structure factor for these low-order reflections is not a result of the refinement with resolution-dependent scaling, but can be ascribed to scaling problems arising from the attenuator used for frames with topped pixels. The Smart APEX II

CCD detector has a maximum counting rate of 64000. A frame exceeding this limit, is collected again, if the option ‘retake if topped’ is enabled in the APEX II software suit^[216]. If the exposure time is longer than 8 s it is reduced to 1/8 for the recollection. However, for shorter exposure times an attenuator is used to reduce the incoming X-ray beam.

In order to identify the reflection showing scaling problems caused by the attenuator, the frames were analysed using the program *SUMMARY* in the *APEX II* software suit^[216], which marks the frames that have been recollected. Additionally, the intensities in the *hkl-file* after the data reduction and scaling were checked for unusually large differences between equivalent reflections and large standard deviations. By this procedure 22 strong reflections were identified, which show scaling problems. The reflections were deleted from the integration output (**_0m.raw*) and scaling, absorption correction and error model determination were repeated. Because 21 of these reflections were also measured on other frames without attenuator, the completeness was not affected by this correction. After the correction, the calculated and observed structure factor are in good accordance also for the low-order reflections and the model quality (Figure 48) is further improved (Figure 49e and f; Table 16). It is quite remarkable that the improvement achieved by this correction is comparable to or even larger than the improvement by resolution dependent scaling. The $R(F^2)$ is reduced by another 0.20 percentage points, the e_{gross} by 1.8 e. The highest peak as well as the deepest hole show no significant change, but the $d^f(0)$ is slightly increased by 0.01. This impressively illustrates the importance of an accurate data collection especially for the very inner data.

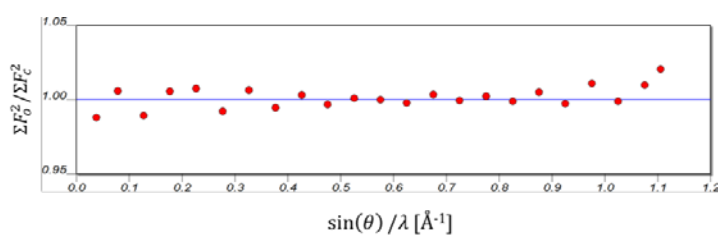


Figure 48: Plot of $\Sigma F_o^2 / \Sigma F_c^2$ vs. $\sin(\theta) / \lambda$ (DRK-plot) for **3** after refinement with resolution-dependent scaling and ‘overload’ correction.

Table 16: Model quality indicators for the MM refinement after the different corrections.

	R [%]	e_{gross} [e]	$d^f(0)$	highest peak [e·Å ⁻³]	deepest hole [e·Å ⁻³]
1 scale factor	2.47	33.2	2.68	0.31	-0.24
10 scale factors	2.26	32.4	2.68	0.28	-0.23
10 scale factors + ‘overload’ cor.	2.06	30.6	2.69	0.28	-0.22
‘best’ box + ‘overload’ cor.	2.46	25.7	2.65	0.22	-0.21
emp. correction + ‘overload’ cor.	1.81	25.3	2.68	0.23	-0.21

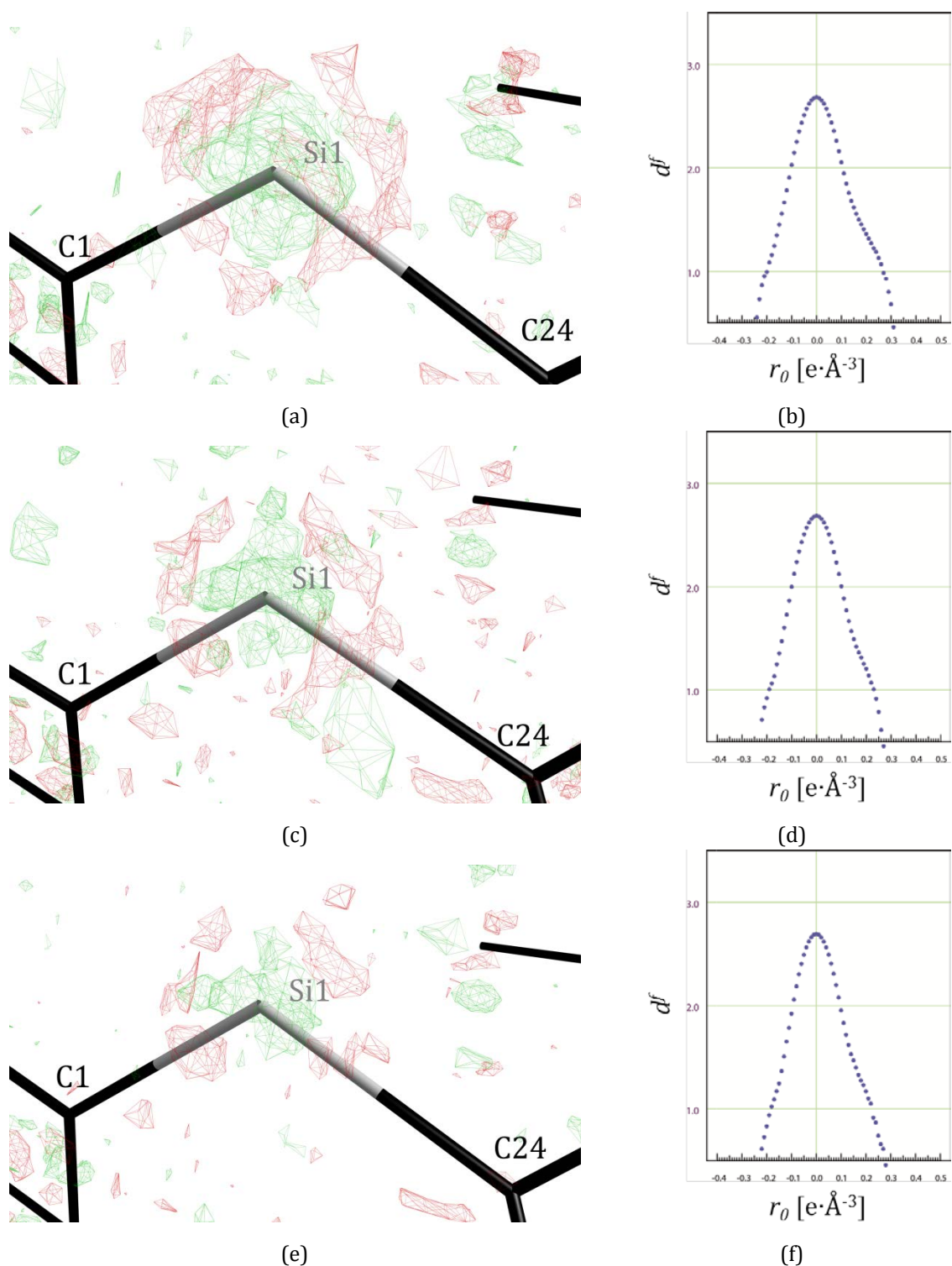
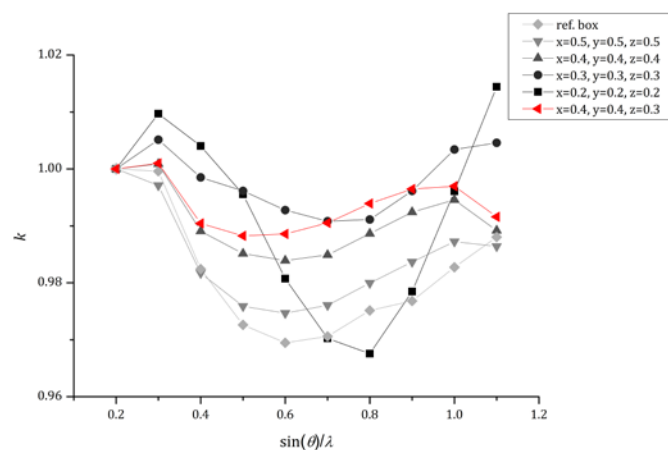
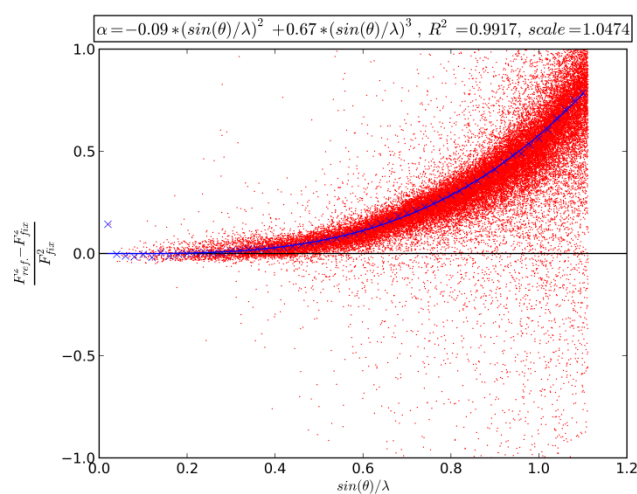


Figure 49: Residual density map around silicon atom and fractal dimension plots after MM refinement with one scale factor (a, b), with resolution-dependent scale factor against whole dataset (c, d) and with resolution-dependent scale factor against 'overload' corrected dataset (e, f). Atomic displacement parameters are depicted at 50 % probability level. Hydrogen atoms are omitted for clarity. Positive residual density is shown in green, negative in red. Isolevels are depicted at $\pm 0.1 e \text{\AA}^{-3}$.



(a)



(b)

Figure 50: (a) Resolution dependence of the scale factors for **3** with different integration box sizes. ‘Best’ box is highlighted in red. (b) α vs. $\sin(\theta) / \lambda$ plots for the ‘best’ integration box. The correction factor for each reflection is depicted as red dot, the mean value in 0.02 \AA^{-1} intervals as blue cross. The fitted curve is shown as blue line.

Despite the correction with resolution-dependent scaling, two additional methods to correct for errors introduced by TDS, the reduction of the integration box and an empirical determined correction factor, were presented in Section 4. These methods were also applied to the ‘overload’ corrected dataset of compound **3**.

By reducing the size of the integration box it is possible to obtain a nearly constant scale factor course (Figure 50a). The best box size was found to be $x = 0.4$, $y = 0.4$, $z = 0.3$ (see appendix). Yet, as already shown in Section 4 this correction can introduce new errors to the intensities, which is mirrored here in the poor improvement of the R value and in the decreased $d^*(0)$ (Table 16). However, the total residual density is improved significantly ($e_{\text{gross}} = 25.7 \text{ e}$). Similar to what was already found for compounds **1** and **2**, the problem of introducing new errors to the data by reducing the size of the integration box can be circumvented by using an empirically derived correction factor. The automatic routine (see Section

4.5) ended up with $a = -0.25$ and $b = 0.8$, which are in the same range as the parameters derived from the ‘best’ box (Figure 50b). The resulting model clearly is superior to those models derived from resolution-dependent scaling or reduced box size (Table 16). The DRK-plot reveals no deviation of the $\Sigma F_o^2 / \Sigma F_c^2$ quotient above $\pm 2\%$. The R value is reduced by 0.66 percentage points in comparison to the completely uncorrected model. The e_{gross} decreases by 7.9 e. A small change can also be found in the highest peak while the deepest hole reveals only marginal changes. An inspection of the residual density map (Figure 52) shows that the largest residual density is located close to one of the isopropyl groups (C44-C46), which is not refined anharmonic. Thus the influence of the remaining errors on the bonding properties of the Si-C bonding can be considered to be small.

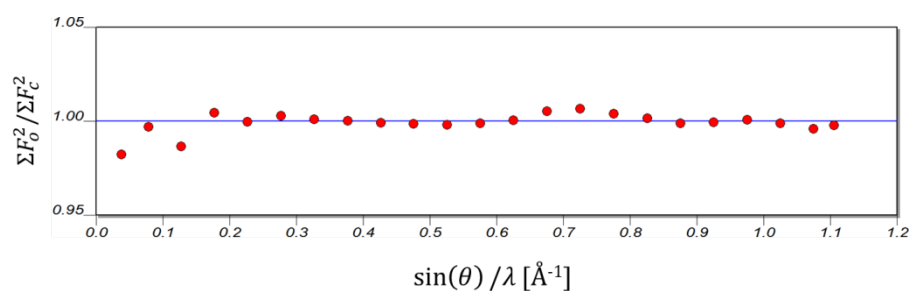


Figure 51: Plot of $\Sigma F_o^2 / \Sigma F_c^2$ vs. $\sin(\theta) / \lambda$ (DRK-plot) for **3** after refinement against empirical TDS and ‘overload’ corrected data using only one scale factor.

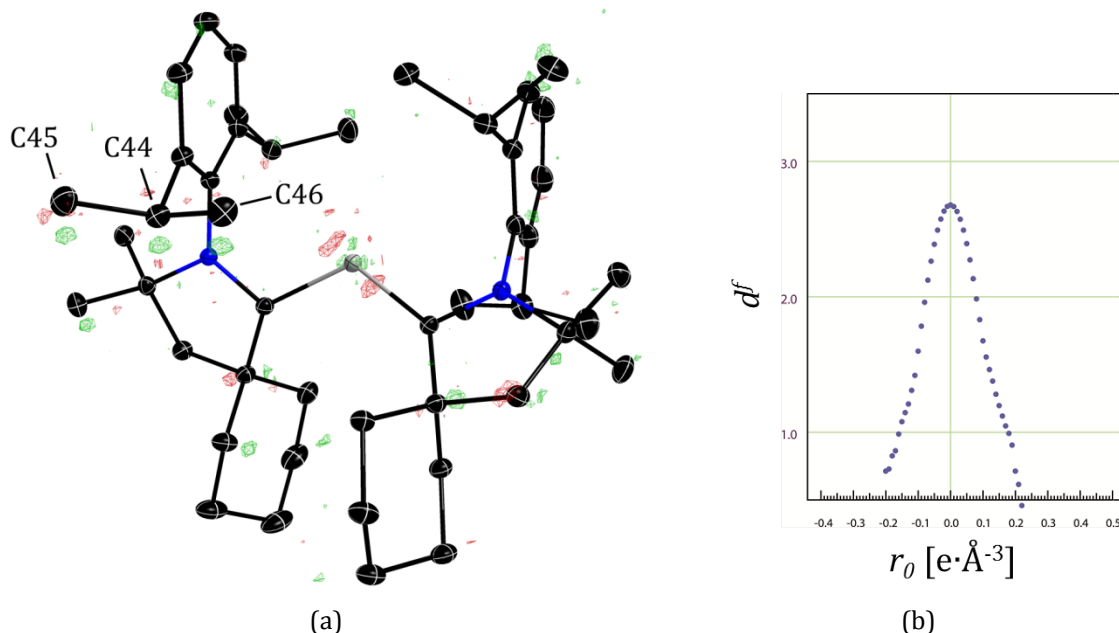


Figure 52: Residual density map (a) and fractal dimension plot (b) after MM refinement against empirical corrected data of **3**. Atomic displacement parameters are depicted at 50 % probability level. Hydrogen atoms are omitted for clarity. Positive residual density is shown in green, negative in red. Isolevel is depicted at $\pm 0.10 e \text{ \AA}^{-3}$.

Summing up it becomes clear that the best model is obtained after the refinement against the empirical TDS corrected dataset, which additionally is revised for outliers arising from the attenuator. Beyond doubt the model's quality benefits from the correction for the resolution dependent error. Of course, it cannot be proven that the resolution dependent error is solely caused by TDS, since only one dataset at 100 K is available. However, the similarities to the results found in Section 4 strongly suggest TDS to be the reason for the residual density around Si1. It has to be stressed that the correction for errors arising from the bad scaling of the attenuated frames is equally important in order to obtain a reasonable model of the ED. The error introduced by bad scaling of the attenuated frames directly affects the most intense reflections, which are usually low-order reflections. These are the most important reflections for the refinement of the ED distribution of the valence shell, which is thus biased. In this study nearly all reflections affected by this error fortunately were also measured without attenuation. Thus it was possible to reduce the scaling error arising from the attenuation. However, since all reflections on an attenuated frame suffer from this error a complete correction is hardly possible. Consequently, a charge density dataset should never be measured with the option 'retake if topped' enabled and highest attention should be focused on a complete collection of the low-order without overloading the detector.

5.5 Topological Analysis of the EDD

The aim of this study is to examine the experimentally derived EDD of **3** and by this settle the question of whether the bonding situation is better described as a silylone using donor-acceptor bonds or by bonding models waiving these bonding types. Therefore, firstly the ED of the Si-C bonds will be examined. Afterwards the topology of the ED around the heteroatoms in the carbene ligands will be analysed, since previous studies^[212] showed that the bonding geometry at the nitrogen atom in the cAAC to be indicative for the bonding mode of the carbene.

The examination will focus on the model, which is obtained from the refinement against the empirical TDS and 'overload' corrected data. For comparison the most important properties of EDD obtained from the refinement of the one scale factor model against the dataset without these corrections are added in the appendix, witnessing that the drawn conclusions are not artefacts of the correction applied to the dataset. For further comparison a QTAIM analysis of the EDD gained from quantum chemical calculations is added. The calculation with periodic boundary conditions using the X-ray structure was performed by *Paul*

Jerabeck from the working group of *Prof. Gernot Frenking* at the BP86/def2-TZVPP level of theory. The values are given in each case in squared brackets.

5.5.1 Topology of the Si-C bonds

The QTAIM analysis of the EDD reveals two distinct VSCCs of -2.78 and $-2.76 \text{ e}\text{\AA}^{-5}$ in the non-bonding region of the silicon atom at a distance of $\sim 0.90 \text{ \AA}$ from the nucleus (Figure 53 and Figure 54). Not involved in any chemical bonding they can be taken as indicators for the lone pairs, which one would expect for a silicon(0) atom. VSCCs in bonding direction cannot be observed in the basin of Si1. The charge within this basin is depleted in bonding direction.

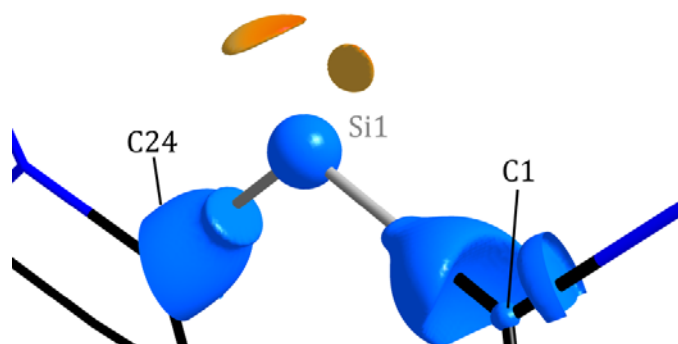


Figure 53: Laplacian distribution around the silicon atoms of **3** at an isolevel of $-2.5 \text{ e}\text{\AA}^{-5}$. Non-bonding VSCCs highlighted.

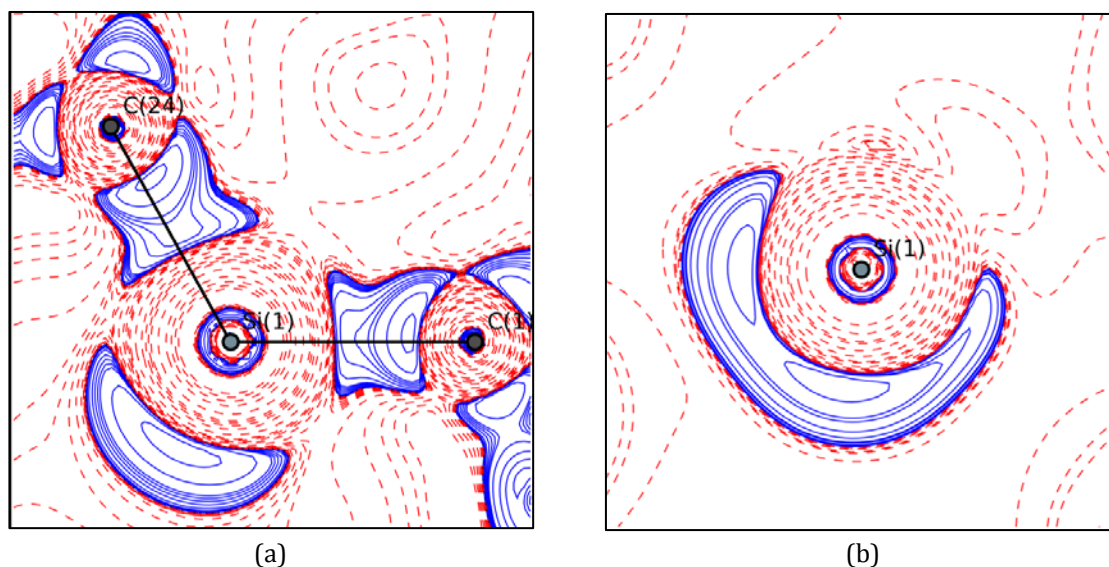


Figure 54: Laplacian distribution in the C1-Si1-C24 plane (a) and orthogonal to the C1-C24 vector (b). Charge concentration depicted in blue solid lines, depletion in red dashed lines. Contour levels drawn at $\pm 1 \cdot 10^n, \pm 2 \cdot 10^n, \pm 4 \cdot 10^n, \pm 8 \cdot 10^n$ ($-2 \leq n \leq 4$).

As already mentioned the vital point for the decision whether a silylone or a silaallene is formed is the spin multiplicity of the carbene ligands and the central silicon atom. For a

silylone the silicon atom and the carbene ligands both have to be in a singlet state. As shown by *Frenking et al.*^[221] the *Laplacian* distribution around the carbene carbon atoms can be used to gain information about the spin state in *Fischer*- and *Schrock*-type transition metal carbene complexes. According to the *Taylor & Hall* model^[222] the metal carbene bonds in *Fischer*-type complexes are formed by donor-acceptor interactions between the metal and a singlet carbene. In contrast, *Schrock*-type complexes are formed by normal covalent bonds between the open-shell metal fragment and a triplet carbene. Analysing the bonding modes in *Fischer*- and *Schrock*-type transition metal carbene complexes, *Frenking et al.*^[221] were able to demonstrate that the two carbene types reveal significant differences in their *Laplacian* distribution in the π -plane of the carbene ligand. While *Fischer*-type carbenes reveal holes in the electron concentration around the carbene carbon atom, the distribution of the *Laplacian* around *Schrock*-type carbenes exhibits a continuous area of charge concentration. Thus the *Laplacian* of *Fischer*-type carbenes is similar to those of a (1A_1) CH_2 and *Schrock*-type carbenes exhibit *Laplacian* distributions similar to (3B_1) CH_2 (Figure 55).

[221]

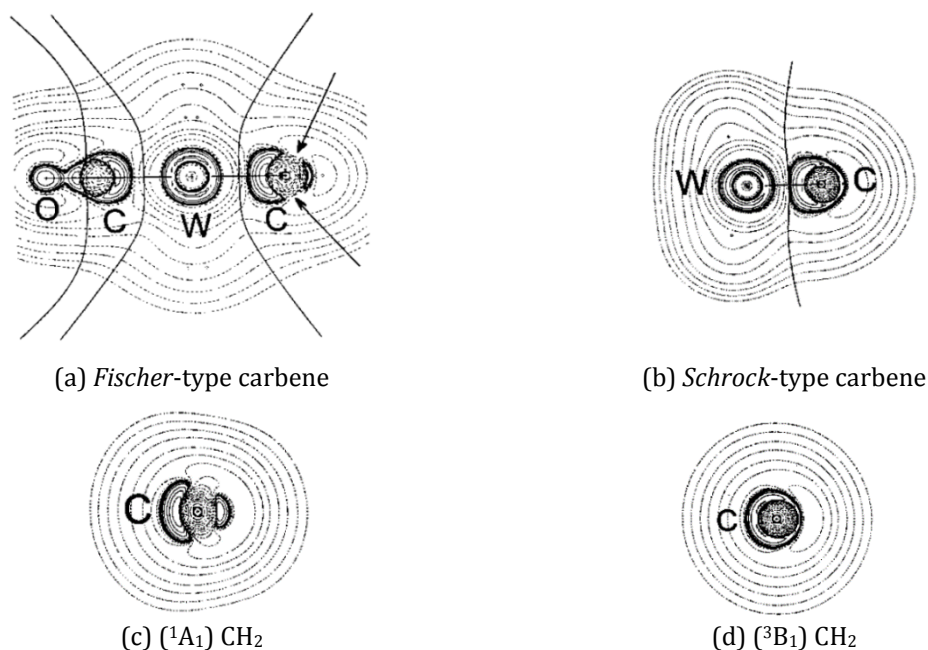


Figure 55: Laplacian distribution the π -plane for (a) *Fischer*-type carbenes, (b) *Schrock*-type carbenes, (c) free (1A_1) CH_2 molecule and (d) free (3B_1) CH_2 molecule. Charge concentration depicted in solid lines, depletion in dashed lines. The arrows in (a) show the hole in charge concentration surrounding the carbene atom. Adapted with permission from *Frenking et al.*^[221]

The *Laplacian* distributions in the π -planes perpendicular to the C1–C2–N1–Si1 mean plane and C24–C25–N2–Si1 mean plane, respectively, are given in Figure 56. Both distributions exhibit large areas of charge depletion, which renders them to be much more alike the *Fischer*-type than the *Schrock*-type carbenes. This can be taken as evidence for the singlet

state of the carbene ligand, which is needed for a donor-acceptor bond. Thus the *Laplacian* distribution clearly supports the interpretation of **3** as a silylone.

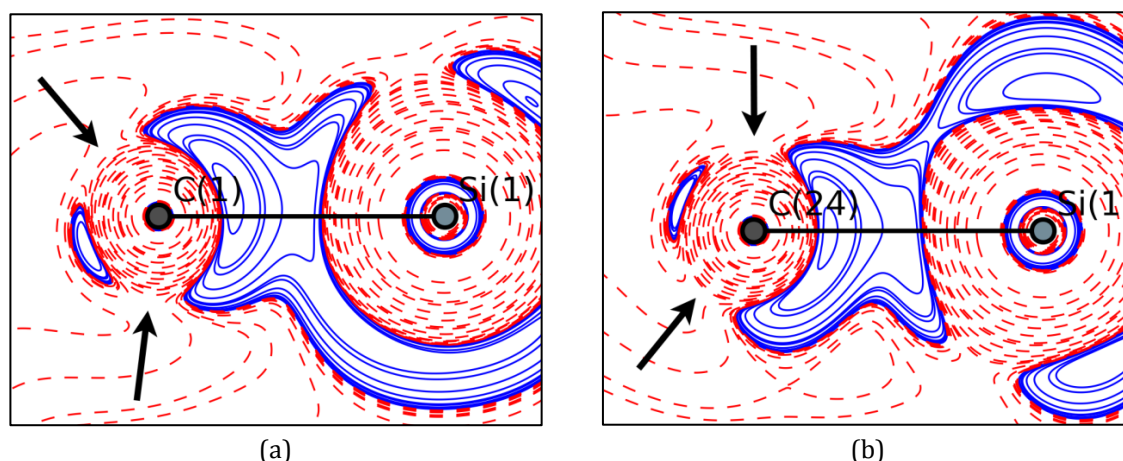


Figure 56: *Laplacian* distribution in **3** in the plane perpendicular to the C1–C2–N1–Si1 mean plane (a) and C24–C25–N2–Si1 mean plane (b), respectively. Charge concentration depicted in blue solid lines, depletion in red dashed lines. Contour levels drawn at $\pm 1 \cdot 10^n$, $\pm 2 \cdot 10^n$, $\pm 4 \cdot 10^n$, $\pm 8 \cdot 10^n$ ($-2 \leq n \leq 4$). The arrows show the hole in charge concentration surrounding the carbene atom.

The integration of the atomic basins results in *Bader* charges (Si1 = 1.24 e [1.27 e], C1 = -0.42 e [-0.51 e] and C24 = -0.31 e [-0.26 e]), which are in good accordance with the results of the NBO analysis that suggests charges of 1.2 e for the silicon and -0.6 e for each carbene carbon atom, respectively. Thus the experimentally determined charges support the localisation of one of the lone pairs at the silicon atom and the delocalization of the second lone pair over a three-centre π -bond with probability distributions of 40% at the silicon atom and 30% at each carbene carbon atom.

Yet, the small difference in the experimentally determined *Bader* charges of the carbene carbon atom, which is even more prominent in the theoretical charges, indicates a slightly enlarged π -backdonation from Si1 to C1 than from Si1 to C24. A different π -backdonation is also supported by the different bond length of the Si–C_{carbene} bonds. The length of the Si1–C1 bond (1.8455(2) Å) is significantly shorter than the length of the Si1–C24 bond (1.8613(2) Å). The latter is in good accordance with the bond length calculated for silylones with NHC ligands (1.869 Å)^[190,192], which are worse π -acceptor than cAACs. Additionally, the deviation of Si1 from the carbene plane is larger for C24 than for C1, which might lead to a hindrance of the π -donation from Si1 to C24. A difference in the bond lengths was also reported for a similar germylone.^[200] Herein the germanium atom shows different distances to the carbene planes, as well. However, compounds with dimethyl groups instead of the cyclohexyl group do not show significant differences in the two Si/Ge–C bonds (Table 17).^[200,223]

Table 17: Si–C bond length and deviation of the Si/Ge atom from the carbene planes in silylones and germylones.

	(cAAC ^{Me})Si ^[16]	(cAAC ^{Cy}) ₂ Si ^[212]	(cAAC ^{Cy}) ₂ Si ·n-hexane	(cAAC ^{Me})Ge ^[200]	(cAAC ^{Cy}) ₂ Ge ^[200]
Si/Ge–C _{carbene} No. 1 [Å]	1.844(3)	1.840(1)	1.8454(2)	1.941(2)	1.939(2)
Si/Ge–C _{carbene} No. 2 [Å]	1.845(3)	1.853(1)	1.8615(2)	1.943(3)	1.954(2)
d _{Si/Ge} -plane No. 1 [Å]	0.423	0.371	0.366	0.469	0.438
d _{Si/Ge} -plane No. 2 [Å]	0.418	0.498	0.476	0.476	0.558

In order to investigate this difference in more detail, the properties of the EDD at the BCP and along the bond path are investigated (Table 18). The *Laplacian* along the bond paths feature similar shapes for both bonds (Figure 57). The charge is concentrated in the carbon basin and depleted over the whole silicon basin indicating the high polarity of the Si–C_{carbene} bonds. At the BCPs the *Laplacian* (Si1–C1: 5.13(3) e Å⁻⁵ and Si1–C24: 3.22(3) e Å⁻⁵) exhibit distinct positive values. They reach their minimum at about -30 e Å⁻⁵ close to the carbene carbon atoms at about 0.6 Å. The theoretical determined *Laplacian* distribution along the bond path features a very similar shape, with even slightly larger values at the BCP.

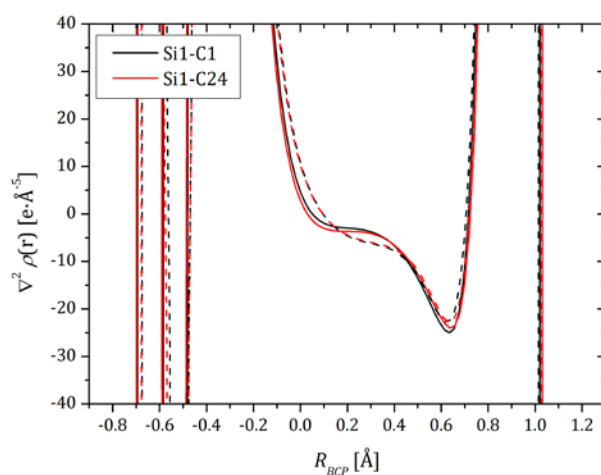
**Figure 57:** Laplacian along the Si1–C1 (black) and Si1–C24 (red) bond. Values of the experimental analysis are shown as solid lines; values of the theoretical analysis are shown as dashed lines.

Table 18: Properties of the ED at the Si–C BCPs of **3** and in RSiCl₂Me-cAACH^[224]. The total electronic energy density and the relative kinetic energy were calculated from the ED and the Laplacian according to Abramov^[98].

Bond	d_{BP} [Å]	$d1_{BP}$ [Å]	$d2_{BP}$ [Å]	ρ_{BCP} [e Å ⁻³]	$\nabla^2\rho_{BCP}$ [e Å ⁻⁵]	H_{BCP} [a.u.]	G_{BCP}/ρ_{BCP}	ϵ	η
Si1–C1	1.8464 [1.8482]	0.7315 [0.7308]	1.1149 [1.1147]	0.781(7) [0.742]	5.13(3) [10.838]	-0.061 [-0.035]	0.99 [1.34]	0.51 [0.29]	0.35 [0.21]
Si1–C24	1.8630 [1.8644]	0.7365 [0.7354]	1.1265 [1.1262]	0.793(7) [0.762]	3.22(3) [10.301]	-0.070 [-0.040]	0.88 [1.30]	0.11 [0.21]	0.37 [0.21]
Si–C ^[224]	-	-	-	0.823	1.57	-0.081	0.80	0.07	-

In both Si–C_{carbene} bonds η is less than unity. The negative total electronic energy densities are only slightly negative (Si1–C1: -0.061 a.u. and Si1–C24: -0.070 a.u.). Typical values of H_{BCP} for covalent single bonds cluster around -0.35^[96] and are thus much smaller. Additionally the relative kinetic energy (G_{BCP}/ρ_{BCP}) is close to unity (Si1–C1: -0.99. and Si1–C24: -0.88.), a value which is in good accordance with those found for dative bonds.^[91] Nevertheless, since the approximation by Abramov only gives a semi-quantitative description of the energy density^[98], it is quite easy to overestimate the accuracy of the values. Yet in combination with the very low ED at the BCP (Si1–C1: 0.781(7) e Å⁻³ and Si1–C24: 0.793(7) e Å⁻³) a low covalent character of the Si–C_{carbene} bonds can be stated, but a difference between the two Si–C_{carbene} bonds cannot be identified.

It is worth to compare the properties at the BCPs with those that were recently reported for theoretical QTAIM investigation of the EDD of RSiCl₂Me-cAACH (R= 2,6-*i*Pr₂C₆H₃-(SiMe₃)N), in which the Si–C single bond was shown to have predominantly open-shell character.^[224] The total ED in RSiCl₂Me-cAACH is slightly higher and the *Laplacian* indicates smaller charge depletion at the BCP (Table 18). However, the difference is barely significant. Nonetheless it becomes clear that the Si–C bonds in **3** do not show a higher ED than a Si–C single bond. In contrast the ED for a C=C double bond (2.4476 e Å⁻³) is considerably larger than for a C–C single bond (1.7026 e Å⁻³).^[83]

As already stated above, the difference found in the bond length of the Si–C, which might be ascribed to different amounts of π -backdonation, is neither mirrored in the ED nor in the *Laplacian* at the BCP. However, as indicated by Farrugia *et al.*^[225] the influence of π -density on the properties can be relatively small arising from the close proximity of the BCP to the nodal plane of the π -orbital.

A closer inspection of the π -contribution in the Si–C_{carbene} bonds is possible in terms of the ellipticity ϵ , which is a measure for the deviation of the bonding electrons from cylindrical

shape. By inspection of the ellipticities at the BCP (Si1–C1: $\epsilon = 0.51$ and Si1–C24: $\epsilon = 0.11$) it becomes clear that the two Si–C bonds in **3** exhibit a completely different behaviour.

However, an interpretation only based on the ellipticity at the BCP may be misleading in some cases.^[102] Therefore, a much more reliable statement about the bonding situation can be given by an examination of the ellipticity along the entire bond path. If π -delocalisation is present in a bond not only the ellipticity should significantly deviate from zero along the bond path but also the angle between the major axis of the ellipticity λ_2 and the potential π -plane should be zero.^[225-226]

Scherer *et al.*^[227] investigated the course of the ellipticities along the Si–C $_{\alpha}$ bond in the alkyllithium complex $[\{2-(\text{Me}_3\text{Si})_2\text{CLiC}_5\text{H}_4\text{N}\}_2]$. They compared it with the path of several theoretically calculated reference paths. These were the Si–C single bond in methylsilane ($\text{H}_3\text{C}-\text{SiH}_3$), in the related carbanion ($\text{H}_2\text{C}-\text{SiH}_3^-$) and the Si=C double bond in methylenesilane ($\text{H}_2\text{C}=\text{SiH}_2$). The ellipticities are given in Figure 58. The single bond exhibits a constant ellipticity of zero along the whole bond path. For the deprotonated $\text{H}_2\text{C}-\text{SiH}_3^-$ the global maximum is located in the carbon basin. A second much smaller maximum can be found near the BCP. For the Si=C double bond only one maximum in close proximity to the BCP can be observed. According to Scherer *et al.*^[227], a shoulder in the course of ϵ close to the BCP, as it can be found for the Si–C $_{\alpha}$ bond, can be related to a pronounced degree of π -contribution in the bonding.

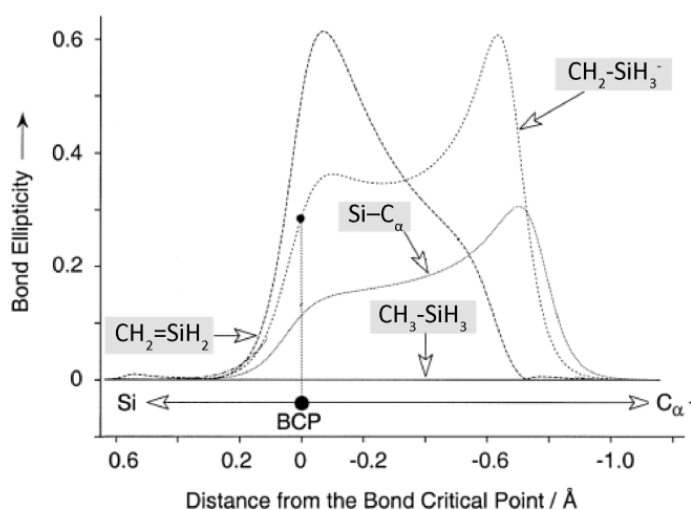


Figure 58: Bond ellipticity profiles along the C–Si bond path of $[\{2-(\text{Me}_3\text{Si})_2\text{CLiC}_5\text{H}_4\text{N}\}_2]$ (Si–C $_{\alpha}$), $\text{H}_3\text{C}-\text{SiH}_3$, $\text{H}_2\text{C}-\text{SiH}_3^-$ and $\text{H}_2\text{C}=\text{SiH}_2$. Adapted with permission from Scherer *et al.*^[227]

The inspection of the ellipticity along the bond path of the Si–C bonds in **3** reveals significant deviation from cylindrical shape with the major axis in the direction of the π -plane from -0.6 – 0.8 Å for both bonds (Figure 59a). Additionally a shoulder close to the BCP can be found for both Si–C bonds. However, while the ellipticity along the bond path of Si1–C1 has got its maximum at this point it is just a saddle point along the Si1–C24 bond path, indicating

much less π -backdonation from Si1 to C24. The ellipticity in the carbon basin for both bonds remains considerably high. The course of ϵ reveals a saddle point at about 0.6 Å for Si1–C1 and its global maximum for Si1–C24. The still considerably high value of $\epsilon \sim 0.2$ for both bonds can be ascribed to the bond directed VSCC of the carbene carbon atoms.

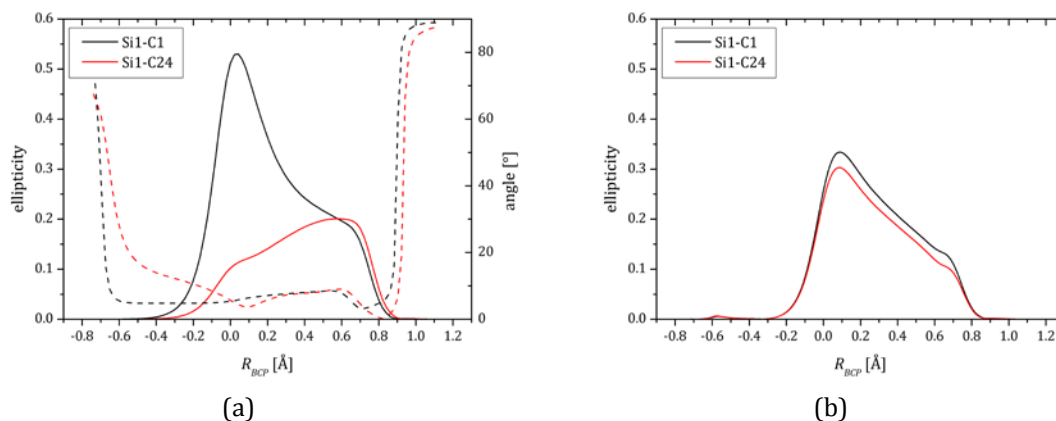


Figure 59: Ellipticity (solid line) and angle of the major axis (dashed line) along the bond path of Si–C bonds in **3** from (a) experimental and (b) theoretical determined EDD.

Thus the ellipticities along the bond path as well as the different Bader charges support the hypothesis that the significant difference in the bond length arises from a much lower π -backdonation in the Si1–C24 bond in relation to the Si1–C1 bond. However, differences in the other properties along the bond path are not visible. Yet, an inspection of the *Laplacian* between the bonds, not only along the bond path, reveals differences (Figure 60). The plot of the *Laplacian* at an isosurface level of $1.0 \text{ e} \cdot \text{Å}^{-5}$ exhibits a charge concentration connecting the lone pairs at the Si1 with C1. Inspection of the *Laplacian* at further levels shows that the ‘connection’ between Si1 and C1 starts at $\sim 1.2 \text{ e} \cdot \text{Å}^{-5}$ and between Si1 and C24 at $\sim 0.4 \text{ e} \cdot \text{Å}^{-5}$ (see appendix).

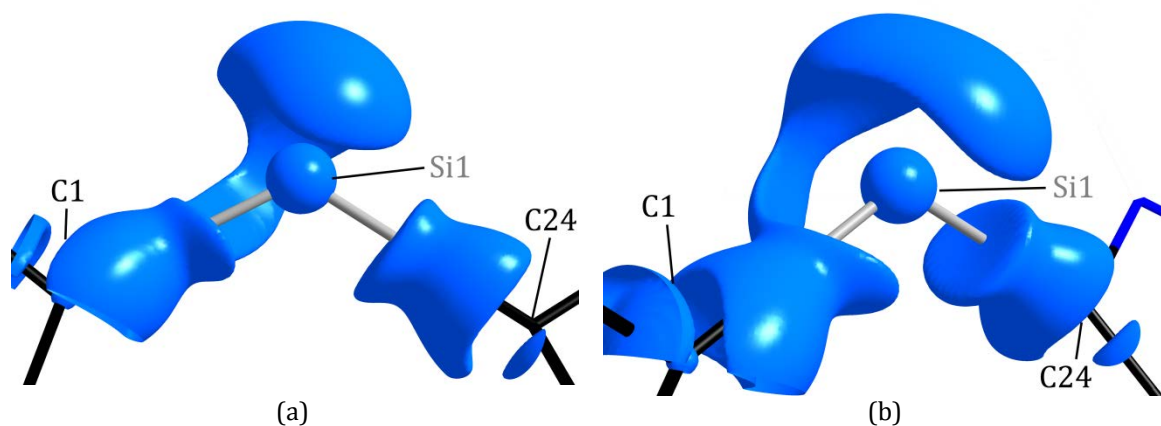


Figure 60: Laplacian distribution at Si1 from different directions at an isosurface level of $-1 \text{ e} \cdot \text{Å}^{-5}$.

It is worth mentioning that the difference between the two Si–C_{carbene} bonds is much smaller for the ellipticity obtained from quantum chemical calculations (Figure 59b). Both courses

of ϵ show the shoulder close to the BCP. The absolute values ($\epsilon_{BCP}(\text{Si1-C1}) = 0.29$, $\epsilon_{BCP}(\text{Si1-C24}) = 0.21$) are in-between those obtained for the Si1-C1 and the Si1-C24 bond from the experimental ED. Nevertheless, a slightly smaller ellipticity can again be found for the elongated Si1-C24 bond. Yet, this difference cannot be observed, if the wave function is calculated without periodic boundary conditions ($\epsilon_{BCP}(\text{Si1-C1}) = 0.29$, $\epsilon_{BCP}(\text{Si1-C24}) = 0.28$).^[32] This indicates that the differences are caused by weak intermolecular interactions, which only can be modelled with periodic solid state calculations.^[228] However, modelling the crystal packing for such a big molecule as the present silylone is ambitious and almost inevitably leads to differences between the values obtained from experimental data.

5.5.2 Topology around the Nitrogen Atoms

The comparison of the geometry of the nitrogen atoms in cAACs even in IAM structures can give interesting insights into the bonding situation.^[212] The relatively small singlet-triplet exaltation energy of cAACs enables them to react either as triplet or as singlet carbenes.^[195] For electron sharing bonds, such as in $(\text{cAAC})_2\text{SiCl}_2$, a deviation from the planar geometry at the nitrogen atom can be observed. However, molecules with a cAAC-X donor-acceptor bond (X = Si, BH) as well as the free cAAC do not show any deviation from a planar nitrogen environment. Moreover, the C-N bond in cAAC forming electron sharing bonds is much more elongated in relation to the free cAAC than for donor-acceptor bonds. Recently *Andrada et al.*^[229] reported on the geometry optimised structure $\text{cAAC}=\text{C}=\text{Si}\leftarrow\text{cAAC}$, in which both bonding types are present at the same silicon atom. The different bonding geometries at the nitrogen atoms in these compounds support their indicative role for the bonding situation. The nitrogen of the covalent bonded cAAC reveals a non-planar bonding geometry while the other exhibits a perfect planar environment (Table 19).

Table 19: Bonding geometry around the nitrogen atoms in different cAAC compounds.

	cAAC ^[197]	$(\text{cAAC})_2\text{Si}$	$(\text{cAAC})_2\text{BH}$ ^[199]	$(\text{cAAC})_2\text{SiCl}_2$ ^[195]	$\text{cAAC}=\text{C}=\text{Si}\leftarrow\text{cAAC}$ ^[229]
N-C No. 1 [Å]	1.312(2)	1.3842(3)	1.377(1)	1.395(2)	1.403
N-C No. 2 [Å]	-	1.3718(3)	1.390(1)	1.400(2)	1.330
$\Sigma\angle\text{N}$ No. 1 [°]	360.0	359.9	359.1	355.3	351.7
$\Sigma\angle\text{N}$ No. 2 [°]	-	360.0	359.1	355.5	359.9

The different bonding geometry can be rationalised as follows. To provide a donor-acceptor bond the carbene carbon atom needs to be in the singlet state. The vacant p orbital at the carbene carbon atom enables the lone pair of the nitrogen to donate ED and the C-N bond shows more π -character. However, a delocalisation of the nitrogen lone pair into the vacant p-orbital is hampered, if the carbene is in the triplet state. Thus the lone pair orbital of the nitrogen atom acquires less s-character and the geometry tends to be more pyramidal. This is expected to be mirrored in the EDD as well.

The ED and the *Laplacian* at the BCP in the bonds between the nitrogen atoms (N1, N2) and the carbene carbon atoms (C1, C24) are higher in absolute value than at the other BCPs (Table 20), which indicates a donation of ED from the heteroatoms in the N-C_{carben} bonds. The BCP itself is more shifted towards the carbene carbon atom in relation to the other carbon atoms.

Table 20: Properties of the ED at the N-C BCPs of **3**.

Bond	d_{BP} [Å]	d_{1BP} [Å]	d_{2BP} [Å]	ρ_{BCP} [$e \cdot \text{Å}^{-3}$]	$\nabla^2 \rho_{BCP}$ [$e \cdot \text{Å}^{-5}$]	ϵ	η
N1-C1	1.3842	0.7822	0.6021	2.093(15)	-16.74(7)	0.16	1.15
N1-C4	1.4896	0.8415	0.6480	1.680(14)	-11.37(6)	0.03	0.94
N1-C5	1.4370	0.8102	0.6268	1.887(17)	-12.90(8)	0.03	0.93
N2-C24	1.3720	0.8006	0.5714	2.107(16)	-18.20(8)	0.13	1.27
N2-C27	1.4960	0.8629	0.6331	1.649(14)	-12.46(6)	0.06	1.03
N2-C28	1.4397	0.7970	0.6427	1.907(16)	-13.55(7)	0.05	0.95

The ED at the BCP in the N-C_{carbene} bonds (2.093(15) and 2.107(16) $e \cdot \text{Å}^{-3}$) is comparable to that found in the 1,3-dimethylimidazolium cation (2.12 $e \cdot \text{Å}^{-3}$)^[226], in which the nitrogen lone pair is delocalised over the hole five-membered ring. Both EDs are substantially higher than the ED at the BCP in normal N-C single bonds. For example, the averaged ED at the BCP of the N-C bonds in the α -lithiated benzylsilane quinuclidine adduct was found to be 1.85 $e \cdot \text{Å}^{-3}$.^[230] The values of the density at the BCP of all other N-C bonds in **3** are similar or even below this value. Recently *Roesky et al.*^[224] reported on the theoretical QTAIM analysis of the bonding in RSiCl₂Me-cAACH (R= 2,6-*i*Pr₂C₆H₃-(SiMe₃)N). In this compound with a protonated carbene carbon atom the bonding geometry of the nitrogen is found to be pyramidal (sum of angles 351.1°) and the ED (1.707 $e \cdot \text{Å}^{-3}$) is much lower than for the N-C_{carbene} bonds in **3**.

A closer inspection of the lone pair donation of the nitrogen atoms is possible by using the ellipticity of the bond ϵ . As shown by *Farrugia et al.*^[225] as well as *Strohmann et al.*^[230-231] the ellipticity of a bond can be used to investigate the delocalisation and polarisation of electrons in a system. By inspection of the ellipticities at the BCP it becomes clear that only the N-C_{carbene} in **3** bonds show significant deviation from zero. However, as already stated before the interpretation of the π -contribution only based on the ellipticity at the BCP may be misleading in some cases.^[102] Therefore, again the ellipticity along the entire bond path as well as the angle between the major axis of the ellipticity λ_2 and the potential π -plane is examined.

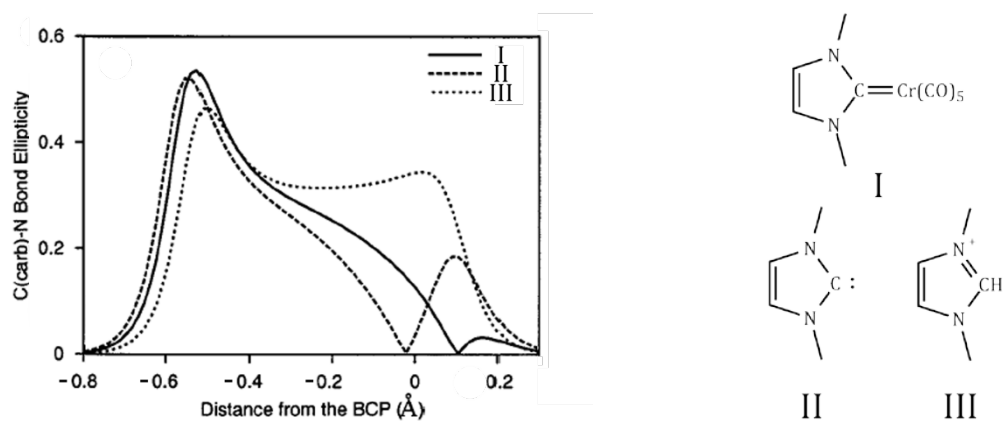


Figure 61: Ellipticity along the bond path of N–C bonds in $\text{NHC}^{\text{Me}}\text{Cr}(\text{CO})_5$, NHC^{Me} and $(\text{NHC}^{\text{Me}})\text{H}^+$. Adapted with permission from Scherer *et al.*^[226]

Scherer *et al.*^[226] investigated the delocalisation of π -density in the free 1,3-dimethylimidazol-2-ylidene carbene, the corresponding chromium pentacarbonyl complex and the 1,3-dimethylimidazolium cation. The theoretically calculated ellipticities of the N–C_{carbene} bonds along the bond path are given in Figure 61. Only the imidazolium cation (dotted line in Figure 61) exhibits complete delocalisation of the π -electrons in the ring system, indicated by high ellipticity along the whole bond path. The delocalisation in the free carbene NHC^{Me} (dashed line in Figure 61) as well as in the carbene complex $\text{NHC}^{\text{Me}}\text{Cr}(\text{CO})_5$ (solid line in Figure 61) is significantly hindered. However, the latter shows a larger area of perpendicular non-zero ellipticity, which was taken as a sign for an enhanced delocalisation.

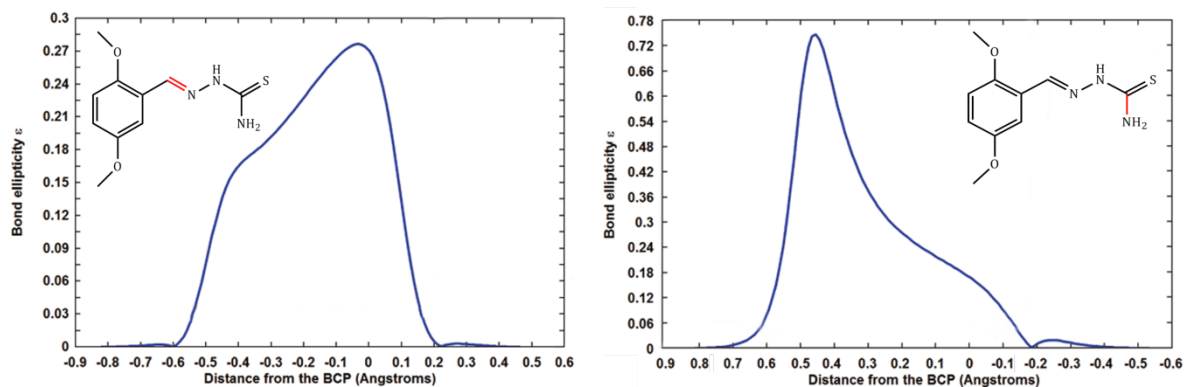


Figure 62: Ellipticity along the bond path of N–C bonds in 2,5-Dimethoxybenzaldehyde-thiosemicarbazone. The corresponding bond is highlighted in red in the Lewis structure. Adapted with permission from Farrugia *et al.*^[225].

A further study of π -delocalisation in N–C bonds was made by Farrugia *et al.*^[225], who investigated the π -delocalisation in the side-chain of 2,5-Dimethoxybenzaldehyde-thiosemicarbazone by a combined experimental and theoretical charge density study. The theoretically calculated ellipticities of two N–C bonds along the bond paths are given in Figure 62. The first shows the ellipticity along the bond path of an N=C double bond. The

high values of ϵ along the whole bond path again indicate accumulation of the π -density in the bond. The second graph shows the ellipticity along the bond path of a $N_{sp^2}-C_{sp^2}$ single bond, in which the lone pair of the nitrogen delocalises into the side-chain. A maximum between 0.3-0.6 Å can be observed, which is attributed to VSCC of the nitrogen and not arising from the π -character of the bond. *Farrugia et al.*^[225] thus stated that it is difficult to ascribe any π -contribution to the N-C bond, although the profile is not inconsistent with a π -contribution. However, further studies using the delocalisation index revealed the substantial π -contribution to the bonding.

The course of the ellipticities along the bond path in **3** can give useful information about the degree of delocalization of π -electrons into the N-C bond, especially because bonds with (N1-C1/N2-C24) and without (N1-C4/N2-C27) potential π -contribution can be investigated at the same time. The experimentally determined ellipticities of the N-C bonds as well as the angle between the major axis and the unit vector on the $C_{\text{carbene}}-N-C_{\text{phenyl}}$ plane along the bond path are given in Figure 63. The bond path between the nitrogen and the phenyl carbon atom (N1-C5/N2-C28) can be found in the appendix and will not be discussed here. The course of ϵ along the bond paths of the two N- C_{carbene} bonds (blue in Figure 63) by no means assumes the shape of the N=C double bond by *Farrugia et al.*^[225] or of the completely delocalised N-C in the imidazolium cation by *Scherer et al.*^[226] The paths resemble those of the partially delocalised N-C bond in the chromium pentacarbonyl carbene complex and in 2,5-Dimethoxybenzaldehyde-thiosemicarbazone, respectively. The ellipticities of both N- C_{carbene} bonds show relatively high maxima of $\epsilon \sim -0.5$ at -0.4 Å. The N-C bonds without π -delocalisation (red in Figure 63) exhibit a lower maximum ($\epsilon \sim -0.3$ - -0.4) that is additionally slightly more shifted towards the nitrogen atom (~ -0.45 - -0.5 Å).

The comparison of the angle between the major axis and the potential π -plane of the N1-C1/N2-C24 and N1-C4/N2-C27 shows further differences between the bonds. The areas, in which the angle between the major axis and the potential π -plane is close to zero, are much larger for the N1-C1/N2-C24 bond than for the N1-C4/N2-C27 bonds. Additionally, the angles at BCPs are nearly zero for the N1-C1/N2-C24 bond, while N1-C4 and N2-C27 both show a large deviation from zero at the BCP. These results are consistent with the findings by *Scherer et al.*^[226], who found an enlarged area, in which the major axis is perpendicular to the ring plane, if the π -delocalisation is enlarged.

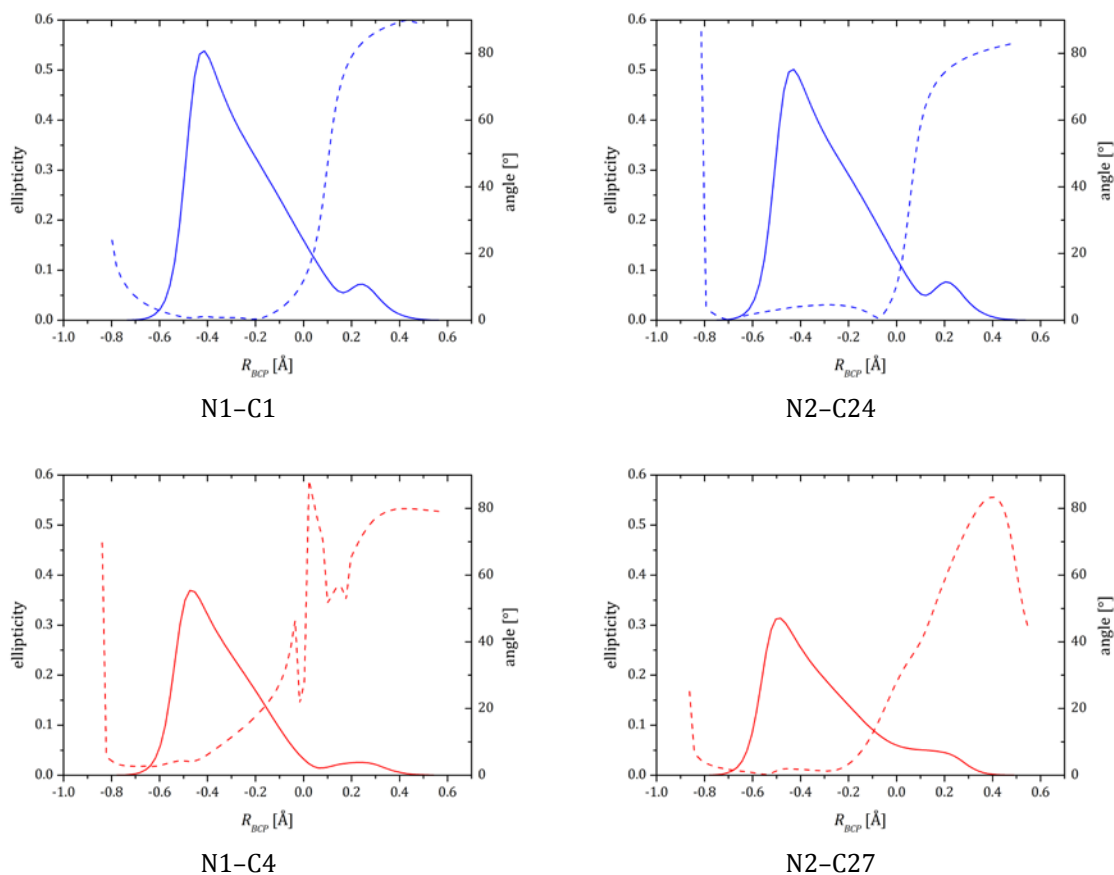


Figure 63: Ellipticity (solid line) and angle of the major axis (dashed line) along the bond path of N–C bonds in **3**. The strange behaviour of the angle of the major axis for N1–C4 bond between 0.0 and 0.2 Å arises from the small ellipticity. As the values for λ_1 and λ_2 in this area are nearly identical the angle of the principle axis can change drastically by small in λ_1 and λ_2 , respectively.

Additionally, to the ellipticity Scherer *et al.*^[226] proposed the absence of local charge concentrations above and/or below the nitrogen atom as an indicator of π -delocalisation. The *Laplacian* distributions around both nitrogen atoms in **3** are shown in Figure 64. A concentration of the ED above and below the nitrogen atoms can be found. However, in contrast to the results by Scherer *et al.* only three VSCCs are found pointing towards the three neighbouring carbon atoms. The VSCC pointing towards the carbene carbon atoms C1 and C24 reveals a slightly broader spreading of the *Laplacian* in the π -plane. A VSCC in the non-bonding area could neither be found at N1 nor at N2. This can be understood as a sign for a significant delocalisation of the nitrogen lone pair into the N–C_{carbene} bonds.

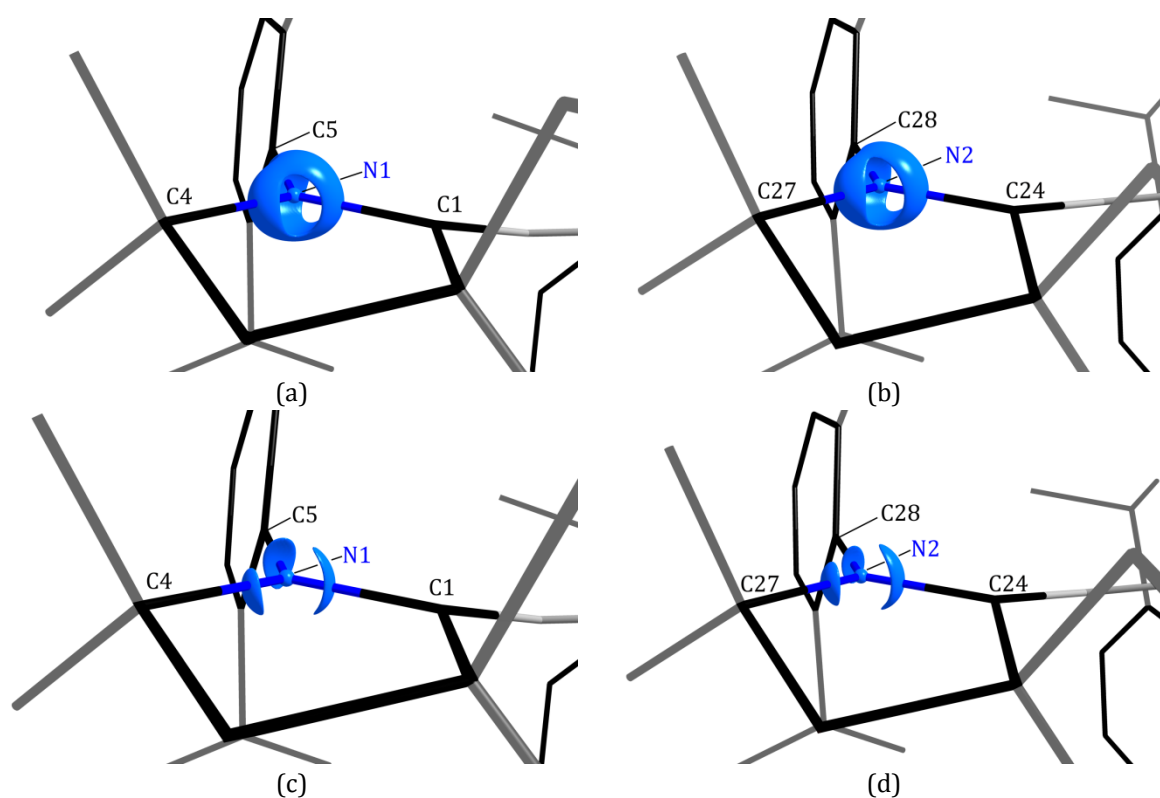


Figure 64: Laplacian distribution at N1 (a, c) and N2 (b, d) atoms of **3** at an isosurface level of $-30 e\cdot\text{\AA}^{-5}$ (a, b) and $-45 e\text{\AA}^{-5}$ (c, d).

All in all, the topology of the EDD around the nitrogen atoms of the two carbenes supports the suggestions drawn from the pure bonding geometry of the heteroatoms. The planar geometry of the bonding around the heteroatoms is mirrored in the missing VSCC in the non-bonding area. The lone pair density of the nitrogen atoms tends to donate ED into the N-C_{carbene} bonds, which reveal a significantly larger total and more concentrated ED at the BCP than the other N-C bonds. A comparison of the ellipticities and their major axes along the bond path allows the separation of two different bonding types; the N-C bonds with π -contribution from the lone pair donation (N1-C1 and N2-C24) and those without (N1-C4 and N2-C27). This donation is only possible, if the carbenes show predominately a singlet multiplicity. Thus the topological parameters of the EDD around the nitrogen heteroatoms can be used to prove the bonding situation of **3** to be the one of a silylone and not the one of a bent silaallene, since this would need a triplet state of the carbenes.

5.5.3 Intramolecular Interactions

The geometry of the 2,6-diisopropylphenyl (Dipp) groups of the carbenes in **3** suggests an interaction of the isopropyl groups with the lone pairs of the central silicon atom. The isopropyl groups are not in plane with the phenyl ring but are bent by 5.7–6.9° pointing towards the silicon atom.

In order to investigate the intramolecular non-covalent interactions between the central silicon atom and the hydrogen atoms of the isopropyl groups in **3** the reduced density gradient (RDG) can be a useful tool. The RDG depicts the deviation of the ED from a homogenous electron gas and thus usually assumes large values at points with low ED e.g. far away from atoms. However, in regions of non-covalent interaction, in which the ED is also very low, the RDG assumes low values.^[104-106] The RDG around Si1 was calculated using the program *NCImilano*^[104]. A plot of the RDG against the ED is shown in Figure 65a. Three regions with a low RDG can be identified. An assignment of the different interactions is possible by mapping the ED on an isosurface at a low level (see Figure 65b). The first area showing a low RDG and relatively high ED (≤ 0.225 a.u. / $1.5 \text{ e}\cdot\text{\AA}^{-3}$) refers to the covalent interactions depicted in blue. The donor-acceptor bonds between the carbene carbon atoms and the central silicon atom ($0.1 \text{ a.u.} < \rho < 0.125 \text{ a.u.}$ (green)) are clearly separated from these interactions. The remaining interactions showing an ED lower than 0.05 a.u. ($\sim 0.34 \text{ e}\cdot\text{\AA}^{-3}$) are not represented in the molecular graph. They indicate non-covalent interactions between the lone pairs of the silicon atom and the four hydrogen atoms (H20B, H23A, H43B, H46A).

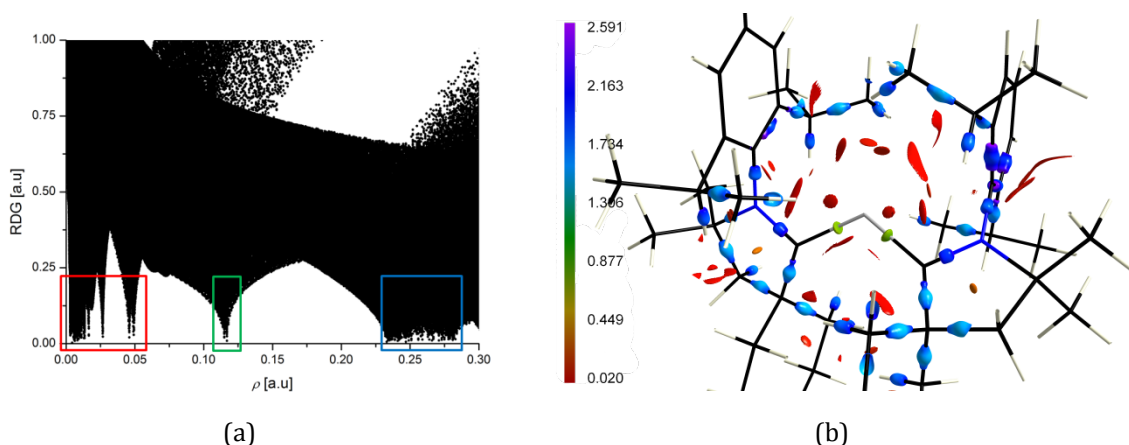


Figure 65: Plots of the RDG versus the ED in **3** (a). Isosurface of the RDG $s = 0.05$ (b). The surface is coloured according to $\rho(r)$.

In order to distinguish between attractive and repulsive interaction it is common to map the $\text{sign}(\lambda_2) \cdot \rho$ onto a surface of the RDG at a reasonable level. For attractive interactions the second eigenvalue of the *Hessian* matrix λ_2 is negative; for repulsive interactions the opposite is true. In Figure 66 the RDG on an isolevel of 0.3 a.u. is depicted. For the sake of

clarity only points are shown where $\rho(r) \leq 0.05$ a.u. The surface is coloured according to $\text{sign}(\lambda_2) \cdot \rho$; green colour indicates attractive interactions, red repulsive. Additionally, the VSCCs at the silicon atom are indicated by the *Laplacian* at an isolevel of $2.5 \text{ e} \cdot \text{\AA}$ (blue). This representation of the intramolecular non-covalent interaction clearly reveals an attractive interaction between four hydrogen atoms of the isopropyl groups (H20B, H23A, H43B, H46A) and the lone pairs of the silicon atom. This explains the deviation of the Dipp-groups from the planar geometry.

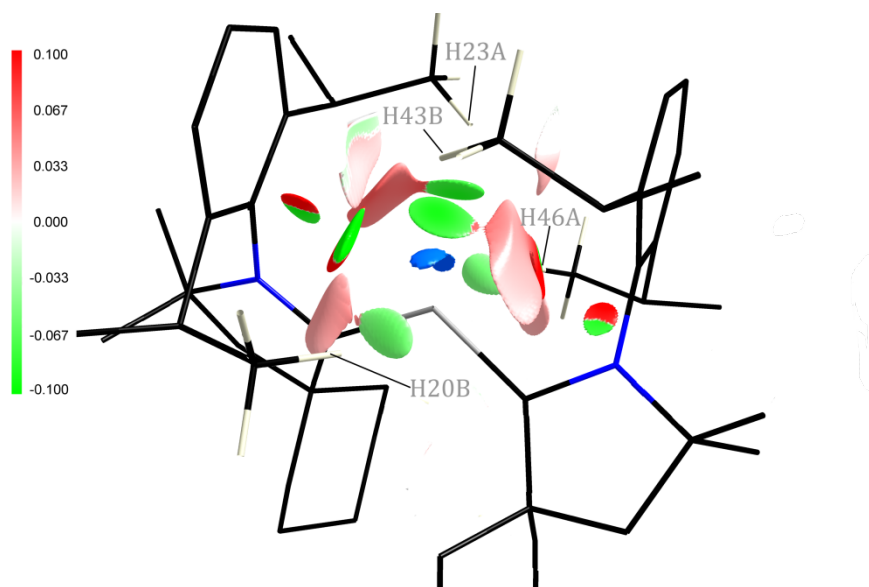


Figure 66: Non-covalent intramolecular interaction around the silicon atoms in **3**. Isosurface of the RDG $s = 0.3$. The surface is coloured according to $\text{sign}(\lambda_2) \cdot \rho$; green attractive interactions, red repulsive. In blue an isosurface at a level of $0.25 \text{ e} \cdot \text{\AA}^{-5}$ of the Laplacian is shown indicating the two lone pairs at the silicon atom.

Additionally, Figure 66 visualises effective shielding of the silylone by the Dipp groups. This is in good accordance with the reactivity found for the silylone **3**. As reported by *Roesky et al.*^[232] the crystalline silylone $(\text{cAAC})_2\text{Si}$ is stable in an inert atmosphere for about two years without any decomposition. Moreover, it does not react with molecular hydrogen, ammonia, and carbon dioxide unlike e.g. silylenes. To date the only reported reaction of $(\text{cAAC})_2\text{Si}$ is the electron-induced conversion into a six-membered cyclic silylene (Figure 67).

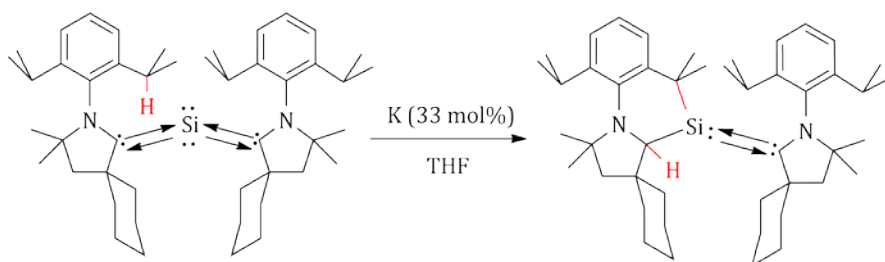


Figure 67: Conversion of a silylone $(\text{cAAC})_2\text{Si}$ into cyclic silylene via an intramolecular proton transfer.

5.6 Conclusion

The experimental charge density investigation presented here shows that the refinement of a MM against high-resolution X-ray data can lead to results of excellent quality even for complex molecules such as of the silylone (cAAC^{cv})₂Si. Although the low symmetry and the large number of atoms in the molecule lead to a very time consuming data collection and model refinement, the investigation of **3** could show that the experimental investigation of the EDD can give insights into the structure of a molecule, which are not always possible via quantum chemical calculations.

However, in order to obtain these results, it is essential to collect data of extraordinary quality. The investigation of **3** confirmed the importance of an accurate collection of the low-order data especially for the refinement of the subtle bonding features. A limiting factor here is the low dynamic range of the CCD detectors, which are often used in charge density investigations. As a result, the most intense low-order reflections very often exceed the counting rate of the detector. It could be proven in this investigation, that the use of an attenuator recollecting the frames, which exceed the dynamic range, is not useful as it introduces scaling problems. Therefore, the automatic attenuation should not be used for charge density data collections. Thus most attention should also be paid to the crystal selection, in order to find a crystal that allows the measurement of reflection up to high resolution and at the same time allows a measurement of the intense reflection within the counting rate of the detector.

A suitable alternative to circumvent these problems could be the collection of 'fast' scans, in which the scan interval per frame is increased or the reduction of the incident beam for complete runs. Future studies will be necessary to test the suitability of these strategies. In the present study the error arising from the bad scaling of the attenuated reflection could be minimised by rejection of 22 reflections affected by this error. The completeness of the data was not affected by this since 21 reflections were also collected without attenuation.

Similar to the refinements shown in Section 4 model **3** showed signs of resolution dependent errors. Positive residual density was found in close proximity to the silicon atom and the course of the scale factor mimics a u-shape. Parallel to what was found in Section 4 the model could be improved by a refinement with resolution-dependent scaling, by reduction of the size of the integration box or by the application of an empirical determined correction factor. This strongly suggests TDS to be the reason for the observed errors, although the temperature dependence of these errors could not be proven because only one dataset of **3** is available. The best model was obtained from the refinement against the empirical corrected dataset, which was used for the topological analysis.

The topological analysis of the EDD could clearly prove that the bonding situation in **3** is best described as a central silicon of formally oxidation state zero that is stabilised by donor-acceptor bonds of the cAAC ligands. Thus **3** should be named silylone. The singlet state of the carbenes could be proven by the *Laplacian* distribution that resembles that of the 1A_1 CH₂ molecule and that found for *Fischer*-type carbenes. Additionally, it was shown that the nitrogen atom in the cAAC tends to donate lone pair density into the N-C_{carbene} bond, which results in higher s-character of the lone pair. Since this donation is only feasible for a singlet carbene, the bonding geometry of the nitrogen can be used as an indicator for the electronic state of the nitrogen. The properties of the Si-C bonds are in good accordance with those found for other donor bonds. They reveal an ED that is equally or even slightly lower than in normal Si-C single bonds, which is in strict contrast to what is found for covalent double bonds with triplet states, such as C=C double bonds. The ellipticities found for the two Si-C bonds indicate a different amount of π -backdonation, which is also mirrored in the bond length as well as the *Bader* charges of the carbene carbon atoms. Via periodic solid state calculations, it can be shown, that this is due to the different geometry of the two cAACs caused by weak intermolecular interactions. In order to obtain more information about these weak interactions and their role for the different back donation further quantitative studies of the silylones with cyclohexyl- and dimethyl groups at the C _{α} carbon would be needed.

However, both bonds show a significant π -backdonation. Therefore, a double bond could be drawn in a *Lewis* diagram of **3**, but it should always be kept in mind that the bond is not formed between two fragments in triplet state. The carbenes and the silicon atom both are in singlet state. Thus the interaction is better described by a donor-acceptor bond indicated by two arrows, as only this description also includes the lone pair density remaining at the silicon atom.

6 Unveiling Disorder in $[\text{Ge}_8\{\text{N}(\text{SiMe}_3)_2\}_6]$

In 2003 *Schnepf & Köppe*^[233] reported on the synthesis of the ligand stabilised germanium cluster $[\text{Ge}_8\{\text{N}(\text{SiMe}_3)_2\}_6]$ (Figure 68). The structural analysis revealed a slightly distorted cube of germanium atoms, in which two of the eight germanium atoms are only bound to three other germanium atoms. Thus an oxidation state of formally zero can be assigned to these two germanium atoms and the compound can be regarded as a low valent tetrel. The average oxidation state of the germanium atoms is less than unity (+0.75). The bonds between the ligand substituted germanium atoms ($\text{Ge}(\text{R})\text{-Ge}(\text{R})$; 2.67 Å) were found to be significantly longer than those to the unsubstituted germanium atoms ($\text{Ge}(\text{R})\text{-Ge}$; 2.50 Å). Quantum chemical calculations on the model compounds $[\text{Ge}_8(\text{NH}_2)_6]$ and $[\text{Ge}_8(\text{SiMe}_3)_6]$ showed that this difference is only present for the amide stabilised cluster, indicating a strong influence of the ligand. Furthermore, by comparing the structure of $[\text{Ge}_8\{\text{N}(\text{SiMe}_3)_2\}_6]$ with the fully substituted perfectly cube-shaped cluster the authors could show that the additional two electrons delocalise into the cube leading to the distortion of the cube.^[233]

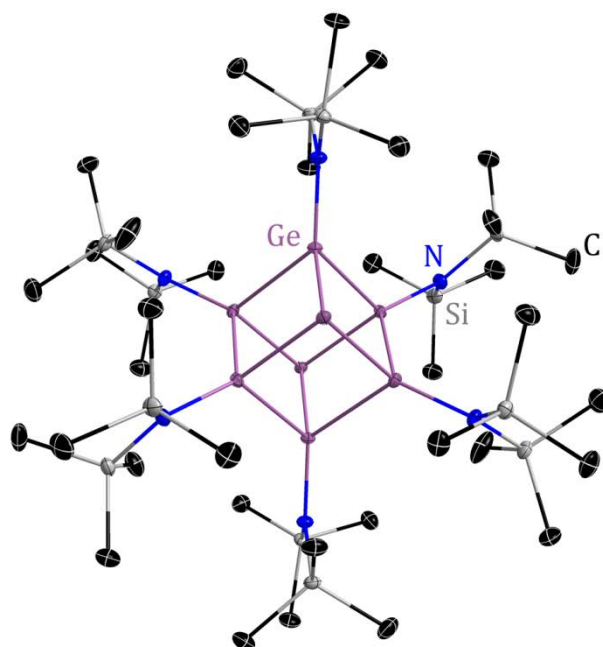


Figure 68: The molecular structure of compound **4**. Hydrogen atoms and solvent molecule are omitted for clarity. Anisotropic displacement parameters are depicted at the 50% probability level.

In order to investigate the electron delocalisation and the charge distribution in this low valent germanium compound experimentally, it was the aim of this work to perform a charge density investigation. The crystals for this investigation were supplied by *Dr.*

Christian Schenk of the group of Prof. Andreas Schnepf. In contrast to the crystals used for the investigation by Schnepf & Köppe^[233] these crystals were grown from benzene instead of toluene. $[\text{Ge}_8\{\text{N}(\text{SiMe}_3)_2\}_6] \cdot (\text{C}_6\text{H}_6)$ (**4**) crystallises in the triclinic space group $P\bar{1}$ with half a molecule of the cluster and one benzene molecule in the asymmetric unit. Crystals suitable for the collection of a high-resolution dataset were chosen under a polarisation microscope and mounted from inert oil at low temperature using the X-Temp2 device.^[214-215] One dataset (**4·Mo**) was collected on a Bruker D8 three circle goniometer equipped with a Smart APEX II CCD, a TXS Mo rotating anode, Incoatec Helios mirror optics and with a Bruker Kryoflex II device. A second measurement (**4·Ag**) was done simultaneously on a Bruker D8 three circle goniometer equipped with a Smart APEX II CCD, INCOATEC Ag $I\mu\text{S}$ with QUAZAR mirror optics and with an Oxford Cryostream device.

However, already during the data collection problems within the structure emerged. The preliminary refined IAMs for both datasets showed high residual density peaks, which cannot be explained by unmodelled bonding density. The highest peaks in the residual density (**4·Mo**: $11.37 \text{ e}\cdot\text{\AA}^{-3}$; **4·Ag**: $7.17 \text{ e}\cdot\text{\AA}^{-3}$) map of both models are extremely high and located $\sim 0.5 \text{ \AA}$ from the Ge1 atom of oxidation state zero. Slightly lower but still considerably high peaks of residual density can be found close to the remaining germanium atoms (**4·Mo**: $7.11, 6.78, 6.42 \text{ e}\cdot\text{\AA}^{-3}$; **4·Ag**: $3.79, 3.72$ and $3.54 \text{ e}\cdot\text{\AA}^{-3}$) (Table 21).

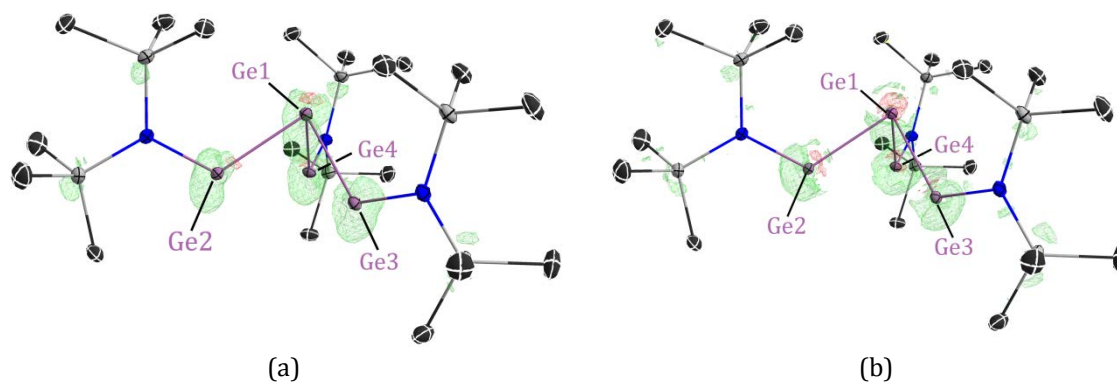


Figure 69: Residual density map after IAM refinement of **4** for the datasets collected with molybdenum (a) and silver (b) radiation. Atomic displacement parameters are depicted at 50 % probability level. Hydrogen atoms are omitted for clarity. Positive residual density is shown in green, negative in red. Isolevel is depicted at $\pm 0.50 \text{ e}\cdot\text{\AA}^{-3}$.

Table 21: Residual density peaks for the dataset **4·Mo** and **4·Ag**.

	4·Mo				4·Ag			
	x	y	z	Dist. to core [Å]	x	y	z	Dist. to core [Å]
PK 1	0.3577	0.0791	0.0639	0.529	0.3589	0.0802	0.0646	0.530
PK 2	0.4614	0.0904	-0.1431	0.468	0.4659	0.0980	-0.1484	0.478
PK 3	0.3620	-0.1283	0.1303	0.465	0.3587	0.1299	0.1364	0.453
PK 4	0.5606	0.0927	0.0700	0.441	0.5656	0.0977	0.0617	0.469

The residual density peaks are also present, if the model is only refined against the low-order data ($d \geq 0.8 \text{ \AA}$). Therefore, TDS can be excluded as reason for the observed errors, since TDS only introduces scaling errors in refinements against high-resolution datasets. Moreover, the residual density could neither be modelled by the introduction of the multipole expansion nor by the refinement of *Gram-Charlier* coefficients in order to model potential anharmonic motion. Further tests using different models for the absorption correction also did not improve the model, though the observed residual density distribution is unusual for problems arising from absorption altogether.

It is striking that the residual density peaks are located at nearly the same position in both datasets (Table 21). Thus a possible reason for the observed residual density might be a disorder of the germanium cube. This disorder was refined using restraints for the 1,2- and 1,3-distances and displacement parameter similarity restraints (SIMU) were applied to all germanium atoms. The refinement of the germanium cube on two different positions results in occupancies of 94.7% and 96.3% for the main position in **4·Mo** and **4·Ag**, respectively (Figure 70).

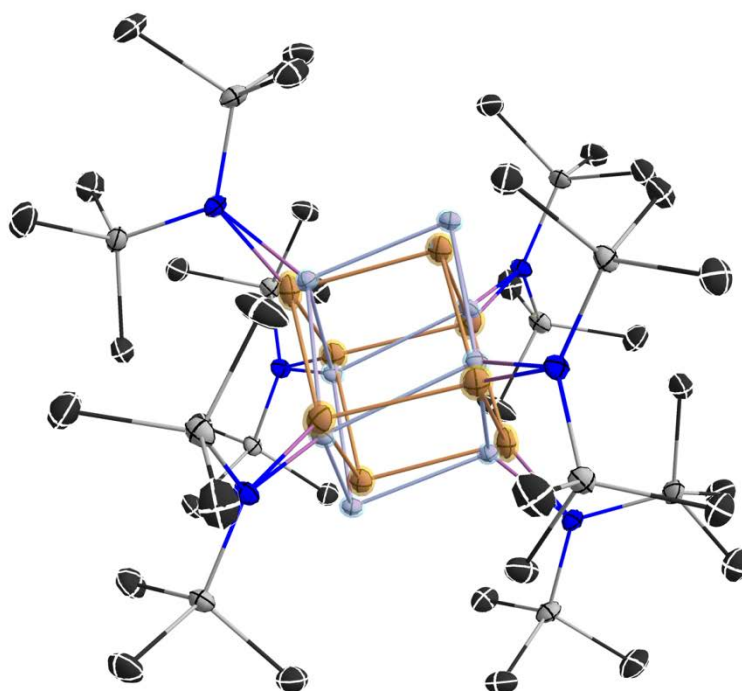


Figure 70: The molecular structure of compound **4·Mo** after refinement with disorder of the germanium cube. The main part is highlighted in blue; the minor part in yellow. Hydrogen atoms and solvent molecule are omitted for clarity. Anisotropic displacement parameters are depicted at the 50% probability level.

Refinement only against the low-order data ($d \geq 0.8 \text{ \AA}$) reveals the exact same occupancies of the two domains. After the refinement of the disordered model some structured residual density is still present around the germanium atoms. However, the highest peak decreases significantly (**4•Mo**: $3.01 \text{ e}\cdot\text{\AA}^{-3}$; **4•Ag**: $1.10 \text{ e}\cdot\text{\AA}^{-3}$). Several further crystals were tested showing varying occupancies of the two domains from 88.1% to 98.8%. Yet, a crystal showing no disorder was not found. Therefore, a meaningful investigation of the EDD of the molecule on the basis of a high-resolution X-ray diffraction dataset is not possible, since it is impossible to deconvolute the thermal motion, the disorder and the valence destiny.

7 Cross-validation

The aim of a charge density study is to obtain a model that describes the EDD of the investigated compound best. This usually is achieved using a least-square refinement. However, in statistics it is a well-known fact that a model, which is refined against certain data tends to underestimate the errors. This means that the prediction made on basis of this model will be of higher quality than it is actually the case.^[234] The data would be overfitted.

In order to avoid overfitting, it is essential to monitor the quality of the model, since for example introduction of additional parameters will certainly increase the agreement of the model and the data, but the model is not necessarily improved. However, the use of conventional R values does not prevent overfitting. A method to circumvent this pitfall is the use of cross-validation for finding the best model. Essential this statistical method tests whether a model derived from a certain dataset is also able to predict values for data points not involved in the model refinement thus monitoring overfitting. Therefore, the dataset is divided into two parts. One part is used to derive the model, while the rest of the data is used to check whether the predictions of the model are correct. By this, cross-validation is able to identify which model really describes the actual situation best.

This section will give a short overview about the use of cross-validation in X-ray crystallography in general and in charge density investigations in particular. A python based program will be presented, which enables the use of cross-validation with *XD2006* and two examples of the use of cross-validation in MM refinements will be given.

7.1 Cross-validation in Macromolecular Crystallography

The question of overfitting is well known in macromolecular crystallography. *Brünger*^[30] introduced the concept of cross-validation to macromolecular crystallography in order to detect overfitting during the refinement process. To perform cross-validation the dataset H of measured intensities is divided into a 'working set' W and a 'test set' T . Thus each reflection is either in the working set or the test set. This procedure is possible since the structure solution and refinement from diffraction data usually is an overdetermined problem. Thus omitting data does not lead to significant errors in the refinement, because the number of reflections in the working set still is sufficient for a refinement. The residual value R_{free} calculated for the reflections of the test set T , which are not used during the refinement, can be used to judge the model quality and to detect overfitting of the data.^[31]

$$R_{free} = \sum_{h \in T} \frac{\sum_h |F_o^2(h) - F_c^2(h)|}{\sum_h F_o^2(h)} \quad T := H/W \quad \text{Eq. 7-1}$$

The precision of the R_{free} value is dependent on the number of reflections contained in the test set T as well as the residual value itself (Eq. 7-2).^[235] Moreover the R_{free} value is also dependent on the choice of the test set.^[31]

$$\sigma(R_{free}) = \frac{R_{free}}{\sqrt{2|T|}} \quad \text{Eq. 7-2}$$

Several attempts have been made to increase the accuracy of R_{free} such as k -fold cross-validation.^[31,236] For this the dataset is divided not only once, but k times, into pairwise disjoint subsets ($H = \cup_{i=1}^k T_i$), of which each is used as a test set in a separate cross-validation process. The refinement of the model is done k times against the respective working set. The mean $\langle R_{free} \rangle$ and the $\sigma(R_{free})$ are then calculated from the k single R_{free} values.

$$\langle R_{free} \rangle = \frac{1}{k} \sum_{i=1}^k \frac{\sum_{h \in T_i} |F_o^2(h) - F_c^2(h)|}{\sum_h F_o^2(h)} \quad \text{Eq. 7-3}$$

An alternative way to calculate an R value for the k -fold cross-validation was suggested by Brunger^[31] and will be named R_{cross} within this work.

$$R_{cross} = \frac{\sum_{i=1}^k \sum_{h \in T_i} |F_o^2(h) - F_c^2(h)|}{\sum_{i=1}^k \sum_h F_o^2(h)} \quad \text{Eq. 7-4}$$

This different way of calculation of the R value has one major advantage over the $\langle R_{free} \rangle$. The accuracy of R_{cross} is not dependent on the size of the individual test set, because the whole dataset is used for the calculation (Eq. 7-4). Therefore, the size of the test set can be chosen as a compromise between computation time and the completeness of the dataset used for the refinement.^[236] By this R_{cross} enables the use of cross-validation for small datasets and up to high precision.

7.2 Cross-validation in Charge Density Investigations

The refinement of an MM with *Gram-Charlier* expansion up to 4th order and without any local symmetry restriction or any parameters constrained to be the same (chemical constraint) would require 65 parameters to be modelled per atom. However, despite the fact that such a model will have problems in convergence, it will hardly be the best

description of the reality, as it would underestimate the errors of the model drastically. On the other hand, it is the aim of charge density studies to push the interpretation of the X-ray data to the limit in order to extract as much information as possible. Therefore, it is essential to monitor the reasonability of the model during the refinement process.^[35,103,237]

Although cross-validation is widely accepted in the community of macromolecular crystallography only a few reports about using cross-validation in charge density refinements can be found in the literature.^[238-243] All these refinements were performed using the program *MoPro*.^[244-246] In contrast to the refinement program *XD2006*^[136], used in this work, it is possible to define restraints using *MoPro*. In the reported studies R_{free} was used to determine the weighting factor for the restraint during the refinement. The more accurate R_{cross} has not been used in charge density refinements until now.

The determination of the weighting factor for restraints is by far not the only possible application of cross-validation in charge density refinements. Cross-validation could be used to determine, if loosening the non-crystallographic symmetry or chemical constraints is an overfitting of the data. Moreover, it could be used to determine the level to which the multipole expansion should be performed.

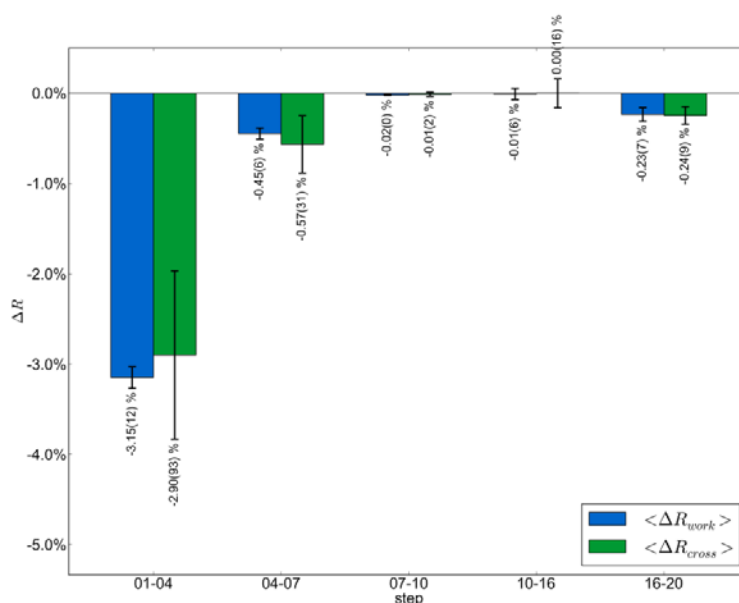
7.2.1 Cross-validation using *XD2006*

As it is not possible to calculate R_{free} values within *XD2006* two python based programs *XDRfree*^[247] and *XDCalRfree* were written in our work group in order to perform the refinements and the evaluation for the test sets, respectively. *XDRfree*, written by Lennard Krause, enables the user to run a k -fold cross-validation on a *XD2006* refinement. *XDCalRfree*, which was developed within this work, calculates the R_{free} and R_{cross} values and produces a graphical output.

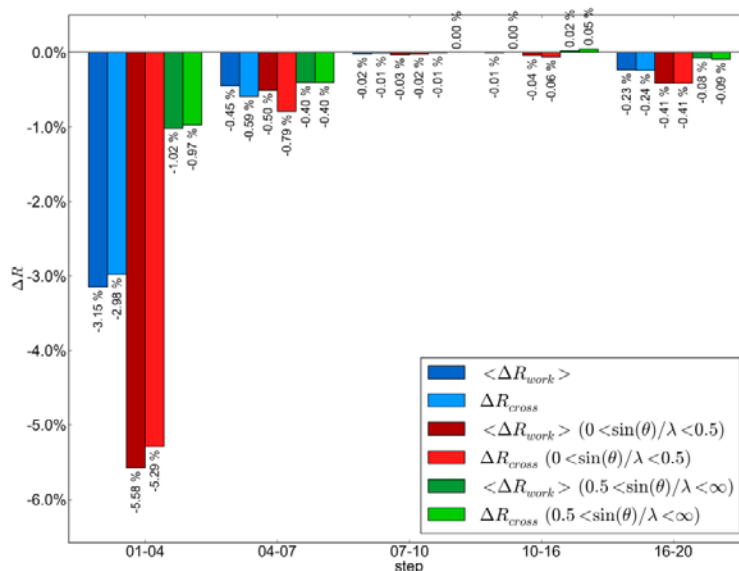
First tests with cross-validation showed that in most cases it is more appropriate to investigate not the absolute R_{free} or R_{cross} , but their change by introducing an additional parameter. Therefore, *XDCalRfree* calculates the change in R_{free} and R_{cross} between certain refinement steps and plots the results in a histogram. Additionally, it calculates the change in R_1 for the data of the working set, the so called R_{work} . The R_{cross} is additionally determined in resolution batches because the information for some parameters is only present in the high- or low-order data. Overfitting the data is indicated by a decrease of the R_{work} while R_{free} and $R_{complete}$ increase (Figure 71).

The changes in the R values for MM refinements are usually very small. Therefore, the accuracy of the R_{free} value has to be extremely high. This causes a problem similar to that appearing in macromolecular crystallography for small datasets. On the one hand it is inevitable for the precision of the R_{free} value to have a test set that is big enough. On the

other hand, especially for MM refinements it is essential to have a high completeness in order to guarantee a meaningful refinement. First studies^[29] using *XDRfree* and *XDCalRfree* revealed that dividing the dataset into ten subsets is a good compromise between accuracy completeness and computation time. Moreover, the R_{cross} showed nearly no dependency on the size of the test set MM refinements. The use of cross-validation in charge density refinements is shown in the following two examples.



(a)



(b)

Figure 71: Difference of residuals for working and test sets from 10-fold cross-validation, calculated as mean R_{free} (a) and $R_{complete}$ (b). Plots generated by *XDCalRfree*.

7.2.2 Example I: Mg(0) or Mg(+II)

The decision whether an alkali or earth alkali metal atom should be refined as a cation or neutral atom is always difficult.^[228,248-249] This has two main reasons. Firstly, the difference in the atomic form factor is very small and only affects a small number of low-order reflections. Secondly it is hard to measure whether the model has really improved by refining a monopole for the metal atom or whether the residual only is lowered because of the increased number of parameters. Therefore, R_{cross} was used to choose the best model for the magnesium atom in compound number **1**. To the best of my knowledge this is the first time the concept of cross-validation was used to investigate whether a metal in charge density refinements should be described as neutral or cationic. The refinements were done against the **1-TXS-15K** dataset, because this dataset was expected to have the smallest systematic errors. For the cationic refinement the monopole population of the magnesium was set to zero and the scattering factor for cationic magnesium was used. The charge was added to the connected nitrogen atoms in order to fulfil the electro-neutrality of the molecule. For the neutral magnesium only the monopole population was refined. The cross-validation was performed with ten datasets using *XDRfree* and *XDCalRfree*. Since the two models do not have the same starting model the use of the differences in R_{free} is not as sensible. The absolute values are used instead. In order to have a rough estimate of the precision for R_{cross} the error for R_{free} defined by Eq. 7-5 is used. Since the R_{cross} is based on the whole dataset the number of reflection in the test set $|T|$ is equal to the number of unique reflections. Assuming an R value of roughly 2% the precision can be estimated with 0.02 percentage points (Eq. 7-2).

The R_{work} and R_{cross} value are given in Table 22. It becomes clear that the improvement of the model after refining the monopole population is not overfitting of the data. Both values, R_{work} and R_{cross} , are lower when the magnesium is refined as neutral magnesium instead of a magnesium dication. This becomes even more evident when only the low-order reflections, which hold the information about the valence electrons, are taken into account. The R values for the high-order data do not differ. These results clearly indicate that it is possible to refine the monopole population of the magnesium atom in **1**. However, it should be noted that the improvement is no final proof for a parameter to be physically meaningful. Therefore, the results should be checked carefully (Section 4.1.3).

Table 22: $\langle R_{work} \rangle$ and $R_{complete}$ values for the refinement of neutral ($Mg(0)$) and cationic ($Mg(+II)$) magnesium.

	all data		$0 \leq \sin(\theta)/\lambda \leq 0.5$		$0.5 < \sin(\theta)/\lambda \leq \infty$	
	Mg(0)	Mg(+II)	Mg(0)	Mg(+II)	Mg(0)	Mg(+II)
$\langle R_{work} \rangle$	2.14%	2.19%	1.99%	2.10%	2.27%	2.26%
$R_{complete}$	2.30%	2.35%	2.25%	2.37%	2.35%	2.33%

7.2.3 Example II: Validation of Refinement Strategies

This second example of the use of cross-validation in charge density refinements will deal with the development of the refinement procedure. The two main questions will be: Is it reasonable to refine a model without chemical constraints and without local symmetry restrictions for the multipole parameters? And: Is it reasonable to refine the *Gram-Charlier* coefficients for the atoms that show signs of anharmonic motion? Especially the first question is of highest importance, but was to the best of my knowledge never investigated systematically. In order to stabilise the model during the refinement it is best-practice to apply chemical constraints and local symmetry restrictions to the multipole parameters. However, within the refinement procedure they are usually released, although it is not clear if the refinement of all possible parameters is an overfitting of the data. Therefore, the R_{cross} was calculated for every step of the refinement procedure of the MM of **3**. The change in R_{work} and R_{cross} between certain crucial steps of the refinement for the low- and high-order data as well as for the complete dataset are shown in Figure 72. The refinement procedure used for this investigation differs from the one reported in Section 5. This has mainly two reasons. On the one hand, it is necessary to increase the parameters in a way that allows to distinguish between the different effects of adding the *Gram-Charlier* coefficients, loosening the local symmetry restrictions or the chemical constraints. On the other hand, it was shown recently^[29] that it is possible to refine the MM using much shorter refinement procedures, without changing the results. Therefore, a shorter refinement procedure was chosen (see appendix), which strikingly decreases the time required for the calculation.

By inspection of the first refinement step in the histogram it becomes apparent that the introduction of the multipole expansion with highest local symmetry restrictions (see appendix) and all chemical constraints (see appendix) improves R_{work} and R_{cross} . As expected, for the introduction of parameters modelling the valence density, the improvement is larger for the low-order than for the high-order data. However, both R_{work} and R_{cross} show an improvement indicating that the data is not overfitted. The subsequent refinement of the displacement and positional parameters shows an equal improvement in the R values for high- and low-order reflections. Again no signs of overfitting can be observed. The same is true for the refinement of κ as well as for the refinement of the hydrogen positions. It is worth mentioning that the later shows much larger improvement of the low-order data than of the high-order data. Also for the refinement of κ' cross-validation does not indicate any overfitting. The next steps of the refinement procedure, in which the *Gram-Charlier* coefficients for the two cyclohexyl groups, the phenyl group and the silicon atom are introduced, mainly affect the high-order data. Again a decreasing R_{work} and R_{cross} is observed. Thus no signs of overfitting are visible.

In the subsequent steps the local symmetry constraint of the silicon atom is dismissed. The change in R_{work} is very small, which can be explained by the small number of additional parameters. The change in R_{cross} is also very small, showing a small improvement for the low-order data and no change for the high-order data. A similar effect can be observed, if the $mm2$ symmetry of the cyclohexyl groups is reduced to m symmetry. This indicates that a refinement without the most restrictive local symmetry restrictions is possible. In contrast, the loosening of the other symmetry restriction shows a much larger improvement in R_{work} than in R_{cross} . However, R_{cross} still slightly improves. This is an indication of overfitting, but the slight decrease in R_{cross} could mean that some of the atoms are better modelled without symmetry constraints.

However, in strict contrast to all these refinement steps the release of the chemical constraints between the atoms of the two carbene heterocycles as well as all other chemical constraints show an improvement in R_{work} , but not in R_{cross} . This becomes even more obvious by looking only at the low-order data. This means that the accordance of model and data is only improved for those reflections, which are used for the refinement, and thus it indicates overfitting.

Thus the investigation of the refinement protocol of **3** using cross-validation indicates that a refinement of the multipole parameters without local symmetry restrictions is an overfitting for most atoms. However, it is not for the silicon atom. The refinement of the *Gram-Charlier* coefficients does not show any sign of overfitting. Nevertheless, it has to be emphasised that this is of course only a necessary criterion for the refinement of anharmonic motion. Further tests on the residual density, the PDFs etc. are necessary.^[68] For the refinement of a model without chemical constraints cross-validation indicates an overfitting of the data. The improvement of the accordance between model and data does not lead to a better description of the actual situation. Although the possibility of releasing individual constraints arises, it seems better to refine only 21 different sets of multipole parameters for the model **3**. Thus the electron density of the individual atoms even in the two cAAC is constraint to be the same.

This is in marked contrast to the refinement procedure reported in Section 5. However, since the application of cross-validation using *XD2006*^[136] was not possible at that time, this overfitting of the data could not be detected. Therefore, the refinement procedure without any chemical constraints was published and thus also reported in Section 5. Yet, as shown in the following the influence of this small overfitting on the derived properties is small and all conclusions drawn in Section 5 are still valid.

7.2.3.1 Refinement with Chemical Constraints

As cross-validation indicates that the refinement of a model without any symmetry restriction and with individual multipole parameters for the two cAACs is an overfitting of the data, the question arises whether the differences found for the Si–C_{carbene} bonds are still present in a model with chemical constraints and local symmetry. Thus a refinement with all chemical constraints and local non-crystallographic symmetry for all atoms except the silicon atom (step 15) was performed.

The properties at the BCP are given in Table 23. It becomes clear that the ED and the *Laplacian* show slightly smaller deviations for the constraint model. However, even the larger differences in the free model are barely significant. Yet, the small differences in the *Bader* charges are still present (Si1: 1.20 e, C1: -0.56 e, C24: -0.50) even though the multipole parameters for C1 and C24 are constraint.

Table 23: Properties of the ED at the Si–C BCPs of **3** with and without chemical constraints (*chemcons*) and local symmetry.

	Bond	d_{BP} [Å]	$d1_{BP}$ [Å]	$d2_{BP}$ [Å]	ρ_{BCP} [e Å ⁻³]	$\nabla^2\rho_{BCP}$ [e Å ⁻⁵]	ϵ	η
All chemcons	Si1–C1	1.8468	0.7365	1.1104	0.793(8)	3.92(2)	0.48	0.39
No chemcons		1.8465	0.7342	1.1122	0.770(7)	5.04(2)	0.56	0.36
All chemcons	Si1–C24	1.8627	0.7422	1.1205	0.774(7)	2.87(2)	0.14	0.38
No chemcons		1.8624	0.7342	1.1211	0.795(7)	3.32(2)	0.11	0.41

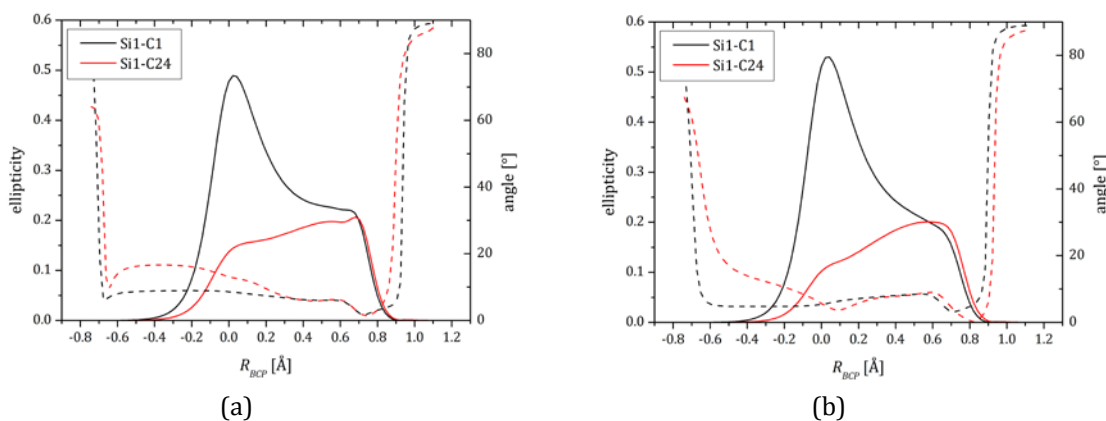


Figure 73: Ellipticity (solid line) and angle of the major axis (dashed line) along the bond path of Si–C bonds in **3** for the model with (a) and without chemical constraints (*chemcons*) and local symmetry (b).

Moreover, the difference in the ellipticities at the BCP is nearly unchanged. This becomes even clearer by comparing the ellipticities along the bond paths for the different models (Figure 73). The difference in the heights of the shoulder close to the BCP is more or less unchanged. It is a quite astonishing result that the two bonds still show this significantly different behaviour even though the two carbene molecules share the same multipole population parameters. This can be explained with the fact the silicon atom does not fulfil

the mirror symmetry. Before the loosening of the local symmetry restrictions of the silicon (step 13) the ellipticities are found to be the same ($\epsilon = 0.25$). This clearly supports the hypothesis that the difference is caused by a different back donation of the silicon atom, which is a result of the different coordination angle of the two cAACs. The influence of the cAACs on this effect seems to be rather small.

Knowing this, it is not surprising that the other findings indicating a silylone such as the two non-bonding VSCCs at the silicon atom (see appendix), the *Laplacian* distribution in the π -plane of the carbene carbon atoms (see appendix) or the evidence for the lone pair donation into the N-C bond (Table 24), are still present in the constraint model. Thus a significant distortion of the model by overfitting can be excluded and the conclusions drawn in Section 5 are still valid.

Table 24: Properties of the ED at the N-C BCPs of **3** with and without chemical constraints (*chemcons*) and local symmetry.

	Bond	d_{BP} [Å]	$d1_{BP}$ [Å]	$d2_{BP}$ [Å]	ρ_{BCP} [$e \text{ \AA}^{-3}$]	$\nabla^2\rho_{BCP}$ [$e \text{ \AA}^{-5}$]	ϵ	η
All chemcons	N1-C1	1.3845	0.7923	0.5922	2.074(9)	-16.67(5)	0.16	1.17
No chemcons		1.3845	0.7831	0.6011	2.088(12)	-16.97(6)	0.16	1.16
All chemcons	N1-C4	1.4896	0.8523	0.6364	1.657(8)	-11.27(3)	0.07	0.96
No chemcons		1.4897	0.8385	0.6511	1.681(11)	-10.94(5)	0.05	0.92
All chemcons	N1-C5	1.4369	0.8051	0.6319	1.897(9)	-13.47(4)	0.03	0.95
No chemcons		1.4370	0.8122	0.6248	1.886(13)	-13.19(6)	0.02	0.96
All chemcons	N2-C24	1.3720	0.7919	0.5801	2.112	-18.11	0.16	1.25
No chemcons		1.3724	0.8005	0.5718	2.097(13)	-18.05(6)	0.16	1.28
All chemcons	N2-C27	1.4962	0.8543	0.6449	1.642	-10.85	0.07	0.94
No chemcons		1.4961	0.8621	0.6339	1.640(11)	-11.83(5)	0.05	1.07
All chemcons	N2-C28	1.4398	0.8058	0.6341	1.889	-13.25	0.03	0.94
No chemcons		1.4398	0.8002	0.6395	1.889(12)	-13.81(5)	0.03	0.96

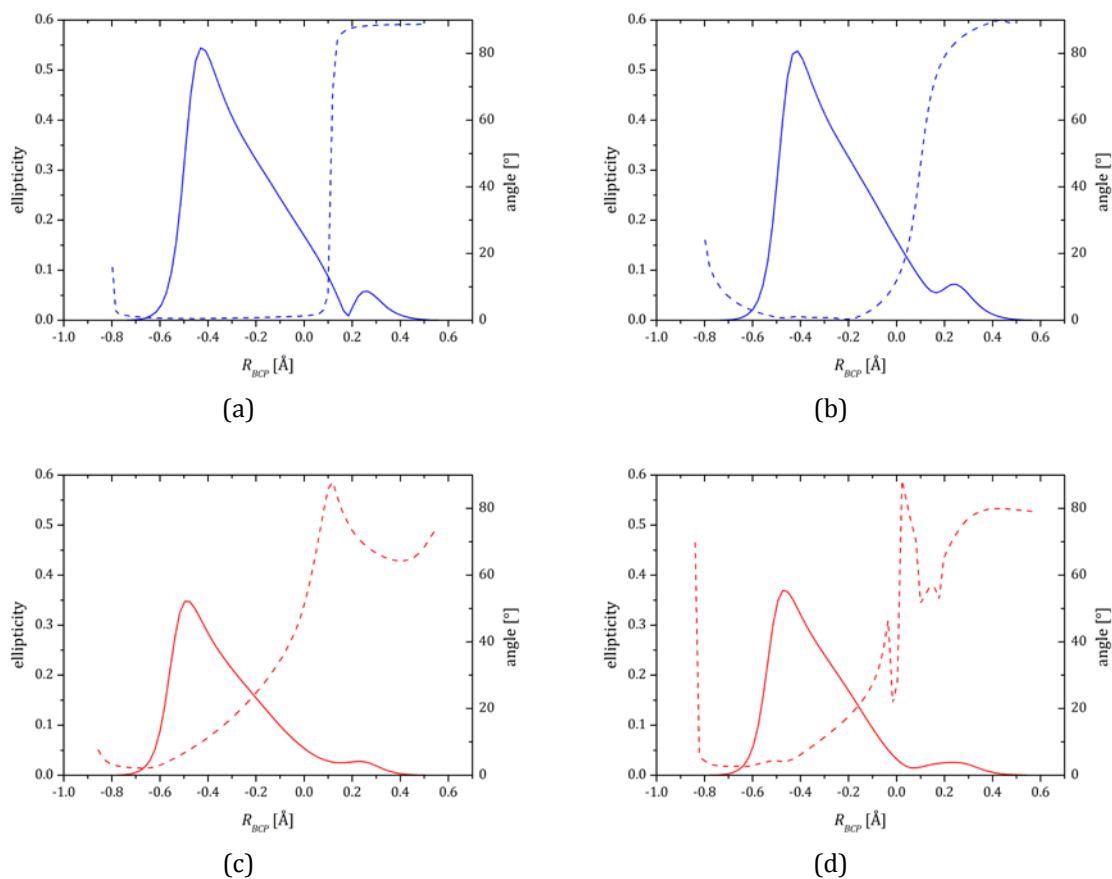


Figure 74: Ellipticity (solid line) and angle of the major axis (dashed line) along the bond path of the N1-C1 (a, b) and N1-C4 bonds in **3** for the model with (a, c) and without chemical constraints (chemcons) and local symmetry (b, d).

7.3 Conclusion

As a résumé, the two examples of cross-validation in charge density refinements show, that cross-validation^[31] is a helpful tool for judging the quality of the model. The development of the programs *XDRfree*^[247] and *XDCalRfree* make cross-validation an easy-to-use tool for the detection of overfitting in refinements using *XD2006*.

The comparison of the R_{cross} values for the refinement of **1** with Mg(+II) and Mg(0), respectively, clearly shows that a refinement of the valence population of the magnesium atom in the organometallic molecule is reasonable. This becomes ever more obvious when the R_{cross} is only calculated for the low-order data.

The second example proves that a refinement of the multipole parameters without local symmetry restrictions for the silicon atom is possible. However, for most of the other atoms a refinement without local symmetry restrictions is not possible. Overfitting may occur especially, if the actual symmetry fulfils the local non-crystallographic symmetry well. Moreover, it is shown that refinement of the *Gram-Charlier* coefficients is not an overfitting of the data. Especially for the *Gram-Charlier* coefficients, it has to be stressed that an improvement in R_{cross} is only a necessary, but never a sufficient condition for the refinement of a certain parameter. Therefore, a critical examination of the refined model parameters is inevitable. In contrast, an increase in R_{cross} in combination with a decreasing R_{work} , as found for the refinement of a model without chemical constraints, indicates overfitting. This suggests that the loosening of chemical constraints, which is common practise in most charge density refinements, should be seriously scrutinised. Further studies will have to investigate if this is valid for MM refinements in general. Additionally, investigations will have to analyse the influence of this overfitting on the properties of the EDD.

8 Summary and Outlook

The current thesis deals with the bonding situation of low valent tetrels. More precisely an experimental charge density study of the silylone $(\text{cAAC}^{\text{cy}})_2\text{Si}^{[16,32,212]}$ was carried out in order to investigate whether the bonding in this new type of molecule is best described by the dual donor-acceptor bond or if silylones should be considered silicon congeners of allenes, showing cumulated double bonds. Furthermore, this work focuses on the improvement of the precision, reliability and validity of charge density studies of such complex organometallic molecules. In the following the results of the work and possible implications for prospective studies will briefly be revised.

In the effort to improve the accuracy of charge density studies TDS was proven to be one of the most important unsolved problems in modern charge density investigations responsible for distorting the results. Since TDS is dependent on the hardness of a material, problems arising from TDS can especially show up for relatively soft organometallic molecular crystals. Therefore, a multi-temperature study was performed on di-(tris(3,5-dimethylpyrazolyl)methane)-magnesium(II) **(1)**^[126-127] and 9-diphenylthiophosphinoylanthracene **(2)**^[68,128-130]. It was confirmed that TDS introduces errors to the modelled valence density^[124], although the low-order reflections are not directly affected by TDS. It could be shown that the distortion of the scaling factor by the high order reflection introduces a change of the valence density. Furthermore, it could be demonstrated that the refinement of resolution-dependent scaling can be used as a validation tool to check whether a correction of TDS induced errors is needed. Typical signs for problems arising from TDS were found to be positive residual density close to or even at the atomic position as well as a u-shaped course of the scale factor with resolution.

The model was found to benefit from data integration with a drastically reduced size of the integration box. This improvement in outcome can be attributed to the peak broadening caused by the TDS contribution to the Bragg peak. However, the best way to reduce the errors introduced by TDS turned out to be the correction of the *hkl*-file with a correction factor $\alpha = a \cdot (\sin(\theta)/\lambda)^2 + b \cdot (\sin(\theta)/\lambda)^3$. An automatized routine was developed to deduce the parameters *a* and *b* from a refinement with resolution dependent scaling.

Unfortunately, no physical meaning could be attributed to the derived correction factors, which can be explained by the strong correlation between the scaling factor and the atomic displacement parameters. Therefore, a correction for other resolution dependent errors

could not be excluded completely. Nonetheless, the temperature dependence of the correction could clearly prove that the errors in the datasets are at least partly arising from TDS.

Future studies are needed to verify TDS to be the main reason for the resolution dependent error. However, as reported in the literature the knowledge of the elastic constants is not sufficient for a proper TDS correction as the experimental setting seems to be even more important.^[113,117] Therefore a data collection on a crystal with known elastic constants would not help in validating the correction factor. In order to treat TDS in a physically more meaningful way an implementation of a TDS correction as it was used for point detector data by *Zavodnik et al.*^[80,122] would be most helpful. By analysing the peak profile of the low-order reflections, it might be possible to derive a learned profile that could be used to evaluate the peak broadening of the high order reflections. From this a correction could be calculated. However, such a correction necessarily has to be incorporated in the integration programs. Meanwhile the presented empirical correction seems to be the best way of reducing the errors arising from TDS.^[125]

The importance of a TDS correction also became apparent in the investigation of the silylone (cAAC)₂Si (**3**). Typical signs for TDS introduced errors were found after the MM refinement. However, using the empirical correction developed in this work the errors arising from TDS could be reduced to an acceptable level. An additional systematic error was found in the scaling of the automatically attenuated frames, which otherwise would exceed the dynamic range of the CCD detector. This error was eliminated using the program *SUMMARY* in the *APEX II* software suit^[216] and a manual identification of reflections showing unusually large differences between equivalent reflections and large standard deviations. Because this procedure is very time consuming, the automatic attenuation should not be used for future charge density data collections.

Yet, especially for molecule crystals showing strong thermal motion it can be difficult to find a crystal of good size that allows the measurement of reflection up to high resolution and at the same time allows a measurement of the intense reflection within the counting rate of the detector. Suitable alternatives to circumvent these problems could be the collection of 'fast' scans, in which the scan interval per frame is increased or the reduction of the incident beam for complete runs. Future studies will be necessary to test the suitability of these strategies. Additionally, concerning this question further studies using the new single-photon counting hybrid pixel area detector might lead to data of outstanding quality.^[145,147]

However, using the additional corrections developed within this work the model obtained for the silylone shows an excellent quality and the topological analysis of the EDD was able to give detailed insights into its bonding situation. The two carbene carbon atoms in **3** revealed a Laplacian distribution typically found for *Fischer*-type carbenes. Additionally, two non-bonding VSCCs were found at the central silicon atom, indicating the presence of two non-bonding lone pairs. The indicative role of the bonding geometry of the nitrogen for the electronic state of the cAAC ligand suggested from earlier IAM studies could be confirmed by the EDD obtained from the more detailed MM. Thus the bonding situation in **3** was considered to be best described as two donor-acceptor bonds between two singlet cAAC ligands and a singlet silicon central atom of formally oxidation state zero. Thus it could be demonstrated that widening of bonding models of the main group chemistry by those originating from coordination chemistry certainly is justified, since it gives a chance to describe the untypical bonding features found in a silylone.

A comparison of the two Si–C bonds revealed a different amount of π -backdonation in the two Si–C bonds, reflected in slightly different bond length. In cooperation with the working group of *Prof. Gernot Frenking* it was possible to reproduce this different bonding situation via periodic solid state quantum chemical calculation at least partly. The calculations suggested that it is most likely that weak intermolecular interactions force the different π -backdonation via a different coordination angle of the two cAACs. However, further quantitative studies of the intermolecular interactions especially in comparison with the dimethyl substituted cAACs, which do not show this behaviour,^[212] are needed in order to completely understand this effect.

A future target for further investigations of the difference between covalent and donor-acceptor Si–C bonds certainly would be the dichloride biradical precursor (cAAC)₂SiCl₂. However, since the crystals of this compound were found to crystallise with two slightly different polymorphs within the same crystal, an investigation by high-resolution X-ray crystallography is impossible.^[195] Therefore the four-coordinate silaimine (PhC(*Nt*Bu)₂)(N(*Ad*)SiMe₃)SiN(SiMe₃)^[250] might be a better target molecule for the investigation of the difference of covalent and donor-acceptor bonds in silicon compounds. A charge density investigation of this molecule would allow the comparison of covalent single and double bonds with donor-acceptor bonds not only within the same molecule but at the same silicon centre.

The germanium cluster [Ge₈{N(SiMe₃)₂}₆]^[233] should be investigated within this work as a representative of a heavier low valent tetrel. However, it could be shown from the high-resolution data that the germanium core of the cluster shows a small disorder, while the

ligand periphery stays in place. Therefore, a meaningful experimental charge density investigation is prevented and new insights into the bonding situation could not be drawn.

The last section of this thesis deals with the limitations of the models that can be obtained via refinement against high-resolution X-ray data. Cross-validation^[31] was used as a statistical method to detect overfitting. A program was written to facilitate cross-validation for refinements performed with *XD2006*.^[29] Two examples of the applicability of cross-validation have been carried out. Firstly, it was possible to prove that the refinement of the valence electrons of a magnesium atom in **1** is not an overfitting. Secondly, it was investigated for the refinement of **3**, whether it is reasonable to refine a model without chemical any chemical constraint atoms and without local symmetry restrictions for the multipole parameters. Moreover, the reasonability of the refinement of the *Gram-Charlier* coefficients for the atoms showing signs of anharmonic motion was tested. The results indicated that a refinement of *Gram-Charlier* coefficients up to third order is possible without overfitting the data. However, the refinement without symmetry restriction of the multipole parameters an overfitting for most of the atoms. However, it is not for the silicon atom. Moreover, for the chemical constraints it could be shown that the refinement of individual multipole parameters for the two carbene ligands is not advisable. Yet, it was also proven that the different π -backdonation in the Si-C bonds is independent from the chemical constraints. Further studies are needed in order to find out whether these implications concerning the local symmetry restrictions and the chemical constraints are valid for MM refinements in general. Cross-validation will give interesting insights into this topic.

9 Crystal Structure Determination in Collaboration

9.1 Crystal Selection and Manipulation

Crystals suitable for the measurement of a single crystal X-ray diffraction dataset was chosen under a polarisation microscope and mounted from inert oil at low temperature using the X-Temp2 device.^[214-215] Air or moisture sensitive crystals were extracted the mother liquor using *Schlenk*-technique under an argon atmosphere. The crystals were placed on a slide in drops of per fluorinated polyether oil. The crystal quality was judged using a polarisation filter incorporated into a microscope. The crystals were mounted on MiTeGens Kryoloops or glass fibre and quickly placed into the nitrogen cold stream of the diffractometer.

9.2 Data Acquisition

Diffraction data were collected on three different diffractometers with different radiation and or beam size and energies in order to collect the best data possible. All machines are Bruker D8 three circle diffractometers equipped with INCOATEC Helios or Quazar focusing mirror optics and CCD detectors. The used radiation sources are a rotating Mo-Anode, an Incoatec μ S Mo and Incoatec μ S Ag. The crystal cooling was carried out either with a Bruker Kryoflex II device or with an Oxford Cryostream device. The data acquisition strategy was planned with the APEXII^[216] plugin *COSMO* or *QUEEN*.

9.3 Data Processing and Model Refinement

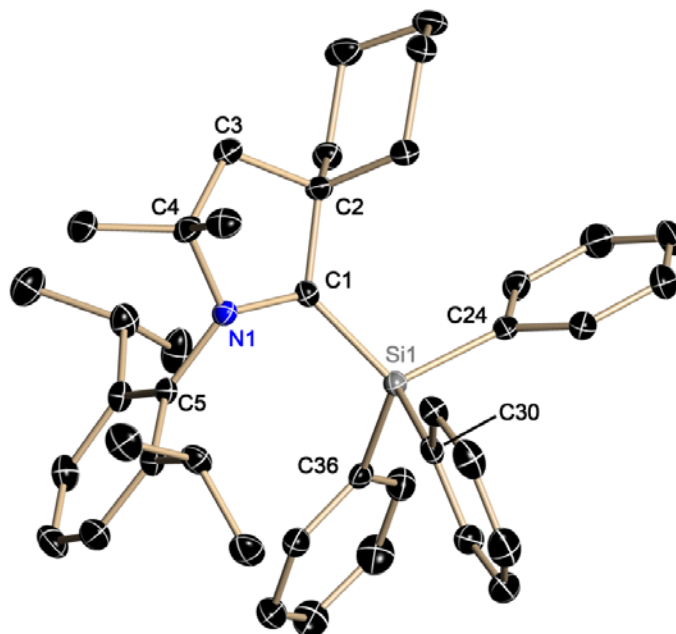
The dataset were integrated with *SAINTE* 7.68A and 8.30C^[131] and data reduction and scaling was done using *SADABS*^[71]. The space group was determined using the systematic absences with the program *XPREP*^[72] and structure solution was done using direct methods in *SHELXT*^[53]. The structure refinement was done by full-matrix least-squares methods on F^2 using *SHELXL*^[132-133] inside the *GUI ShelxLe*^[251] against all data. If not stated otherwise the hydrogen atoms have been refined using a riding model with their U_{iso} values constrained to 1.5 times U_{eq} of their pivot atoms for terminal sp^3 carbon atoms and 1.2 times for all other

carbon atoms. All non-hydrogen atoms have been refined anisotropically. Disorder was treated using restraints and if necessary constraints and by refining the site occupation factor with a free variable.

9.4 Determined Structures

9.4.1 Structures determined for Dr. Kartik C. Mondal (Prof. Dr. H. W. Roesky)

9.4.1.1 bn_km_111



Graphical representation of the asymmetric unit. Hydrogen atoms are omitted for clarity.

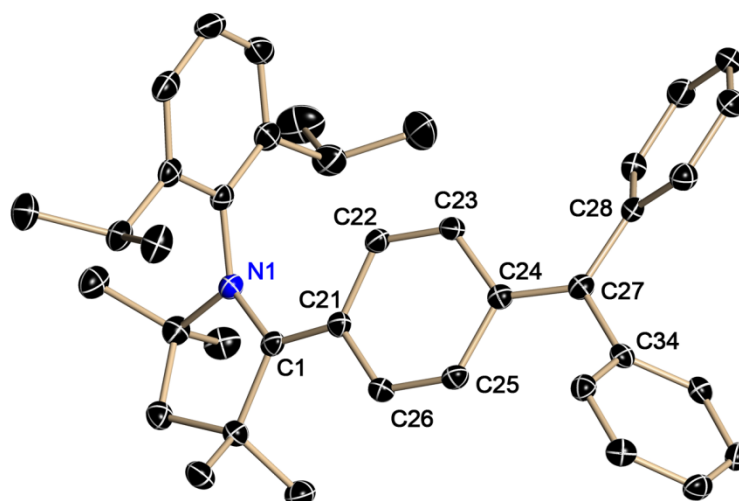
Structure published in:

Kartik Chandra Mondal, Prinson P. Samuel, Herbert W. Roesky, Benedikt Niepötter, Regine Herbst-Irmer, Dietmar Stalke, Fabian Ehret, Wolfgang Kaim, Bholanath Maity, Debasis Koley *Chem. Eur. J.* **2014**, *20*, 9240-9245.

Structural information in CIF format available with CSD number: **934726**

Structure code	bn_km_111	ρ_{calc} [g cm ⁻³]	1.154
Empirical formula	C ₄₁ H ₅₀ NSi	μ [mm ⁻¹]	0.099
Formula Weight [g mol ⁻¹]	584.91	F(000)	1268
Temperature [K]	100(2)	Crystal Size [mm]	0.16 x 0.10 x 0.07
Wavelength [Å]	0.71073	θ range [°]	1.331 to 26.412
Crystal System	Monoclinic	Reflections Collected	49249
Space Group	<i>P2</i> ₁ / <i>n</i>	Unique reflections	6890
Unit cell dimensions [Å]	<i>a</i> = 10.312(2)	Completeness to θ_{max} :	100.0 %
	<i>b</i> = 30.603(3)	Data/Restraints/Parameters	6890 / 0 / 394
	<i>c</i> = 11.300(2)	<i>R</i> _{int}	0.0659
	α = 90°	<i>R</i> 1 [<i>I</i> > 2 σ (<i>I</i>)]	0.0417
	β = 109.27(2)°	<i>wR</i> 2 (all data)	0.0929
	γ = 90°	<i>Goof</i>	1.018
Volume [Å ³]	3366.2(12)	Largest Diff. peak and hole [e Å ⁻³]	0.338 and -0.310
<i>Z</i>	4		

9.4.1.2 bn_km_171_cu



Graphical representation of the asymmetric unit. Hydrogen atoms are omitted for clarity.

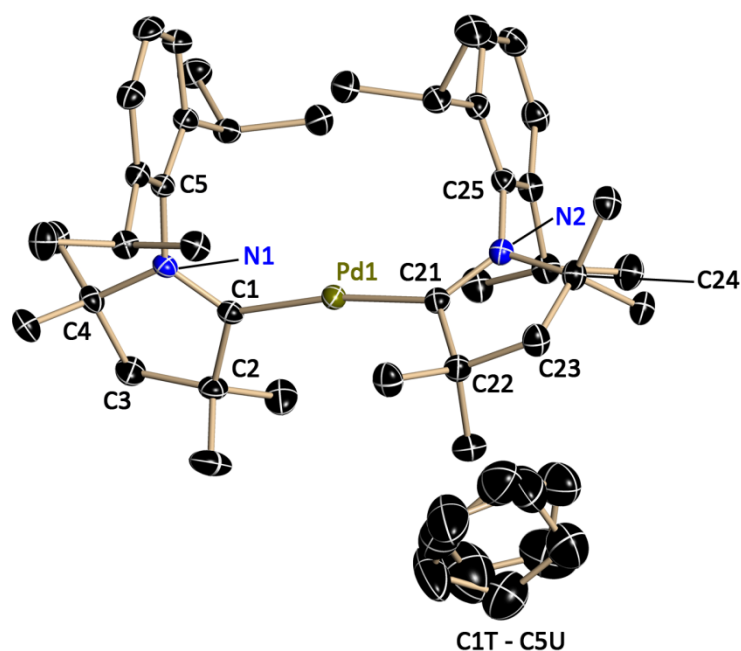
Structure published in:

Kartik Chandra Mondal, Prinson P. Samuel, Herbert W. Roesky, Benedikt Niepötter, Regine Herbst-Irmer, Dietmar Stalke, Fabian Ehret, Wolfgang Kaim, Bholanath Maity, Debasis Koley *Chem. Eur. J.* **2014**, *20*, 9240-9245.

Structural information in CIF format available with CSD number: **971426**

Structure code	bn_km_171_cu	ρ_{calc} [g cm ⁻³]	1.135
Empirical formula	C ₃₉ H ₄₅ N	μ [mm ⁻¹]	0.480
Formula Weight [g mol ⁻¹]	527.76	F(000)	2288
Temperature [K]	100(2)	Crystal Size [mm]	0.21 x 0.18 x 0.03
Wavelength [Å]	1.54178	θ range [°]	2.262 to 68.325
Crystal System	Orthorhombic	Reflections Collected	63230
Space Group	<i>Pbcn</i>	Unique reflections	5539
Unit cell dimensions [Å]	$a = 39.060(3)$	Completeness to θ_{max} :	98.7 %
	$b = 9.478(2)$	Data/Restraints/Parameters	5539 / 1 / 376
	$c = 16.680(2)$	R_{int}	0.0298
	$\alpha = 90^\circ$	$R1$ [$I > 2\sigma(I)$]	0.0332
	$\beta = 90^\circ$	$wR2$ (all data)	0.0867
	$\gamma = 90^\circ$	<i>Goof</i>	1.036
Volume [Å ³]	6175.1(16)	Largest Diff. peak and hole [e Å ⁻³]	0.238 and -0.187
Z	8		

9.4.1.3 bn_km_178



Graphical representation of the asymmetric unit. Hydrogen atoms are omitted for clarity. The disordered THF was refined on two positions. Since it was not possible to locate the oxygen in the disordered THF it was refined as C5H10. The occupancy of the main position refined to 0.53(1). The disorder was refined using restraints for the 1,2- and 1,3-distances and displacement parameter similarity restraints were applied to C1T–C5U.

The data for this structure was measured by PD Dr. Birger Dittrich at PETRA3 at DESY.

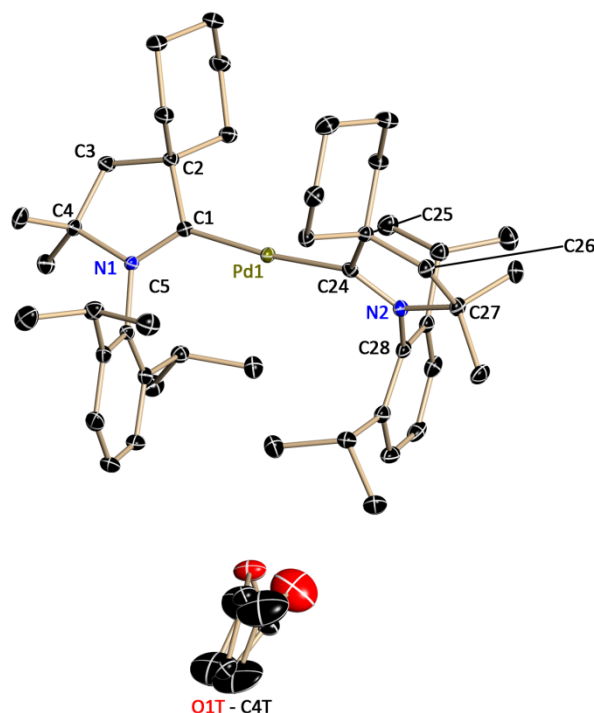
Structure published in:

Sudipta Roy, Kartik C. Mondal, Jann Meyer, Benedikt Niepötter, Christian Köhler, Regine Herbst-Irmer, Dietmar Stalke, Birger Dittrich, Diego M. Andrada, Gernot Frenking, and Herbert W. Roesky, *Chem. Eur. J.*, **2015**, *21*, 9312–9318.

Structural information in CIF format available with CSD number: **1045831**

Structure code	bn_km_178	ρ_{calc} [g cm ⁻³]	1.213
Empirical formula	C ₄₂ H ₆₆ N ₂ O _{0.50} Pd	μ [mm ⁻¹]	0.361
Formula Weight [g mol ⁻¹]	713.36	F(000)	764
Temperature [K]	100(2)	Crystal Size [mm]	0.30 x 0.20 x 0.18
Wavelength [Å]	0.6199	θ range [°]	1.030 to 26.273
Crystal System	Triclinic	Reflections Collected	46253
Space Group	$P\bar{1}$	Unique reflections	10716
Unit cell dimensions [Å]	$a = 9.121(2)$	Completeness to θ_{max} :	93.5 %
	$b = 12.275(3)$	Data/Restraints/Parameters	10716 / 304 / 495
	$c = 17.751(5)$	R_{int}	0.0221
	$\alpha = 83.39(2)^\circ$	$R1$ [$I > 2\sigma(I)$]	0.0243
	$\beta = 77.42(2)^\circ$	$wR2$ (all data)	0.0662
	$\gamma = 85.77(2)^\circ$	$Goof$	1.035
Volume [Å ³]	1924.4(9)	Largest Diff. peak and hole [e Å ⁻³]	0.418 and -0.863
Z	2		

9.4.1.4 bn_km_179



Graphical representation of the asymmetric unit. Hydrogen atoms are omitted for clarity. The disordered THF was refined on two positions. The occupancy of the main position refined to 0.870(5). The disorder was refined using restraints for the 1,2- and 1,3-distances and displacement parameter similarity restraints were applied to O1T-C4U.

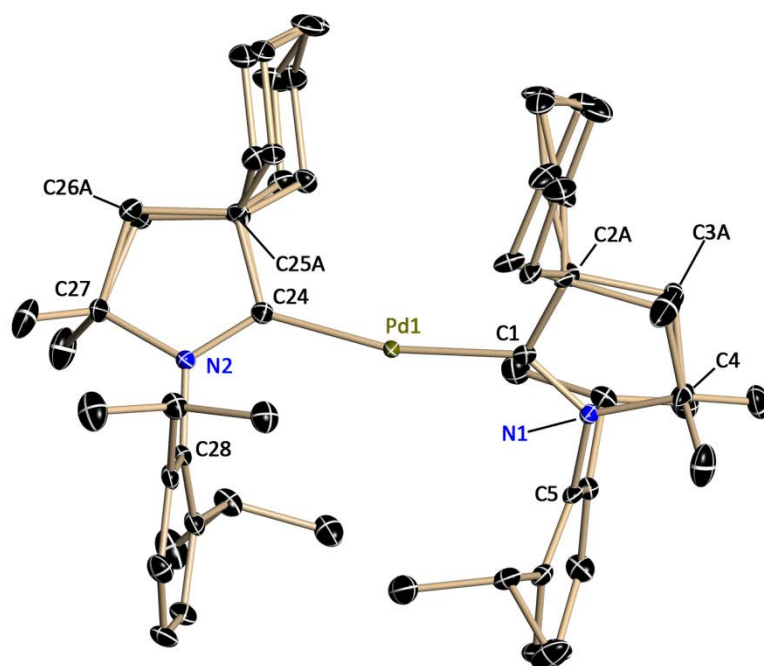
Structure published in:

Sudipta Roy, Kartik C. Mondal, Jann Meyer, Benedikt Niepötter, Christian Köhler, Regine Herbst-Irmer, Dietmar Stalke, Birger Dittrich, Diego M. Andrada, Gernot Frenking, and Herbert W. Roesky, *Chem. Eur. J.*, **2015**, *21*, 9312-9318.

Structural information in CIF format available with CSD number: **1045830**

Structure code	bn_km_179	ρ_{calc} [g cm ⁻³]	1.230
Empirical formula	C ₅₀ H ₇₈ N ₂ OPd	μ [mm ⁻¹]	0.451
Formula Weight [g mol ⁻¹]	829.54	F(000)	892
Temperature [K]	100(2)	Crystal Size [mm]	0.11 x 0.11 x 0.05
Wavelength [Å]	0.71073	θ range [°]	1.337 to 28.722
Crystal System	Triclinic	Reflections Collected	73606
Space Group	$P\bar{1}$	Unique reflections	11424
Unit cell dimensions [Å]	$a = 12.389(2)$	Completeness to θ_{max} :	100.0 %
	$b = 13.123(2)$	Data/Restraints/Parameters	11424 / 245 / 454
	$c = 15.710(3)$	R_{int}	0.0462
	$\alpha = 82.17(2)^\circ$	$R1$ [$I > 2\sigma(I)$]	0.0278
	$\beta = 77.91(3)^\circ$	wR2 (all data)	0.0653
	$\gamma = 64.78(2)^\circ$	Goof	1.048
Volume [Å ³]	1924.4(9)	Largest Diff. peak and hole [e Å ⁻³]	0.478 and -0.331
Z	2		

9.4.1.5 bn_km_179b



Graphical representation of the asymmetric unit. Hydrogen atoms are omitted for clarity. The disordered ligands were refined in two positions each. The occupancy of the main positions refined to 0.63(2) and 0.53(2). The disorder was refined using restraints for the 1,2- and 1,3-distances and displacement parameter similarity restraints were applied.

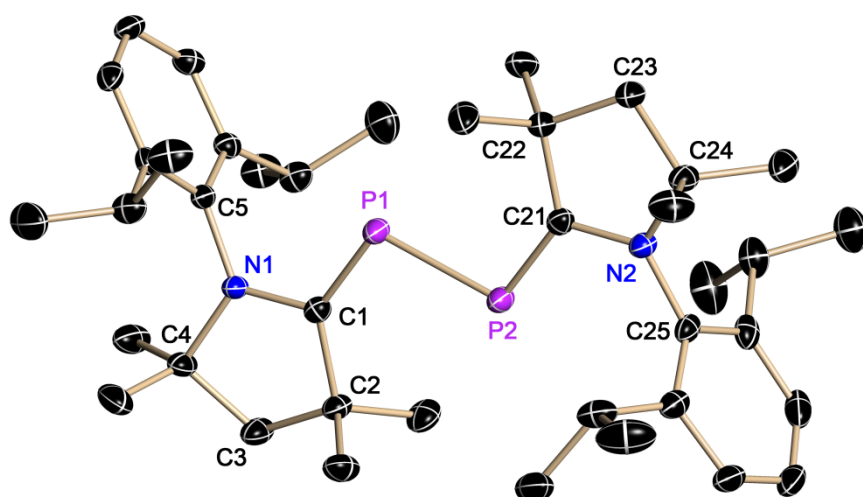
Structure published in:

Sudipta Roy, Kartik C. Mondal, Jann Meyer, Benedikt Niepötter, Christian Köhler, Regine Herbst-Irmer, Dietmar Stalke, Birger Dittrich, Diego M. Andrada, Gernot Frenking, and Herbert W. Roesky, *Chem. Eur. J.*, **2015**, *21*, 9312-9318.

Structural information in CIF format available with CSD number: **1045829**

Structure code	bn_km_179b	ρ_{calc} [g cm ⁻³]	1.239
Empirical formula	C ₄₆ H ₇₀ N ₂ Pd	μ [mm ⁻¹]	0.267
Formula Weight [g mol ⁻¹]	757.44	F(000)	1624
Temperature [K]	100(2)	Crystal Size [mm]	0.16 x 0.10 x 0.06
Wavelength [Å]	0.71073	θ range [°]	1.783 to 22.284
Crystal System	Monoclinic	Reflections Collected	98113
Space Group	<i>P</i> 2 ₁ / <i>n</i>	Unique reflections	10488
Unit cell dimensions [Å]	<i>a</i> = 11.898(2)	Completeness to θ_{max} :	99.9 %
	<i>b</i> = 15.316(3)	Data/Restraints/Parameters	10488 / 1022 / 584
	<i>c</i> = 22.300(3)	<i>R</i> _{int}	0.0434
	α = 90.00°	<i>R</i> 1 [<i>I</i> > 2 σ (<i>I</i>)]	0.0272
	β = 92.01(2)°	<i>wR</i> 2 (all data)	0.0638
	γ = 90.00°	<i>Goof</i>	1.055
Volume [Å ³]	4061.2(11)	Largest Diff. peak and hole [e Å ⁻³]	0.439 and -0.515
<i>Z</i>	4		

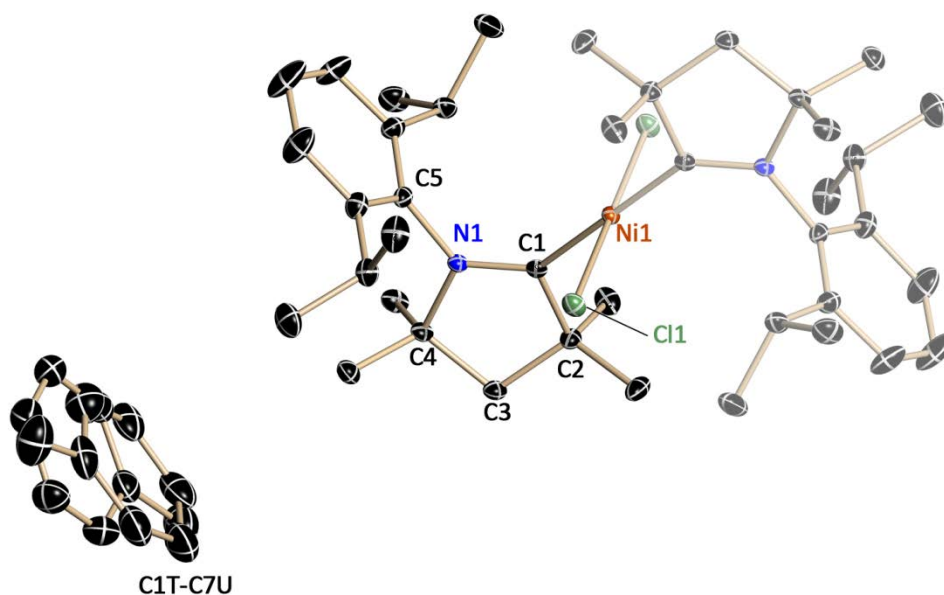
9.4.1.6 bn_km_127



Graphical representation of the asymmetric unit. Hydrogen atoms are omitted for clarity.

Structure code	bn_km_127	ρ_{calc} [g cm ⁻³]	1.119
Empirical formula	C ₄₀ H ₆₂ N ₂ P ₂	μ [mm ⁻¹]	0.145
Formula Weight [g mol ⁻¹]	632.85	F(000)	1384
Temperature [K]	100(2)	Crystal Size [mm]	0.17 x 0.11 x 0.1
Wavelength [Å]	0.71073	θ range [°]	1.371 to 26.420
Crystal System	Monoclinic	Reflections Collected	56869
Space Group	<i>P</i> 2 ₁ / <i>c</i>	Unique reflections	7696
Unit cell dimensions [Å]	<i>a</i> = 16.140(2)	Completeness to θ_{max} :	99.9 %
	<i>b</i> = 14.907(2)	Data/Restraints/Parameters	7696 / 0 / 413
	<i>c</i> = 16.968(3)	<i>R</i> _{int}	0.0669
	α = 90.00°	<i>R</i> 1 [<i>I</i> > 2 σ (<i>I</i>)]	0.0397
	β = 113.06(2)°	<i>wR</i> 2 (all data)	0.1010
	γ = 90.00°	<i>Goof</i>	1.055
Volume [Å ³]	3756.3(11)	Largest Diff. peak and hole [e Å ⁻³]	0.307 and -0.263
<i>Z</i>	4		

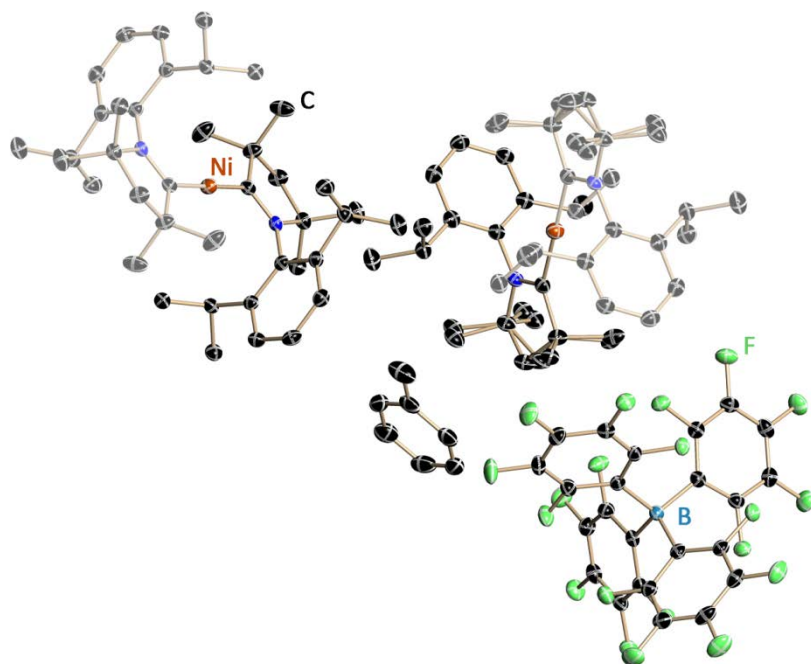
9.4.1.7 bn_km_317_tol_30mg



Graphical representation of the asymmetric unit. Hydrogen atoms are omitted for clarity. The disordered toluene was refined on two positions. The occupancy of the main position refined to 0.792(3). The disorder was refined using restraints for the 1,2- and 1,3-distances and displacement parameter similarity restraints were applied to C1T-C7U.

Structure code	bn_km_317_tol_30mg	ρ_{calc} [g cm ⁻³]	1.201
Empirical formula	C ₅₄ H ₇₈ Cl ₂ N ₂ Ni	μ [mm ⁻¹]	0.542
Formula Weight [g mol ⁻¹]	884.79	F(000)	956
Temperature [K]	100(2)	Crystal Size [mm]	0.21 x 0.15 x 0.06
Wavelength [Å]	0.71073	θ range [°]	1.473 to 28.721
Crystal System	Monoclinic	Reflections Collected	52856
Space Group	<i>P</i> 2 ₁ / <i>c</i>	Unique reflections	6316
Unit cell dimensions [Å]	<i>a</i> = 13.829(4)	Completeness to θ_{max} :	100.0 %
	<i>b</i> = 16.402(5)	Data/Restraints/Parameters	6316 / 451 / 342
	<i>c</i> = 10.788(3)	<i>R</i> _{int}	0.0434
	α = 90.00°	<i>R</i> 1 [<i>I</i> > 2 σ (<i>I</i>)]	0.0303
	β = 91.22(2)°	<i>wR</i> 2 (all data)	0.0788
	γ = 90.00°	<i>Goof</i>	1.055
Volume [Å ³]	2446.4(12)	Largest Diff. peak and hole [e Å ⁻³]	0.544 and -0.264
<i>Z</i>	2		

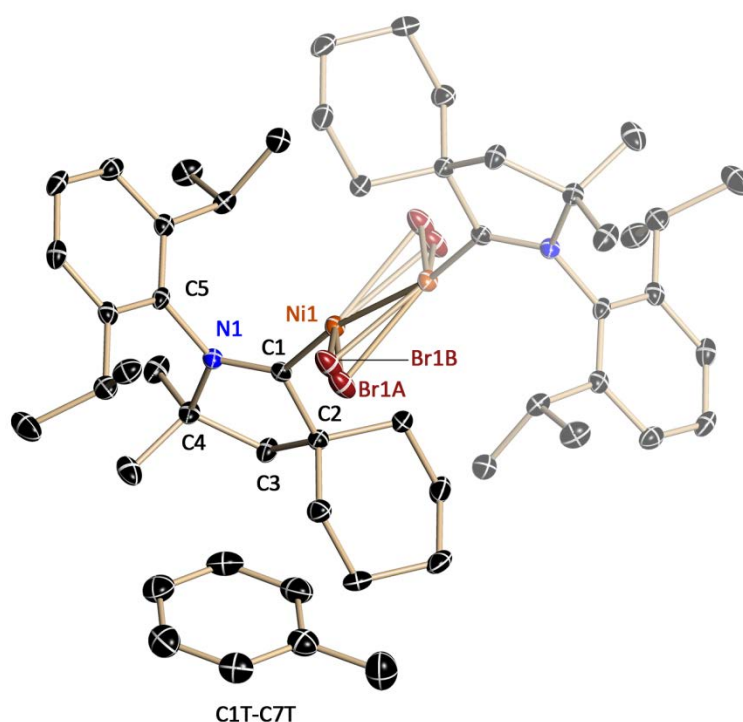
9.4.1.8 bn_km_317_tol_cu



Graphical representation of the asymmetric unit. Hydrogen atoms are omitted for clarity. The disordered ligand was refined in two positions. The occupancy of the main positions refined to 0.885(17). The disorder was refined using restraints for the 1,2- and 1,3-distances and displacement parameter similarity restraints were applied.

Structure code	bn_km_317_tol_cu	ρ_{calc} [g cm ⁻³]	1.434
Empirical formula	C ₇₁ H ₇₀ BF ₂₀ N ₂ Ni	μ [mm ⁻¹]	1.327
Formula Weight [g mol ⁻¹]	1400.81	F(000)	1446
Temperature [K]	100(2)	Crystal Size [mm]	0.07 x 0.05 x 0.04
Wavelength [Å]	0.71073	θ range [°]	2.765 to 68.236
Crystal System	Triclinic	Reflections Collected	135558
Space Group	$P\bar{1}$	Unique reflections	11429
Unit cell dimensions [Å]	$a = 14.353(2)$	Completeness to θ_{max} :	97.0 %
	$b = 15.860(2)$	Data/Restraints/Parameters	11429 / 315 / 914
	$c = 17.605(2)$	R_{int}	0.0536
	$\alpha = 65.92(2)^\circ$	$R1$ [$I > 2\sigma(I)$]	0.0373
	$\beta = 84.38(3)^\circ$	$wR2$ (all data)	0.1040
	$\gamma = 63.12(2)^\circ$	$Goof$	1.030
Volume [Å ³]	3245.0(10)	Largest Diff. peak and hole [e Å ⁻³]	0.607 and -0.959
Z	2		

9.4.1.9 bn_km_183b

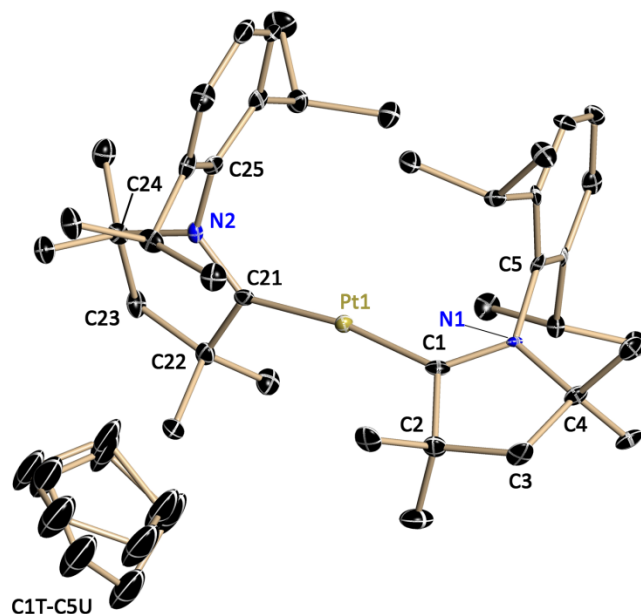


Graphical representation of the asymmetric unit. Hydrogen atoms are omitted for clarity. The disordered bromine was refined in two positions. The occupancy of the main positions refined to 0.958(8). The disorder was refined using restraints for the 1,2- and 1,3-distances. The displacement parameters of the two bromine positions were constraint.

Structure code	bn_km_183b	ρ_{calc} [g cm ⁻³]	1.348
Empirical formula	C ₆₀ H ₈₆ Br ₂ N ₂ Ni ₂	μ [mm ⁻¹]	2.183
Formula Weight [g mol ⁻¹]	1112.54	F(000)	1172
Temperature [K]	100(2)	Crystal Size [mm]	0.11 x 0.07 x 0.07
Wavelength [Å]	0.71073	θ range [°]	1.843 to 26.478
Crystal System	Monoclinic	Reflections Collected	61495
Space Group	<i>P</i> 2 ₁ / <i>c</i>	Unique reflections	5654
Unit cell dimensions [Å]	<i>a</i> = 9.845(2)	Completeness to θ_{max} :	100.0 %
	<i>b</i> = 12.598(2)	Data/Restraints/Parameters	5654 / 4 / 309
	<i>c</i> = 22.109(2)	<i>R</i> _{int}	0.0507
	α = 90.00°	<i>R</i> 1 [<i>I</i> > 2 σ (<i>I</i>)]	0.0306
	β = 91.12(2)°	<i>wR</i> 2 (all data)	0.0721
	γ = 90.00°	<i>Goof</i>	1.038
Volume [Å ³]	2741.6(7)	Largest Diff. peak and hole [e Å ⁻³]	0.356 and -0.328
<i>Z</i>	2		

9.4.2 Structures determined for Dr. Sudipta Roy (Prof. Dr. H. W. Roesky)

9.4.2.1 bn_sr_4



Graphical representation of the asymmetric unit. Hydrogen atoms are omitted for clarity. The crystal was non-merohedrally twinned with two domains. The data reduction and scaling was done using TWINABS, structure solution was done using a HKLF4 file with only the reflections of the strong domain while the refinement was done using the HKLF5 file which includes the reflections of both domains. The batch scale factor refined to 0.2992(7).

The disordered THF was refined on two positions. Since it was not possible to locate the oxygen in the disordered THF it was refined as C₅H₁₀. The occupancy of the main position refined to 0.38(2). The disorder was refined using restraints for the 1,2- and 1,3-distances and displacement parameter similarity restraints were applied to C1T-C5U.

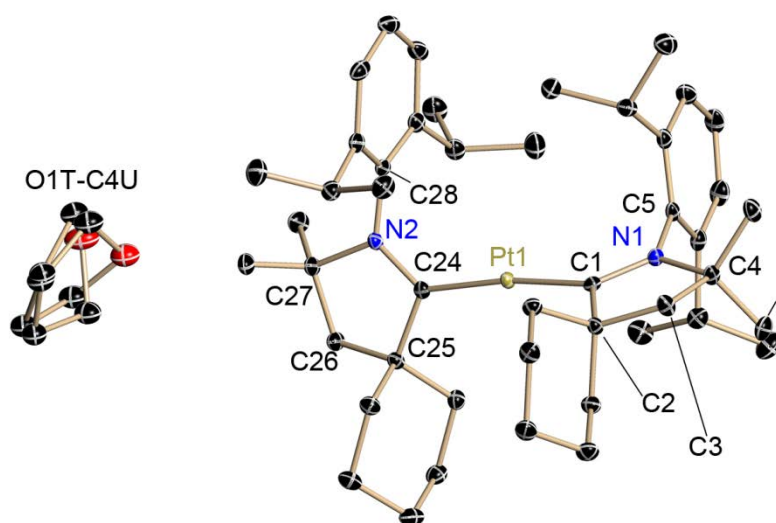
Structure published in:

Sudipta Roy, Kartik C. Mondal, Jann Meyer, Benedikt Niepötter, Christian Köhler, Regine Herbst-Irmer, Dietmar Stalke, Birger Dittrich, Diego M. Andrada, Gernot Frenking, and Herbert W. Roesky, *Chem. Eur. J.*, **2015**, *21*, 9312-9318.

Structural information in CIF format available with CSD number: **1045834**

Structure code	bn_sr_4	ρ_{calc} [g cm ⁻³]	1.391
Empirical formula	C ₄₂ H ₆₆ N ₂ O _{0.50} Pt	μ [mm ⁻¹]	2.015
Formula Weight [g mol ⁻¹]	802.05	F(000)	828
Temperature [K]	100(2)	Crystal Size [mm]	0.12 x 0.09 x 0.06
Wavelength [Å]	0.56086	θ range [°]	1.691 to 20.560°
Crystal System	Triclinic	Reflections Collected	29440
Space Group	$P\bar{1}$	Unique reflections	7613
Unit cell dimensions [Å]	$a = 9.113(2)$	Completeness to θ_{max} :	99.6 %
	$b = 12.231(3)$	Data/Restraints/Parameters	7613 / 304 / 496
	$c = 17.705(4)$	R_{int}	0.0613
	$\alpha = 83.86(3)^\circ$	$R1$ [$I > 2\sigma(I)$]	0.0382
	$\beta = 77.55(3)^\circ$	$wR2$ (all data)	0.0695
	$\gamma = 86.46(3)^\circ$	$Goof$	1.025
Volume [Å ³]	1914.4(8)	Largest Diff. peak and hole [e Å ⁻³]	0.694 and -1.016
Z	2		

9.4.2.2 bn_sr_5



Graphical representation of the asymmetric unit. Hydrogen atoms are omitted for clarity. The disordered THF was refined on two positions. The occupancy of the main position refined to 0.897(3). The disorder was refined using restraints for the 1,2- and 1,3-distances and displacement parameter similarity restraints were applied to O1T-C4U.

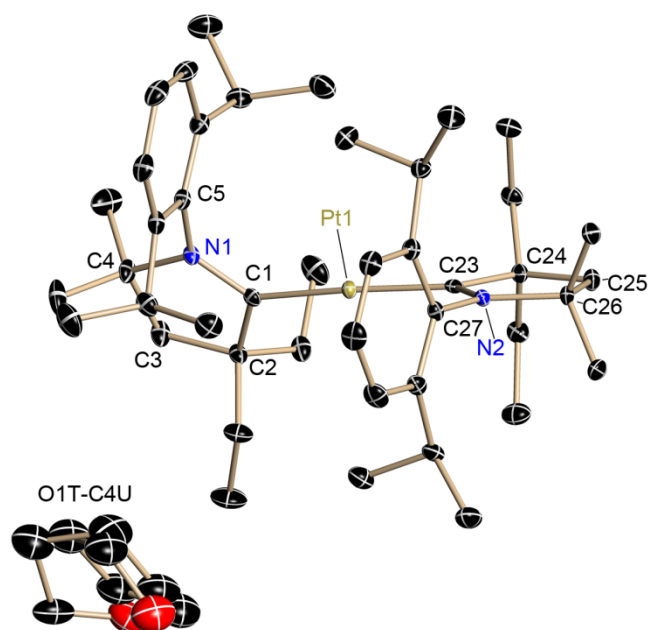
Structure published in:

Sudipta Roy, Kartik C. Mondal, Jann Meyer, Benedikt Niepötter, Christian Köhler, Regine Herbst-Irmer, Dietmar Stalke, Birger Dittrich, Diego M. Andrada, Gernot Frenking, and Herbert W. Roesky, *Chem. Eur. J.*, **2015**, *21*, 9312-9318.

Structural information in CIF format available with CSD number: **1045832**

Structure code	bn_sr_5	ρ_{calc} [g cm ⁻³]	1.382
Empirical formula	C ₅₀ H ₇₈ N ₂ OPt	μ [mm ⁻¹]	3.218
Formula Weight [g mol ⁻¹]	918.23	F(000)	956
Temperature [K]	100(2)	Crystal Size [mm]	0.21 x 0.17 x 0.14
Wavelength [Å]	0.71073	θ range [°]	1.342 to 27.621
Crystal System	Triclinic	Reflections Collected	117439
Space Group	$P\bar{1}$	Unique reflections	10185
Unit cell dimensions [Å]	$a = 12.272(2)$ $b = 13.052(2)$ $c = 15.658(2)$ $\alpha = 82.12(2)^\circ$ $\beta = 75.83(2)^\circ$ $\gamma = 65.23(2)^\circ$	Completeness to θ_{max} :	100.0 %
Volume [Å ³]	2206.3(7)	Data/Restraints/Parameters	10185 / 244 / 545
Z	2	R_{int}	0.0446
		$R1$ [$I > 2\sigma(I)$]	0.0149
		wR2 (all data)	0.0367
		Goof	1.067
		Largest Diff. peak and hole [e Å ⁻³]	0.732 and -0.309

9.4.2.3 bn_sr_23



Graphical representation of the asymmetric unit. Hydrogen atoms are omitted for clarity. The disordered THF was refined on two positions. The occupancy of the main position refined to 0.0.863(6). The disorder was refined using restraints for the 1,2- and 1,3-distances and displacement parameter similarity restraints were applied to O1T-C4U.

Structure published in:

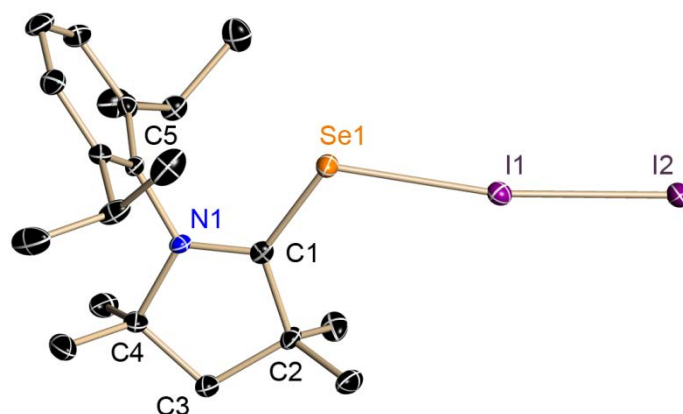
Sudipta Roy, Kartik C. Mondal, Jann Meyer, Benedikt Niepötter, Christian Köhler, Regine Herbst-Irmer, Dietmar Stalke, Birger Dittrich, Diego M. Andrada, Gernot Frenking, and Herbert W. Roesky, *Chem. Eur. J.*, **2015**, *21*, 9312-9318.

Structural information in CIF format available with CSD number: **1045833**

Structure code	bn_sr_23	ρ_{calc} [g cm ⁻³]	1.353
Empirical formula	C ₄₆ H ₇₄ N ₂ O _{0.50} Pt	μ [mm ⁻¹]	1.834
Formula Weight [g mol ⁻¹]	858.16	F(000)	3568
Temperature [K]	100(2)	Crystal Size [mm]	0.30 x 0.20 x 0.20
Wavelength [Å]	0.56086	θ range [°]	2.470 to 23.638
Crystal System	Monoclinic	Reflections Collected	126884
Space Group	<i>C2c</i>	Unique reflections	12870
Unit cell dimensions [Å]	$a = 32.926(4)$	Completeness to θ_{max} :	99.8 %
	$b = 16.431(3)$	Data/Restraints/Parameters	12870 / 239 / 531
	$c = 16.304(3)$	R_{int}	0.0457
	$\alpha = 90.00^\circ$	$R1$ [$I > 2\sigma(I)$]	0.0169
	$\beta = 107.20(2)^\circ$	$wR2$ (all data)	0.0370
	$\gamma = 90.00^\circ$	<i>Goof</i>	1.031
Volume [Å ³]	8426(3)	Largest Diff. peak and hole [e Å ⁻³]	0.444 and -0.485
Z	8		

9.4.3 Structure determined for Mykyta Tretiakov (Prof. Dr. H. W. Roesky)

9.4.3.1 bn_ni_88_1



Graphical representation of the asymmetric unit. Hydrogen atoms are omitted for clarity.

Structure published in:

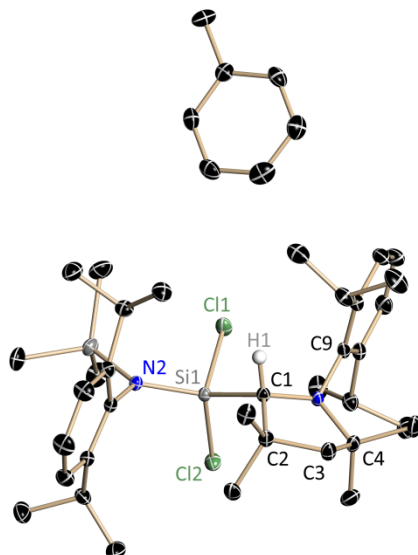
Mykyta Tretiakov, Yuriy G. Shermolovich, Amit Pratap Singh, Prinson P. Samuel, Herbert W. Roesky, Benedikt Niepötter, Arne Visscher, Dietmar Stalke, Dalton Trans. 2013, 42, 12940–12946.

Structural information in CIF format available with CSD number: **933420**

Structure code	bn_ni_88_1	ρ_{calc} [g cm ⁻³]	1.794
Empirical formula	C ₂₀ H ₃₁ I ₂ NSe	μ [mm ⁻¹]	2.303
Formula Weight [g mol ⁻¹]	618.22	F(000)	596
Temperature [K]	100(2)	Crystal Size [mm]	0.13 x 0.06 x 0.05
Wavelength [Å]	0.56086	θ range [°]	1.366 to 21.395
Crystal System	Triclinic	Reflections Collected	33744
Space Group	$P\bar{1}$	Unique reflections	5274
Unit cell dimensions [Å]	$a = 9.869(1)$ $b = 9.876(2)$ $c = 11.968(1)$ $\alpha = 92.04(10)^\circ$ $\beta = 100.33(2)^\circ$ $\gamma = 93.28(1)^\circ$	Completeness to θ_{max} :	100.0 %
Volume [Å ³]	1144.4(3)	Data/Restraints/Parameters	5274 / 0 / 225
Z	2	R_{int}	0.0361
		$R1$ [$I > 2\sigma(I)$]	0.0194
		$wR2$ (all data)	0.0407
		$Goof$	1.031
		Largest Diff. peak and hole [e Å ⁻³]	0.769 and -0.746

9.4.4 Structure determined for Dr. Chandrajeet Mohapatra (Prof. Dr. H. W. Roesky)

9.4.4.1 bn_cm_13nh3_1



Graphical representation of the asymmetric unit. Hydrogen atoms, except H1, are omitted for clarity. The toluene molecule was refined on two equally occupied positions ignoring the inversion centre ("PART -1"). For the 1,2- and 1,3 distances -restraints were applied. The atomic displacement parameters were refined using displacement parameter similarity restraints. The position of the hydrogen atom H1 was refined freely

Structure published in:

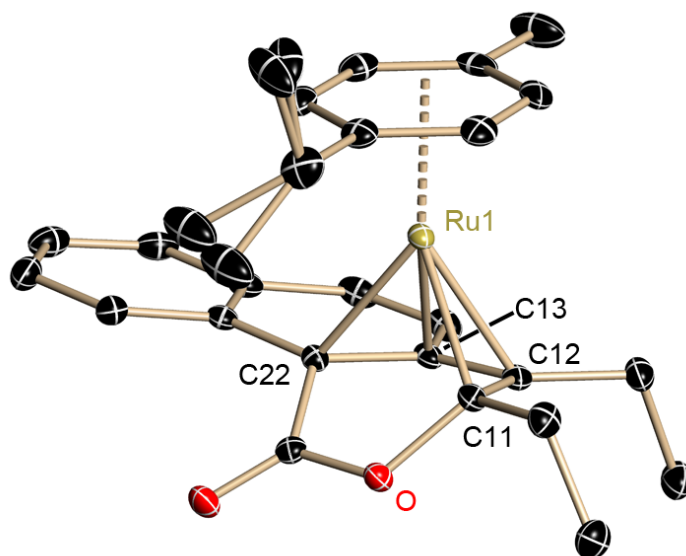
C. Mohapatra, P. P. Samuel, H. W. Roesky, B. Niepötter, R. Herbst-Irmer, D. Stalke, B. Maity, D. Koley, *Inorganic Chemistry* **2015**, submitted for publication.

Structural information in CIF format available with CSD number: **1419453**

Structure code	bn_cm_13nh3_1	ρ_{calc} [g cm ⁻³]	1.162
Empirical formula	C _{38.50} H ₆₂ Cl ₂ N ₂ Si ₂	μ [mm ⁻¹]	0.257
Formula Weight [g mol ⁻¹]	679.98	F(000)	1476
Temperature [K]	100(2)	Crystal Size [mm]	0.19 x 0.11 x 0.10
Wavelength [Å]	0.71073	θ range [°]	1.174 to 28.695
Crystal System	Monoclinic	Reflections Collected	84942
Space Group	<i>P</i> 2 ₁ / <i>c</i>	Unique reflections	10040
Unit cell dimensions [Å]	<i>a</i> = 19.688(3)	Completeness to θ_{max} :	100.0 %
	<i>b</i> = 11.024(2)	Data/Restraints/Parameters	10040 / 50 / 453
	<i>c</i> = 20.330(3)	<i>R</i> _{int}	0.0340
	α = 90.00°	<i>R</i> 1 [<i>I</i> > 2 σ (<i>I</i>)]	0.0304
	β = 118.24(2)°	<i>wR</i> 2 (all data)	0.0829
	γ = 90.00°	<i>Goof</i>	1.035
Volume [Å ³]	3887.2(13)	Largest Diff. peak and hole [e Å ⁻³]	0.419 and -0.209
<i>Z</i>	4		

9.4.5 Structures determined for Svenja Warratz (Prof. Dr. L. Ackermann)

9.4.5.1 bn_swb_040



Graphical representation of the asymmetric unit. Hydrogen atoms are omitted for clarity. The disordered isopropyl group was refined in two positions. The occupancy of the main positions refined to 0.868(18). The disorder was refined using restraints for the 1,2- and 1,3-distances and displacement parameter similarity restraints were applied.

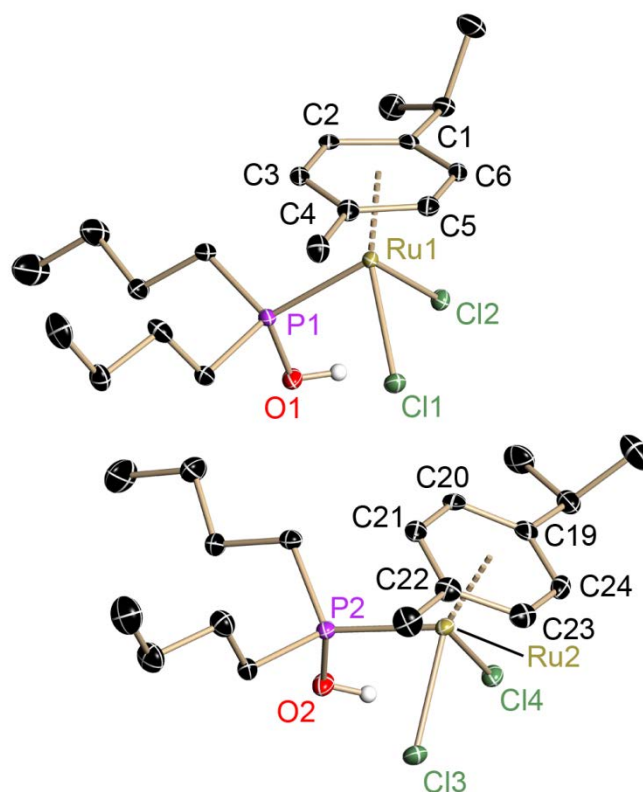
Structure published in:

Svenja Warratz, Christoph Kornhaaß, Ana Cajaraville, Benedikt Niepötter, Dietmar Stalke, and Lutz Ackermann, *Angew. Chem.* **2015**, *127*, 5604–5608; *Angew. Chem. Int. Ed.* **2015**, *54*, 5513–5517

Structural information in CIF format available with CSD number: **1044827**

Structure code	bn_swc_b040	ρ_{calc} [g cm ⁻³]	1.484
Empirical formula	C ₂₇ H ₃₀ O ₂ Ru	μ [mm ⁻¹]	0.739
Formula Weight [g mol ⁻¹]	487.58	F(000)	1008
Temperature [K]	100(2)	Crystal Size [mm]	0.14 x 0.08 x 0.05
Wavelength [Å]	0.71073	θ range [°]	1.278 to 28.731
Crystal System	Monoclinic	Reflections Collected	52106
Space Group	<i>P</i> 2 ₁ / <i>c</i>	Unique reflections	5655
Unit cell dimensions [Å]	<i>a</i> = 17.311(3)	Completeness to θ_{max} :	100.0 %
	<i>b</i> = 8.420(2)	Data/Restraints/Parameters	5655 / 88 / 289
	<i>c</i> = 16.273(2)	<i>R</i> _{int}	0.0536
	α = 90.00°	<i>R</i> 1 [<i>I</i> > 2 σ (<i>I</i>)]	0.0253
	β = 113.03(2)°	<i>wR</i> 2 (all data)	0.0613
	γ = 90.00°	<i>Goof</i>	1.056
Volume [Å ³]	2182.9(8)	Largest Diff. peak and hole [e Å ⁻³]	0.482 and -0.544
<i>Z</i>	4		

9.4.5.2 bn_swc_126

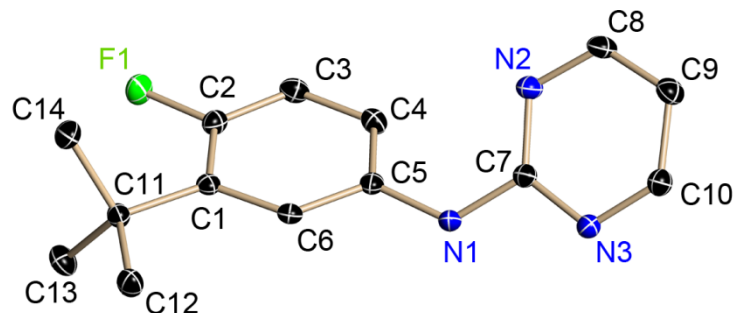


Graphical representation of the asymmetric unit. Hydrogen atoms are omitted for clarity.

Structure code	bn_swc_126	ρ_{calc} [g cm ⁻³]	1.460
Empirical formula	C ₁₈ H ₃₃ Cl ₂ OPRu	μ [mm ⁻¹]	0.560
Formula Weight [g mol ⁻¹]	468.38	F(000)	968
Temperature [K]	100(2)	Crystal Size [mm]	0.15 x 0.10 x 0.05
Wavelength [Å]	0.56086	θ range [°]	1.333 to 20.599°
Crystal System	Triclinic	Reflections Collected	66169
Space Group	$P\bar{1}$	Unique reflections	8768
Unit cell dimensions [Å]	$a = 9.191(2)$ $b = 12.646(3)$ $c = 19.372(4)$ $\alpha = 83.09(2)^\circ$ $\beta = 83.18(3)^\circ$ $\gamma = 73.13(2)^\circ$	Completeness to θ_{max} :	100.0 %
Volume [Å ³]	2130.7(9)	Data/Restraints/Parameters	8768 / 0 / 427
Z	4	R_{int}	0.0607
		$R1$ [$I > 2\sigma(I)$]	0.0317
		$wR2$ (all data)	0.0640
		$Goof$	1.020
		Largest Diff. peak and hole [e Å ⁻³]	0.886 and -0.612

9.4.6 Structure determined for Dr. Jie Li (Prof. Dr. L. Ackermann)

9.4.6.1 bn_ljf_1

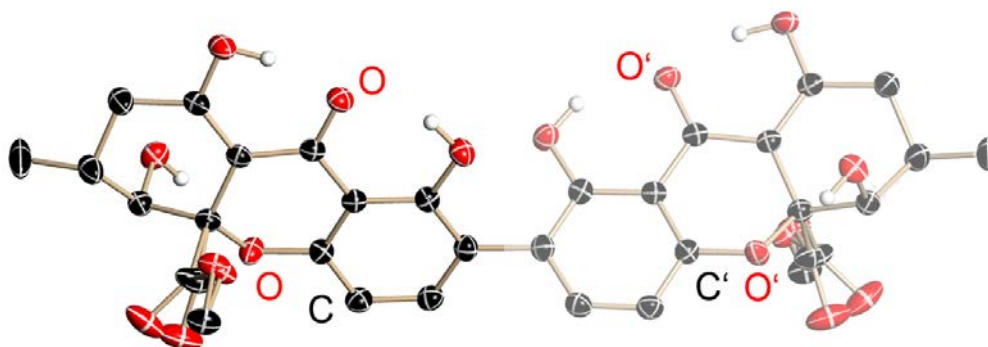


Graphical representation of the asymmetric unit. Hydrogen atoms are omitted for clarity.

Structure code	bn_ljf_1	ρ_{calc} [g cm ⁻³]	1.299
Empirical formula	C ₁₄ H ₁₆ FN ₃	μ [mm ⁻¹]	0.090
Formula Weight [g mol ⁻¹]	245.30	F(000)	260
Temperature [K]	100(2)	Crystal Size [mm]	0.18 x 0.14 x 0.08
Wavelength [Å]	0.71073	θ range [°]	2.174 to 28.667
Crystal System	Triclinic	Reflections Collected	22324
Space Group	$P\bar{1}$	Unique reflections	3201
Unit cell dimensions [Å]	$a = 8.397(2)$	Completeness to θ_{max} :	100.0 %
	$b = 8.520(2)$	Data/Restraints/Parameters	3201 / 1 / 170
	$c = 9.695(2)$	R_{int}	0.0306
	$\alpha = 102.13(2)^\circ$	$R1$ [$I > 2\sigma(I)$]	0.0385
	$\beta = 93.70(2)^\circ$	$wR2$ (all data)	0.0969
	$\gamma = 110.64(3)^\circ$	$Goof$	0.993
Volume [Å ³]	627.3(3)	Largest Diff. peak and hole [e Å ⁻³]	0.370 and -0.206
Z	2		

9.4.7 Structure determined for Dr. Dhandapani Ganapathy (Prof. Dr. L. F. Tietze)

9.4.7.1 bn_ga_1



Graphical representation of the asymmetric unit. Hydrogen atoms, except hydroxyl groups, are omitted for clarity. The disordered ether group was refined in two positions. The occupancy of the main positions refined to 0.57(2). The disorder was refined using restraints for the 1,2- and 1,3-distances and displacement parameter similarity restraints were applied. The positions of the hydrogen atom of the hydroxyl groups were refined freely.

Structure published in:

Dhandapani Ganapathy, Johannes R. Reiner, Lorenz E. Löffler, Ling Ma, Boopathny Gnanaprakasam, Benedikt Niepötter, Ingo Köhne, Lutz F. Tietze, „Enantioselective Total Synthesis of Secalonic Acid E“, *Chem Eur. J.*, **2015**, *21*, 16807-16810

Structural information in CIF format available with CSD number: **1412118**

Structure code	bn_ga_1	ρ_{calc} [g cm ⁻³]	1.535
Empirical formula	C ₃₂ H ₃₀ O ₁₄	μ [mm ⁻¹]	0.122
Formula Weight [g mol ⁻¹]	638.56	F(000)	1336
Temperature [K]	100(2)	Crystal Size [mm]	0.23 x 0.18 x 0.16
Wavelength [Å]	0.71073	θ range [°]	1.934 to 28.723
Crystal System	Tetragonal	Reflections Collected	39946
Space Group	<i>P</i> 4 ₃ 2 ₁ 2	Unique reflections	3570
Unit cell dimensions [Å]	<i>a</i> = 8.099(2) <i>b</i> = 8.099(2) <i>c</i> = 42.124(3)	Completeness to θ_{max} :	100.0 %
	α = 90.00° β = 90.00° γ = 90.00°	Data/Restraints/Parameters	3570 / 155 / 254
Volume [Å ³]	2763.1(14)	<i>R</i> _{int}	0.0443
<i>Z</i>	4	<i>R</i> 1 [<i>I</i> > 2 σ (<i>I</i>)]	0.0389
		<i>wR</i> 2 (all data)	0.0963
		<i>Goof</i>	1.022
		Largest Diff. peak and hole [e Å ⁻³]	0.312 and -0.136

10 Appendix

10.1 Additional Information on the Refinement of 1

Table S 1: Crystallographic data for the datasets of 1. For each datasets four ways of data treatment are shown: Refinement against the refined box size with one scale factor / Refinement against the refined box size with 10 scale factors / against the 'best' integration box /corrected *.hkl file

Dataset	1-TXS-100K	1- μ S-100K	1-TXS-15K
Empirical formula	C ₃₂ H ₄₂ Mg N ₁₂	C ₃₂ H ₄₂ Mg N ₁₂	C ₃₂ H ₄₂ Mg N ₁₂
Molecular weight	691.15	691.15	691.15
Crystal size [mm]	0.26 x 0.24 x 0.13	0.16 x 0.10 x 0.06	0.26 x 0.23 x 0.18
Wavelength [Å]	0.71073	0.56086	0.6199
Crystal system	Rhombohedral	Rhombohedral	Rhombohedral
Space group	$R\bar{3}$	$R\bar{3}$	$R\bar{3}$
<i>a</i> [Å]	10.6712(5)	10.6769(5)	10.6434(5)
<i>b</i> [Å]	10.6712(5)	10.6769(5)	10.6434(5)
<i>c</i> [Å]	24.6546(12)	24.6539(12)	24.6108(12)
α [°]	90	90	90
β [°]	90	90	90
γ [°]	120	120	120
<i>V</i> [Å ³]	2431.4(2)	2433.9(2)	2414.4(2)
<i>Z</i>	1	1	1
Temperature [K]	100(2)	100(2)	15(2)
ρ [Mgm ⁻³]	1.268	1.267	1.277
μ [mm ⁻¹]	0.098	0.098	0.099
<i>F</i> (000)	990	990	990
θ -area [°]	2.354 - 52.268	2.352 - 49.987	2.483 - 52.155
Total number of reflections	113986/113986/114801/113986	34349/34349/34622/34349	71496/71496/71532/71496
Unique reflections	5973/5973/5983/5973	5046/5046/5093/5046	6030/6030/6010/6030
Unique reflections (<i>I</i> > 3 σ)	5457/5457/5422/5303	4524/4524/4511/4323	5457/5457/5421/5364
<i>R</i> _{int}	0.0267/0.0267/0.0363/0.0267	0.0167/0.0167/0.0213/0.0167	0.0299/0.0299/0.0344/0.0299
Parameters	163/172/163/163	163/172/163/163	163/172/163/163
<i>R</i> { <i>F</i> } (<i>I</i> > 3 σ)	0.0157/0.0137/0.0138/0.0131	0.0184/0.0171/0.0190/0.0162	0.0159/0.0150/0.0156/0.0147
<i>R</i> { <i>F</i> ² } (<i>I</i> > 3 σ)	0.0232/0.0163/0.0177/0.0166	0.0238/0.0216/0.0246/0.0212	0.0213/0.0198/0.0221/0.0203
<i>wR</i> { <i>F</i> } (<i>I</i> > 3 σ)	0.0145/0.0129/0.0193/0.0127	0.0188/0.0181/0.0244/0.0185	0.0188/0.0183/0.0192/0.0181
<i>wR</i> { <i>F</i> ² } (<i>I</i> > 3 σ)	0.0277/0.0244/0.0356/0.0241	0.0351/0.0335/0.0436/0.0331	0.0352/0.0341/0.0362/0.0337
Goof	3.3798/2.9880/2.0238/2.6713	3.1557/3.0147/2.7103/2.7455	2.4079/2.3310/2.1388/2.1549
Highest peak [10 ³ ·e ⁻ ·Å ⁻³]	0.283/0.154/0.121/0.132	0.264/0.160/0.202/0.135	0.237/0.217/0.192/0.192
Deepest hole [10 ³ ·e ⁻ ·Å ⁻³]	-0.152/-0.148/-0.135/-0.121	-0.188/-0.180/-0.163/-0.150	-0.195/-0.210/-0.182/-0.193

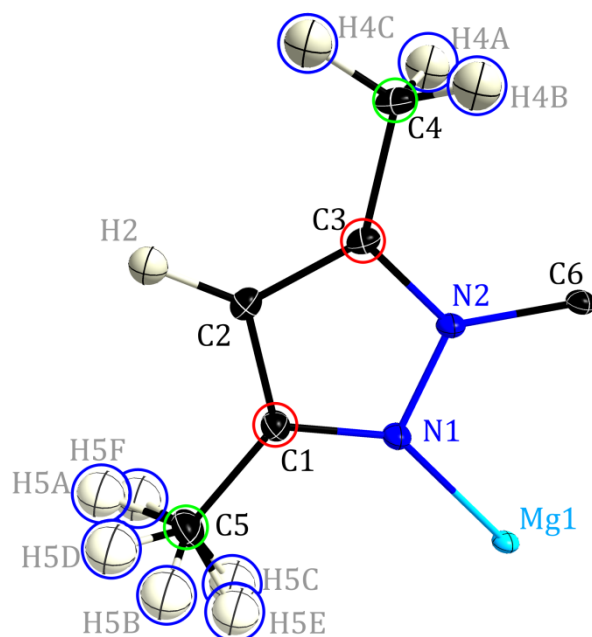


Figure S 1: Schematic representation of atoms, which share the same pole populations (Chemcon) in **1**.

Table S 2: Local symmetry restrictions of **1**

Atom	Mg1	N2	C1	C2	C4	C6	H
Symmetry	$\bar{3}$	<i>m</i>	<i>m</i>	<i>m</i>	<i>3m</i>	3	6

Table S 3: Refinement strategy. Abbreviations: *M*, monopole; *D*, dipole; *Q*, quadrupole; *O*, octopole; *H*, hexadecapole; U_{ij} , atomic displacement parameters; *XYZ*, atom positions; κ , contraction/expansion coefficient

1.	scale	12.	M
2.	M	13.	M, κ
3.	D, Q, O, H	14.	M, D, Q, O, H, U_{ij} , XYZ (non-H)
4.	M, D, Q, O, H	15.	κ
5.	U_{ij}	16.	M, D, Q, O, H, U_{ij} , XYZ (non-H), κ
6.	M, D, Q, O, H	17.	XYZ (only H)
7.	M, D, Q, O, H, U_{ij}	18.	M, D, Q, O, H, U_{ij} , XYZ (non-H)
8.	XYZ (non-H)	19.	D, Q, O, H, U_{ij} , XYZ (non-H), κ
9.	M, D, Q, O, H, XYZ (non-H)	20.	M, D, Q, O, H, U_{ij} , XYZ (non-H), κ
10.	M, D, Q, O, H, U_{ij} , XYZ (non-H)	21.	M, D, Q, O, H, U_{ij} , XYZ (non-H), κ
11.	κ		

10.2 Additional Information on the Refinement of 2

Table S 4: Crystallographic data for the datasets of 2. For each datasets four ways of data treatment are shown: Refinement against the refined box size with one scale factor / Refinement against the refined box size with 10 scale factors / against the 'best' integration box /corrected *.hkl file

Dataset	2-TXS-100K	2- μ S-100K	2-TXS-15K
Empirical formula	C26 H19 P S	C26 H19 P S	C26 H19 P S
Molecular weight	394.44	394.44	394.44
Crystal size [mm]	0.22 x 0.19 x 0.11	0.15 x 0.10 x 0.10	0.20 x 0.15 x 0.15
Wavelength [Å]	0.71073	0.56086	0.6199
Crystal system	Triclinic	Triclinic	Triclinic
Space group	$P\bar{1}$	$P\bar{1}$	$P\bar{1}$
a [Å]	10.223(2)	10.225(2)	10.213(2)
b [Å]	12.326(2)	12.336(3)	12.290(2)
c [Å]	17.357(3)	17.371(4)	17.335(3)
α [°]	101.55(2)	101.58(3)	101.62(3)
β [°]	91.23(2)	91.21(4)	91.370(2)
γ [°]	112.05(3)	111.99(4)	112.09(3)
V [Å ³]	1974.8(8)	1979.1(10)	1962.9(8)
Z	4	4	4
Temperature [K]	100(2)	100(2)	15(2)
ρ [Mgm ⁻³]	1.327	1.324	1.335
μ [mm ⁻¹]	0.254	0.253	0.255
$F(000)$	824	824	824
θ -area [°]	1.204 - 54.761	1.203 - 52.855	1.207 - 53.106
Total number of reflections	305520/305520/305404/305520	272081/272081/273150/272081	111292/111292/ /111292
Unique reflections	46690/46690/46803/46690	43292/43292/43374/43292	41237/41237/ /41237
Unique reflections ($I > 3\sigma$)	40895/40895/40673/39426	36780/36780/36617/35340	34587/34587/ /34237
R_{int}	0.0216/0.0216/0.0219/0.0216	0.0194/0.0194/0.0213/0.0194	0.0248/0.0248/ /
Parameters	720/729/720/720	720/729/720/720	720/729/ /720
$R\{F\}$ ($I > 3\sigma$)	0.0143/0.0134/0.0134/0.0125	0.0173/0.0163/0.0166/0.0150	0.0181/0.0180/ /0.0185
$R\{F^2\}$ ($I > 3\sigma$)	0.0178/0.0160/0.0167/0.0157	0.0177/0.0160/0.0174/0.0152	0.0195/0.0192/ /0.0208
$wR\{F\}$ ($I > 3\sigma$)	0.0123/0.0116/0.0116/0.0120	0.0144/0.0139/0.0166/0.0134	0.0144/0.0142/ /0.0155
$wR\{F^2\}$ ($I > 3\sigma$)	0.0239/0.0225/0.0225/0.0221	0.0271/0.0261/0.0303/0.0250	0.0280/0.0277/ /0.0302
GooF	1.8844/1.7717/1.7285/1.6139	2.0763/1.9978/2.0033/1.8588	1.2973/1.2861/ /1.2701
Highest peak [$10^3 \cdot e \cdot \text{Å}^{-3}$]	0.285/0.225/0.0224/0.202	0.382/0.311/0.326/0.284	0.260/0.259/ /0.266
Deepest hole [$10^3 \cdot e \cdot \text{Å}^{-3}$]	-0.269/-0.275/-0.271/-0.248	-0.186/-0.206/-0.235/-0.198	-0.228/-0.225/ /-0.292

10.3 Tested Boxes for Compound 1

Table S 7: Model quality indicators for different boxes for 1-TXS-100K

	Net Charge Mg (1 scale / 10 scale)	$R_2(F^2)$ (1 scale / 10 scale)	Highest Peak (1 scale / 10 scale)	Deepest Hole (1 scale / 10 scale)	e_{gross} (1 scale / 10 scale)
$x = 0.2, y = 0.2, z = 0.2$	+1.42(16)	0.0335	0.712	-0.12	26.6
$x = 0.2, y = 0.4, z = 0.4$	+1.08(13)	0.0223	0.332	-0.098	22.4
$x = 0.25, y = 0.4, z = 0.4$	+0.77(12)	0.0186	0.151	-0.114	20.7
$x = 0.3, y = 0.3, z = 0.3$	+0.50(12)	0.0185	0.124	-0.132	20.7
$x = 0.3, y = 0.4, z = 0.4$	+0.54(12)	0.0176	0.113	-0.131	20.5
$x = 0.35, y = 0.4, z = 0.4$	+0.53(11)	0.0184	0.13	-0.129	21.1
$x = 0.3, y = 0.4, z = 0.5$	+0.66(12)	0.018	0.136	-0.125	20.7
$x = 0.3, y = 0.4, z = 0.45$	+0.61(12)	0.0179	0.128	-0.128	20.5
$x = 0.3, y = 0.5, z = 0.4$	+0.60(11)	0.0176	0.124	-0.135	20.7
$x = 0.3, y = 0.45, z = 0.4$	+0.59(11)	0.0177	0.12	-0.136	20.6
$x = 0.4, y = 0.3, z = 0.4$	+0.54(12)	0.0187	0.127	-0.136	21.8
$x = 0.4, y = 0.4, z = 0.3$	+0.33(11)	0.0194	0.12	-0.185	21.4
$x = 0.4, y = 0.4, z = 0.4$	+0.62(11)	0.0181	0.128	-0.126	21.8
$x = 0.4, y = 0.4, z = 0.35$	+0.48(11)	0.0185	0.122	-0.151	21.6
$x = 0.4, y = 0.35, z = 0.4$	+0.59(11)	0.0183	0.129	-0.128	21.6
$x = 0.5, y = 0.5, z = 0.5$	+0.96(10)	0.0192	0.149	-0.131	23.3
$x = 0.6, y = 0.6, z = 0.6$	+1.20(10)	0.0203	0.146	-0.138	25.3
ref. Box	+1.57(10)	0.0232	0.28	-0.153	28.6
$\alpha = -0.15 (\sin(\theta)/\lambda)^2 + 0.60 (\sin(\theta)/\lambda)^3$	+0.82(8)	0.0168	0.132	-0.125	23.3
$\alpha = -0.15 (\sin(\theta)/\lambda)^2 + 0.70 (\sin(\theta)/\lambda)^3$	+0.78(8)	0.0166	0.130	-0.121	22.9

Table S 8: Model quality indicators for different boxes for $I-\mu S-100K$.

	Net Charge Mg (1scale / 10 scale)	R2(F2) (1scale / 10 scale)	Highest Peak (1scale / 10 scale)	Deepest Hole (1scale / 10 scale)	e_{gross} (1scale / 10 scale)
$x = 0.2, y = 0.2, z = 0.2$	+1.05(19)	0.0389	0.455	-0.219	38.0
$x = 0.3, y = 0.3, z = 0.3$	+0.36(14)	0.0285	0.19	-0.189	33.8
$x = 0.4, y = 0.4, z = 0.4$	+0.52(12)	0.0246	0.193	-0.173	32.5
$x = 0.4, y = 0.3, z = 0.3$	+0.29(14)	0.0279	0.241	-0.246	33.4
$x = 0.4, y = 0.5, z = 0.5$	+0.72(10)	0.0234	0.165	-0.179	32.9
$x = 0.5, y = 0.3, z = 0.3$	+0.48(13)	0.0272	0.226	-0.183	34.2
$x = 0.5, y = 0.4, z = 0.3$	+0.57(12)	0.0251	0.192	-0.159	33.2
$x = 0.5, y = 0.4, z = 0.5$	+0.79(10)	0.0229	0.192	-0.179	33.1
$x = 0.5, y = 0.5, z = 0.4$	+0.78(9)	0.023	0.173	-0.177	33.5
$x = 0.5, y = 0.5, z = 0.5$	+0.83(9)	0.0226	0.164	-0.186	33.5
ref. Box	+1.09(9)	0.0238	0.23	-0.186	35.3
$\alpha = 0.0 (\sin(\theta)/\lambda)^2 + 0.70 (\sin(\theta)/\lambda)^3$	+0.64(8)	0.212	0.139	-0.152	29.8

Table S 9: Model quality indicators for different boxes for 1-TXS-15K.

	Net Charge Mg (1scale / 10 scale)	R2(F2) (1scale / 10 scale)	Highest Peak (1scale / 10 scale)	Deepest Hole (1scale / 10 scale)	e_{gross} (1scale / 10 scale)
$x = 0.3, y = 0.3, z = 0.3$	+0.38(16)	0.0317	0.168	-0.22	39.2
$x = 0.4, y = 0.4, z = 0.4$	+0.08(13)	0.0256	0.158	-0.207	32.6
$x = 0.4, y = 0.5, z = 0.5$	+0.33(13)	0.0233	0.18	-0.184	31.3
$x = 0.5, y = 0.4, z = 0.5$	+0.86(13)	0.0234	0.204	-0.185	31.3
$x = 0.5, y = 0.5, z = 0.4$	+0.52(12)	0.0224	0.184	-0.177	30.5
$x = 0.5, y = 0.5, z = 0.5$	+0.73(12)	0.0219	0.192	-0.18	30.5
$x = 0.5, y = 0.5, z = 0.6$	+0.74(12)	0.0219	0.196	-0.179	30.6
$x = 0.5, y = 0.6, z = 0.4$	+0.60(11)	0.022	0.186	-0.175	30.2
$x = 0.5, y = 0.6, z = 0.5$	+0.70(12)	0.0212	0.194	-0.174	30.1
$x = 0.6, y = 0.5, z = 0.5$	+0.95(12)	0.0219	0.214	-0.186	30.8
$x = 0.6, y = 0.6, z = 0.6$	+0.89(11)	0.021	0.222	-0.191	30.4
$x = 0.7, y = 0.7, z = 0.7$	+0.96(11)	0.0208	0.221	-0.193	31.0
$x = 0.8, y = 0.8, z = 0.8$	+1.01(11)	0.0208	0.228	-0.191	30.7
ref. Box	+1.14(11)	0.0212	0.231	-0.187	31.4
$\alpha = 0.0 (\sin(\theta)/\lambda)^2 + 0.30 (\sin(\theta)/\lambda)^3$	+0.60(10)	0.0202	0.186	-0.184	29.0

10.4 Tested Boxes for Compound 2

Table S 10: Model quality indicators for different boxes for 2-TXS-100K

	Net Charge P (1scale / 10 scale)	R ² (F ₂) (1scale / 10 scale)	Highest Peak (1scale / 10 scale)	Deepest Hole (1scale / 10 scale)	e _{gross} (1scale / 10 scale)
x = 0.4, y = 0.4, z = 0.4	-1.07(6)	0.0339	0.468	-0.714	39.9
x = 0.5, y = 0.5, z = 0.5	-0.52(3)	0.0198	0.28	-0.342	30.3
x = 0.6, y = 0.6, z = 0.6	-0.10(2)	0.0167	0.228	-0.288	27.2
x = 0.5, y = 0.7, z = 0.7	-0.41(3)	0.0183	0.227	-0.299	28.8
x = 0.6, y = 0.7, z = 0.7	-0.13(2)	0.0167	0.227	-0.287	27.3
x = 0.7, y = 0.6, z = 0.7	+0.02(2)	0.0165	0.227	-0.294	27.0
x = 0.7, y = 0.7, z = 0.6	+0.08(2)	0.0166	0.227	-0.295	27.0
x = 0.7, y = 0.7, z = 0.7	+0.04(2)	0.0166	0.228	-0.295	27.0
x = 0.7, y = 0.7, z = 0.8	+0.04(2)	0.0167	0.227	-0.293	27.1
x = 0.8, y = 0.7, z = 0.7	+0.10(2)	0.0169	0.236	-0.286	27.4
x = 0.8, y = 0.8, z = 0.8	+0.14(2)	0.0171	0.23	-0.288	27.3
Ref. Box	+0.27(2)	0.0178	0.267	-0.287	27.4
$\alpha = -0.05 (\sin(\theta)/\lambda)^2 + 0.45 (\sin(\theta)/\lambda)^3$	-0.34(3)	0.0157	0.206	-0.248	26.2

Table S 11: Model quality indicators for different boxes for 2- μ S-100K.

	Net Charge P (1scale / 10 scale)	R2(F2) (1scale / 10 scale)	Highest Peak (1scale / 10 scale)	Deepest Hole (1scale / 10 scale)	e_{gross} (1scale / 10 scale)
$x = 0.2, y = 0.2, z = 0.2$	+0.76(4)	0.0389	0.903	-0.498	37.6
$x = 0.3, y = 0.3, z = 0.3$	-0.61(4)	0.0289	0.513	-0.385	32.8
$x = 0.4, y = 0.4, z = 0.4$	-0.501(4)	0.0224	0.329	-0.372	31.1
$x = 0.4, y = 0.4, z = 0.5$	-0.34(3)	0.0201	0.394	-0.291	26.9
$x = 0.4, y = 0.5, z = 0.4$	-0.48(3)	0.0207	0.296	-0.332	30.3
$x = 0.5, y = 0.4, z = 0.4$	-0.17(3)	0.0205	0.396	-0.306	30.3
$x = 0.5, y = 0.5, z = 0.5$	-0.09(3)	0.0174	0.324	-0.238	26.1
$x = 0.6, y = 0.6, z = 0.6$	+0.08(3)	0.0169	0.326	-0.207	26.6
$x = 0.7, y = 0.7, z = 0.7$	+0.14(3)	0.0171	0.372	-0.205	27.5
$x = 0.8, y = 0.8, z = 0.8$	+0.20(2)	0.0169	0.395	-0.199	27.5
Ref. Box	+0.29(2)	0.0176	0.4	-0.186	28.1
$\alpha = -0.15 (\sin(\theta)/\lambda)^2 + 0.50 (\sin(\theta)/\lambda)^3$	-0.39(3)	0.0152	0.278	-0.204	23.4

Table S 12: Model quality indicators for different boxes for 2-TXS-15K.

	Net Charge P (1scale / 10 scale)	R2(F2) (1scale / 10 scale)	Highest Peak (1scale / 10 scale)	Deepest Hole (1scale / 10 scale)	e_{gross} (1scale / 10 scale)
$x = 0.4, y = 0.4, z = 0.4$	-0.80(7)	0.0348	0.497	-0.727	36.9
$x = 0.5, y = 0.5, z = 0.5$	-0.67(6)	0.0261	0.342	-0.524	33.2
$x = 0.6, y = 0.6, z = 0.6$	-0.58(5)	0.0219	0.243	-0.384	31.6
$x = 0.7, y = 0.7, z = 0.7$	-0.45(4)	0.0199	0.254	-0.305	31.2
Ref. Box	-0.32(4)	0.0195	0.252	-0.236	31.8
$\alpha = 0.0 (\sin(\theta)/\lambda)^2 + 0.10 (\sin(\theta)/\lambda)^3$	-0.69(5)	0.0208	0.264	-0.289	31.0

10.5 Additional Information on the Refinement of 3

Table S 13: Crystallographic data for the datasets of 3. For each datasets four ways of data treatment are shown: Refinement against the refined box size with one scale factor / Refinement against the refined box size with 10 scale factors / against the 'best' integration box /corrected *.hkl file

Dataset	3
Empirical formula	C49 H77 N2 Si
Molecular weight	722.21
Crystal size [mm]	0.26 x 0.24 x 0.13
Wavelength [Å]	0.71073
Crystal system	Triclinic
Space group	P $\bar{1}$
<i>a</i> [Å]	9.303(2)
<i>b</i> [Å]	12.054(2)
<i>c</i> [Å]	19.881(3)
α [°]	95.57(3)
β [°]	98.26(2)
γ [°]	97.27(3)
<i>V</i> [Å ³]	2173.6(3)
<i>Z</i>	2
Temperature [K]	100(2)
ρ [Mgm ⁻³]	1.103
μ [mm ⁻¹]	0.088
<i>F</i> (000)	798
θ -area [°]	1.042-52.21
Total number of reflections	679314/679314/686238/679314
Unique reflections	46112/46112/46639/46112
Unique reflections (<i>I</i> > 1 σ)	43146/43146/44347/43146
<i>R</i> _{int}	0.0386/0.0386/0.0569/0.0386
Parameters	2017/2026/2017/2017
<i>R</i> { <i>F</i> } (<i>I</i> > 1 σ)	0.0267/0.0250/0.0219/0.0223
<i>R</i> { <i>F</i> ² } (<i>I</i> > 1 σ)	0.0247/0.0206/0.0239/0.0181
<i>wR</i> { <i>F</i> } (<i>I</i> > 1 σ)	0.0288/0.0271/0.0288/0.0222
<i>wR</i> { <i>F</i> ² } (<i>I</i> > 1 σ)	0.0486/0.0452/0.0464/0.0380
GooF	1.0745/0.9919/0.8094/1.0821
Highest peak [10 ³ ·e·Å ⁻³]	0.31/0.28/0.22/0.23
Deepest hole [10 ³ ·e·Å ⁻³]	-0.24/-0.22/-0.21/-0.21

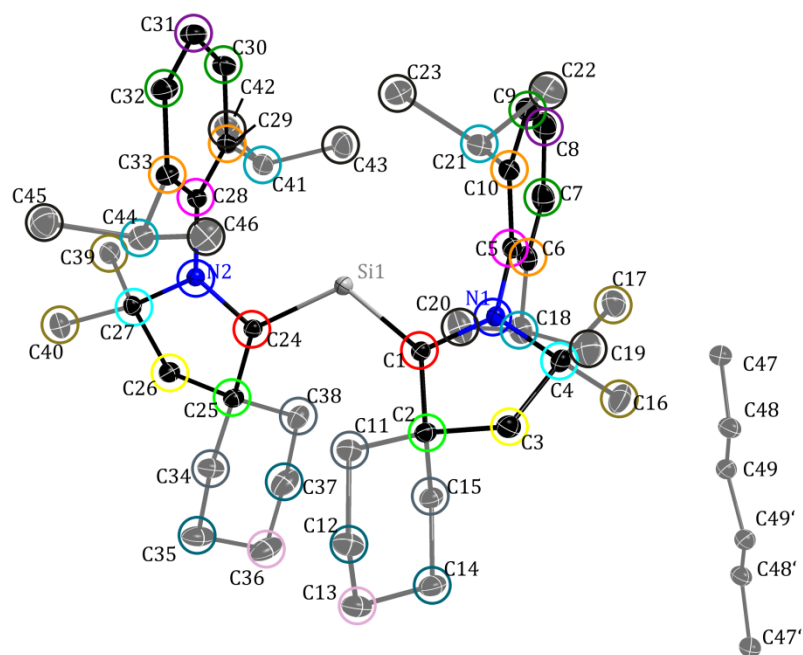


Figure S 3: Schematic representation of atoms, which share the same pole populations (Chemcon) in **3**. Additionally, two all alkyl- and all aryl-hydrogen were constrained.

Table S 14: Local symmetry restrictions of **2**

Atom	Si1	N1	C1	C2	C3	C4
Symmetry	<i>mm2</i>	<i>m</i>	<i>1</i>	<i>mm2</i>	<i>mm2</i>	<i>m</i>
Atom	C5	C6	C7	C8	C11	C12
Symmetry	<i>mm2</i>	<i>m</i>	<i>m</i>	<i>mm2</i>	<i>mm2</i>	<i>mm2</i>
Atom	C13	C16	C18	C19	C47	C48
Symmetry	<i>mm2</i>	<i>3m</i>	<i>m</i>	<i>3m</i>	<i>3m</i>	<i>mm2</i>
Atom	C49	H				
Symmetry	<i>mm2</i>	<i>6</i>				

Table S 15: Refinement strategy. Abbreviations: *M*, monopole; *D*, dipole; *Q*, quadrupole, *O*, octopole; *H*, hexadecapole; U_{ij} , atomic displacement parameters; *XYZ*, atom positions; κ/κ' , contraction/expansion coefficient; *GC*, Gram-Charlier coefficients 3rd order

1.	scale	32	M (less chemcons: two independent molecules)
2	M	33	M, D, Q, O, H, U_{ij} , XYZ (non-H), GC
3	D	34	M, D, Q, O, H, U_{ij} , XYZ (non-H), GC, κ
4	Q	35	GC (C18-C20)
5	O	36	M, D, Q, O, H, U_{ij} , XYZ (non-H), GC (C11-C15; C34-C38)
6	H	37	M, D, Q, O, H, U_{ij} , XYZ (non-H), GC
7	D, Q, O, H	38	M
8	M	39	M, D, Q, O, H, U_{ij} , XYZ (non-H), GC, κ
9	M, D, Q, O, H	40	M (no chemcons)
10	XYZ (non-H)	41	M, D, Q, O, H, U_{ij} , XYZ (non-H), GC
11	U_{ij}	42	M
12	M, D, Q, O, H	43	M, D, Q, O, H, U_{ij} , XYZ (non-H), GC, κ
13	M, D, Q, O, H, U_{ij} , XYZ (non-H)	44	GC (Si)
14	D, Q, O, H (only phenyl sym.)	45	M
15	M, D, Q, O, H, U_{ij} , XYZ (non-H)	46	M, D, Q, O, H, U_{ij} , XYZ (non-H), GC (C11-C15; C18-C20; C34-C38)
16	M	47	M, D, Q, O, H, U_{ij} , XYZ (non-H), GC (C11-C15; C18-C20; C34-C38), κ
17	κ (1-10)	48	M, D, Q, O, H, U_{ij} , XYZ (non-H), GC, κ
18	κ (11-20)	49	D, Q, O, H (no sym.)
19	M	50	M, D, Q, O, H, U_{ij} , XYZ (non-H), GC
20	κ (all)	51	M
21	GC (C34-C38)	52	κ
22	M, D, Q, O, H, U_{ij} , XYZ (non-H)	53	M, D, Q, O, H, U_{ij} , XYZ (non-H), GC, κ
23	M, D, Q, O, H, U_{ij} , XYZ (non-H), GC	54	XYZ (only H)
24	GC (C11-C15)	55	M, D, Q, O, H, U_{ij} , XYZ (non-H), GC, κ
25	M, D, Q, O, H, U_{ij} , XYZ (non-H)	56	κ'
26	M, D, Q, O, H, U_{ij} , XYZ (non-H), GC	57	D, Q, O, H
27	M	58	M
28	M, D, Q, O, H, U_{ij} , XYZ (non-H), GC, κ	59	κ'
29	XYZ (only H)	60	D, Q, O, H
30	M, D, Q, O, H, U_{ij} , XYZ (non-H), GC	61	M
31	M, D, Q, O, H, U_{ij} , XYZ (non-H), GC, κ	62	M, D, Q, O, H, U_{ij} , XYZ (non-H), GC,

63	D, Q, O, H, Uij, XYZ (non-H), GC, κ	70	XYZ (only H)
64	M, D, Q, O, H, Uij, XYZ (non-H), GC, κ	71	M, D, Q, O, H, Uij(non-H), XYZ (non-H), GC
65	M, D, Q, O, H, Uij, XYZ (non-H), GC (σ -cut-off 2)	72	M
66	M, D, Q, O, H, Uij, XYZ (non-H), GC, κ	73	κ
67	M, D, Q, O, H, Uij, XYZ (non-H), GC (σ -cut-off 1)	74	M, D, Q, O, H, Uij, XYZ (non-H), GC
68	M, D, Q, O, H, Uij, XYZ (non-H), GC, κ	75	M, D, Q, O, H, Uij, XYZ (non-H), GC, κ
69	M, D, Q, O, H, Uij, XYZ (non-H), GC, κ (shade-hydrogen)		

10.6 Tested Boxes for Compound 3

Table S 16: Model quality indicators for different boxes for 3.

	Net Charge Si (1 scale / 10 scale)	R2(F2) (1 scale / 10 scale)	Highest Peak (1 scale / 10 scale)	Deepest Hole (1 scale / 10 scale)	egross (1 scale / 10 scale)
x = 0.1, y = 0.1, z = 0.1	+2.032(18)	4.84%	0.60	-0.51	38.2
x = 0.2, y = 0.2, z = 0.2	+2.286(23)	3.27%	0.38	-0.41	28.8
x = 0.3, y = 0.3, z = 0.3	-0.397(50)	2.46%	0.31	-0.21	25.4
x = 0.3, y = 0.4, z = 0.3	-0.499(50)	2.41%	0.27	-0.19	25.5
x = 0.4, y = 0.3, z = 0.3	-0.375(48)	2.43%	0.25	-0.21	25.6
x = 0.4, y = 0.4, z = 0.2	-0.622(53)	2.80%	0.29	-0.23	29.4
x = 0.4, y = 0.4, z = 0.3	-0.440(48)	2.39%	0.22	-0.21	25.7
x = 0.4, y = 0.4, z = 0.4	-0.209(46)	2.33%	0.24	-0.21	25.7
x = 0.4, y = 0.4, z = 0.5	-0.088(45)	2.31%	0.24	-0.24	26.0
x = 0.4, y = 0.4, z = 0.6	-0.023(45)	2.33%	0.25	-0.25	26.4
x = 0.4, y = 0.5, z = 0.5	-0.138(45)	2.30%	0.25	-0.26	26.3
x = 0.5, y = 0.4, z = 0.5	+0.150(42)	2.34%	0.26	-0.25	26.2
x = 0.5, y = 0.5, z = 0.4	+0.044(43)	2.36%	0.26	-0.24	26.2
x = 0.5, y = 0.5, z = 0.5	+0.119(42)	2.32%	0.26	-0.26	26.2
x = 0.6, y = 0.6, z = 0.4	+0.222(41)	2.42%	0.25	-0.23	27.5
x = 0.6, y = 0.6, z = 0.5	+0.122(42)	2.32%	0.26	-0.24	28.2
x = 0.7, y = 0.8, z = 0.4	+0.316(40)	2.51%	0.26	-0.24	29.9
Ref. Box	+0.504(38)	2.45%	0.27	-0.27	30.5
$\alpha = -0.25 \sin(\theta)/\lambda, 2 + 0.85 \sin(\theta)/\lambda, 3$	-0.526(41)	1.81%	0.23	-0.21	25.3

10.7 Additional Information on the Properties of 3

Table S 17: Properties at the BCP

Bond	ρ_{BCP} [$e \text{ \AA}^{-3}$]	$\nabla^2\rho_{BCP}$ [$e \text{ \AA}^{-5}$]	d_{BP} [\AA]	$d1_{BP}$ [\AA]	$d2_{BP}$ [\AA]	λ_1	λ_2	λ_3	ϵ
Si(1)-C(1)	0.781(7)	5.13(3)	1.8464	0.7315	1.1149	-4.34	-2.87	12.34	0.51
Si(1)-C(24)	0.793(7)	3.22(3)	1.863	0.7365	1.1265	-4.14	-3.74	11.11	0.11
N(1)-C(1)	2.093(15)	-16.74(7)	1.3842	0.7822	0.6021	-16.93	-14.57	14.77	0.16
N(1)-C(4)	1.680(14)	-11.37(6)	1.4896	0.8415	0.648	-12.56	-12.18	13.37	0.03
N(1)-C(5)	1.887(17)	-12.90(8)	1.437	0.8102	0.6268	-14.28	-13.92	15.3	0.03
N(2)-C(24)	2.107(16)	-18.20(8)	1.372	0.8006	0.5714	-16.65	-14.68	13.13	0.13
N(2)-C(27)	1.649(14)	-12.46(6)	1.496	0.8629	0.6331	-12.72	-12.03	12.29	0.06
N(2)-C(28)	1.907(16)	-13.55(7)	1.4397	0.797	0.6427	-15.05	-14.27	15.77	0.05
C(1)-C(2)	1.636(11)	-11.08(4)	1.5324	0.7939	0.7384	-11.13	-10.7	10.75	0.04
C(2)-C(3)	1.600(11)	-11.99(4)	1.5474	0.7534	0.794	-10.77	-10.29	9.06	0.05
C(2)-C(11)	1.614(12)	-12.65(4)	1.538	0.7204	0.8176	-10.99	-10.56	8.91	0.04
C(2)-C(15)	1.591(11)	-12.99(4)	1.5531	0.7578	0.7953	-11.01	-10.64	8.66	0.03
C(3)-C(4)	1.634(12)	-13.11(4)	1.5374	0.8113	0.7261	-11.33	-10.59	8.8	0.07
C(3)-H(3A)	1.804(11)	-20.29(4)	1.0856	0.6748	0.4108	-16.37	-15.14	11.22	0.08
C(3)-H(3B)	1.838(10)	-20.43(4)	1.0851	0.6827	0.4024	-16.63	-15.49	11.68	0.07
C(4)-C(16)	1.599(12)	-13.44(4)	1.5353	0.7873	0.748	-11.26	-10.85	8.68	0.04
C(4)-C(17)	1.647(11)	-13.81(4)	1.5296	0.7559	0.7737	-11.58	-11.15	8.93	0.04
C(5)-C(6)	2.033(16)	-16.19(6)	1.4169	0.7258	0.6911	-15.65	-13.08	12.54	0.2
C(5)-C(10)	2.050(16)	-16.70(6)	1.4158	0.7352	0.6806	-16.02	-13.08	12.4	0.22
C(6)-C(7)	2.065(18)	-16.36(7)	1.3979	0.7208	0.6771	-15.89	-12.84	12.38	0.24
C(6)-C(18)	1.665(15)	-12.19(5)	1.5168	0.7428	0.774	-11.52	-11.11	10.43	0.04
C(7)-C(8)	2.12(3)	-18.66(13)	1.39	0.8044	0.5856	-15.63	-13.1	10.07	0.19
C(7)-H(7A)	1.870(16)	-21.14(6)	1.0764	0.6752	0.4012	-17.53	-16.65	13.05	0.05
C(8)-C(9)	2.193(19)	-20.73(8)	1.3909	0.7446	0.6463	-17.46	-15.05	11.78	0.16
C(8)-H(8A)	1.843(17)	-19.65(6)	1.0761	0.6741	0.402	-17.21	-15.83	13.39	0.09
C(9)-C(10)	2.113(16)	-18.29(6)	1.4004	0.6955	0.7049	-16.73	-13.76	12.19	0.22
C(9)-H(9A)	1.950(16)	-22.13(5)	1.0761	0.6943	0.3818	-18.98	-17.75	14.6	0.07
C(10)-C(21)	1.662(13)	-12.76(4)	1.5253	0.8203	0.705	-11.64	-11.34	10.23	0.03
C(11)-C(12)	1.657(12)	-14.28(4)	1.5326	0.7637	0.7689	-11.66	-11.03	8.41	0.06
C(11)-H(11A)	1.897(13)	-23.10(5)	1.0851	0.6493	0.4357	-16.66	-16.52	10.09	0.01
C(11)-H(11B)	1.874(12)	-22.60(4)	1.085	0.6828	0.4022	-17.03	-16.83	11.26	0.01
C(12)-C(13)	1.631(13)	-13.85(4)	1.5304	0.7711	0.7593	-11.13	-11.03	8.3	0.01
C(12)-H(12A)	1.771(13)	-19.59(4)	1.0851	0.6686	0.4165	-15.63	-14.85	10.88	0.05
C(12)-H(12B)	1.802(13)	-20.51(4)	1.085	0.6725	0.4125	-15.94	-15.57	11.01	0.02
C(13)-C(14)	1.701(14)	-15.68(4)	1.5291	0.7759	0.7533	-12.02	-11.94	8.27	0.01
C(13)-H(13A)	1.873(13)	-22.95(4)	1.0852	0.6798	0.4054	-17.41	-16.51	10.97	0.05

Appendix

C(13)-H(13B)	1.821(12)	-21.11(4)	1.085	0.6745	0.4105	-16.17	-15.92	10.97	0.02
C(14)-C(15)	1.659(12)	-14.32(4)	1.5319	0.7718	0.7601	-11.6	-11.12	8.4	0.04
C(14)-H(14A)	1.856(13)	-21.84(4)	1.085	0.6809	0.4041	-16.82	-16.3	11.28	0.03
C(14)-H(14B)	1.805(12)	-20.37(4)	1.0855	0.6759	0.4096	-15.99	-15.54	11.15	0.03
C(15)-H(15A)	1.866(12)	-21.96(4)	1.0851	0.6845	0.4006	-16.87	-16.6	11.52	0.02
C(15)-H(15B)	1.858(12)	-22.09(4)	1.0859	0.6836	0.4022	-17.2	-16.2	11.32	0.06
C(16)-H(16A)	1.822(11)	-20.72(4)	1.085	0.6805	0.4045	-16.41	-15.91	11.59	0.03
C(16)-H(16B)	1.756(11)	-18.47(4)	1.0851	0.6722	0.4128	-15.35	-14.6	11.49	0.05
C(16)-H(16C)	1.839(11)	-20.72(4)	1.085	0.6858	0.3993	-16.74	-15.92	11.94	0.05
C(17)-H(17A)	1.844(11)	-21.35(4)	1.0852	0.6838	0.4014	-16.69	-16.36	11.7	0.02
C(17)-H(17B)	1.800(11)	-19.65(4)	1.0851	0.6789	0.4062	-15.93	-15.37	11.65	0.04
C(17)-H(17C)	1.864(11)	-22.31(4)	1.0851	0.683	0.4022	-17.02	-16.75	11.46	0.02
C(18)-C(19)	1.589(14)	-12.38(4)	1.5315	0.7582	0.7733	-10.65	-10.37	8.65	0.03
C(18)-C(20)	1.609(14)	-13.12(4)	1.5342	0.7708	0.7634	-11.02	-10.76	8.67	0.02
C(18)-H(18A)	1.897(13)	-23.08(4)	1.085	0.6885	0.3965	-17.57	-17.2	11.7	0.02
C(19)-H(19A)	1.784(15)	-19.38(5)	1.087	0.6811	0.4059	-15.94	-15.25	11.81	0.05
C(19)-H(19B)	1.764(14)	-17.57(5)	1.0857	0.6837	0.4019	-15.53	-14.4	12.36	0.08
C(19)-H(19C)	1.704(14)	-16.71(5)	1.0862	0.6684	0.4178	-15.26	-12.98	11.53	0.18
C(20)-H(20A)	1.815(14)	-20.33(4)	1.0857	0.682	0.4037	-16.21	-15.88	11.77	0.02
C(20)-H(20B)	1.753(14)	-18.10(5)	1.0852	0.6739	0.4114	-15.42	-14.32	11.64	0.08
C(20)-H(20C)	1.721(14)	-17.84(5)	1.0851	0.6643	0.4208	-15.13	-13.84	11.13	0.09
C(21)-C(22)	1.579(12)	-12.24(4)	1.5375	0.763	0.7745	-10.51	-10.44	8.71	0.01
C(21)-C(23)	1.592(11)	-12.70(4)	1.5385	0.7592	0.7793	-10.86	-10.49	8.65	0.04
C(21)-H(21A)	1.884(11)	-22.78(4)	1.0851	0.6868	0.3983	-17.51	-16.92	11.65	0.03
C(22)-H(22A)	1.819(12)	-20.82(4)	1.0851	0.6777	0.4074	-16.24	-15.99	11.41	0.02
C(22)-H(22B)	1.829(12)	-20.95(4)	1.0852	0.6802	0.4049	-16.72	-15.81	11.57	0.06
C(22)-H(22C)	1.808(12)	-19.58(4)	1.085	0.6827	0.4023	-15.88	-15.71	12.01	0.01
C(23)-H(23A)	1.831(12)	-20.54(4)	1.0857	0.6859	0.3997	-16.74	-15.84	12.05	0.06
C(23)-H(23B)	1.732(12)	-18.25(4)	1.085	0.6648	0.4202	-15.09	-14.23	11.08	0.06
C(23)-H(23C)	1.751(12)	-17.98(4)	1.0852	0.6748	0.4104	-15.88	-13.87	11.77	0.14
C(24)-C(25)	1.627(11)	-12.24(4)	1.5379	0.8044	0.7335	-11.49	-11	10.25	0.04
C(25)-C(26)	1.573(11)	-11.91(4)	1.5481	0.7689	0.7793	-10.53	-10.26	8.88	0.03
C(25)-C(34)	1.584(12)	-12.07(4)	1.5434	0.753	0.7903	-10.67	-10.33	8.92	0.03
C(25)-C(38)	1.641(12)	-13.97(4)	1.5419	0.8005	0.7414	-11.64	-10.99	8.66	0.06
C(26)-C(27)	1.691(11)	-15.85(4)	1.5327	0.7408	0.7918	-12.27	-11.87	8.29	0.03
C(26)-H(26A)	1.861(10)	-21.44(4)	1.0852	0.685	0.4002	-16.65	-16.45	11.67	0.01
C(26)-H(26B)	1.818(10)	-20.77(4)	1.085	0.6745	0.4105	-16.05	-15.8	11.08	0.02
C(27)-C(39)	1.725(11)	-15.47(4)	1.5263	0.7818	0.7445	-12.4	-12.06	8.99	0.03
C(27)-C(40)	1.600(11)	-13.06(4)	1.5363	0.7653	0.771	-11.1	-10.73	8.78	0.04
C(28)-C(29)	2.064(15)	-17.28(5)	1.4194	0.7114	0.708	-16.32	-13.51	12.56	0.21

C(28)-C(33)	2.051(15)	-15.65(5)	1.4131	0.7187	0.6944	-15.55	-12.98	12.88	0.2
C(29)-C(30)	2.142(15)	-19.37(6)	1.3956	0.6842	0.7114	-17.22	-14.13	11.98	0.22
C(29)-C(41)	1.667(12)	-12.17(4)	1.5248	0.7741	0.7508	-11.55	-11.3	10.68	0.02
C(30)-C(31)	2.142(19)	-19.27(9)	1.389	0.7791	0.6099	-16.38	-13.61	10.73	0.2
C(30)-H(30A)	1.906(15)	-21.59(5)	1.076	0.6832	0.3928	-18.23	-17.06	13.7	0.07
C(31)-C(32)	2.17(2)	-19.55(10)	1.3882	0.8089	0.5793	-16.33	-13.5	10.28	0.21
C(31)-H(31A)	1.905(15)	-21.84(5)	1.076	0.681	0.3951	-18.03	-17.25	13.44	0.05
C(32)-C(33)	2.108(15)	-18.44(6)	1.4024	0.7133	0.6891	-16.42	-14.2	12.18	0.16
C(32)-H(32A)	1.905(15)	-21.02(5)	1.0762	0.6864	0.3898	-17.83	-17.36	14.16	0.03
C(33)-C(44)	1.694(12)	-13.37(4)	1.5198	0.8276	0.6922	-12.13	-11.36	10.13	0.07
C(34)-C(35)	1.632(13)	-14.34(4)	1.5325	0.7408	0.7918	-11.63	-10.8	8.09	0.08
C(34)-H(34A)	1.843(14)	-21.07(5)	1.0857	0.6466	0.4391	-15.88	-15.45	10.26	0.03
C(34)-H(34B)	1.849(13)	-21.64(4)	1.0855	0.6833	0.4021	-16.95	-16.19	11.51	0.05
C(35)-C(36)	1.745(19)	-16.14(5)	1.5329	0.745	0.7879	-12.72	-11.89	8.47	0.07
C(35)-H(35A)	1.820(14)	-21.30(5)	1.085	0.6741	0.4109	-16.38	-15.81	10.9	0.04
C(35)-H(35B)	1.739(14)	-18.55(5)	1.0853	0.6659	0.4194	-14.92	-14.53	10.9	0.03
C(36)-C(37)	1.616(18)	-13.68(5)	1.528	0.7705	0.7575	-11.28	-10.61	8.22	0.06
C(36)-H(36A)	1.751(14)	-19.47(5)	1.085	0.6613	0.4237	-15.25	-14.59	10.36	0.05
C(36)-H(36B)	1.783(15)	-20.30(5)	1.0856	0.6701	0.4155	-16.27	-14.78	10.75	0.1
C(37)-C(38)	1.625(14)	-12.95(4)	1.529	0.7569	0.772	-10.86	-10.57	8.49	0.03
C(37)-H(37A)	1.870(14)	-21.94(5)	1.085	0.6864	0.3986	-17.01	-16.55	11.61	0.03
C(37)-H(37B)	1.772(15)	-19.18(5)	1.0853	0.6724	0.4129	-15.43	-14.91	11.15	0.04
C(38)-H(38A)	1.893(13)	-22.82(4)	1.0852	0.6897	0.3955	-17.57	-16.93	11.68	0.04
C(38)-H(38B)	1.859(12)	-22.02(4)	1.0851	0.6821	0.403	-17.03	-16.33	11.34	0.04
C(39)-H(39A)	1.871(10)	-22.14(4)	1.0851	0.6857	0.3994	-17.44	-16.36	11.67	0.07
C(39)-H(39B)	1.865(11)	-22.04(4)	1.0851	0.6842	0.4009	-17.16	-16.52	11.63	0.04
C(39)-H(39C)	1.892(10)	-22.26(4)	1.0853	0.6934	0.3918	-17.55	-16.88	12.16	0.04
C(40)-H(40A)	1.825(11)	-21.47(4)	1.0851	0.6765	0.4085	-16.5	-16.26	11.3	0.01
C(40)-H(40B)	1.824(11)	-20.48(4)	1.0851	0.6814	0.4036	-16.46	-15.73	11.7	0.05
C(40)-H(40C)	1.845(11)	-20.97(4)	1.085	0.6855	0.3995	-16.55	-16.32	11.91	0.01
C(41)-C(42)	1.589(11)	-12.07(4)	1.5387	0.7623	0.7765	-10.6	-10.4	8.93	0.02
C(41)-C(43)	1.580(12)	-12.65(4)	1.5409	0.7895	0.7514	-10.95	-10.27	8.57	0.07
C(41)-H(41A)	1.878(11)	-22.55(4)	1.0851	0.686	0.399	-17.45	-16.73	11.63	0.04
C(42)-H(42A)	1.913(11)	-22.48(4)	1.0851	0.6983	0.3868	-17.59	-17.42	12.53	0.01
C(42)-H(42B)	1.786(12)	-19.35(4)	1.0862	0.6783	0.4078	-15.87	-15.26	11.78	0.04
C(42)-H(42C)	1.728(12)	-18.41(4)	1.0852	0.6616	0.4236	-15.15	-14.18	10.92	0.07
C(43)-H(43A)	1.830(12)	-19.93(4)	1.085	0.6888	0.3962	-16.43	-15.87	12.37	0.04
C(43)-H(43B)	1.781(12)	-18.58(4)	1.0852	0.6803	0.4049	-15.65	-14.93	12	0.05
C(43)-H(43C)	1.639(12)	-15.36(4)	1.0852	0.6526	0.4326	-13.3	-12.91	10.85	0.03
C(44)-C(45)	1.581(11)	-12.87(4)	1.5364	0.7696	0.7667	-10.79	-10.5	8.43	0.03

Appendix

C(44)-C(46)	1.581(11)	-12.04(4)	1.54	0.7859	0.7541	-10.51	-10.34	8.81	0.02
C(44)-H(44A)	1.983(10)	-24.84(4)	1.0855	0.7062	0.3792	-18.85	-18.61	12.63	0.01
C(45)-H(45A)	1.820(11)	-20.62(4)	1.0853	0.6837	0.4016	-16.62	-15.96	11.96	0.04
C(45)-H(45B)	1.780(11)	-19.21(4)	1.0852	0.675	0.4103	-15.74	-14.94	11.48	0.05
C(45)-H(45C)	1.768(11)	-18.05(4)	1.0878	0.6855	0.4023	-15.74	-14.76	12.45	0.07
C(46)-H(46A)	1.799(11)	-19.91(4)	1.0852	0.6768	0.4083	-16.24	-15.2	11.53	0.07
C(46)-H(46B)	1.786(11)	-19.88(4)	1.0852	0.6757	0.4095	-15.92	-15.47	11.5	0.03
C(46)-H(46C)	1.787(11)	-19.52(4)	1.0857	0.6774	0.4083	-15.83	-15.32	11.63	0.03
C(47)-C(48)	1.637(12)	-15.01(4)	1.5236	0.7752	0.7484	-11.51	-10.26	6.77	0.12
C(47)-H(47A)	1.714(13)	-19.90(5)	1.0883	0.6377	0.4506	-14.18	-13.71	8	0.03
C(47)-H(47B)	1.654(13)	-16.16(5)	1.0861	0.6379	0.4482	-13.24	-11.77	8.86	0.13
C(47)-H(47C)	1.673(13)	-18.76(5)	1.0852	0.6287	0.4565	-13.98	-12.98	8.19	0.08
C(48)-C(49)	1.705(12)	-17.08(4)	1.5245	0.7512	0.7734	-12.01	-11.43	6.36	0.05
C(48)-H(48A)	1.697(12)	-17.73(5)	1.0851	0.6432	0.4419	-13.76	-12.94	8.97	0.06
C(48)-H(48B)	1.610(13)	-15.99(5)	1.0852	0.6154	0.4698	-12.49	-11.17	7.67	0.12
C(49)-H(49A)	1.657(12)	-17.55(5)	1.0884	0.6341	0.4544	-14.02	-11.79	8.26	0.19
C(49)-H(49B)	1.720(12)	-17.52(4)	1.0861	0.6551	0.4311	-14.45	-12.75	9.69	0.13

Table S 18: Integrated Bader charges.

Atom	Bader Charge [e]	Atom	Bader Charge [e]	Atom	Bader Charge [e]	Atom	Bader Charge [e]
Si1	1.24	C31	0.00	H(15B)	0.00	H(37B)	0.01
N1	-0.89	C32	0.18	H(16A)	0.01	H(38A)	0.00
N2	-0.92	C33	0.02	H(16B)	0.03	H(38B)	-0.01
C1	-0.42	C34	0.04	H(16C)	0.02	H(39A)	0.00
C2	0.08	C35	0.09	H(17A)	0.01	H(39B)	-0.01
C3	-0.17	C36	0.08	H(17B)	0.03	H(39C)	0.02
C4	0.40	C37	0.03	H(17C)	-0.01	H(40A)	0.00
C5	0.20	C38	-0.03	H(18A)	0.00	H(40B)	0.02
C6	0.05	C39	-0.08	H(19A)	0.03	H(40C)	0.01
C7	-0.04	C40	-0.05	H(19B)	0.06	H(41A)	-0.01
C8	0.16	C41	-0.04	H(19C)	0.04	H(42A)	0.03
C9	0.11	C42	-0.17	H(20A)	0.02	H(42B)	0.03
C10	0.02	C43	-0.04	H(20B)	0.02	H(42C)	0.01
C11	-0.06	C44	-0.05	H(20C)	0.02	H(43A)	0.04
C12	0.00	C45	-0.11	H(21A)	-0.01	H(43B)	0.02
C13	0.05	C46	0.02	H(22A)	0.01	H(43C)	0.03
C14	0.01	C47	0.26	H(22B)	0.01	H(44A)	0.01
C15	-0.04	C48	0.28	H(22C)	0.03	H(45A)	0.02
C16	0.05	C49	-0.01	H(23A)	0.01	H(45B)	0.02
C17	-0.03	H(3A)	0.00	H(23B)	0.02	H(45C)	0.05
C18	-0.01	H(3B)	0.01	H(23C)	0.04	H(46A)	0.00
C19	-0.15	H(7A)	-0.04	H(26A)	0.00	H(46B)	0.02
C20	-0.01	H(7B)	-0.01	H(26B)	-0.01	H(46C)	0.02
C21	0.14	H(9A)	0.00	H(30A)	-0.03	H(47A)	-0.09
C22	-0.09	H(11A)	-0.11	H(31A)	-0.03	H(47B)	-0.05
C23	-0.07	H(11B)	-0.01	H(32A)	-0.01	H(47C)	-0.09
C24	-0.31	H(12A)	0.00	H(34A)	-0.09	H(48A)	-0.06
C25	0.04	H(12B)	0.00	H(34B)	0.00	H(48B)	-0.08
C26	0.01	H(13A)	-0.01	H(35A)	-0.01	H(49A)	-0.08
C27	0.35	H(13B)	0.00	H(35B)	0.01	H(49B)	-0.04
C28	0.22	H(14A)	0.00	H(36A)	-0.01		
C29	0.07	H(14B)	0.00	H(36B)	0.01		
C30	-0.17	H(15A)	0.00	H(37A)	0.00		

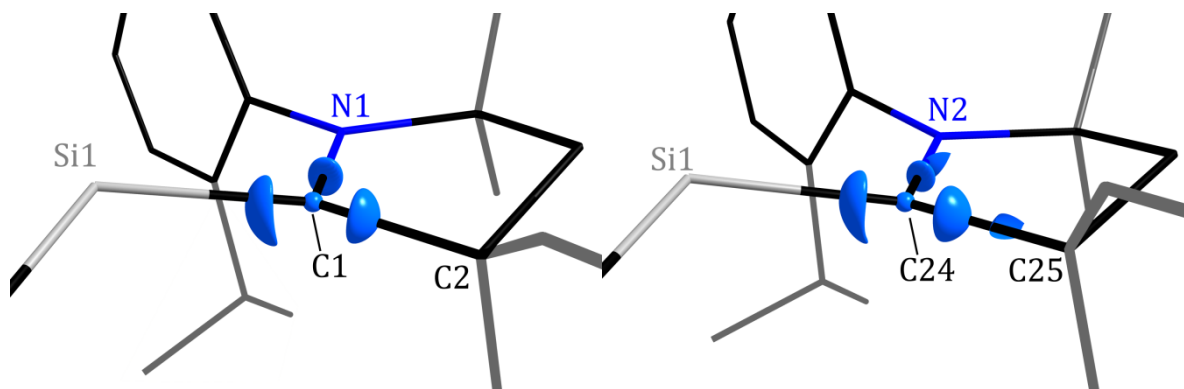


Figure S 4: Laplacian distribution around the carbene carbon atoms (C1 and C24) of **3** at an isolevel of $-15 e \cdot \text{\AA}^{-5}$.

Table S 19: VSCCs for selected atoms.

Atom	$\nabla^2\rho [e \text{\AA}^{-5}]$	VSCC distance [\AA]	direction
Si(1)	-2.7771	0.9059	-
	-2.7637	0.9057	-
C(1)	-25.8019	0.4886	C(2)
	-22.4253	0.4886	N(1)
	-25.9964	0.4791	Si(1)
C(24)	-24.3211	0.4833	Si(1)
	-27.2528	0.4889	C(25)
	-19.7932	0.4912	N(2)
N(1)	-55.5875	0.4045	C(4)
	-53.2475	0.4053	C(1)
	-60.5754	0.4020	C(5)
N(2)	-55.7296	0.4055	C(28)
	-59.3220	0.4013	C(24)
	-60.2104	0.4035	C(27)

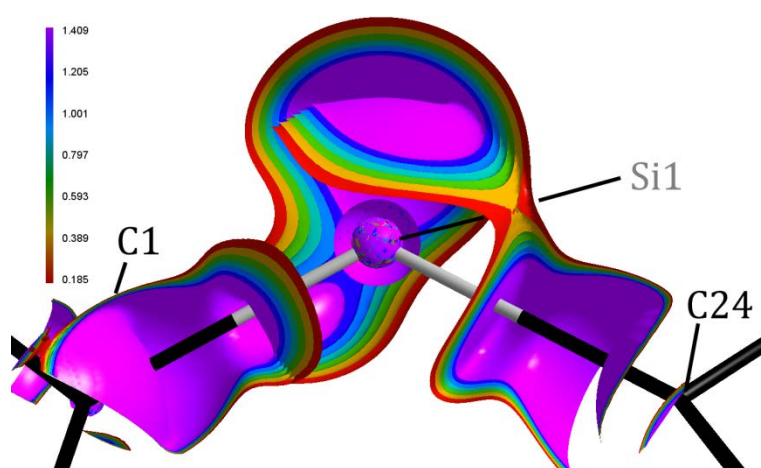


Figure S 5: Laplacian distribution at Si1 at multiple isosurface levels.

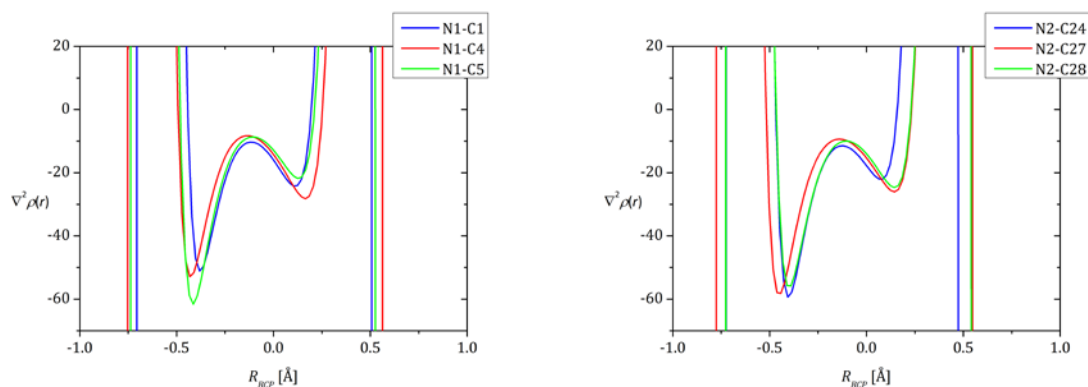


Figure S 6: Laplacian along the bond path N–C bonds in **3**.

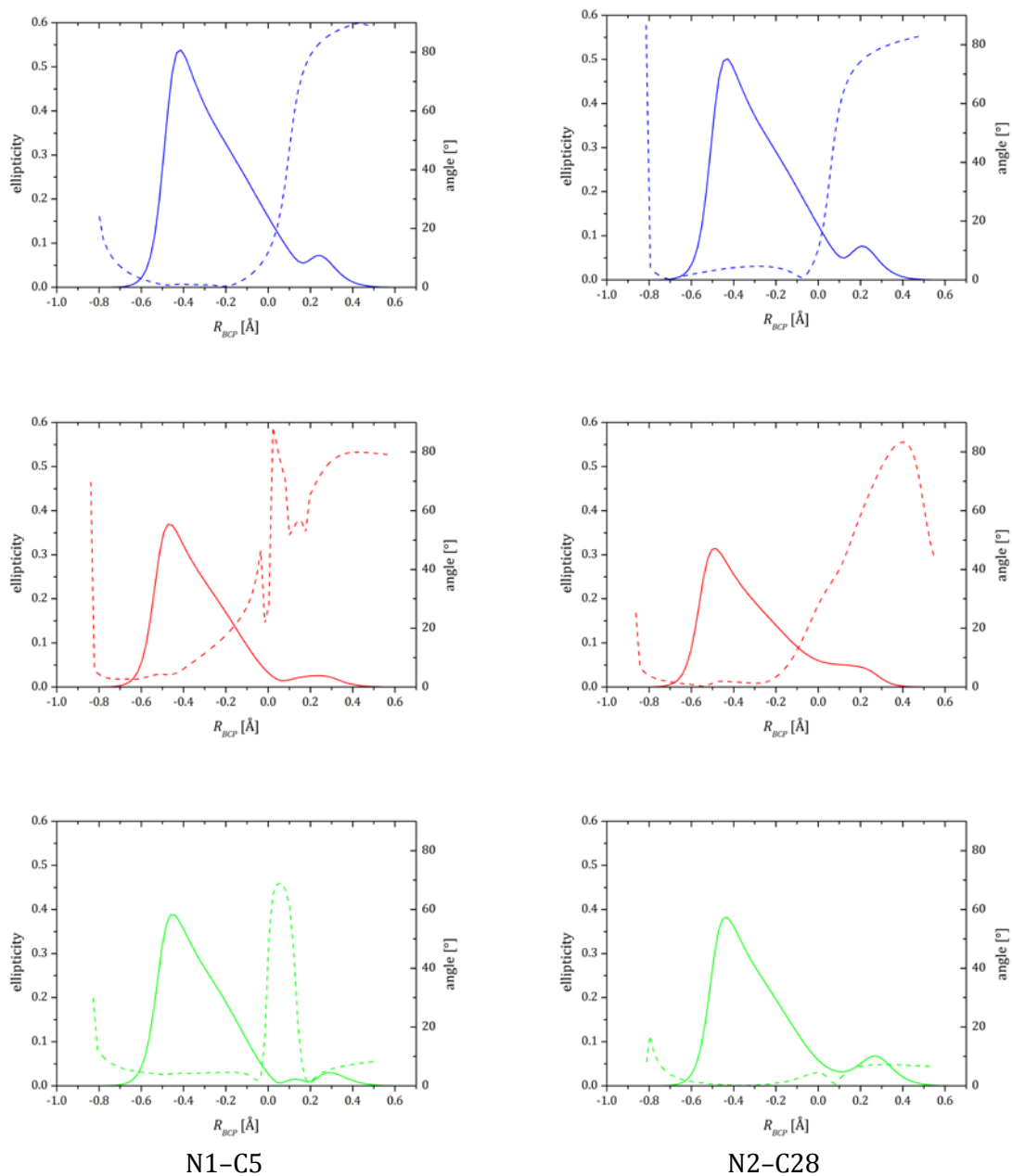


Figure S 7: Ellipticity (solid line) and angle of the major axis (dashed line) along the bond path of N1/2-C5/28 bonds in **3**.

10.8 Properties of the EDD of **3** without Corrections

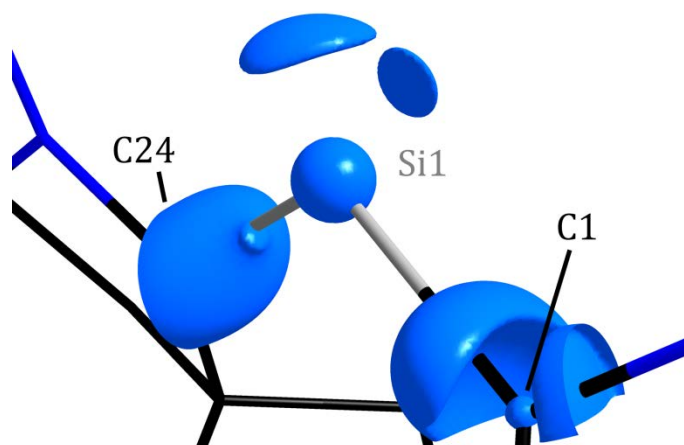


Figure S 8: Laplacian distribution around the silicon atoms of **3** at an isolevel of $-2.5 e\text{-}\text{\AA}^{-5}$. Non-bonding VSCCs highlighted.

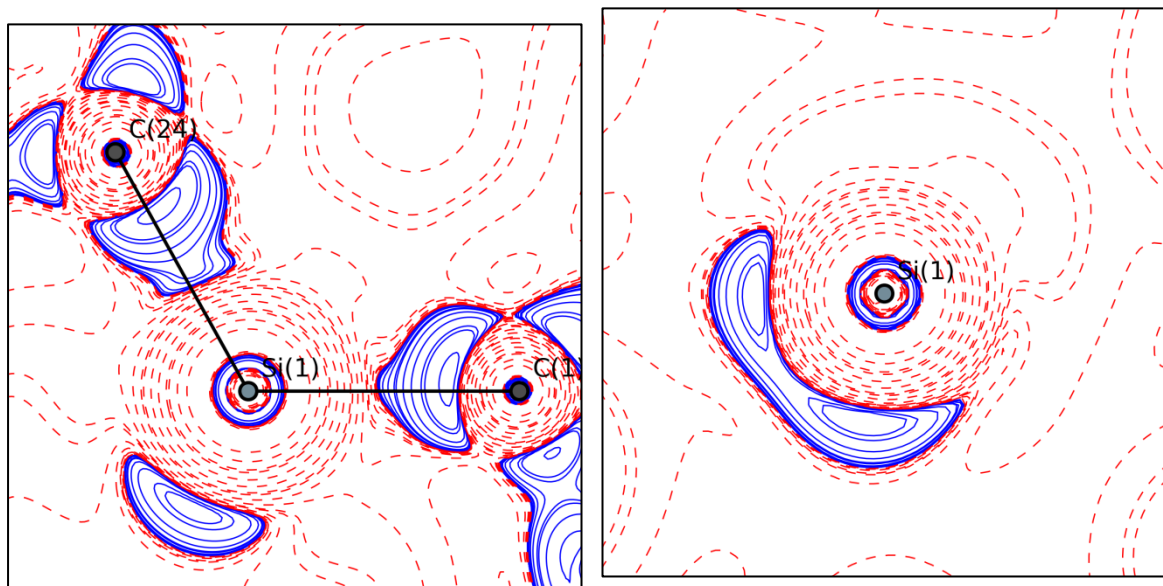


Figure S 9: Laplacian distribution in the C1-Si1-C24 plane (a) and orthogonal to the C1-C24 vector (b). Charge concentration depicted in blue solid lines, depletion in red dashed lines. Contour levels drawn at $\pm 1 \cdot 10^n, \pm 2 \cdot 10^n, \pm 4 \cdot 10^n, \pm 8 \cdot 10^n$ ($-2 \leq n \leq 4$)

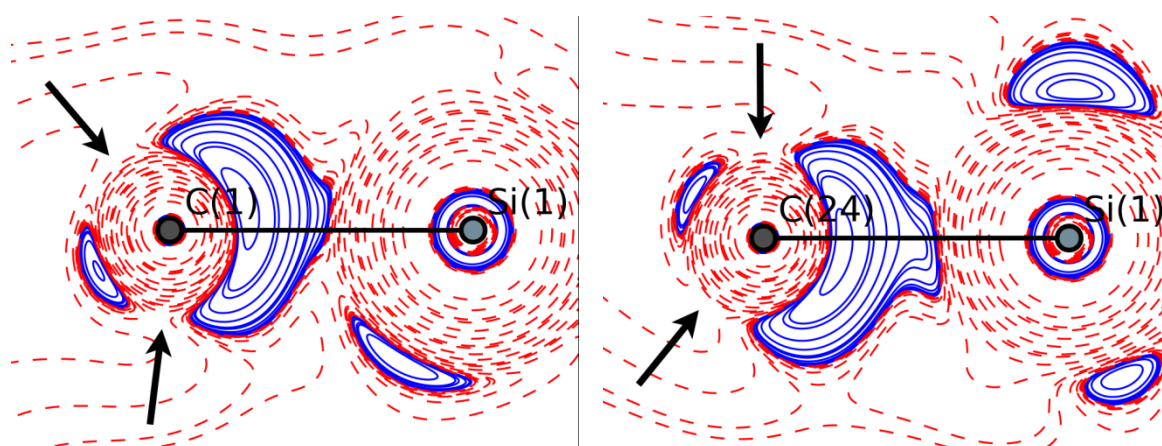


Figure S 10: Laplacian distribution in **3** in the plane perpendicular to the C1–C2–N1–Si1 mean plane (a) and C24–C24–N2–Si1 mean plane (b), respectively. Charge concentration depicted in blue solid lines, depletion in red dashed lines. Contour levels drawn at $\pm 1 \cdot 10^n$, $\pm 2 \cdot 10^n$, $\pm 4 \cdot 10^n$, $\pm 8 \cdot 10^n$ ($-2 \leq n \leq 4$). The arrows show the hole in charge concentration surrounding the carbene atom.

Table S 20: VSCCs for selected atoms.

Atom	$\nabla^2 \rho$ [$e \text{ \AA}^{-5}$]	VSCC	
		distance [\AA]	direction
Si(1)	-1.4651	0.8922	-
	-1.3882	0.8921	-
C(1)	-25.8484	0.4916	C(2)
	-24.4047	0.4874	N(1)
	-27.2445	0.4771	Si(1)
C(24)	-25.3565	0.4793	Si(1)
	-22.2588	0.4912	N(2)
	-26.9367	0.4928	C(25)
N(1)	-54.8349	0.4052	C(4)
	-51.8996	0.4058	C(1)
	-62.2970	0.4021	C(5)
N(2)	-56.4378	0.4056	C(28)
	-59.6316	0.4022	C(24)
	-59.4504	0.4043	C(27)

Table S 21: Properties of the ED at the Si–C BCPs of **3** and in $R\text{SiCl}_2\text{Me-cAACH}^{[224]}$. The total electronic energy density and the relative kinetic energy were calculated from the ED and the Laplacian according to Abramov^[98]

Bond	d_{BP} [\AA]	$d1_{\text{BP}}$ [\AA]	$d2_{\text{BP}}$ [\AA]	ρ_{BCP} [$e \text{ \AA}^{-3}$]	$\nabla^2 \rho_{\text{BCP}}$ [$e \text{ \AA}^{-5}$]	H_{BCP} [a.u.]	$G_{\text{BCP}} / \rho_{\text{BCP}}$	ϵ	η
Si1–C1	1.84634	0.8136	1.0327	0.845(9)	0.86(3)	-0.59	0.77	0.37	0.52
Si1–C24	1.86372	0.8235	1.0391	0.836(7)	-0.54(3)	-0.62	0.69	0.06	0.55

Table S 22: Integrated Bader charges for selected atoms.

Atom	Si1	C1	C24
Bader charge [e]	1.04	-0.08	0.11

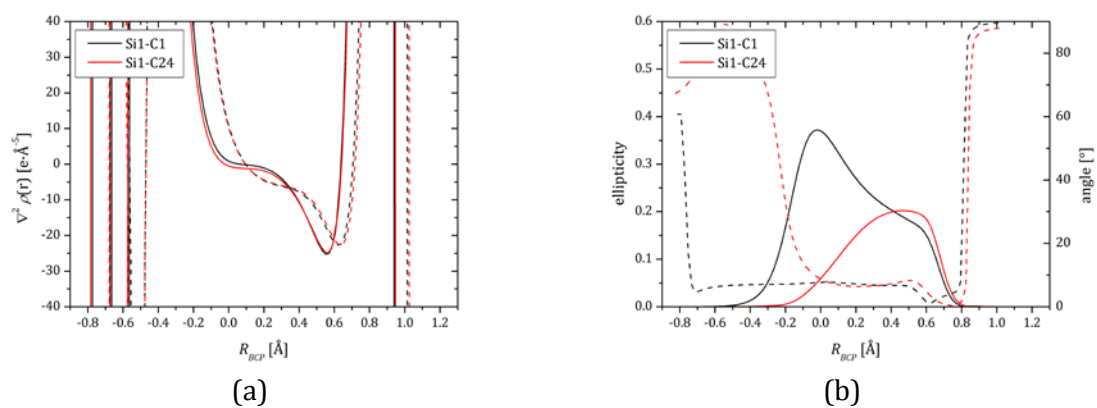


Figure S 11: (a) Laplacian along the Si–C bonds. Values of the experimental analysis are shown as solid lines; values of the theoretical analysis are shown as dashed lines. (b) Ellipticity (solid line) and angle of the major axis (dashed line) along the bond path of Si–C bonds.

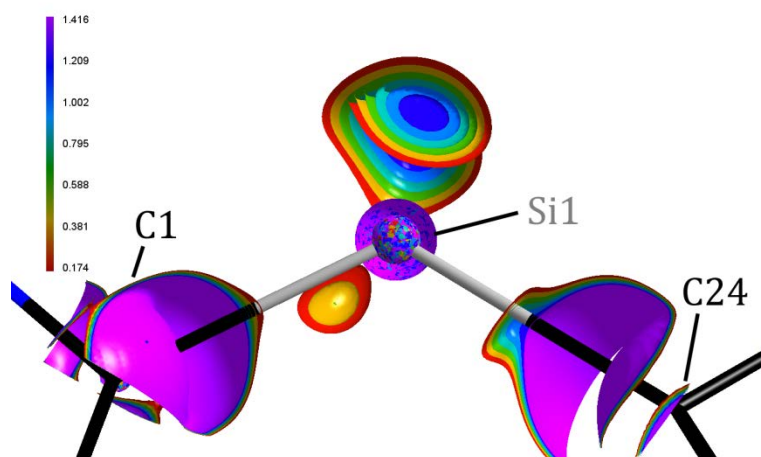
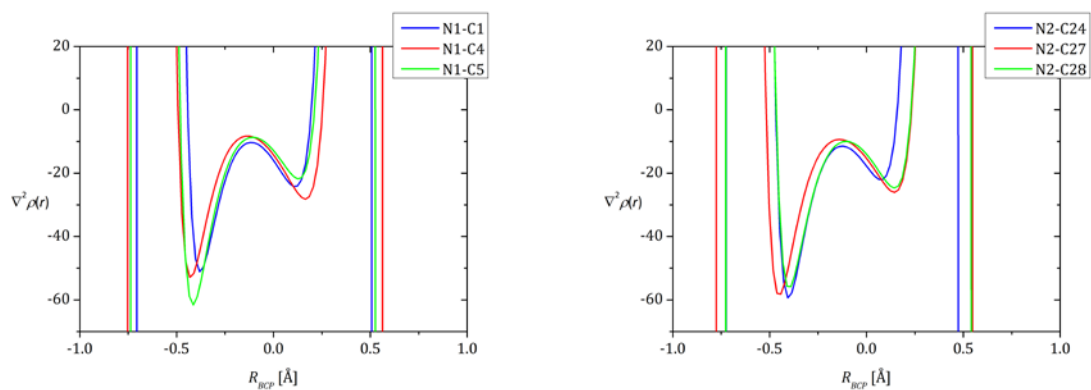


Figure S 12: Laplacian distribution at Si1 at multiple isosurface levels.

Table S 23: Properties of the ED at the N-C BCPs of **3**.

Bond	d_{BP} [Å]	$d1_{BP}$ [Å]	$d2_{BP}$ [Å]	ρ_{BCP} [$e \cdot \text{Å}^{-3}$]	$\nabla^2 \rho_{BCP}$ [$e \cdot \text{Å}^{-5}$]	ϵ	η
N1-C1	1.3843	0.7846	0.5997	2.106(16)	-15.93(7)	0.14	1.04
N1-C4	1.4895	0.8334	0.6561	1.803(14)	-14.18(6)	0.02	1.06
N1-C5	1.4372	0.8183	0.6189	1.902(19)	-12.84(8)	0.01	0.89
N2-C24	1.3718	0.8051	0.5668	2.118(17)	-17.73(8)	0.09	1.12
N2-C27	1.4959	0.8554	0.6405	1.762(14)	-15.29(6)	0.03	1.16
N2-C28	1.4399	0.8061	0.6338	1.921(17)	-13.97(7)	0.02	0.93

**Figure S 13:** Laplacian along the N-C bonds in **3**.

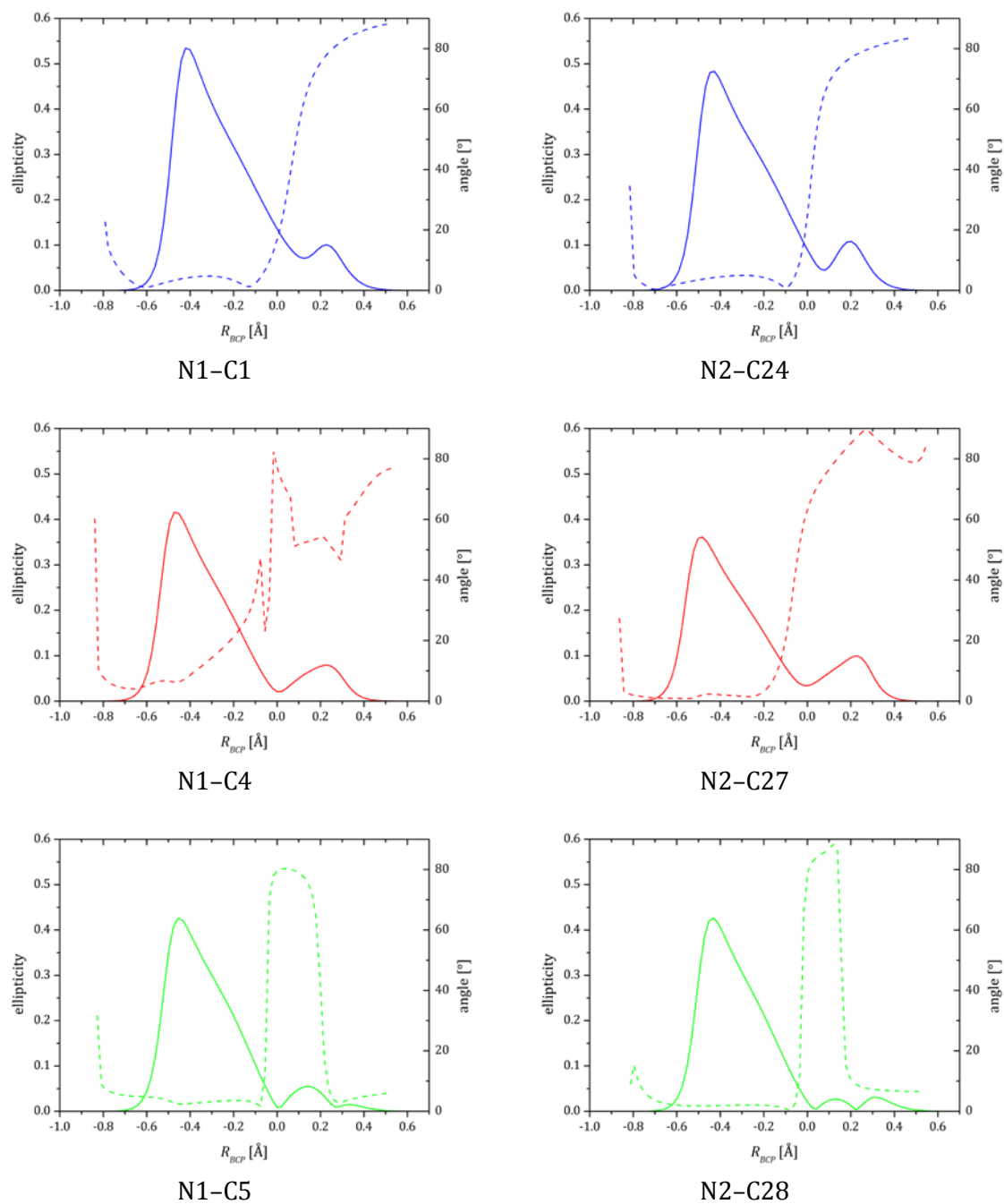


Figure S 14: Ellipticity (solid line) and angle of the major axis (dashed line) along the bond path of N-C bonds in **3**.

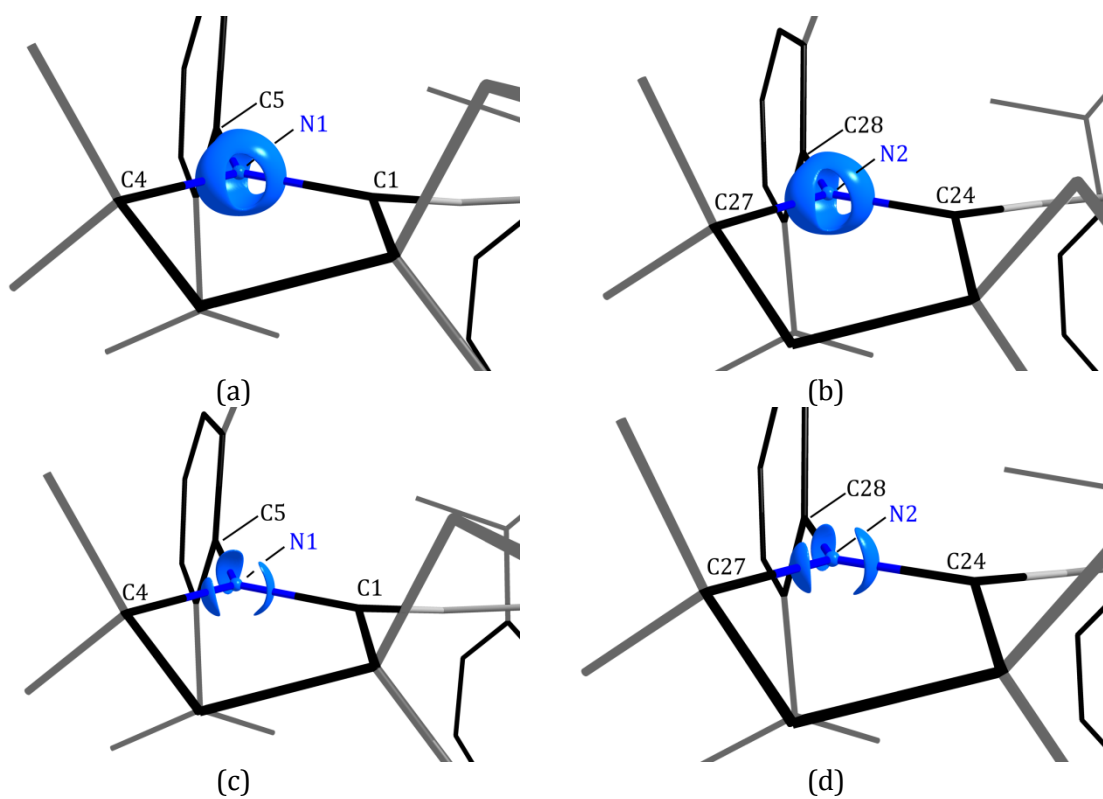


Figure S 15: Laplacian distribution at N1 (a, c) and N2 (b, d) atoms of 3 at an isosurface level of $-30 e \cdot \text{\AA}^{-5}$ (a, b) and $-45 e \cdot \text{\AA}^{-5}$ (c, d).

10.9 Refinement Strategy for Cross-Validation of 3

Table S 15: Refinement strategy. Abbreviations: *M*, monopole; *D*, dipole; *Q*, quadrupole, *O*, octopole; *H*, hexadecapole; U_{ij} , atomic displacement parameters; *XYZ*, atom positions; κ/κ' , contraction/expansion coefficient; *GC*, Gram-Charlier coefficients 3rd order

1.	scale	10	M, D, Q, O, H, U_{ij} , XYZ (non-H), κ
2	M	11	M, D, Q, O, H, U_{ij} , XYZ (non-H), κ (σ -cut-off 1)
3	M, D, Q, O, H	12	M, D, Q, O, H, U_{ij} , XYZ (non-H), κ , GC
4	M, D, Q, O, H, U_{ij}	13	M, D, Q, O, H, U_{ij} , XYZ (non-H), κ , GC (Si: $mm2 \rightarrow m$)
5	M, D, Q, O, H, U_{ij} , XYZ (non-H)	14	M, D, Q, O, H, U_{ij} , XYZ (non-H), κ , GC (Si: $m \rightarrow 1$)
6	M, D, Q, O, H, U_{ij} , XYZ (non-H), κ	15	M, D, Q, O, H, U_{ij} , XYZ (non-H), κ , GC (cyclohexyl: $mm2 \rightarrow m$)
7	XYZ (only H)	16	M, D, Q, O, H, U_{ij} , XYZ (non-H), κ , GC (no chemcon between heterocycle)
8	M, D, Q, O, H, U_{ij} , XYZ (non-H), κ	17	M, D, Q, O, H, U_{ij} , XYZ (non-H), κ , GC (no symmetry)
9	κ'	18	M, D, Q, O, H, U_{ij} , XYZ (non-H), κ , GC (no chemcons)

10.10 Properties of the EDD of **3** with Chemcons

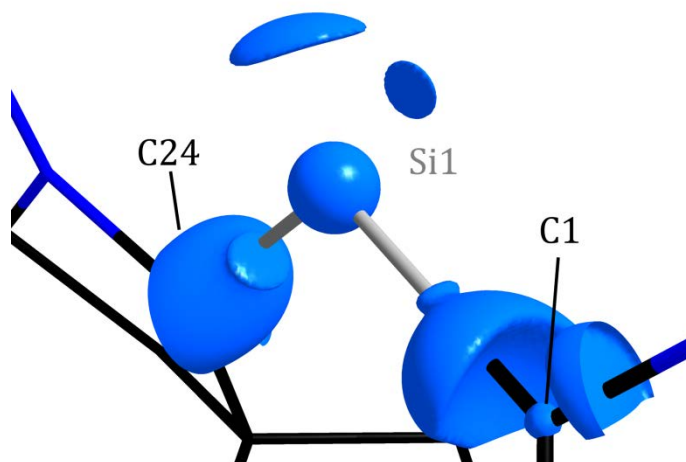


Figure S 16: Laplacian distribution around the silicon atoms of **3** at an isolevel of $-2.5 e \cdot \text{\AA}^{-5}$. Non-bonding VSCCs highlighted.

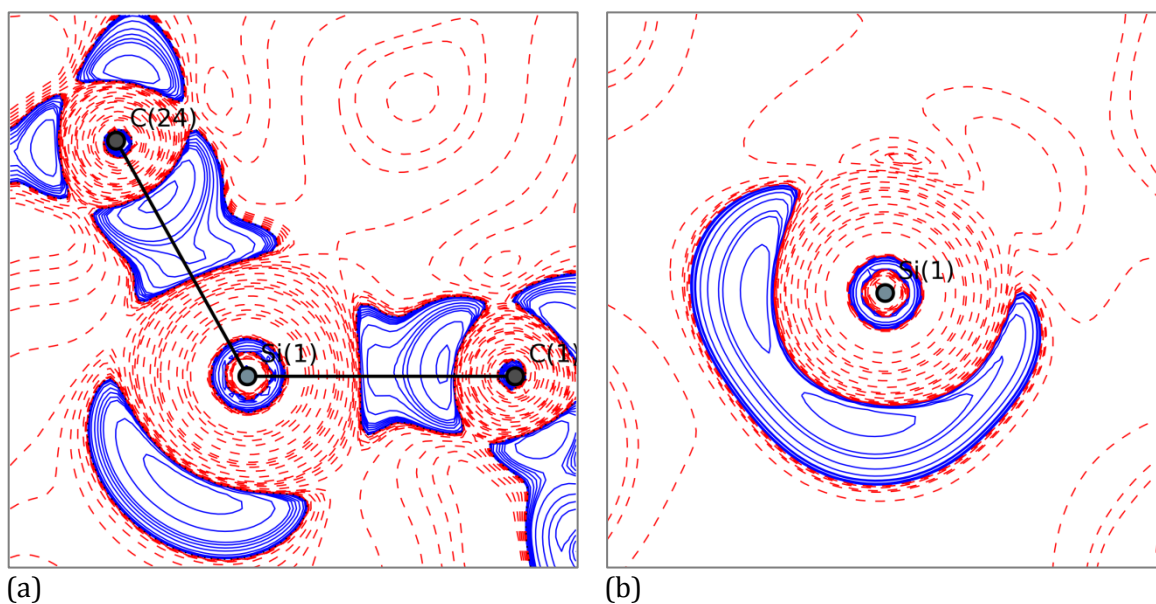


Figure S 17: Laplacian distribution in the C1-Si1-C24 plane (a) and orthogonal to the C1-C24 vector (b). Charge concentration depicted in blue solid lines, depletion in red dashed lines. Contour levels drawn at $\pm 1 \cdot 10^n, \pm 2 \cdot 10^n, \pm 4 \cdot 10^n, \pm 8 \cdot 10^n$ ($-2 \leq n \leq 4$)

Table S 24: VSCCs for selected atoms.

Atom	$\nabla^2\rho$ [$e \text{ \AA}^{-5}$]	VSCC distance [\AA]	direction
Si(1)	-1.8586	0.9094	-
	-2.9359	0.8953	-
C(1)	-27.2002	0.4881	C(2)
	-21.4568	0.4893	N(1)
	-25.0090	0.4800	Si(1)
C(24)	-25.0629	0.4802	Si(1)
	-21.4184	0.4896	N(2)
	-27.1568	0.4880	C(25)
N(1)	-57.0672	0.4026	C(1)
	-59.0048	0.4034	C(4)
	-60.1746	0.4030	C(5)
N(2)	-57.2057	0.4026	C(24)
	-58.9591	0.4034	C(27)
	-60.1435	0.4030	C(28)

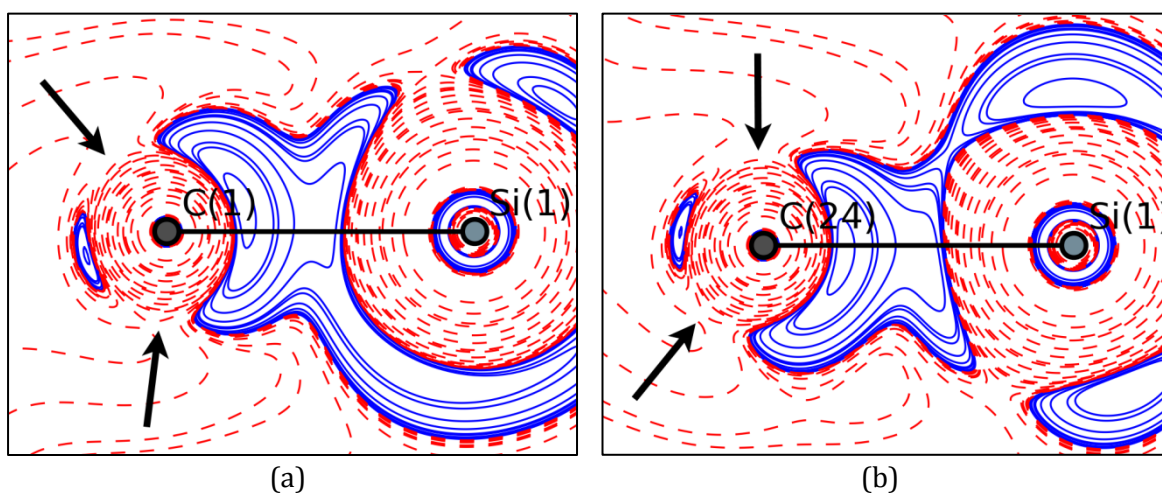


Figure S 18: Laplacian distribution in **3** in the plane perpendicular to the C1–C2–N1–Si1 mean plane (a) and C24–C24–N2–Si1 mean plane (b), respectively. Charge concentration depicted in blue solid lines, depletion in red dashed lines. Contour levels drawn at $\pm 1 \cdot 10^n$, $\pm 2 \cdot 10^n$, $\pm 4 \cdot 10^n$, $\pm 8 \cdot 10^n$ ($-2 \leq n \leq 4$). The arrows show the hole in charge concentration surrounding the carbene atom.

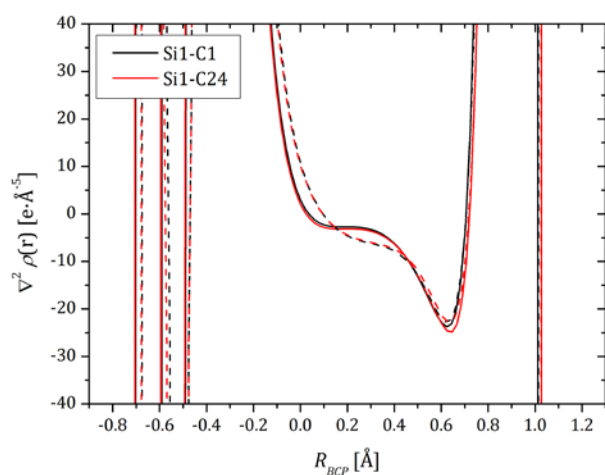


Figure S 19: Laplacian along the Si-C bonds. Values of the experimental analysis are shown as solid lines; values of the theoretical analysis are shown as dashed lines.

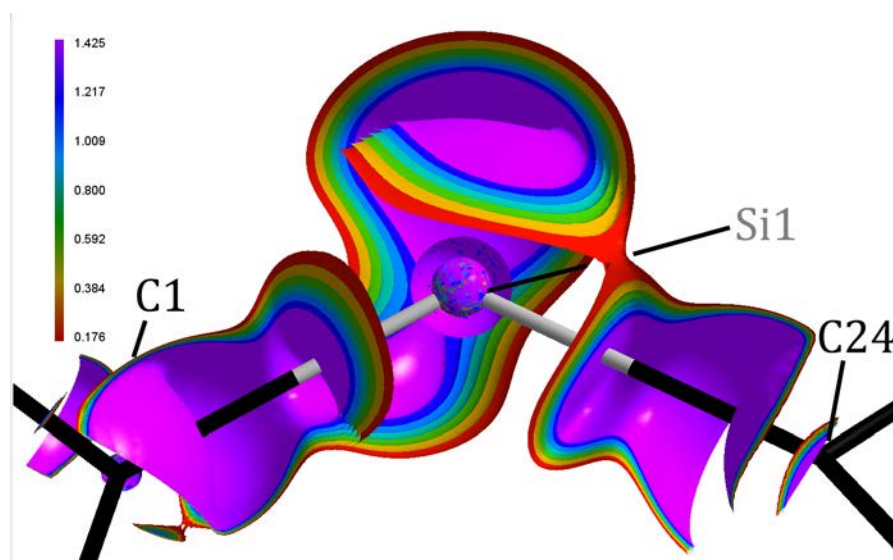


Figure S 20: Laplacian distribution at Si1 at multiple isosurface levels.

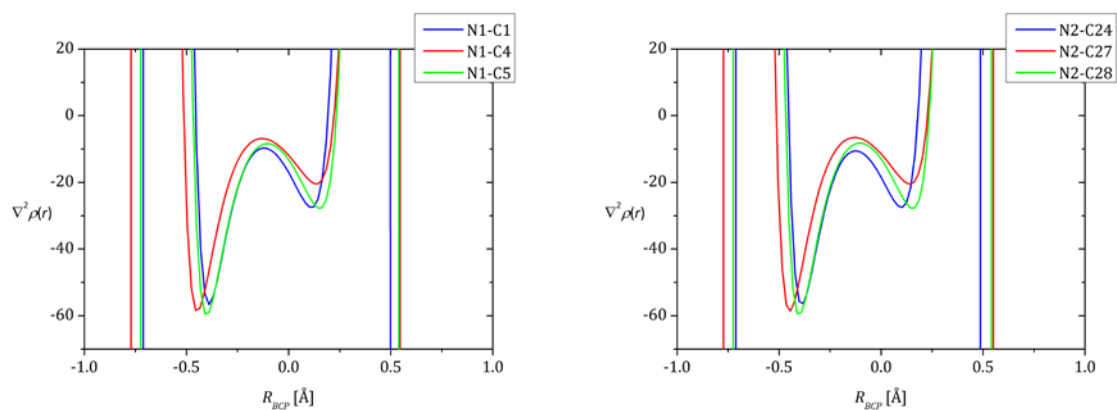


Figure S 21: Laplacian along the N-C bonds in **3**.

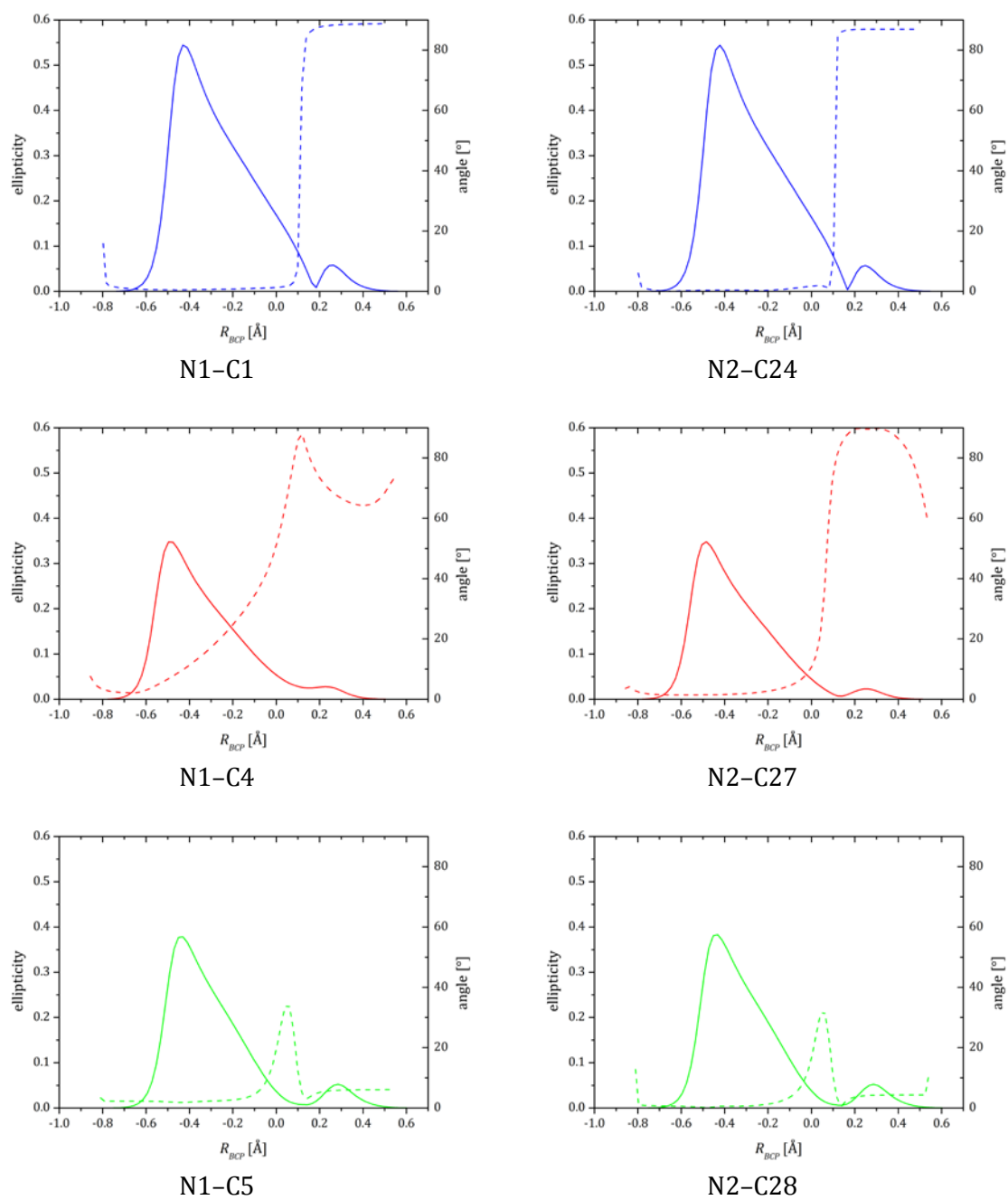


Figure S 22: Ellipticity (solid line) and angle of the major axis (dashed line) along the bond path of N-C bonds in **3**.

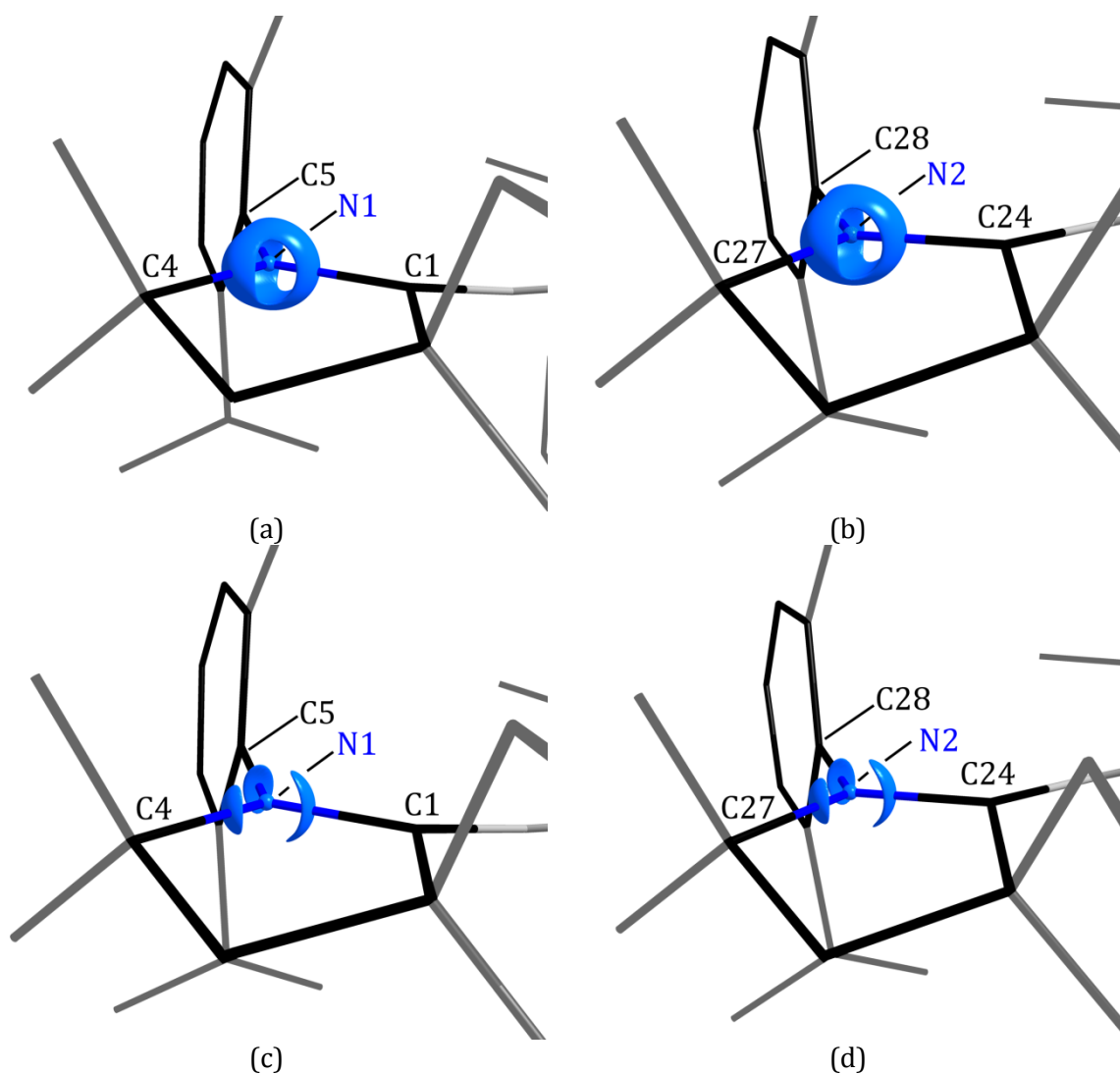


Figure S 23: Laplacian distribution at N1 (a, c) and N2 (b, d) atoms of **3** at an isosurface level of $-30 e \cdot \text{\AA}^{-5}$ (a, b) and $-45 e \cdot \text{\AA}^{-5}$ (c, d).

11 Danksagung

Zuallererst möchte ich meinem Doktorvater Professor Dr. Dietmar Stalke für die hervorragende Betreuung und das in mich gesetzte Vertrauen während der Zeit meines Promotionsstudiums danken. Auch möchte ich ihm dafür danken, dass er mir einen regen Gedankenaustausch durch diverse Forschungs- und Konferenzaufenthalte im In- und Ausland ermöglicht hat.

Professor Dr. Sven Schneider möchte ich für die Übernahme des Korreferats danken. Auch danke ich ganz herzlich den weiteren Mitgliedern der Prüfungskommission Professor Dr. Thomas Waitz, Professor Dr. Ricardo Mata, Dr. Francesca Fabbiani und Dr. Heidrun Sowa für ihre Arbeit.

Dem Fonds der Chemischen Industrie und dem Institut für Anorganische Chemie gilt besonderer Dank für die finanzielle Unterstützung, die mein Promotionsstudium erst ermöglichte.

Meinen Kooperationspartnern der Arbeitskreise von Professor Dr. Herbert W. Roesky, Professor Dr. Lutz Ackermann und Professor Dr. Andreas Schnepf danke ich für ihre interessanten kristallographischen Probleme und die Möglichkeit, mit ihnen Publikationserfahrung zu sammeln. Ganz besonders möchte ich Herrn Dr. Kartik C. Mondal danken, ohne dessen synthetisches Geschick diese Arbeit nicht möglich gewesen wäre. Auch danke ich Professor Dr. Gernot Frenking und Paul Jerabeck für die umfangreichen theoretischen Rechnungen und die engagierte Mitarbeit am Silylonmanuskript.

Ein herzlicher Dank geht an den gesamten Arbeitskreis Stalke für die wunderbare Arbeitsatmosphäre und die Ablenkung vom harten Arbeitsalltag durch das mittägliche Kickern. Auch Timm sei an dieser Stelle gedankt, denn wenn er auch nur zwischen 12:30 und 13:00 zum Arbeitskreis gehört, wäre ohne ihn die Zeit der Promotion sicher nur halb so gut gewesen.

Dem gesamten aktuellen ED-Team (Lennard, Felix, Christian) und auch den Ehemaligen (Hilke, Jakob, Daniel) bin ich sehr dankbar für ihre vielfältigen Hilfestellungen sowie für Lob und Kritik an diversen Manuskripten, Vorträgen, Postern und nicht zuletzt dieser Arbeit.

Unserer eigentlichen Chefin Regine gilt ein großer Dank. Nicht nur dafür, mich in die Ladungsdichteuntersuchung geholt zu haben, auch für den unzähligen Diskussionen über jeden Teil dieser Arbeit und nicht zuletzt für die wunderbare Zusammenarbeit in den Praktika.

Der gesamten „Stammtischtruppe“ Alina, Karina, Timm, Tim und Steffen vielen Dank für die schönste Studienzeit, die ich mir vorstellen kann und dafür, dass wir es bis heute noch immer schaffen uns regelmäßig zu treffen, obwohl uns mittlerweile der eine oder andere Kilometer trennt. Ich hoffe sehr, dass das so bleibt auch wenn es wohl noch mehr Kilometer werden.

Mein allergrößter Dank gilt jedoch den wichtigsten Menschen in meinem Leben. Meiner Mutter, meinem Vater, meinen Brüdern und ihren wundervollen Familien. Für alles was sie je für mich getan haben, für ihre Liebe und Unterstützung. Vielen Dank auch Michael, Ludmilla, Julia und Oliver dafür wie sie mich aufgenommen haben und für ihre Hilfe zu jeder Zeit. Und zu guter Letzt danke Bella, dafür wie Du bist und was Du für mich tust.

.

12 References

- [1] P. P. Power, *Chem. Rev.* **1999**, *99*, 3463-3504.
- [2] P. P. Power, *Organometallics* **2007**, *26*, 4362-4372.
- [3] R. C. Fischer, P. P. Power, *Chem. Rev.* **2010**, *110*, 3877-3923.
- [4] M. Denk, R. West, R. Hayashi, Y. Apeloig, R. Pauncz, M. Kami, in *Organosilicon Chemistry II*, Wiley-VCH, **2008**, pp. 251-261.
- [5] S. Nagendran, H. W. Roesky, *Organometallics* **2008**, *27*, 457-492.
- [6] M. Asay, C. Jones, M. Driess, *Chem. Rev.* **2011**, *111*, 354-396.
- [7] H. W. Roesky, *J. Organomet. Chem.* **2013**, *730*, 57-62.
- [8] V. Y. Lee, A. Sekiguchi, *Angew. Chem.* **2007**, *119*, 6716-6740; *Angew. Chem. Int. Ed.* **2007**, *46*, 6596-6620.
- [9] A. Furstner, H. Krause, C. W. Lehmann, *Chem. Commun.* **2001**, 2372-2373.
- [10] A. Brück, D. Gallego, W. Wang, E. Irran, M. Driess, J. F. Hartwig, *Angew. Chem.* **2012**, *124*, 11645-11649; *Angew. Chem. Int. Ed.* **2012**, *51*, 11478-11482.
- [11] W. Wang, S. Inoue, S. Enthaler, M. Driess, *Angew. Chem.* **2012**, *124*, 6271-6275; *Angew. Chem. Int. Ed.* **2012**, *51*, 6167-6171.
- [12] B. Blom, S. Enthaler, S. Inoue, E. Irran, M. Driess, *J. Am. Chem. Soc.* **2013**, *135*, 6703-6713.
- [13] S. Ishida, T. Iwamoto, C. Kabuto, M. Kira, *Nature* **2003**, *421*, 725-727.
- [14] Y. Wang, Y. Xie, P. Wei, R. B. King, H. F. Schaefer, P. von R. Schleyer, G. H. Robinson, *Science* **2008**, *321*, 1069-1071.
- [15] K. C. Mondal, P. P. Samuel, H. W. Roesky, R. R. Aysin, L. A. Leites, S. Neudeck, J. Lübben, B. Dittrich, N. Holzmann, M. Hermann, G. Frenking, *J. Am. Chem. Soc.* **2014**, *136*, 8919-8922.
- [16] K. C. Mondal, H. W. Roesky, M. C. Schwarzer, G. Frenking, B. Niepötter, H. Wolf, R. Herbst-Irmer, D. Stalke, *Angew. Chem.* **2013**, *125*, 3036-3040; *Angew. Chem. Int. Ed.* **2013**, *52*, 2963-2967.
- [17] Y. Xiong, S. Yao, S. Inoue, J. D. Epping, M. Driess, *Angew. Chem.* **2013**, *125*, 7287-7291; *Angew. Chem. Int. Ed.* **2013**, *52*, 7147-7150.
- [18] M. Alcarazo, C. W. Lehmann, A. Anoop, W. Thiel, A. Furstner, *Nat. Chem* **2009**, *1*, 295-301.
- [19] D. Himmel, I. Krossing, A. Schnepf, *Angew. Chem.* **2014**, *126*, 378-382; *Angew. Chem. Int. Ed.* **2014**, *53*, 370-374.
- [20] D. Himmel, I. Krossing, A. Schnepf, *Angew. Chem.* **2014**, *126*, 6159-6160; *Angew. Chem. Int. Ed.* **2014**, *53*, 6047-6048.
- [21] G. Frenking, *Angew. Chem.* **2014**, *126*, 6152-6158; *Angewandte Chemie International Edition* **2014**, *53*, 6040-6046.
- [22] G. Frenking, S. Shaik, *The Chemical Bond: Chemical Bonding Across the Periodic Table* **2014**, Wiley.
- [23] G. Frenking, S. Shaik, *The Chemical Bond: Fundamental Aspects of Chemical Bonding* **2014**, Wiley, Weinheim.
- [24] W. Friedrich, P. Knipping, M. v. Laue, *Interferenz-Erscheinungen bei Röntgenstrahlen, von W. Friedrich, P. Knipping und M. Lane* **1912**, Verlag der Königlich-Bayerischen Akademie der Wissenschaften, München.
- [25] W. H. Bragg, W. L. Bragg, *Proc. R. Soc.* **1913**, *A 89*, 277-291.
- [26] W. L. Bragg, *Proc. R. Soc.* **1913**, *A 89*, 248-277.
- [27] M. Kaupp, B. Metz, H. Stoll, *Angew. Chem.* **2000**, *112*, 4780-4782; *Angew. Chem. Int. Ed.* **2000**, *39*, 4607-4609.
- [28] D. Kratzert, D. Leusser, J. J. Holstein, B. Dittrich, K. Abersfelder, D. Scheschkewitz, D. Stalke, *Angew. Chem.* **2013**, *125*, 4574-4578; *Angew. Chem. Int. Ed.* **2013**, *52*, 4478-4482.

- [29] R. Herbst-Irmer, L. Krause, B. Niepötter, D. Stalke, *J. Appl. Crystallogr.*, in preparation.
- [30] A. T. Brünger, *Nature* **1992**, 355, 472-475.
- [31] A. T. Brünger, in *Methods Enzymol.*, Vol. Volume 277 (Eds.: R. M. S. Charles W. Carter Jr), Academic Press, **1997**, pp. 366-396.
- [32] B. Niepötter, R. Herbst-Irmer, D. Kratzert, P. P. Samuel, K. C. Mondal, H. W. Roesky, P. Jerabek, G. Frenking, D. Stalke, *Angew. Chem.* **2014**, 126, 2806-2811; *Angew. Chem. Int. Ed.* **2014**, 53, 2766-2770.
- [33] P. Coppens, *X-Ray Charge Densities and Chemical Bonding* **1997**, Oxford University Press, USA.
- [34] P. Coppens, *Coord. Chem. Rev.* **1985**, 65, 285-307.
- [35] T. S. Koritsanszky, P. Coppens, *Chemical Reviews* **2001**, 101, 1583-1628.
- [36] C. Lecomte, M. Souhassou, S. Pillet, *J. Mol. Struct.* **2003**, 647, 53-64.
- [37] P. Macchi, A. Sironi, *Coord. Chem. Rev.* **2003**, 238-239, 383-412.
- [38] P. Coppens, B. Iversen, F. K. Larsen, *Coord. Chem. Rev.* **2005**, 249, 179-195.
- [39] P. Coppens, *Angew. Chem.* **2005**, 117, 6970-6972; *Angew. Chem. Int. Ed.* **2005**, 44, 6810-6811.
- [40] D. Stalke, H. Ott, *Nachrichten aus der Chemie* **2008**, 56, 131-135.
- [41] *Electron Density and Chemical Bonding II: Theoretical Charge Density Studies*, (Eds.: D. Stalke), Springer Berlin Heidelberg, **2012**.
- [42] *Electron Density and Chemical Bonding I: Experimental Charge Density Studies*, (Eds.: D. Stalke), Springer Berlin Heidelberg, **2012**.
- [43] C. Gatti, in *Electron Density and Chemical Bonding II: Theoretical Charge Density Studies* (Eds.: D. Stalke), Springer Berlin, Heidelberg, **2012**.
- [44] D. Stalke *Chem. Eur. J.* **2011**, 17, 9264-9278.
- [45] M. R. V. Jorgensen, V. R. Hathwar, N. Bindzus, N. Wahlberg, Y.-S. Chen, J. Overgaard, B. B. Iversen, *IUCrj* **2014**, 1, 267-280.
- [46] N. K. Hansen, P. Coppens, *Acta Crystallogr.* **1978**, A 34, 909-921.
- [47] R. Stewart, *Acta Crystallogr.* **1976**, A 32, 565-574.
- [48] E. C. o. t. IUCr, *Acta Crystallogr.* **1992**, A 48, 922-946.
- [49] D. W. Bennett, *Understanding Single-Crystal X-Ray Crystallography* **2010**, John Wiley & Sons.
- [50] W. H. Bragg, W. L. Bragg, *Proc. R. Soc.* **1913**, A 88, 428-438.
- [51] P. Coppens, in *International Tables for Crystallography Volume B: Reciprocal space, Vol. B* (Eds.: U. Shmueli), Springer Netherlands, second online edition, **2010**, pp. 10-23.
- [52] C. Giacovazzo, in *Fundamentals of Crystallography* (Eds.: C. Giacovazzo), IUCr/Oxford University Press, New York, **2002**.
- [53] G. Sheldrick, *Acta Crystallogr.* **2015**, A 71, 3-8.
- [54] G. M. Sheldrick, H. A. Hauptman, C. M. Weeks, R. Miller, I. Usón, in *International Tables for Crystallography Volume F: Crystallography of biological macromolecules, Vol. F* (Eds.: M. G. Rossmann, E. Arnold), Springer Netherlands, second online edition, **2012**, pp. 333-345.
- [55] C. Giacovazzo, in *International Tables for Crystallography Volume B: Reciprocal space, Vol. B* (Eds.: U. Shmueli), Springer Netherlands, second online edition, **2010**, pp. 215-243.
- [56] P. Macchi, P. Coppens, *Acta Crystallogr.* **2001**, A 57, 656-662.
- [57] Z. Su, P. Coppens, *Acta Crystallogr.* **1998**, A 54, 646-652.
- [58] D. Jayatilaka, B. Dittrich, *Acta Crystallogr.* **2008**, A 64, 383-393.
- [59] A. Volkov, P. Coppens, *Acta Crystallogr.* **2001**, A 57, 395-405.
- [60] A. Volkov, C. Gatti, Y. Abramov, P. Coppens, *Acta Crystallogr.* **2000**, A 56, 252-258.
- [61] A. Volkov, Y. Abramov, P. Coppens, C. Gatti, *Acta Crystallogr.* **2000**, A 56, 332-339.
- [62] T. Koritsanszky, A. Volkov, M. Chodkiewicz, in *Electron Density and Chemical Bonding II, Vol. 147* (Eds.: D. Stalke), Springer Berlin Heidelberg, **2012**, pp. 1-25.

- [63] A. Fischer, D. Tiana, W. Scherer, K. Batke, G. Eickerling, H. Svendsen, N. Bindzus, B. B. Iversen, *J. Phys. Chem.* **2011**, *A 115*, 13061-13071.
- [64] N. Bindzus, T. Straaso, N. Wahlberg, J. Becker, L. Bjerg, N. Lock, A.-C. Dippel, B. B. Iversen, *Acta Crystallogr.* **2014**, *A 70*, 39-48.
- [65] E. Clementi, C. Roetti, *At. Data Nucl. Data Tables* **1974**, *14*, 177-478.
- [66] C. K. Johnson, H. A. Levy, in *International Tables for X-ray Crystallography, Vol. 4*, Kynoch Press, Birmingham, **1974**, pp. 311-336.
- [67] K. N. Trueblood, H.-B. Burgi, H. Burzlaff, J. D. Dunitz, C. M. Gramaccioni, H. H. Schulz, U. Shmueli, S. C. Abrahams, *Acta Crystallogr.* **1996**, *A 52*, 770-781.
- [68] R. Herbst-Irmer, J. Henn, J. J. Holstein, C. B. Hübschle, B. Dittrich, D. Stern, D. Kratzert, D. Stalke, *J. Phys. Chem.* **2013**, *A 117*, 633-641.
- [69] P. Müller, *Crystallogr. Rev.* **2009**, *15*, 57-83.
- [70] G. M. Sheldrick, *SADABS*, 2014/2, Göttingen, **2014**.
- [71] L. Krause, R. Herbst-Irmer, G. M. Sheldrick, D. Stalke, *J. Appl. Crystallogr.* **2015**, *48*, 3-10.
- [72] G. M. Sheldrick, *XPREF*, 2015/2, Göttingen, **2015**.
- [73] M. S. Weiss, *J. Appl. Crystallogr.* **2001**, *34*, 130-135.
- [74] K. Diederichs, P. A. Karplus, *Nat. Struct. Mol. Biol.* **1997**, *4*, 269-275.
- [75] K. Diederichs, *Acta Crystallogr.* **2010**, *D 66*, 733-740.
- [76] H. Wolf, M. R. V. Jorgensen, Y.-S. Chen, R. Herbst-Irmer, D. Stalke, *Acta Crystallogr.* **2015**, *B 71*, 10-19.
- [77] D. Schwarzenbach, S. C. Abrahams, H. D. Flack, W. Gonschorek, T. Hahn, K. Huml, R. E. Marsh, E. Prince, B. E. Robertson, J. S. Rollett, A. J. C. Wilson, *Acta Crystallogr.* **1989**, *A 45*, 63-75.
- [78] V. V. Zhurov, E. A. Zhurova, A. A. Pinkerton, *J. Appl. Crystallogr.* **2008**, *41*, 340-349.
- [79] K. Meindl, J. Henn, *Acta Crystallogr.* **2008**, *A 64*, 404-418.
- [80] V. Zavodnik, A. Stash, V. Tsirelson, R. de Vries, D. Feil, *Acta Crystallogr.* **1999**, *B 55*, 45-54.
- [81] L. Farrugia, *J. Appl. Crystallogr.* **2012**, *45*, 849-854.
- [82] S. C. Abrahams, E. T. Keve, *Acta Crystallogr.* **1971**, *A 27*, 157-165.
- [83] R. F. W. Bader, *Atoms in Molecules : A Quantum Theory* **1990**, Clarendon Press, Oxford; New York.
- [84] R. F. W. Bader, P. J. MacDougall, *J. Am. Chem. Soc.* **1985**, *107*, 6788-6795.
- [85] R. F. W. Bader, *Acc. Chem. Res.* **1975**, *8*, 34-40.
- [86] R. F. W. Bader, P. M. Beddall, *J. Chem. Phys.* **1972**, *56*, 3320-3329.
- [87] R. F. W. Bader, H. Essén, *J. Chem. Phys.* **1984**, *80*, 1943-1960.
- [88] A. M. Pendás, E. Francisco, M. A. Blanco, C. Gatti, *Chem. Eur. J.* **2007**, *13*, 9362-9371.
- [89] R. F. W. Bader, *J. Phys. Chem.* **2009**, *A 113*, 10391-10396.
- [90] R. F. W. Bader, *J. Phys. Chem.* **1998**, *A 102*, 7314-7323.
- [91] C. Gatti, *Z. Kristallogr.* **2005**, *220*, 399-457.
- [92] R. F. W. Bader, P. J. MacDougall, C. D. H. Lau, *J. Am. Chem. Soc.* **1984**, *106*, 1594-1605.
- [93] R. J. Gillespie, *Coord. Chem. Rev.* **2008**, *252*, 1315-1327.
- [94] R. J. Gillespie, R. S. Nyholm, *Chem. Soc. Rev.* **1957**, *11*, 339-380.
- [95] R. F. W. Bader, R. J. Gillespie, P. J. MacDougall, *J. Am. Chem. Soc.* **1988**, *110*, 7329-7336.
- [96] D. Cremer, E. Kraka, *Angew. Chem.* **1984**, *96*, 612-614; *Angew. Chem. Int. Ed.* **1984**, *23*, 627-628.
- [97] M. Stokkebro Schmøkel, J. Overgaard, B. Brummerstedt Iversen, *Z. Anorg. Allg. Chem.* **2013**, *639*, 1922-1932.
- [98] Y. Abramov, *Acta Crystallogr.* **1997**, *A 53*, 264-272.
- [99] P. Macchi, D. M. Proserpio, A. Sironi, *J. Am. Chem. Soc.* **1998**, *120*, 13429-13435.
- [100] R. F. W. Bader, T. S. Slee, D. Cremer, E. Kraka, *J. Am. Chem. Soc.* **1983**, *105*, 5061-5068.
- [101] D. Cremer, E. Kraka, T. S. Slee, R. F. W. Bader, C. D. H. Lau, T. T. Nguyen Dang, P. J. MacDougall, *J. Am. Chem. Soc.* **1983**, *105*, 5069-5075.

- [102] J. R. Cheeseman, M. T. Carroll, R. F. W. Bader, *Chem. Phys. Lett.* **1988**, *143*, 450-458.
- [103] U. Flierler, D. Stalke in *Electron Density and Chemical Bonding I (Experimental)* (Eds.: D. Stalke), Springer, Berlin, New York, **2012**, pp. 1-20.
- [104] G. Saleh, C. Gatti, L. Lo Presti, J. Contreras-García, *Chem. Eur. J.* **2012**, *18*, 15523-15536.
- [105] E. R. Johnson, S. Keinan, P. Mori-Sánchez, J. Contreras-García, A. J. Cohen, W. Yang, *J. Am. Chem. Soc.* **2010**, *132*, 6498-6506.
- [106] J. Contreras-García, W. Yang, E. R. Johnson, *J. Phys. Chem.* **2011**, *A 115*, 12983-12990.
- [107] A. D. Becke, in *Modern Electronic Structure Theory - Part II* (Eds.: D. Yarkony), World Scientific, River Edge, **1995**, pp. 1022-1046.
- [108] P. Seiler, in *Accurate Molecular Structures: Their Determination and Importance* (Eds.: A. Domenicano, I. Hargittai), International Union of Crystallography, Oxford, **1992**.
- [109] N. G. Alexandropoulos, M. J. Cooper, P. Suortti, B. T. M. Willis, in *International Tables for Crystallography, Mathematical, Physical and Chemical Tables, Vol. Volume C* (Eds.: E. Prince), online edition, **2006**, pp. 653-665.
- [110] B. T. M. Willis, in *International Tables for Crystallography, Reciprocal Space, Vol. Volume B* (Eds.: U. Shmueli), online edition, **2001**, pp. 400-406.
- [111] B. T. M. Willis, A. W. Pryor, *Thermal Vibrations in Crystallography* **1975**, Cambridge University Press, London.
- [112] E. Bärnighausen, *J. Appl. Crystallogr.* **1978**, *11*, 221-228.
- [113] V. G. Tsirelson, R. P. Ozerov, *Electron Density and Bonding in Crystals: Principles, Theory and X-ray Diffraction Experiments in Solid State Physics and Chemistry* **1996**, Institute of Physics Publishing, Bristol / Philadelphia.
- [114] B. Dorner, E. Burkel, T. Illini, J. Peisl, *Z. Phys.* **1987**, *B 69*, 179-183.
- [115] D. A. O'Connor, N. M. Butt, *Phys. Lett.* **1963**, *7*, 233-235.
- [116] T. R. Welberry, J. Goossens Darren, P. Heerdegen Aidan, L. Lee Peter, *Z. Kristallogr.* **2005**, *220*, 1052.
- [117] A. G. Tsarkov, V. G. Tsirelson, *Z. Naturforsch.* **1993**, *A 48*, 21-24.
- [118] A. W. Stevenson, J. Harada, *Acta Crystallogr.* **1983**, *A 39*, 202-207.
- [119] L. Jennings, *Acta Crystallogr.* **1970**, *A 26*, 613-622.
- [120] R. H. Blessing, *Crystallogr. Rev.* **1987**, *1*, 3-58.
- [121] R. Blessing, *J. Appl. Crystallogr.* **1986**, *19*, 412.
- [122] A. Stash, V. Zavodnik, *Crystallography Reports* **1995**, *41*, 404-412.
- [123] A. G. Tsarkov, V. G. Tsirelson, *Phys. Status Solidi* **1991**, *B 167*, 417-428.
- [124] R. B. Helmholdt, A. Vos, *Acta Crystallogr.* **1977**, *A 33*, 38-45.
- [125] B. Niepotter, R. Herbst-Irmer, D. Stalke, *J. Appl. Crystallogr.* **2015**, *48*, 1485-1497.
- [126] H. R. Bigmore, J. Meyer, I. Krummenacher, H. Rügger, E. Clot, P. Mountford, F. Breher, *Chem. Eur. J.* **2008**, *14*, 5918-5934.
- [127] D. Kratzert, D. Leusser, D. Stern, J. Meyer, F. Breher, D. Stalke, *Chem. Commun.* **2011**, *47*, 2931-2933.
- [128] Z. Fei, N. Kocher, C. J. Mohrschladt, H. Ihmels, D. Stalke, *Angew. Chem.* **2003**, *115*, 807-811; *Angew. Chem. Int. Ed.* **2003**, *42*, 783-787.
- [129] G. Schwab, D. Stern, D. Stalke, *J. Org. Chem.* **2008**, *73*, 5242-5247.
- [130] G. Schwab, D. Stern, D. Leusser, D. Stalke, *Z. Naturforsch.* **2007**, *B 62*, 711-716.
- [131] Bruker AXS Inc., *SAINT v8.30C*, WI, USA, Madison, **2013**.
- [132] G. Sheldrick, *Acta Crystallogr.* **2015**, *C 71*, 3-8.
- [133] G. Sheldrick, *Acta crystallographica. Section A, Foundations of crystallography; Acta Crystallogr.* **2008**, *A 64*, 112-122.
- [134] F. H. Allen, I. J. Bruno, *Acta Crystallogr.* **2010**, *B 66*, 380-386.
- [135] B. Dittrich, C. B. Hübschle, K. Pröpper, F. Dietrich, T. Stolper, J. J. Holstein, *Acta Crystallogr.* **2013**, *B 69*, 91-104.
- [136] A. Volkov, P. Macchi, L. J. Farrugia, C. Gatti, P. R. Mallinson, T. Richter, T. Koritsanszky, *XD2006*, **2006**.

- [137] E. Clementi, D. L. Raimondi, *J. Chem. Phys.* **1963**, *38*, 2686-2689.
- [138] A. Volkov, Y. A. Abramov, P. Coppens, *Acta Crystallogr.* **2001**, *A 57*, 272-282.
- [139] H. Wolf, *Data Quality Bench-Marking for High Resolution Bragg Data*, Institut für Anorganische Chemie, Georg-August-Universität (Göttingen), **2014**.
- [140] B. Dittrich, *Acta Cryst.* **2009**, *A 65*, s 75.
- [141] W. Kabsch, *J. Appl. Crystallogr.* **1988**, *21*, 916-924.
- [142] Bruker AXS Inc., *SAINT - Manual 2003*, WI, USA, Madison.
- [143] E. D. Stevens, P. Coppens, *Acta Crystallogr.* **1975**, *A 31*, 612-619.
- [144] R. Blessing, *J. Appl. Crystallogr.* **1997**, *30*, 421-426.
- [145] D. Stalke, *Acta Crystallogr.* **2014**, *B 70*, 781-782.
- [146] C. Broennimann, E. F. Eikenberry, B. Henrich, R. Horisberger, G. Huelsen, E. Pohl, B. Schmitt, C. Schulze-Briese, M. Suzuki, T. Tomizaki, H. Toyokawa, A. Wagner, *J. Synchrotron Radiat.* **2006**, *13*, 120-130.
- [147] E. Wenger, S. Dahaoui, P. Alle, P. Parois, C. Palin, C. Lecomte, D. Schaniel, *Acta Crystallogr.* **2014**, *B 70*, 783-791.
- [148] A. G. Brook, F. Abdesaken, B. Gutekunst, G. Gutekunst, R. K. Kallury, *J. Chem. Soc., Chem. Commun.* **1981**, 191-192.
- [149] R. West, M. J. Fink, J. Michl, *Science* **1981**, *214*, 1343-1344.
- [150] M. J. Fink, M. J. Michalczyk, K. J. Haller, R. West, J. Michl, *J. Chem. Soc., Chem. Commun.* **1983**, 1010-1011.
- [151] P. Rademacher, *Strukturen organischer Moleküle 1987*, 2, VCH, Weinheim.
- [152] A. Sekiguchi, R. Kinjo, M. Ichinohe, *Science* **2004**, *305*, 1755-1757.
- [153] N. Wiberg, S. K. Vasisht, G. Fischer, P. Mayer, *Z. Anorg. Allg. Chem.* **2004**, *630*, 1823-1828.
- [154] C. A. Pignedoli, A. Curioni, W. Andreoni, *ChemPhysChem* **2005**, *6*, 1795-1799.
- [155] C. A. Pignedoli, A. Curioni, W. Andreoni, *ChemPhysChem* **2006**, *7*, 801-802.
- [156] G. Frenking, A. Krapp, S. Nagase, N. Takagi, A. Sekiguchi, *ChemPhysChem* **2006**, *7*, 799-800.
- [157] M. Denk, R. Lennon, R. Hayashi, R. West, A. V. Belyakov, H. P. Verne, A. Haaland, M. Wagner, N. Metzler, *J. Am. Chem. Soc.* **1994**, *116*, 2691-2692.
- [158] A. J. Arduengo, R. L. Harlow, M. Kline, *J. Am. Chem. Soc.* **1991**, *113*, 361-363.
- [159] R. West, M. Denk, *Pure & Appl. Chem.* **1996**, *68*, 785-788.
- [160] N. J. Hill, D. F. Moser, I. A. Guzei, R. West, *Organometallics* **2005**, *24*, 3346-3349.
- [161] M. Kira, S. Ishida, T. Iwamoto, C. Kabuto, *J. Am. Chem. Soc.* **1999**, *121*, 9722-9723.
- [162] M. Driess, S. Yao, M. Brym, C. van Wüllen, D. Lentz, *J. Am. Chem. Soc.* **2006**, *128*, 9628-9629.
- [163] C.-W. So, H. W. Roesky, J. Magull, R. B. Oswald, *Angew. Chem.* **2006**, *118*, 4052-4054; *Angew. Chem. Int. Ed.* **2006**, *45*, 3948-3950.
- [164] G.-H. Lee, R. West, T. Müller, *J. Am. Chem. Soc.* **2003**, *125*, 8114-8115.
- [165] R. S. Ghadwal, H. W. Roesky, S. Merkel, J. Henn, D. Stalke, *Angew. Chem.* **2009**, *121*, 5793-5796; *Angew. Chem. Int. Ed.* **2009**, *48*, 5683-5686.
- [166] G. Trinquier, *J. Am. Chem. Soc.* **1990**, *112*, 2130-2137.
- [167] E. A. Carter, W. A. Goddard, *J. Phys. Chem.* **1986**, *90*, 998-1001.
- [168] J. P. Malrieu, G. Trinquier, *J. Am. Chem. Soc.* **1989**, *111*, 5916-5921.
- [169] G. Trinquier, J.-P. Malrieu, in *The Chemistry of functional groups, Suppl. A: The chemistry of double bonded functional groups, Vol. 2* (Eds.: S. Patai), Wiley, Chichester, **1989**, pp. 1-52.
- [170] G. Trinquier, J. P. Malrieu, *J. Am. Chem. Soc.* **1987**, *109*, 5303-5315.
- [171] M. C. Holthausen, W. Koch, Y. Apeloig, *J. Am. Chem. Soc.* **1999**, *121*, 2623-2624.
- [172] M. Kosa, M. Karni, Y. Apeloig, *J. Am. Chem. Soc.* **2013**, *135*, 9032-9040.
- [173] M. Melaimi, M. Soleilhavoup, G. Bertrand, *Angew. Chem.* **2010**, *122*, 8992-9032; *Angew. Chem. Int. Ed.* **2010**, *49*, 8810-8849.
- [174] D. Bourissou, O. Guerret, F. P. Gabbaï, G. Bertrand, *Chem. Rev.* **2000**, *100*, 39-92.
- [175] P. Jiang, P. P. Gaspar, *J. Am. Chem. Soc.* **2001**, *123*, 8622-8623.

- [176] A. Sekiguchi, T. Tanaka, M. Ichinohe, K. Akiyama, P. P. Gaspar, *J. Am. Chem. Soc.* **2008**, *130*, 426-427.
- [177] A. Sekiguchi, T. Tanaka, M. Ichinohe, K. Akiyama, S. Tero-Kubota, *J. Am. Chem. Soc.* **2003**, *125*, 4962-4963.
- [178] R. Tonner, F. Öxler, B. Neumüller, W. Petz, G. Frenking, *Angew. Chem.* **2006**, *118*, 8206-8211; *Angew. Chem. Int. Ed.* **2006**, *45*, 8038-8042.
- [179] R. Tonner, G. Frenking, *Angew. Chem.* **2007**, *119*, 8850-8853; *Angew. Chem. Int. Ed.* **2007**, *46*, 8695-8698.
- [180] F. Ramirez, N. B. Desai, B. Hansen, N. McKelvie, *J. Am. Chem. Soc.* **1961**, *83*, 3539-3540.
- [181] A. Fürstner, M. Alcarazo, R. Goddard, C. W. Lehmann, *Angew. Chem.* **2008**, *120*, 3254-3258; *Angew. Chem. Int. Ed.* **2008**, *47*, 3210-3214.
- [182] C. A. Dyker, V. Lavallo, B. Donnadiou, G. Bertrand, *Angew. Chem.* **2008**, *120*, 3250-3253; *Angew. Chem. Int. Ed.* **2008**, *47*, 3206-3209.
- [183] G. Frenking, R. Tonner, S. Klein, N. Takagi, T. Shimizu, A. Krapp, K. K. Pandey, P. Parameswaran, *Chem. Soc. Rev.* **2014**, *43*, 5106-5139.
- [184] H. Tanaka, S. Inoue, M. Ichinohe, M. Driess, A. Sekiguchi, *Organometallics* **2011**, *30*, 3475-3478.
- [185] M. Kira, *Chem. Commun.* **2010**, *46*, 2893-2903.
- [186] M. Kira, T. Iwamoto, S. Ishida, H. Masuda, T. Abe, C. Kabuto, *J. Am. Chem. Soc.* **2009**, *131*, 17135-17144.
- [187] M. Kosa, M. Karni, Y. Apeloig, *J. Am. Chem. Soc.* **2004**, *126*, 10544-10545.
- [188] M. Kosa, M. Karni, Y. Apeloig, *J. Chem. Theory Comput.* **2006**, *2*, 956-964.
- [189] T. Veszprémi, K. Petrov, C. T. Nguyen, *Organometallics* **2006**, *25*, 1480-1484.
- [190] N. Takagi, T. Shimizu, G. Frenking, *Chem. Eur. J.* **2009**, *15*, 3448-3456.
- [191] S. Sarmah, A. K. Guha, A. K. Phukan, A. Kumar, S. R. Gadre, *Dalton Trans.* **2013**, *42*, 13200-13209.
- [192] N. Takagi, T. Shimizu, G. Frenking, *Chem. Eur. J.* **2009**, *15*, 8593-8604.
- [193] N. Takagi, R. Tonner, G. Frenking, *Chem. Eur. J.* **2012**, *18*, 1772-1780.
- [194] A. Guha, B. Konwar, S. Sarmah, A. Phukan, *Theor. Chem. Acc.* **2012**, *131*, 1-11.
- [195] K. C. Mondal, H. W. Roesky, M. C. Schwarzer, G. Frenking, I. Tkach, H. Wolf, D. Kratzert, R. Herbst-Irmer, B. Niepötter, D. Stalke, *Angew. Chem.* **2013**, *125*, 1845-1850; *Angew. Chem. Int. Ed.* **2013**, *52*, 1801-1805.
- [196] V. Lavallo, Y. Canac, A. DeHope, B. Donnadiou, G. Bertrand, *Angew. Chem.* **2005**, *117*, 7402-7405; *Angew. Chem. Int. Ed.* **2005**, *44*, 7236-7239.
- [197] V. Lavallo, Y. Canac, C. Präsang, B. Donnadiou, G. Bertrand, *Angew. Chem.* **2005**, *117*, 5851-5855; *Angew. Chem. Int. Ed.* **2005**, *44*, 5705-5709.
- [198] M. Soleilhavoup, G. Bertrand, *Acc. Chem. Res.* **2015**, *48*, 256-266.
- [199] R. Kinjo, B. Donnadiou, M. A. Celik, G. Frenking, G. Bertrand, *Science* **2011**, *333*, 610-613.
- [200] Y. Li, K. C. Mondal, H. W. Roesky, H. Zhu, P. Stollberg, R. Herbst-Irmer, D. Stalke, D. M. Andrada, *J. Am. Chem. Soc.* **2013**, *135*, 12422-12428.
- [201] D. S. Weinberger, N. Amin Sk, K. C. Mondal, M. Melaimi, G. Bertrand, A. C. Stückl, H. W. Roesky, B. Dittrich, S. Demeshko, B. Schwederski, W. Kaim, P. Jerabek, G. Frenking, *J. Am. Chem. Soc.* **2014**, *136*, 6235-6238.
- [202] D. S. Weinberger, M. Melaimi, C. E. Moore, A. L. Rheingold, G. Frenking, P. Jerabek, G. Bertrand, *Angew. Chem.* **2013**, *125*, 9134-9137; *Angew. Chem. Int. Ed.* **2013**, *52*, 8964-8967.
- [203] K. C. Mondal, P. P. Samuel, Y. Li, H. W. Roesky, S. Roy, L. Ackermann, N. S. Sidhu, G. M. Sheldrick, E. Carl, S. Demeshko, S. De, P. Parameswaran, L. Ungur, L. F. Chibotaru, D. M. Andrada, *Eur. J. Inorg. Chem.* **2014**, *2014*, 818-823.
- [204] S. Roy, K. C. Mondal, J. Meyer, B. Niepötter, C. Köhler, R. Herbst-Irmer, D. Stalke, B. Dittrich, D. M. Andrada, G. Frenking, H. W. Roesky, *Chem. Eur. J.* **2015**, *21*, 9312-9318.

- [205] P. P. Samuel, K. C. Mondal, H. W. Roesky, M. Hermann, G. Frenking, S. Demeshko, F. Meyer, A. C. Stückl, J. H. Christian, N. S. Dalal, L. Ungur, L. F. Chibotaru, K. Pröpper, A. Meents, B. Dittrich, *Angew. Chem.* **2013**, *125*, 12033-12037; *Angew. Chem. Int. Ed.* **2013**, *52*, 11817-11821.
- [206] P. P. Samuel, R. Neufeld, K. Chandra Mondal, H. W. Roesky, R. Herbst-Irmer, D. Stalke, S. Demeshko, F. Meyer, V. C. Rojisha, S. De, P. Parameswaran, A. C. Stückl, W. Kaim, J. H. Christian, J. K. Bindra, N. S. Dalal, *Chem. Sci.* **2015**, *6*, 3148-3153.
- [207] A. P. Singh, P. P. Samuel, H. W. Roesky, M. C. Schwarzer, G. Frenking, N. S. Sidhu, B. Dittrich, *J. Am. Chem. Soc.* **2013**, *135*, 7324-7329.
- [208] G. Ung, J. Rittle, M. Soleilhavoup, G. Bertrand, J. C. Peters, *Angew. Chem.* **2014**, *126*, 8567-8571; *Angew. Chem. Int. Ed.* **2014**, *53*, 8427-8431.
- [209] V. Lavallo, Y. Canac, B. Donnadiou, W. W. Schoeller, G. Bertrand, *Angew. Chem.* **2006**, *118*, 3568-3571; *Angew. Chem. Int. Ed.* **2006**, *45*, 3488-3491.
- [210] G. D. Frey, V. Lavallo, B. Donnadiou, W. W. Schoeller, G. Bertrand, *Science* **2007**, *316*, 439-441.
- [211] V. Lavallo, G. D. Frey, B. Donnadiou, M. Soleilhavoup, G. Bertrand, *Angew. Chem.* **2008**, *120*, 5302-5306; *Angew. Chem. Int. Ed.* **2008**, *47*, 5224-5228.
- [212] K. C. Mondal, P. P. Samuel, M. Tretiakov, A. P. Singh, H. W. Roesky, A. C. Stückl, B. Niepötter, E. Carl, H. Wolf, R. Herbst-Irmer, D. Stalke, *Inorg. Chem.* **2013**, *52*, 4736-4743.
- [213] V. Y. Lee, A. Sekiguchi, *Organometallic Compounds of Low-Coordinate Si, Ge, Sn and Pb: From Phantom Species to Stable Compounds* **2010**, Wiley, Chichester, U.K.
- [214] D. Stalke, *Chem. Soc. Rev.* **1998**, *27*, 171-178.
- [215] T. Kottke, D. Stalke, *J. Appl. Crystallogr.* **1993**, *26*, 615-619.
- [216] *APEX2 v2.2012.2-0*, WI, USA, Madison, **2012**.
- [217] A. Ø. Madsen, *J. Appl. Crystallogr.* **2006**, *39*, 757-758.
- [218] C. B. Hübschle, B. Dittrich, *J. Appl. Crystallogr.* **2011**, *44*, 238-240.
- [219] C. Scherlinger, *Acta Crystallogr.* **1988**, *A 44*, 343-349.
- [220] P. R. Mallinson, T. Koritsanszky, E. Elkaim, N. Li, P. Coppens, *Acta Crystallogr.* **1988**, *A 44*, 336-343.
- [221] S. F. Vyboishchikov, G. Frenking, *Chem. Eur. J.* **1998**, *4*, 1428-1438.
- [222] T. E. Taylor, M. B. Hall, *J. Am. Chem. Soc.* **1984**, *106*, 1576-1584.
- [223] K. C. Mondal, P. P. Samuel, M. Tretiakov, A. P. Singh, H. W. Roesky, A. C. Stückl, B. Niepötter, E. Carl, H. Wolf, R. Herbst-Irmer, D. Stalke, *Inorg. Chem.* **2013**, *52*, 4736-4743.
- [224] C. Mohapatra, P. P. Samuel, H. W. Roesky, B. Niepötter, R. Herbst-Irmer, D. Stalke, B. Maity, D. Koley, *Inorg. Chem.* **2015**, *submitted for publication*.
- [225] L. J. Farrugia, A. D. Khalaji, *J. Phys. Chem.* **2011**, *A 115*, 12512-12522.
- [226] M. Tafipolsky, W. Scherer, K. Öfele, G. Artus, B. Pedersen, W. A. Herrmann, G. S. McGrady, *J. Am. Chem. Soc.* **2002**, *124*, 5865-5880.
- [227] W. Scherer, P. Sirsch, D. Shorokhov, G. S. McGrady, S. A. Mason, M. G. Gardiner, *Chem. Eur. J.* **2002**, *8*, 2324-2334.
- [228] J. Hey, D. M. Andrada, R. Michel, R. A. Mata, D. Stalke, *Angew. Chem.* **2013**, *125*, 10555-10559; *Angew. Chem. Int. Ed.* **2013**, *52*, 10365-10369.
- [229] D. M. Andrada, G. Frenking, *Angew. Chem.* **2015**, *127*, 12494-12500; *Angew. Chem. Int. Ed.* **2015**, *54*, 12319-12324.
- [230] H. Ott, C. Däschlein, D. Leusser, D. Schilbach, T. Seibel, D. Stalke, C. Strohmann, *J. Am. Chem. Soc.* **2008**, *130*, 11901-11911.
- [231] H. Ott, U. Pieper, D. Leusser, U. Flierler, J. Henn, D. Stalke, *Angew. Chem.* **2009**, *121*, 3022-3026; *Angew. Chem. Int. Ed.* **2009**, *48*, 2978-2982.
- [232] S. Roy, K. C. Mondal, L. Krause, P. Stollberg, R. Herbst-Irmer, D. Stalke, J. Meyer, A. C. Stückl, B. Maity, D. Koley, S. K. Vasa, S. Q. Xiang, R. Linser, H. W. Roesky, *J. Am. Chem. Soc.* **2014**, *136*, 16776-16779.

- [233] A. Schnepf, R. Köppe, *Angew. Chem.* **2003**, *115*, 940-942; *Angew. Chem. Int. Ed.* **2003**, *42*, 911-913.
- [234] R. R. Picard, R. D. Cook, *JASA* **1984**, *79*, 575-583.
- [235] I. J. Tickle, R. A. Laskowski, D. S. Moss, *Acta Crystallogr.* **2000**, *D 56*, 442-450.
- [236] J. Luebben, T. Gruene, *Proc. Natl. Acad. Sci. U.S.A.* **2015**.
- [237] A. Volkov, P. Macchi, L. J. Farrugia, C. Gatti, P. R. Mallinson, T. Richter, T. Koritsanszky, *XD2006 - Manual* **2007**.
- [238] B. Zarychta, J. Zaleski, J. Kyziol, Z. Daszkiewicz, C. Jelsch, *Acta Crystallogr.* **2011**, *B 67*, 250-262.
- [239] B. Zarychta, J. Zaleski, J. Kyziol, Z. Daszkiewicz, C. Jelsch, *Acta Crystallogr.* **2011**, *B 67*, 379.
- [240] A. Paul, M. Kubicki, C. Jelsch, P. Durand, C. Lecomte, *Acta Crystallogr.* **2011**, *B 67*, 365-378.
- [241] S. Domagala, B. Fournier, D. Liebschner, B. Guillot, C. Jelsch, *Acta Crystallogr.* **2012**, *A 68*, 337-351.
- [242] F. F. Porcher, M. Souhassou, C. E. P. Lecomte, *Phys. Chem. Chem. Phys.* **2014**, *16*, 12228-12236.
- [243] M. Ahmed, M. Yar, A. Nassour, B. Guillot, C. Lecomte, C. Jelsch, *J. Phys. Chem.* **2013**, *A 117*, 14267-14275.
- [244] B. Zarychta, V. Pichon-Pesme, B. Guillot, C. Lecomte, C. Jelsch, *Acta Crystallogr.* **2007**, *A 63*, 108-125.
- [245] C. Jelsch, B. Guillot, A. Lagoutte, C. Lecomte, *J. Appl. Crystallogr.* **2005**, *38*, 38-54.
- [246] B. Guillot, L. Viry, R. Guillot, C. Lecomte, C. Jelsch, *J. Appl. Crystallogr.* **2001**, *34*, 214-223.
- [247] L. Krause, *XDRfree* unpublished program,
- [248] M. S. Schmökel, S. Cenedese, J. Overgaard, M. R. V. Jørgensen, Y.-S. Chen, C. Gatti, D. Stalke, B. B. Iversen, *Inorg. Chem.* **2012**, *51*, 8607-8616.
- [249] J. Hey, *From X-ray diffraction data annealing to comprehensive charge density analysis*, Institut für Anorganische Chemie, Georg-August-Universität (Göttingen), **2013**.
- [250] P. P. Samuel, R. Azhakar, R. S. Ghadwal, S. S. Sen, H. W. Roesky, M. Granitzka, J. Matussek, R. Herbst-Irmer, D. Stalke, *Inorg. Chem.* **2012**, *51*, 11049-11054.
- [251] C. B. Hubschle, G. M. Sheldrick, B. Dittrich, *J. Appl. Crystallogr.* **2011**, *44*, 1281-1284.

13 Curriculum vitae

PERSONAL DETAILS

Surname: Niepötter
First name: Benedikt
Date of Birth: March 30th 1988
City of Birth: Hannover
Nationality: German
Address: Kurze-Geismar Str. 37, 37073 Göttingen, Germany
Email address: bnipoetter@chemie.uni-goettingen.de

SCIENTIFIC CAREER

Oct. 2012-Current **PhD:** *Prof. Dr. D. Stalke, Georg August University Göttingen, Germany*
PhD Thesis: 'Structural analysis of low valent tetrels'

Oct. 2010 – Oct. 2012 **Master in chemistry and mathematics (M.Ed.):**
Prof. Dr. D. Stalke, Georg August University Göttingen, Germany
Master thesis: "Structure Analysis of Low Valent Silicon Compounds"
Master's degree - mark "excellent with distinction" (1.1)

Oct. 2007 – Oct. 2010 **Bachelor in chemistry and mathematics:**
Prof. Dr. U. Diederichsen, Georg August University Göttingen, Germany
Bachelor thesis: "Dynamic chemistry on modified DNA"
Bachelor's degree - mark "excellent" (1.5)

Aug. 2002 – June 2007 **Allgemeine Hochschulreife (baccalaureate):**
Grammar school Hölty-Gymnasium, Wunstorf, Germany
Abitur - mark "good" (1.7)

PROFESSIONAL CAREER

Mar. 2013-Current	Radiation protection commissioner in the group of <i>Prof. Dr. D. Stalke, Georg August University Göttingen, Germany</i>
Oct. 2012-Current	Scientific co-worker in the group of <i>Prof. Dr. D. Stalke, Georg August University Göttingen, Germany</i>
Mar. 2012- Oct. 2012	Undergraduate scientific co-worker in the group of <i>Prof. Dr. D. Stalke, Georg August University Göttingen, Germany</i>
Oct. 2011-Mar. 2012	Undergraduate scientific co-worker in the group <i>Prof. Dr. T. Waitz, Georg August University Göttingen, Germany</i>

SCHOLARSHIPS

Mar. 2015-Oct. 2015	Scholarship of the Institute of Inorganic Chemistry Georg August University Göttingen
Mar. 2013-Feb. 2015	Scholarship of the German Chemical Industry Fund for PhD students
Mar. 2012	Scholarship of the German Chemical Industry Fund for students of the Master of Education
Oct. 2010	Scholarship of the Ministry of science and culture for excellent Bachelor degrees
Apr. 2010-Sep. 2012	Scholarship of the German National Academic Foundation for gifted students (Studienstiftung des deutschen Volkes)

SCIENTIFIC RESEARCH PLACEMENTS:

Jan. 2015	XPAD experiments at CRM2 lab, <i>Université de Lorraine, Nancy, France</i>
Nov. 2013 – Dec. 2013	Spallation Neutron Source, <i>Oak Ridge National Laboratory, Tennessee, USA</i>
Mar. 2013	Advanced Photon Source, <i>Argonne National Laboratory, Illinois, USA</i>

PUBLICATIONS:

- Kartik Chandra Mondal, Herbert W. Roesky, Felix Klinke, Martin C. Schwarzer, Gernot Frenking, Benedikt Niepötter, Hilke Wolf, Regine Herbst-Irmer, Dietmar Stalke „A stable singlet biradicaloid siladiborene - (L:)2Si” *Angew. Chem.* **2013**, *125*, 1845-1850; *Angew. Chem. Int. Ed.* **2013**, *52*, 1801-1805 [Highlighted in *Nachrichten aus der Chemie*, **2014**, *62*, 3].

- Kartik Chandra Mondal, Herbert W. Roesky, Martin C. Schwarzer, Gernot Frenking, Sven Neudeck, Igor Tkach, Hilke Wolf, Daniel Kratzert, Regine Herbst-Irmer, Benedikt Niepötter, Dietmar Stalke „Conversion of a Singlet Silylene to a stable Biradical” *Angew. Chem.* **2013**, 125, 3036-3040; *Angew. Chem. Int. Ed.* **2013**, 52, 2963-2967 [VIP article, selected for back cover page; Highlighted in *Nachrichten aus der Chemie*, **2014**, 62, 3].
- Kartik Chandra Mondal, Prinson P. Samuel, Mykyta Tretiakov, Amit Pratap Singh, Herbert W. Roesky, A. Claudia Stückl, Benedikt Niepötter, Elena Carl, Hilke Wolf, Regine Herbst-Irmer, Dietmar Stalke „Easy Access to Silicon(0) and Silicon(II) Compounds” *Inorg. Chem.* **2013**, 52, 4736-4743.
- Mykyta Tretiakov, Yuriy G. Shermolovich, Amit Pratap Singh, Prinson P. Samuel, Herbert W. Roesky, Benedikt Niepötter, Arne Visscher, Dietmar Stalke „Lewis-Base Stabilized Diiodine Adducts with N-Heterocyclic Chalcogenamides” *Dalton Trans.* **2013**, 42, 12940–12946.
- Benedikt Niepötter, Regine Herbst-Irmer, Daniel Kratzert, Prinson P. Samuel, Kartik C. Mondal, Herbert W. Roesky, Paul Jerabek, Gernot Frenking, Dietmar Stalke „Experimental Charge Density Study of a Silylone” *Angew. Chem.* **2014**, 126, 2806–2811; *Angew. Chem. Int. Ed.* **2014**, 53, 2766-2770.
- Kartik Chandra Mondal, Prinson P. Samuel, Herbert W. Roesky, Benedikt Niepötter, Regine Herbst-Irmer, Dietmar Stalke, Fabian Ehret, Wolfgang Kaim, Bholanath Maity, Debasis Koley „Synthesis and Characterization of a Triphenyl-Substituted Radical and an Unprecedented Formation of a Carbene-Functionalized Quinodimethane” *Chem. Eur. J.* **2014**, 20, 9240-9245.
- Sudipta Roy, Kartik C. Mondal, Jann Meyer, Benedikt Niepötter, Christian Köhler, Regine Herbst-Irmer, Dietmar Stalke, Birger Dittrich, Diego M. Andrada, Gernot Frenking, and Herbert W. Roesky, „Synthesis, Characterization, and Theoretical Investigation of Two-Coordinate Palladium(0) and Platinum(0) Complexes Utilizing π -Accepting Carbenes.” *Chem. Eur. J.*, **2015**, 21, 9312-9318.
- Svenja Warratz, Christoph Kornhaas, Ana Cajaraville, Benedikt Niepötter, Dietmar Stalke, and Lutz Ackermann, „Ruthenium(II)-Catalyzed C-H Activation/Alkyne Annulation by Weak Coordination with O₂ as the Sole Oxidant.” *Angew. Chem.* **2015**, 127, 5604–5608; *Angew. Chem. Int. Ed.* **2015**, 54, 5513–5517.
- Chandrajeet Mohapatra, Kartik C. Mondal, Prinson P. Samuel, Helena Keil, Benedikt Niepötter, Regine Herbst-Irmer, Dietmar Stalke, Sayan Dutta, Debasis Koley, „A Stable Dimer of SiS₂ Arranged between Two Carbene Molecules.” *Chem. Eur. J.* **2015**, 21, 12572-12576.

- Benedikt Niepötter, Regine Herbst-Irmer, Dietmar Stalke, „Empirical Correction for Resolution- and Temperature-Dependent Errors Caused by Factors such as Thermal Diffuse Scattering”, *J. Appl. Cryst.*, **2015**, *48*, 1485-1497
- Dhandapani Ganapathy, Johannes R. Reiner, Lorenz E. Löffler, Ling Ma, Boopathny Gnanaprakasam, Benedikt Niepötter, Ingo Köhne, Lutz F. Tietze, „Enantioselective Total Synthesis of Secalonic Acid E”, *Chem Eur. J.*, **2015**, *21*, 16807-16810

SCIENTIFIC CONFERENCES:

Sep. 2012	Wöhlertagung, <i>Göttingen, Germany</i> - Poster
June 2013	Gordon Research Conference for Electron Distribution & Chemical Bonding, <i>Les Diablerets, Switzerland</i> - Poster
June 2013	Center for Materials Crystallography Conference, <i>Aarhus, Denmark</i> - Poster
Dec. 2013	Annual meeting of the German Chemical Industry Fond fellows, <i>Jena, Germany</i> - Talk
Mar. 2014	Center for Materials Crystallography Conference, <i>Göttingen, Germany</i> - Talk
June 2015	Center for Materials Crystallography Conference, <i>Aarhus, Denmark</i> - Talk
July 2015	Jung Chemiker Forum (GDCh), <i>Göttingen, Germany</i> - Poster

MISCELLANEOUS SKILLS:

Languages	German (native language) English (fluent) Latin (latin proficiency certificate) Dutch (basic knowledge)
Radiation protection	Qualification: S1.1, S1.2, S1.3, S2.1, S2.2, S5, S6.1 (StrSchV) and R2.1 (RöV)
EDV	Advanced knowledge in crystallographic refinement software: Shelxtl package, ApexII, Platon, Mercury, MolecoolQt and XD2006 Advanced knowledge in MS-Office software
Programming	Python (advanced)
Voluntary work	Speaker of the des Khg-hostel Göttingen (2009-2012) Elected member of the council of the Catholic Church in Hohnhorst/Lindhorst (2006-2010)